OAK RIDGE NATIONAL LABORATORY LIBRARIES
3 4456 0570481 4

CENTRAL RESEARCH LIBRARY

ORNL-4963

Cy 3

MECHANICAL PROPERTIES TEST DATA FOR STRUCTURAL MATERIALS

QUARTERLY PROGRESS REPORT

FOR PERIOD ENDING APRIL 30, 1974

LIBRARY
REFERENCE COPY

[redacted]

OAK RIDGE NATIONAL LABORATORY
OPERATED BY UNION CARBIDE CORPORATION • FOR THE U.S. ATOMIC ENERGY COMMISSION

Printed in the United States of America. Available from
the U.S. Atomic Energy Commission, Technical Information Center
P.O. Box 62, Oak Ridge, Tennessee 37830
Price: Printed Copy $7.60 ; Microfiche $1.45

This report was prepared as an account of work sponsored by the United States Government. Neither the United States nor the United States Atomic Energy Commission, nor any of their employees, nor any of their contractors, subcontractors, or their employees, makes any warranty, express or implied, or assumes any legal liability or responsibility for the accuracy, completeness or usefulness of any information, apparatus, product or process disclosed, or represents that its use would not infringe privately owned rights.

ORNL-4963
UC-79b, -h, -k
(Liquid Metal Fast
Breeder Reactors)

Contract No. W-7405-eng-26

METALS AND CERAMICS DIVISION

MECHANICAL PROPERTIES TEST DATA FOR STRUCTURAL MATERIALS QUARTERLY PROGRESS REPORT FOR PERIOD ENDING APRIL 30, 1974

Aerojet Nuclear Company
Argonne National Laboratory
Hanford Engineering Development Laboratory
Naval Research Laboratory
Oak Ridge National Laboratory
Westinghouse Advanced Reactors Division
University of Cincinnati
University of California at Los Angeles

Compiled by M. R. Hill

JUNE 1974

OAK RIDGE NATIONAL LABORATORY
Oak Ridge, Tennessee 37830
operated by
UNION CARBIDE CORPORATION
for the
U.S. ATOMIC ENERGY COMMISSION

Reports previously issued in this series are as follows:

ORNL-4936	Period Ending October 31, 1973
ORNL-4948	Period Ending January 31, 1974

CONTENTS

SUMMARY ix

1. AEROJET NUCLEAR COMPANY 1

1.1 INTRODUCTION 1

1.2 INCONEL 718 CODE CASE AND RELATED INVESTIGATIONS 2

1.2.1 Development of a Modified Heat Treatment for Inconel 718 2

2. ARGONNE NATIONAL LABORATORY 11

2.1 INTRODUCTION 11

2.2 FRACTURE AND FATIGUE STUDIES ON STAINLESS STEELS 11

2.2.1 Low-cycle, Creep-fatigue Behavior of Type 304 Stainless Steel 11

2.2.2 Crack-propagation of SMA Type 304/308 Stainless Steel Weldments 18

2.2.3 Effects of Surface Roughness on the Low-cycle Fatigue Behavior of Type 304 Stainless Steel . . . 23

2.2.4 Effect of Environment and Frequency on Low-cycle Fatigue Life of Type 304 Stainless Steel 37

2.3 REFERENCES 42

3. HANFORD ENGINEERING DEVELOPMENT LABORATORY (no report) 45

4. NAVAL RESEARCH LABORATORY 47

4.1 INTRODUCTION 47

4.2 FATIGUE CRACK GROWTH IN TYPE 304 AND 316 STAINLESS STEEL WELDMENTS 47

4.2.1 Background 47

4.2.2 Test Procedures 47

4.2.3 Results 48

4.3 TOUGHNESS OF TYPE 316 STAINLESS STEEL WELD METAL USING THE J INTEGRAL 55

4.3.1 Background 55

4.3.2 Experimental Investigation 55

4.3.2.1 Material and Specimen Types 55

4.3.2.2 Results 56

4.3.3 Discussion 56

4.4 REFERENCES 59

5. OAK RIDGE NATIONAL LABORATORY 61

5.1 INTRODUCTION 61

5.2 MECHANICAL PROPERTIES AND BEHAVIOR FOR STRUCTURAL MATERIALS 61

5.2.1 Base-Line Mechanical Property Testing of Reference Heat of Type 304 Stainless Steel 61

5.2.1.1 Creep Properties of the 2-in. (51-mm) Plate of Reference Heat 61

5.2.2 Heat-to-Heat Variation Study of Type 304 Stainless Steel 81

5.2.2.1 Long-Term Creep Tests in Heat-to-Heat Variation Study 81

5.2.2.2 Effect of Aging on the Tensile Properties. 84

5.2.2.2.1 Effect of Aging Temperature . . 94

5.2.2.2.2 Effect of Aging Time 98

5.2.2.3 Transmission Electron Microscopy of Heat-to-Heat Variations of Type 304 Stainless Steel 104

5.2.2.4 Influence of Aging on the Creep Properties of Type 304 Stainless Steel . . 108

5.2.3 Mechanical Properties of Type 316 Stainless Steel . 109

5.2.3.1 Procurement of Type 316 Stainless Steel Reference Heat 109

5.2.3.2 Heat-to-Heat Variation Studies of Type 316 Stainless Steel 110

5.2.4 Failure Criteria — Strain Limits 119

5.2.5 Measurement of Elastic Constants of 2 1/4 Cr-1 Mo Steel by the Dynamic Method 126

5.2.6 Analytical Studies of Mechanical Properties Testing 131

5.2.6.1 Investigation of Bending in an Axially Loaded Specimen 133

5.2.6.2 Stress Analysis of the Hourglass Fatigue Specimen 134

5.2.6.3 Buckling Analysis of a Hollow Tubular Biaxial Specimen 135

5.3 MECHANICAL AND METALLURGICAL BEHAVIOR OF WELDMENTS FOR LMFBR 135

5.3.1 Effect of Postweld Heat Treatment on the Tensile Properties of Type 308 Stainless Steel Weld Metal with Controlled Residual Elements 135

5.3.2 Creep and Creep-Rupture Properties of Type 308 CRE Stainless Steel Weld Metal From the FFTF Vessel Test Welds 140

5.3.3 Deformation Characteristics of Whole Weldment Cross Sections 143

5.4 MECHANICAL PROPERTIES OF STEAM GENERATOR MATERIALS 152

5.4.1 Tensile Properties of 2 1/4 Cr-1 Mo Steel 152

5.4.2 Cyclic Creep of Decarburized 2 1/4 Cr-1 Mo Steel Tubes 158

5.4.3 Mechanical Properties of Weld-Overlaid Stainless Steel Forgings 161

5.4.3.1 Tensile Properties 161

5.4.3.2 Creep-Rupture Properties 168

5.4.4 Minimum Creep Rate of 2 1/4 Cr-1 Mo Steel 169

5.4.5 Subcritical Crack Growth and Fatigue of 2 1/4 Cr-1 Mo Steel 172

5.5 HIGH-TEMPERATURE DESIGN 174

5.5.1 Exploratory Testing to Identify Behavioral Features 174

5.5.1.1 Development of Laboratory Facilities . . . 174

5.5.1.2 Stress-STrain Testing 175

5.5.1.3 Creep Testing 190

5.5.2 Characterization of Product Form 195

5.5.3 Investigation of Creep Failure Under Uniaxial and Multiaxial Conditions 195

5.6 MECHANICAL PROPERTIES OF HTGR STEAM GENERATOR AND PRIMARY CIRCUIT MATERIALS. 195

5.7 REFERENCES 197

6. WESTINGHOUSE ADVANCED REACTORS DIVISION 201

6.1 INTRODUCTION 201

6.2 BASIC SPECIMEN TESTING 201

6.2.1 Uniaxially Loaded Specimen Models with Uniform Gage Section (304 SS, Heat 9T2796) 201

6.2.1.1 Test Piece Description 201

6.2.1.2 Current Results 201

6.2.2 Uniaxially Loaded Specimen Models with Non-Uniform Gage Section 201

6.2.2.1 Test Piece Description 201

6.2.2.2 Current Results 209

6.2.3 Specimens with Welds 209

6.2.4 Discussion of Permanent Strain Limits 209

6.2.4.1 Flow and Fracture 209

6.2.4.2 Deformation Characteristics 212

6.2.4.2.1 Influence of State of Stress . . 215

6.2.4.2.2 Strain Limits. 216

6.3 TUBULAR SPECIMEN TESTING 219

6.3.1 Test Piece Description 219

6.3.2 Uniaxial Creep Testing (304SS, Heat 9T2796 ORNL Reference Heat) 219

REFERENCES 221

7. UNIVERSITY OF CINCINNATI 225

7.1 INTRODUCTION 225

7.2 EXPERIMENTAL PROGRAM 225

7.2.1 Some Aspects of Dislocation Mechanisms During Creep of AISI 316 and 304 Stainless Steel 226

7.2.2 Deformation Substructure of AISI 304 and Incoloy 800 from Push-Pull Fatigue at Elevated Temperatures 228

7.2.3 Substructure Strengthening of Room Temperature Mechanical Properties in Incoloy 800 and AISI 304 Stainless Steel 235

7.2.4 Comparison of Fatigue Properties When Tested in the Bend and Push-Pull Mode 237

7.2.5 Effect of Hold Time During Low Cycle Fatigue on the Substructure Formation Developed at Elevated Temperatures in 304 Stainless Steel 241

7.2.6 Analysis of Relationships of Creep Rate, Stress and Temperature for 304 Stainless Steel 242

7.2.7 Estimation of Activation Energy for Creep from Hot Hardness Measurements of 304 Stainless Steel . . 249

7.2.8 Correlation of Hot Hardness with Elevated Temperature Tensile Properties of Cold Worked 316 Stainless Steel 252

7.2.9 Recovery and Recrystallization Behavior of Cold Worked 316 Stainless Steel 254

7.3 REFERENCES 259

8. UNIVERSITY OF CALIFORNIA AT LOS ANGELES 261
8.1 INTRODUCTION 261
8.2 MICROSTRUCTURAL RESULTS 261
8.2.1 Normalized and Normalized and Tempered Conditions . 261
8.2.2 Long-Term Tempered Conditions of Low Carbon (0.009% C) 2 1/4 Cr-1 Mo Alloy 262
8.2.2.1 Tempering at 850°F 262
8.2.2.2 Tempering at 950°F 265
8.2.2.3 Tempering at 1050°F 271
8.3 MECHANICAL PROPERTIES 276
8.3.1 Room-Temperature Tensile Properties 276
8.3.2 Creep Properties 279
8.4 REFERENCES. 281
INDEX 283

SUMMARY

1. AEROJET NUCLEAR COMPANY

Additional tests are reported from efforts to improve the mechanical properties of Inconel Alloy 718 through modifications of conventional thermal treatments. The data include tensile properties at both ambient and elevated temperatures, stress-rupture properties at 1400°F (760°C), and room temperature Charpy impact properties, for one heat of material, plus tensile data from 1000°F (538°C) to 1600°F (871°C) for control and simulated heat-affected zone samples of other heats. Tensile and bend test data from weldability studies are also presented.

Data are summarized for one heat of material for various conditions resulting from solution annealing at 2000°F (1093°C), followed by cooling at three different rates to below 1000°F (538°C), and subsequent duplex aging at either 1400/1200°F (760/649°C) or 1325/1150°F (718/621°C). For the simulated HAZ studies, the samples were heated to 2250-2270°F (1232-1243°C) and cooled, followed by a 2000°F (1093°C) solution anneal and slow cool to below 1000°F (<538°C). Preweld conditioning heat treatments were attempted. These involved both 2000°F (1093°C) and 1750°F (954°C) solution anneals plus fast and slow cooling rates before thermally cycling to 2250°F (1232°C). In the weldability studies, postweld solution annealing was done at both 1900°F (1038°C) and 2000°F (1093°C). Slow (100°F/hr, 55.5°C/hr), intermediate (400°F/hr, 222°C/hr), and fast (1200°F/hr, 667°C/hr) cooling rates were used, and both the 1400/1200°F (760/649°C) and 1325/1150°F (718/621°C) aging cycles were used.

2. ARGONNE NATIONAL LABORATORY

A number of slow strain-rate and tension-hold-time low-cycle fatigue tests on Type 304 stainless steel have been completed, and the data have been plotted in the log time to failure versus log cycles to failure representation suggested by Esztergar. The 482°C (900°F) slow strain-rate and tension hold-time data are rather sparse, but a smaller than anticipated influence of strain rate on fatigue life at this temperature is indicated. At 649°C (1200°F), the ANL data verify a tendency toward a saturation in cycles to failure with increasing tension hold time, a tendency previously suggested by the data of Conway. At 593°C (1100°F), however, the data show an unexpected tendency toward a saturation in <u>time</u> to failure with increasing tension hold time. In view of this dichotomy, the utility of the log time-log cycles plot in extrapolating data of this type must be questioned.

Crack-propagation studies of SMA Type 304/308 stainless steel weldments indicate that when the stress-intensity factor range (ΔK) is corrected for the plastic zone and designated as $\Delta K'$ a good logarithmic linear fit of $\Delta K'$ versus the crack-growth rate (da/dN) is obtained. The slopes (m) were 1.99 ± 0.06, 2.69 ± 0.10, and 1.75 ± 0.04 for aged base metal, aged weld metal, and as-welded weld metal, respectively. Without plastic zone correction, changes in logarithmic slopes are necessary for ΔK versus da/dN. The tests were conducted with single-edge-notch (SEN)

specimens under uniaxial tension loading in sawtooth stress wave form at 1100°F temperature, 0.5 stress ratio, and 30 cpm frequency with 1-min tension hold time at 50-mil crack-length intervals.

The effects of surface roughness on low-cycle fatigue life of Type 304 stainless steel at 593°C in air have been investigated. It is observed that, at a strain rate of 4×10^{-3} sec^{-1} and a total strain range of 1%, the fatigue life decreases with an increase in surface roughness. Information on crack growth versus strain cycles has been generated as a function of surface roughness by the measurement of striation spacing on fractured surfaces of specimens tested to failure. An analysis of the data is presented to show how surface roughness decreases the crack-initiation time and not the number of cycles spent in crack propagation. Furthermore, an analysis of the data based on current crack-propagation models shows that the effect of surface roughness is to reduce the crack-propagation rate.

The influence of frequency and environment on the low-cycle fatigue life of Type 304 stainless steel at 650°C has been examined. It is shown that Coffin's high-temperature modification of the low-temperature Coffin-Manson equation is capable of predicting fatigue life within $\pm$ 50% error, when the data obtained in air with zero hold time and tension hold times as long as 10 hr are included in the analysis of the data. A comparison of the ANL data obtained in air at 650°C with those obtained in vacuum $< 10^{-7}$ torr reported in the literature has been made for two frequencies (0.39 and 39 cpm). It is observed that frequency effects are present and small in high vacuum, but are pronounced in an air environment.

3. HANFORD ENGINEERING DEVELOPMENT LABORATORY

(No Report)

4. NAVAL RESEARCH LABORATORY

The fatigue crack growth resistance of Type 304 and 316 stainless steel submerged arc weldments was investigated at 77, 800, and 1100 F (24, 427, and 593 C). Rates of crack growth were determined as a function of the stress intensity factor range. In general, the crack growth resistance of weld metal was about the same or greater than that of the base metal. The superior fatigue resistance of weld metal appears to be related to microstructure differences between the weld and plate material.

The J Integral is being employed to characterize the elevated temperature toughness of austenitic stainless steel and nickel-base alloys for FBR application. Notched, three point bend specimens having a/W ratios between 0.3 and 0.5 were loaded statically and J Integral was calculated using an approximate equation. The R curve technique has been used to define the critical J_{Ic} for Type 316 stainless steel weld metal at 500 F (260 C). The J values were found to vary significantly with the slow stable (rising load) crack extension that occurred between the point of crack initiation, corresponding to J_{Ic}, and the point of maximum load.

5. OAK RIDGE NATIONAL LABORATORY

Creep and creep-rupture testing of the type 304 stainless steel reference heat (9T2796) is continuing. Rupture data taken thus far over the range 538 to 704°C (1000–1300°F) compared with minimum stress-rupture plots from Code Case 1331-8 indicate that the Code is conservative for this heat. Interim creep data as well as partially constructed isochronous stress-strain curves are given. Comparisons of the isochronous stress-strain curves with those given in the Code for this heat over the temperature range of 427 to 704°C (800–1300°F) are presented. Comparison of strain-time data for this heat at 483°C (900°F) with predicted strain behavior as given by the HEDL double-exponential equation showed considerable variation, primarily because this heat exhibits more primary creep than predicted by the double-exponential equation. Comparisons at 593 and 704°C (1100 and 1300°C) were also made. An eight-term polynomial equation expressing strain as a function of time was used to fit the data over both the primary and secondary stages of creep.

Aging of several heats of type 304 stainless steel substantially changed creep behavior. Both $\dot{\varepsilon}_m$ and fracture strain increased with aging, and both increases and decreases in rupture time were found, depending upon aging temperature and specific material. Aging generally increased the yield strength; however, the extent to which this occurred was also temperature and time dependent. Both increases and decreases in ductility were found, depending upon specific material, aging time, temperature, and the measure of ductility chosen.

Procurement of the type 316 stainless steel reference heat is under way, with delivery of forging product expected in June and the pipe in September.

Seven wrought and one as-cast heat of type 316 stainless steel are currently undergoing mechanical property evaluation. Results from tensile tests conducted thus far on as-received material have indicated that all yield strengths are above ASME Code Case 1331-8 values except that for the as-cast material. However, upon annealing the number of heats falling below Code values increases with temperature. Aging for 1000 hr at 649°C (1200°F) increased the yield strength and slightly decreased tensile ductility in comparison with reannealed material. Stress-rupture lifetimes of the cast material were inferior to that of wrought material. Comparisons are made with Code values.

Progress is reported concerning recent data correlations and planned experimentation for establishing a material-based strain limit for both base and weldment materials.

Elastic property (i.e., Young's and shear moduli and Poisson's ratio) determinations are currently under way for reactor structural materials over the range 25 to 825°C (77 to 1517°F). Values for 2 1/4 Cr-1 Mo steel over the interval 25 to 760°C (77 to 1400°F) are given.

Finite element analysis is currently under way for a number of specimen geometries currently in use or proposed for future testing. Results are reported.

The testing program to obtain design data on type 308 stainless steel welds with controlled residual elements (CRE) that are prototypic of certain FFTF vessel welds is continuing. Creep testing is complete at 482, 565, 593, and 649°C (900, 1050, 1100, and 1200°F) except for four long-time tests that have accumulated up to two years test time. The ductility of all failed longitudinal, all-weld-metal creep specimens exceeded 12%. The effects of postweld heat-treating for 2 hr at 982, 1038, 1093, 1149, and 1204°C (1800, 1900, 2000, 2100, and 2200°F) on the room-temperature properties of longitudinal all-weld-metal tensile specimens was explored. The yield strength was less than the minimum value for type 304 stainless steel base metal for heat treatment temperatures of 1149 and 1204°C (2100 and 2200°F). Room-temperature tensile tests were conducted on whole weldment cross-section specimens to assess the magnitude and distribution of stress and strain concentrations. The results indicated critical areas for location of strain gage monitors in later tests.

We completed a series of tensile tests on annealed 2 1/4 Cr-1 Mo steel over the range 25 to 593°C (77—1100°F) at strain rates of 0.4, 0.04, 0.004, and 0.0004/min. The portion of the true stress-true strain data between the 0.2% yield strength and the ultimate tensile strength were fitted to the Hollomon and Ludwik equations; the Hollomon equation gave the best fit. Cyclic creep tests on decarburized 2 1/4 Cr-1 Mo steel tubes were begun.

Further tensile tests from room temperature to 593°C (1100°F) were completed on specimens taken from a weld-overlaid type 304 stainless steel forging. Radial and tangential specimens from immediately adjacent to the overlay-forging fusion line were tested and showed that this material was stronger than the forging at some distance from the fusion line [further than 2 in. (approx 51 mm)] and stronger than the type 308 stainless steel weld metal. The creep-rupture properties of axial, radial, and tangential specimens from the forging unaffected by the overlay were determined at 593°C (1100°F).

We are preparing inputs on 2 1/4 Cr-1 Mo steel for the *Nuclear Systems Materials Handbook*. After examining a data base of approximately 200 creep tests, an interim model of an equation for calculating expected values of minimum creep rate has been formulated. We are also investigating the tolerance limits for these expected values. A test matrix has been defined for the fatigue testing of 2 1/4 Cr-1 Mo steel in air, steam, sodium, and helium. Subcritical crack growth studies are also under way.

Yield strength, ultimate strength, and uniform tensile strain data for the 1-in. (25.4-mm) plate of the reference heat of type 304 stainless steel were used to map surfaces showing the influence of strain rate and temperature on inelastic behavior. Significant progress was made in developing a model to describe the stress-strain behavior for this material over a broad range of strain, strain rate, and temperature. Interfaces between tensile and creep behavior are being examined. The parameters in the Norton equation describing the stress dependence of minimum creep rate, time to tertiary creep, and time to rupture have been evaluated for the range 538 to 816°C (1000–1500°F).

A laboratory is being set up for studying creep and other properties of Incoloy 800 and other alloys in steam and contaminated helium under anticipated HTGR conditions.

6. WESTINGHOUSE ADVANCED REACTORS DIVISION

Creep testing of the reference ORNL Type 304 stainless steel heat (9T2796) was continued with a variety of test specimen designs and conditions. Tests were performed on a variety of plate specimens with different loading conditions and testing of welded plate specimens was continued. One uniaxial and one multiaxial tubular tests were initiated and two multiaxial tests were completed.

7. UNIVERSITY OF CINCINNATI

Preliminary investigations were made on the comparison of the microstructure and room temperature hardness levels of Incoloy 800 specimens tested in the push-pull or bend fatigue mode. As expected, a strong hardness and microstructural gradient was observed across the thickness in the bend and not in the push-pull specimens.

Computer studies are carried out to evaluate the various creep parameters of the 304 stainless steel reference heat 9T2796. Preliminary results suggest an activation energy for creep of about 84 kcal/mole in reasonable agreement with the value of 87 kcal/mole obtained from hot hardness tests.

The interactions between the dislocations which form the subgrain boundaries and those which are sufficiently mobile to contribute to creep deformation are evaluated.

A prediction of the ultimate tensile stress of 20 percent cold worked 316 stainless steel based on hot hardness measurements is in reasonable agreement with experimental tensile results of similar material.

8. UNIVERSITY OF CALIFORNIA AT LOS ANGELES

The microstruture and deformation of 2 1/4 Cr—1 Mo steels are being studied as affected by aging time and temperature. For the steel having 0.12% C the normalized-and-tempered alloy has a bainitic structure, with heavy carbide precipitation. Low-carbon steels (0.009% C) consisted of polygonal ferrite. After aging the low-carbon steel for 12 to 19 months at 454°C (850°F), complete recrystallization and consequent grain growth were observed. At 566°C (1050°F), the same type of behavior was observed after about 4 months.

The room-temperature yield stress of the 0.12%-C steel in the normalized-and-tempered condition was effectively unchanged after aging at 454 and 510°C (850° and 950°F) for times up to 570 days. At 566°C (1050°F), the yield stress progressively decreased with time. Therefore the normalized-and-tempered alloy was relatively stable at 510°C (950°F) but not at 566°C (1050°F).

1. AEROJET NUCLEAR COMPANY

W. C. Francis

1.1 INTRODUCTION

Aerojet Nuclear Company is conducting mechanical properties investigations under two programs sponsored by the AEC Division of Reactor Research and Development. Program 06031, Fatigue Tests on Cladding and Structural Materials, involves experimental fatigue tests on stainless steel Types 304 and 316 as well as Type 304 weldments. These tests are intended to determine the influence of irradiation, cold work, heat treatment, heat-to-heat property variations, and temperature on fatigue behavior. Irradiated, thermal control, as-received, and annealed specimens are being tested at temperatures of 900 to 1300°F (482-703°C). Current work on the stainless steel program has dealt primarily with irradiation effects and this work will be reported in the Irradiation Effects Bi-annual Report compiled at HEDL.

Program 06084, Inconel Alloy 718 Code Case Project has as its objective the planning and testing activities deemed necessary to provide data and information on base metal and welded metal properties to satisfy requirements for Code Case approval from the ASME Boiler and Pressure Vessel Committee. The service temperature ranges: ambient to 800°F (427°C) and 800 to 1200°F (427-649°C), are covered in two separate phases of the experimental work, and a separate code case application will be submitted for each temperature range. Data from the literature are used wherever they appear sufficient. Otherwise, experimental programs were initiated to acquire the necessary data. Both base material and weldments are to be covered by the applications.

What has been considered standard heat treatments for Inconel 718 has not consistently yielded acceptable ductility values for the welded material. Current work involves scoping tests on material subjected to modified thermal treatments in an effort to optimize the heat treatment that will yield the best mechanical properties of both base and weld metal.

1.2 INCONEL 718 CODE CASE AND RELATED INVESTIGATIONS - D. D. Keiser, W. G. Reuter, G. R. Smolik, and H. L. Brown

1.2.1 Development of a Modified Heat Treatment for Inconel 718

Additional data are available from the program to improve the mechanical properties of Inconel 718 via modified heat treatment. The work reported here covers the behavior of base metal, simulated weld heat-affected zone material, and weldments. The effects of preweld conditioning heat treatments were examined briefly. Work is continuing on elevated temperature tensile testing for strain-age cracking susceptibility, elevated temperature stress-rupture testing, and strain-controlled fatigue testing. It must be emphasized that the data presented here are preliminary and may not be sufficient to adequately describe the general behavior of Inconel 718.

Tables 1.1 and 1.2 present, respectively, the room temperature tensile and impact data for heat 87C0EK-1. Data for heat 83C2EK3 are also included in Table 1.1. Table 1.3 summarizes the 1400°F (760°C) stress-rupture data for this heat. Material given the slow and intermediate cooling rates showed improved ductility at elevated temperatures over the results from a fast cool. Room temperature tensile and impact tests appear to show similar improvements in ductility and toughness, with minor loss of strength. Although the use of two different aging cycles precludes a complete comparison, results for different cooling rates for the same aging cycle would indicate that cooling rate may be the controlling factor.

Table 1.4 summarizes the elevated temperature (1000°F-1600°F) (538-871°C) tensile test data for parent material and simulated HAZ samples of heat 83C2EK3. The HAZ samples were induction-heated to 2250-2270°F (1232-1243°C). These samples and the parent material were then solution annealed at 2000°F (1093°C) and cooled at indicated rates below 1000°F (<530°C) before testing at the indicated temperature. In general, the HAZ samples show slightly lower ductility than the parent material, under the stated conditions for either slow or fast cooling.

A few data from the preliminary investigation of preweld conditioning heat treatments are given in Table 1.5. Samples were

solution annealed at both 1725°F (940°C) and 2000°F (1093°C), plus fast or slow cool as indicated. Some were then tensile tested at 1400°F (760°C), others were thermally cycled to 2250°F and then tested at 1400°F (760°C). The slower cooling rate appears to give improved ductility for samples which are subsequently thermally cycled. Further work on this approach is in progress.

Transverse tensile and side bend tests were made at room temperature on weldment material from several sources, subjected to a variety of heat treatments. Both manual and automatic welds were tested. Solution anneals at 2000°F (1093°C) gave improved ductility over 1900°F (1038°C) solution anneals. The data are summarized in Table 1.6.

Table 1.1. Room Temperature Tensile Properties

Heat 87COEK-1 Specimen	Thermal Treatment	0.2% Y.S. MPa	0.2% Y.S. ksi	U.T.S. MPa	U.T.S. ksi	% Elongation	% Reduction in Area
FS7	Solution-annealed at 1093°C, cooled. Aged 4 hr. at 718°C plus 16 hours @ 621°C	986	143	1372	199	20	31
FS8		1000	145	1386	201	20	29
FS9		1007	146	1393	202	20	29
F 7		1034	150	1344	195	25	36
FI8		1089	158	1351	196	24	33
FI9		1082	157	1351	196	24	35
FA7	Solution-annealed at 1093°C, cooled. Aged 10 hr. @ 760°C + 8 hr. @ 649°C	1062	154	1413	205	18	25
FA8		1103	160	1393	202	17	23
FA9		1055	153	1386	201	18	24
		Cooling Rates: 55.5°C/hr (FS), 400°C/hr (FI), and 667°C/hr. (FA)					
Heat 83C2EK3 Specimen							
BB-5	982°C S.R. 1093°C S.A., cooled 55.5°C/hr + age: 718°C (4 hr) + 621°C (24 hr)	1034	150	1361	197.4	16	14
-6		993	144	1351	196.0	17	17
BB-7	982°C S.R. 1093°C S.A., cooled 222° C/hr + age: 718°C (4 hr) 621°C (16 hr)	---	---	1302	188.8	24	27
-8		---	---	1306	189.5	25	26

Table 1.2. Room Temperature Impact Properties, Heat 87COEK-1

Specimen	Thermal Treatment	Energy-Absorbed Joule	Energy-Absorbed ft-lb	Lateral Deformation cm	Lateral Deformation inch	Shear
FS10	Solution-annealed	66.4	49.0	•069	.027	100%
FS11	@ 1093°C, cooled	69.8	51.5	•071	.028	100%
FS12	Aged 4 hr. ± 718°C + 16 hr. @ 621°C	72.5	53.5	•074	.029	100%
FI10		80.0	59.0	•079	.031	100%
FI11		81.3	60.0	•081	.032	100%
FI12		82.7	61.0	•081	.032	100%
FA10	Solution annealed	54.2	40.0			
FA11	@ 1093°C, cooled	54.9	40.5			
FA12	Aged 10 hr. @ 760°C + 8 hr. @ 649°C	59.6	44.0			

Cooling Rates: 55.5°C/hr (FS), 222°C/hr (FI), 667°C/hr (FA).

Table 1.3. 760°C (1400°F) Stress Rupture Test Data
Heat 87COEK-1

Specimen	Thermal Treatment	Stress Level MPa	Stress Level ksi	Specimen Insertion Temp. °F	Specimen Insertion Temp. °C	Time, Hours: to 760°C (1400°F)-Total	Temp. @ Failure °F	Temp. @ Failure °C	% Elong.	% Reduction in Area
FS1	All material solution-annealed @ 1093°C (2000°F), cooled as indicated, not aged	545	79	700	371	1.0 - 3.9	1400	760	19	26
FS2		483	70	500	260	1.9 - 11.4	1400	760	22	29
FS3		483	70	810	432	1.0 - 9.3	1400	760	23	30
FS4		545	79	700	371	1.3 - 3.6	1400	760	25	29
FS5		414	60	700	371	0.9 - 29.3	1400	760	22	32
FS6		Tensile Test				Y.S. - 95,200	U.T.S. 110,000		14	18
FI1		545	79	675	357	1.3 - 2.2	1400	760	8	14
FI2		483	70	725	385	0.9 - 8.7	1400	760	25	28
FI3		483	70	750	399	1.2 - 8.4	1400	760	21	20
FI4		545	79	750	399	0.8 - 1.4	1400	760	5	16
FI5		414	60	690	366	0.8 - 26.0	1400	760	23	28
FI6		Tensile Test				Y.S. - 87,900	U.T.S. 103,000		10	16
FA1		545	79	800	427	0.7 - 0.7	1400	760	5	19
FA2		483	70	830	443	0.9 - 5.3	1400	760	9	13
FA3		483	70	770	410	0.7 - 2.8	1400	760	5	10
FA4		414	60	950	510	0.6 - 31.1	1400	760	25	27
FA5		414	60	800	427	0.6 - 30.0	1400	760	23	31
FA6		414	60	800	427	0.8 - 28.2	1400	760	25	34

Cooling Rates: 55.5°C/hr (100°F/hr) (FS), 222°C/hr (400°F/hr) (FI), 649 °C/hr (1200°F/hr) (FA)

Table 1.4. Elevated Temperature Tensile Tests of Simulated Heat-Affected Zone and Parent Metal Samples Heat 83C2EK3

Specimen	Testing Temperature °F	Testing Temperature °C	.2% Y.S. ksi	.2% Y.S. MPa	U.T.S. ksi	U.T.S. MPa	% Elongation	% Reduction in Area
HS1	1200	649	101	696	142	979	13	16
HS2	1300	704	100	689	127	876	15	17
HS3*	1200	649	116	800	148	1020	6	9
HS4	1300	704	104	717	134	924	12	16
HS5	1500	816	74	510	80.2	553	18	19
HS6	1100	573	103	710	153	1055	9	14
HS7	1000	538	104	717	150	1034	8	14
HS8*	1200	649	120	827	150	1034	5	9
HS9	1300	704	102	703	133	917	5	9
HS10	1400	760	93.8	647	114	786	12	15
PS1	1300	704	101	696	138	951	15	17
PS3*	1200	649	118	813	151	1041	16	18
PS4*	1200	649	118	813	155	1069	13	16
PS5	1400	760	93	641	103	710	17	19
PS7	1200	649	100	689	152	1048	15	17
PS8	1000	538	100	689	158	1089	16	17
PS9	1500	816	70.4	485	80.6	556	16	18
PS10	1100	593	103	710	159	1096	14	15
HF1	1300	704	92	634	124	855	15	22
HF2	1400	760	84.7	584	97.8	674	7	9
HF3	1500	816	73.4	506	84.6	583	7	14
HF4	1600	871	45.9	316	46.7	322	41	56
HF5	1200	649	86.5	596	120	827	13	20
HF6	1100	593	84.4	582	108	745	9	21
HF7	1400	760	86.3	595	103	710	7	14
HF8	1250	677	91.1	628	121	834	11	20
HF9	1550	843	60.9	420	64.8	44.8	28	44
HF10**	1200	649	131	903	157	1082	7	8
HF11**	1200	649	130	896	159	1096	8	12
PF1**	1200	649	130	896	159	1096	14	19
PF2**	1200	649	129	889	158	1089	16	16
PF3	1300	704	89.6	618	122	841	22	35
PF4	1500	816	71.0	490	83.4	575	9	15
PF5	1400	760	85.5	590	98	676	7	16
PF6	1400	760	89.3	616	110	758	10	16
PF7	1600	871	44.7	308	46.1	318	41	61
PF8	1200	649	78.2	539	118	813	30	33
PF9	1550	843	62.8	433	67.4	465	19	22

Table 1.4 (Continued)

Nomenclature:

HS: Heat Affected Zones with slow cool (55.5°C/hr, 100°F/hr) from solution anneal temperature.
PS: Parent Metal with slow cool (55.5°C/hr, 100°F/hr) from solution anneal temperature.
HF: Heat Affected Zones with fast cool (649°C/hr, 1200°F/hr) from solution anneal temperature.
PS: Parent Metal with fast cool (649°C/hr, 1200°F/hr) from solution anneal temperature.

Note: HAZ simulated by induction heating to 1232-1243°C (2250-2270°F). All material subsequently solution annealed at 1093°C (2000°F).

*Aged 718°C (1325°F) (4 hr)/621°C (1150°F) (16 hr.)

**Aged 760°C (1400°F) (10 hr)/649°C (1200°F) (8 hr.)

Table 1.5. Thermal History and 760°C (1400°F) Tensile Properties of Preweld Conditioned Simulated HAZ Samples Heat 2180-2-9247

Specimen Number	Solution Anneal Temperature °F	°C	Cooling Rate	Subsequent Thermal History	0.2% Y.S. ksi	MPa	U.T.S. ksi	MPa	Red. Area %
2-1-4-36	2000	1093	Air Cool	None	57.3	395	100.3	692	23.4
-38	1725	940	Air Cool	None	100.0	689	113.0	779	43.8
-37	1725	940	Air Cool	1232°C (2250°F) Cycle	85.5	590	115.1	794	13.5
-46	1725	940	55.5°C/hr (100°F/hr)	None	85.0	586	122.6	845	39.9
-45	1725	940	55.5°C/hr (100°F/hr)	1232°C (2250°F) Cycle	94.6	652	116.2	801	24.3

Table 1.6. Summary of Weld Transverse Tensile and Bend Test Data for Various Lots of Inconel 718

Material Source or Application	Weld Process	Thermal History	U.T.S. ksi	U.T.S. MPa	Y.S. ksi	Y.S. MPa	R.A. %	1" G.L. Elong., %	Side Bend Test Results
Car Tech 80694	Manual GTA	1093°C S.A., Air cool + 760/649°C	188	1296			23	12	3 samples passed 5t,
			186.8	1288			17	9	(one extended to 2-1/2t)
		1038°C S.A., Air Cool + 760/649°C							3 samples failed 5t with minimal deflection
PBF Acoustic Filter	Manual GTA	1093°C S.A., Air Cool + 760/649°C	180.6	1245			27		#4 passed 5t and 2-1/2t
									#5 passed 5t
			182.8	1260			38		#6 passed 5t
									(#1,2,3 failed 5t with minimal deflection)
HAPD HT 17F8EY	Automatic GTA	1093°C S.A., Air Cool + 760/649°C							#3 and #8 passed 5t
		1093°C S.A., 222°C/hr + 718/621°C							#1 passed 2-1/2t
									#2 passed 3-1/3t
									#4 passed 5t
		1093°C S.A., 55.5°C/hr + 718/621°C							#5 passed 2-1/2t
									#6 passed 3-1/3t
									#7 passed 5t

Table 1.6. (Continued)

Material Source of Application	Weld Process	Thermal History	U.T.S. ksi	U.T.S. MPa	Y.S. ksi	Y.S. MPa	R.A. %	1" G.L. Elong., %	Side Bend Test Results
Cabot 2180-2-9247	Automatic GTA	1093°C S.A., 55.5°C/hr + 718/621°C	185.9	1282	140.2	967	12	10	
			193.3	1333	141.4	975	20	16	
			193.1	1331	141.4	975	35	20	

2. ARGONNE NATIONAL LABORATORY

R. W. Weeks

2.1 INTRODUCTION

Argonne National Laboratory (ANL) is conducting an extensive program to provide low-cycle, high-temperature fatigue data on Types 304 and 316 stainless steel in support of LMFBR component design, as outlined in the previous report.[1] The present report describes the low-cycle, creep-fatigue behavior of Type 304 stainless steel, crack-propagation work on Type 304/308 stainless steel weldments, and the effects of environment, frequency, and surface roughness on the low-cycle fatigue behavior of Type 304 stainless steel.

2.2 FRACTURE AND FATIGUE STUDIES ON STAINLESS STEELS -- D. R. Diercks, C. F. Cheng, and P. S. Maiya

2.2.1 Low-cycle, Creep-fatigue Behavior of Type 304 Stainless Steel -- D. R. Diercks

Ellis and Esztergar[2] have proposed a low-cycle fatigue data correlation scheme based upon the observation that a plot of log time to failure versus log cycles to failure is approximately linear for constant strain range, loading type, and temperature. They suggest that the family of such lines obtained when the strain range is permitted to vary should meet at a common focus, and that the position of the focus will shift with changes in loading (continuous cycling, cyclic relaxation, or cyclic creep) and temperature. In principle, this method of data representation should enable one to predict fatigue lives in the design-life region in which laboratory testing is generally impractical.

Esztergar[3] has proposed that a series of low-cycle fatigue tests be performed on Type 304 stainless steel in connection with the LMFBR testing program, based upon the data representation scheme described above. The proposed tests were chosen to locate critical points on the log time versus log cycle plots, using data previously generated by Conway[4] and his co-workers at GE-NSP as a guide. After review, the tests in Esztergar's proposed program were divided into categories of high, medium,

and low priority. A number of the high-priority test groups have been completed by ANL, and the present report will be concerned with these results.

The data reported are summarized in Table 2.1. The data are listed according to the group designation used by Esztergar in Ref. 3. With the exception of Esztergar's proposed test 7.1, all high-priority tests within the four groups listed have been completed and are reported. In addition, a number of supplemental tests not specifically requested in the Esztergar matrix are included. The majority of the tests in Groups 1, 2, and 5 was performed on material from heat 9T2796 in the solution-annealed condition. The majority of the tests in Group 7 was performed on material from heat 55697. The heats and heat treatments are differentiated in Table 2.1, but not in the data plots.

Figure 2.1 shows the results of the high-prority 482°C (900°F) zero hold-time tests (Group 1). The dashed lines are reproduced from Fig. 31 of Ref. 3 and are an estimate of how the data might fall. It may be seen that the 4×10^{-3} sec^{-1} strain-rate points fall reasonably near the intersections of the appropriate strain-rate and strain-range curves. However, the two points obtained at slower strain rates fall to the right of their anticipated positions, indicating that the fatigue life does not decrease as rapidly as was expected with a decrease in strain rate at this temperature. Although all high-priority tests in Group 1 have been completed, the number of points generated is not adequate to verify or refute the usefulness of this method for the type of data shown in Fig. 2.1.

The four data points from tension hold-time tests at 482°C (900°F) corresponding to Group 2 are not plotted in this report. Three of the four points fell near their anticipated position, but the 600-min hold-time test at 2% failed after only about half the expected number of cycles (see Table 2.1). Again the data are too sparse to serve as a basis for judging the validity of the Esztergar plot for the particular data shown.

Considerable tension hold-time data have been generated at 593°C (1100°F) and a strain rate of 4×10^{-3} sec^{-1}, and these data are plotted in Fig. 2.2. The continuous cycle data lie reasonably near their

Table 2.1 Elevated-temperature, Low-cycle Fatigue Data for Type 304 Stainless Steel

Test Number, ANL[a]	Test Number, Ref. 2	Total Strain Range, %	Plastic Strain Range, %	Strain Rate, sec^{-1}	Tension Hold Time, min	Cycles to Failure	Expected Cycles to Failure, Ref. 3	Time to Failure, hr	Expected Time to Failure, hr
				Group 1 482°C (900°F)					
192	1.1	0.60	0.36	4×10^{-3}	0	27,628	23,000	23.1	17
437	1.2	0.60	0.33	4×10^{-4}	0	26,139	14,000	218.5	96
404	1.3	1.00	0.69	4×10^{-3}	0	6,026	4,000	8.4	6
438	1.4	2.01	1.55	4×10^{-3}	0	1,299	1,200	3.6	3
439	1.5	1.98	1.51	4×10^{-5}	0	955	680	266.7	170
				Group 2 482°C (900°F)					
488	2.1	0.59	0.29	4×10^{-4}	10	5,104	5,200	891.0	910
478	2.2	0.99	0.61	4×10^{-5}	45	1,324	970	1175.6	1020
451	2.3	2.02	1.52	4×10^{-5}	45	388	400	230.5	430
520	2.4	1.98	1.54	4×10^{-5}	600	123	250	1248.8	1600
				Group 5 593°C (1100°F)					
116[b]	(5.1)	0.50	0.31	4×10^{-3}	0	26,832	-	18.7	-
134	(5.1)	0.51	0.31	4×10^{-3}	0	30,498	-	21.2	-
187[b]	5.2	1.02	0.68	4×10^{-3}	0	3,740	2,600	5.2	4
408	5.2	1.00	0.66	4×10^{-3}	0	3,395	2,600	4.7	4
114[b]	5.3	2.01	1.61	4×10^{-3}	0	941	780	2.6	2
132	5.3	2.02	1.60	4×10^{-3}	0	937	780	2.6	2
107[b,c]	-	0.48	0.25	4×10^{-3}	1	9,365	-	156.7	-
112	-	0.49	0.29	4×10^{-3}	1	14,970	-	250.2	-
198[b]	-	0.50	0.28	4×10^{-3}	1	10,441	-	176.8	-
154	-	0.50	0.28	4×10^{-3}	10	3,803	-	635.1	-
416	5.5	0.60	0.39	4×10^{-3}	15	2,765	2,200	694.5	420
443	5.6	0.59	0.41	4×10^{-3}	180	1,284	1,050	3849.5	3100
135	-	1.00	0.70	4×10^{-3}	1	1,664	-	28.8	-
145[b]	-	1.01	0.70	4×10^{-3}	1	1,046	-	18.5	-

Table 2.1 Elevated-temperature, Low-cycle Fatigue Data for Type 304 Stainless Steel (Contd.)

Test Number, ANL[a]	Test Number, Ref. 2	Total Strain Range, %	Plastic Strain Range, %	Strain Rate, sec^{-1}	Tension Hold Time, min	Cycles to Failure	Expected Cycles to Failure, Ref. 3	Time to Failure, hr	Expected Time to Failure, hr
				Group 5 (Contd.)					
401[c]	-	0.99	0.68	4×10^{-3}	1	1,235	-	21.4	-
150	-	1.01	0.71	4×10^{-3}	10	636	-	106.3	-
189[c]	-	1.01	0.73	4×10^{-3}	10	553	-	92.7	-
418	5.7	1.00	0.74	4×10^{-3}	15	666	620	167.2	110
152	-	0.99	0.72	4×10^{-3}	60	338	-	337.2	-
509	5.8	1.02	0.76	4×10^{-3}	180	170	350	499.6	980
543	-	2.05	1.68	4×10^{-3}	1	378	-	7.3	-
412	5.9	2.00	1.66	4×10^{-3}	15	237	260	59.6	50
463	-	1.98	1.66	4×10^{-3}	60	112	-	111.3	-
510	5.10	2.02	1.74	4×10^{-3}	180	63	150	183.2	480
				Group 7 649°C (1200°F)					
66[b,c]	-	0.33	0.16	4×10^{-3}	0	64,929	-	29.1	-
61[b]	-	0.50	0.31	4×10^{-3}	0	9,504	-	6.6	-
63[b]	-	1.01	0.76	4×10^{-3}	0	2,406	-	3.3	-
70[b,d]	-	1.00	0.69	4×10^{-3}	0	2,217	-	3.1	-
193[b]	-	1.00	0.71	4×10^{-3}	0	3,082	-	4.3	-
52[b]	-	1.99	1.64	4×10^{-3}	0	775	-	2.1	-
67[b,d]	-	2.01	1.62	4×10^{-3}	0	701	-	1.9	-
68[b,d]	-	0.50	0.33	4×10^{-3}	1	3,198	-	53.8	-
74	-	1.00	0.80	4×10^{-3}	1	930	-	16.3	-
72[b,d]	7.9	0.98	0.77	4×10^{-3}	10	645	480	107.9	100

Table 2.1 Elevated-temperature, Low-cycle Fatigue Data for Type 304 Stainless Steel (Contd.)

Test Number, ANL[a]	Test Number, Ref. 2	Total Strain Range, %	Plastic Strain Range, %	Strain Rate, sec^{-1}	Tension Hold Time, min	Cycles to Failure	Expected Cycles to Failure, Ref. 3	Time to Failure, hr	Expected Time to Failure, hr
				Group 7 (Contd.)					
410	7.9	1.00	0.79	4×10^{-3}	10	525	480	88.1	100
477	7.5	1.05	0.87	4×10^{-3}	180	313	260	935.3	900
9[b,d]	-	2.06	1.76	4×10^{-3}	1	311	-	5.7	-
53[b]	-	2.02	1.77	4×10^{-3}	10	253	-	42.5	-

[a]Except as indicated, all material was from heat 9T2796, and was tested in the solution-annealed and aged condition.

[b]Heat 55697.

[c]Tested in the solution-annealed condition.

[d]Tested in the stress-relieved condition.

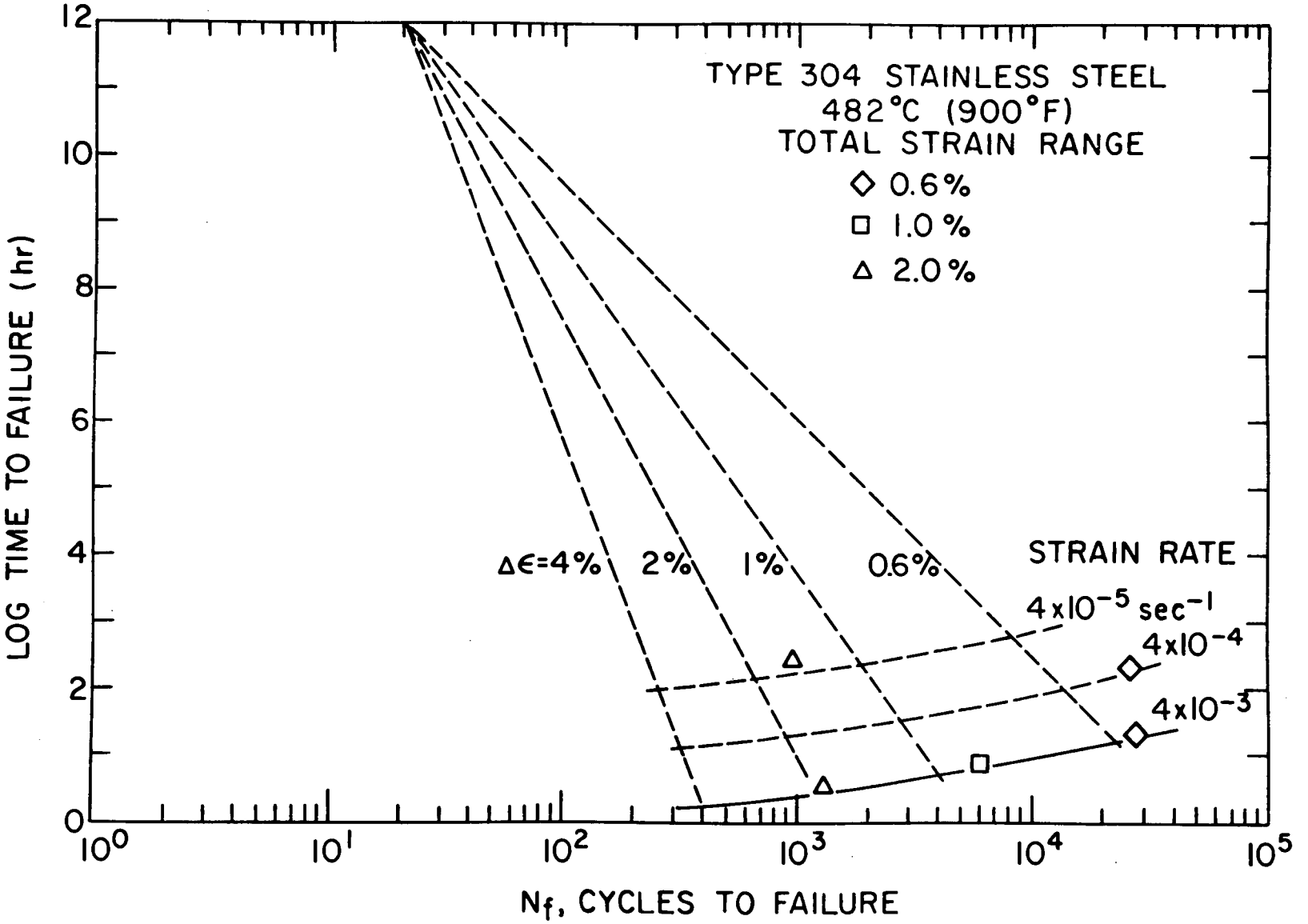

Fig. 2.1. Continuous Cycling Data at 482°C.

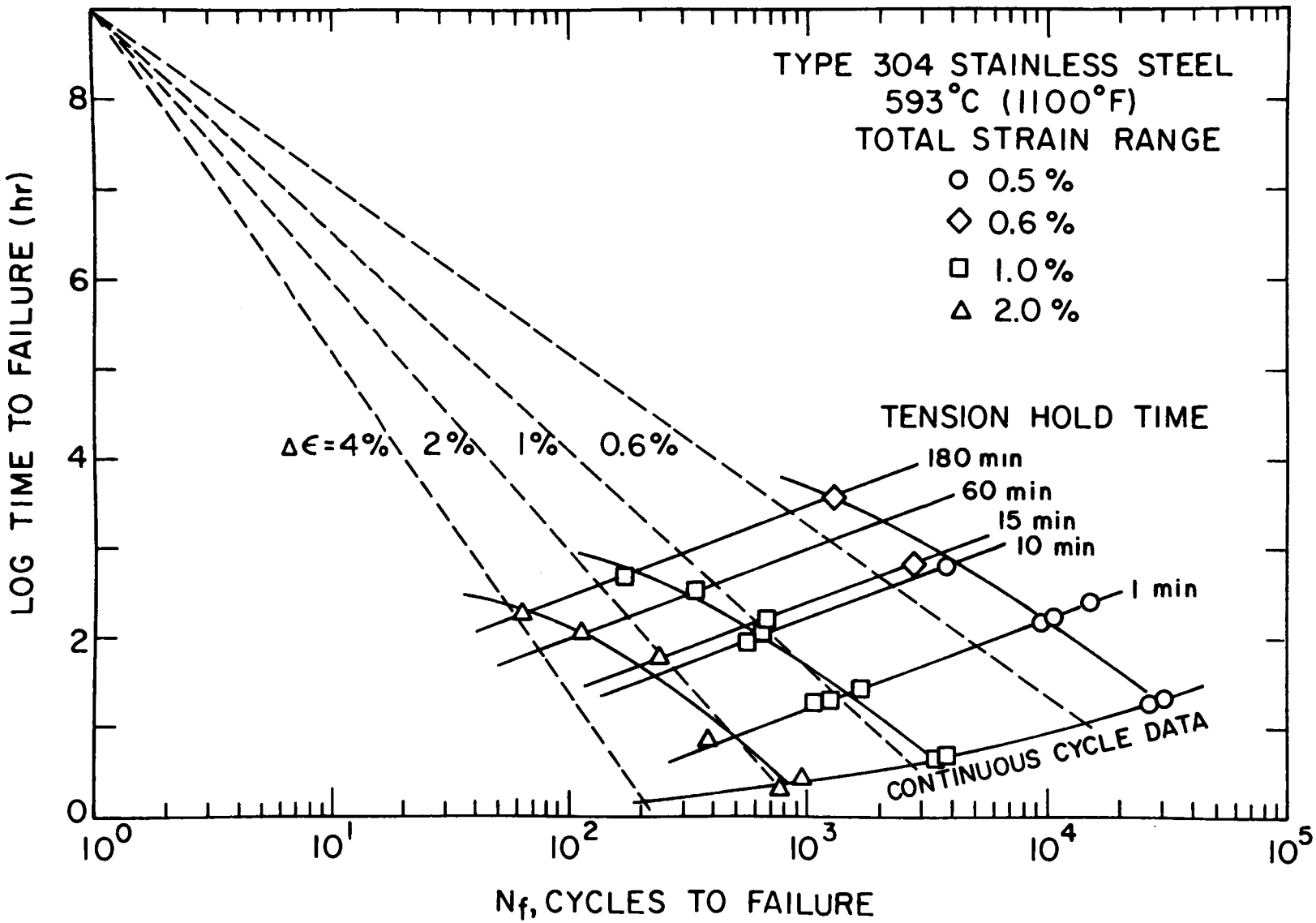

Fig. 2.2. Tension Hold-time Data at 593°C.

anticipated positions, with the exception of the 0.5% strain-range tests. However, with increasing tension hold time, the data tend to depart from linearity in the direction of a saturation in time to failure. This is a rather surprising development, and is contrary to the behavior anticipated by Esztergar (see Ref. 3, Fig. 35).

Tension hold-time data have also been generated at 649°C (1200°F), and these data are plotted in Fig. 2.3 along with the data of Conway. It may be seen that the ANL data verify the trend toward a saturation in cycles to failure with increasing hold time. The behavior at 593°C (Fig. 2.2) and 649°C (Fig. 2.3) are thus difficult to reconcile. In fact, at the 1 and 2% total strain ranges for hold times of 60 min or more, the fatigue lives at 649°C are actually greater than those at 593°C. The possibility that some precipitation-hardening process is occurring at the higher temperature is immediately suggested, but the detailed microstructural study necessary to verify this hypothesis has not been performed. In any case, the utility of the log time-log cycles plot in extrapolating data of this type must be questioned.

2.2.2 Crack-propagation of SMA Type 304/308 Stainless Steel Weldments -- C. F. Cheng

ANL is studying the crack growth of SMA Type 304/308 stainless steel welded plates with controlled residual elements made by Combustion Engineering to simulate the seam and girth welds of the FFTF vessel. The details of the fabrication of the welded plates and subsequent machining into single-edge-notch (SEN) specimens have been described in a previous report.[5] Each specimen was cycled under uniaxial tension loading in sawtooth wave form at a constant stress ratio $R(\sigma_{min}/\sigma_{max})$. The crack growth was viewed through a microscope, and the number of cycles was recorded as the crack traversed a series of parallel scribed marks at 50-mil increments from the side notch. The average crack length is determined by the cross-sectional area of the cracked surface up to the crack front of the fracture surface divided by the thickness of the specimen. The test conditions and results are summarized in Table 2.2. The crack-growth rate da/dN was calculated for each increment of crack extension, and the stress-intensity factor range was based on the average crack length for

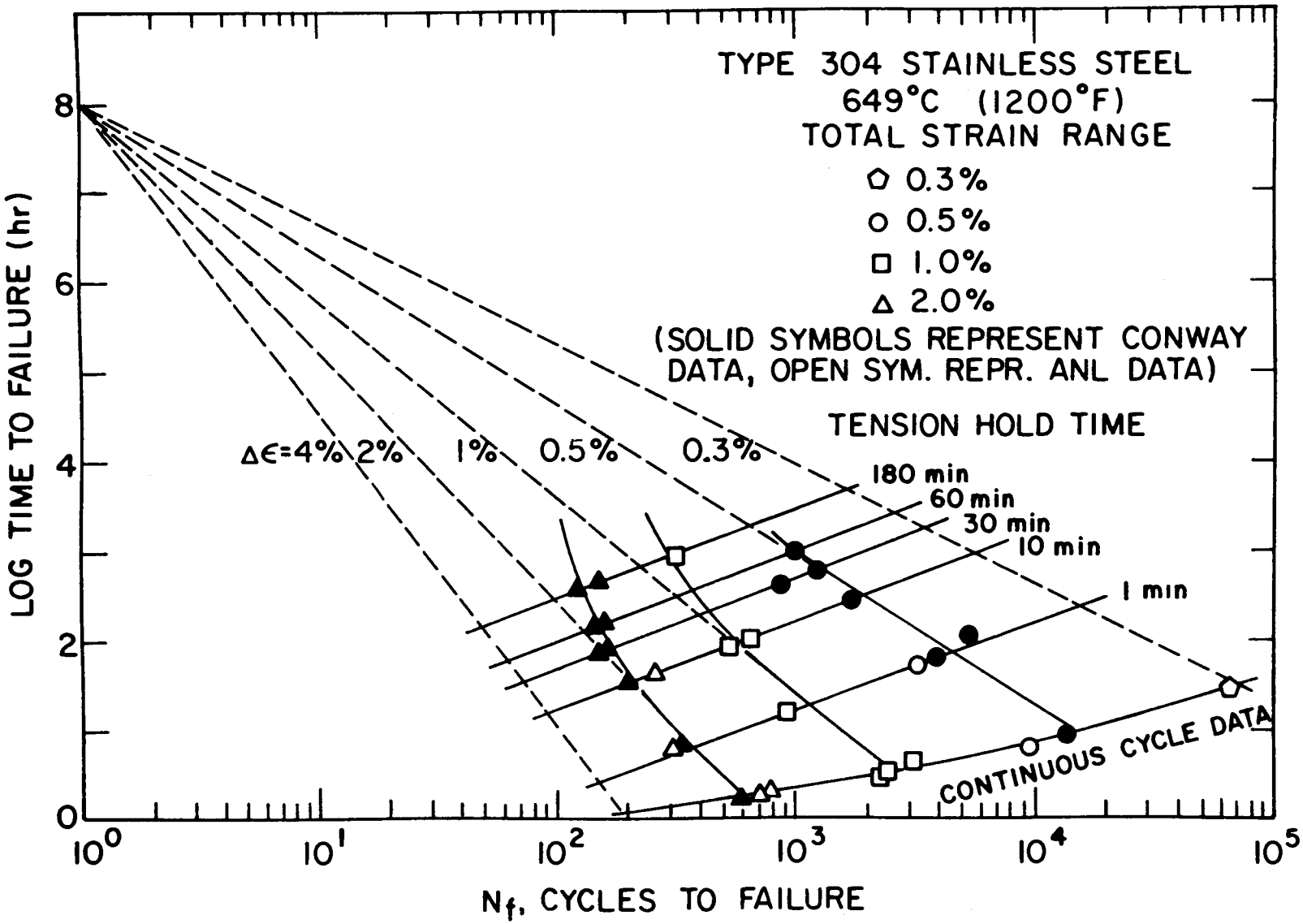

Fig. 2.3. Tension Hold-time Data at 649°C.

that increment from the expression[6]

$$\Delta K' = (\Delta P/BW) \cdot Y \sqrt{A + r_p}\ , \tag{1}$$

or noting that

$$\Delta K = (\Delta P/BW) \cdot Y \sqrt{a} \tag{2}$$

$$\Delta K' = \frac{\sqrt{a + r_p}}{\sqrt{a}} \cdot \Delta K, \tag{3}$$

where

$\Delta K'$, ΔK = stress-intensity factor range, with and without plastic zone correction factor, respectively,

ΔP = cycling load range,

B = specimen thickness (0.400 in.),

W = specimen width (1.00 in.),

Y = calibration factor from ASTM STP-410 (1969),

$= [1.99 - 0.41\ (W/a) + 18.70\ (W/a)^2 - 38.48\ (W/a)^3 + 53.85\ (W/a)^4]$,

a = crack length,

and

r_p = plastic zone correction factor.

In Irwin's[6] expression [Eq. (1)], r_p can be calculated from

$$r_p = (\Delta K/\sigma_{yc})^2/n\pi,$$

where n is 2 for plane stress, and σ_{yc} is the cyclic yield strength.

Analysis of the fatigue crack-growth data was made on the basis of the power law relating da/dN to $\Delta K'$, which is expressed as

$$da/dN = C\ (\Delta K')^m,$$

where C and m are constants, and $\Delta K'$ is selected over ΔK because $\Delta K'$ corrects for plastic zone.

Figures 2.4(a)-(c) are plots of da/dN versus $\Delta K'$ for aged base metal, aged weld metal, and as-welded weld metal, respectively. All data analyzed are for the test condition of 1-min tension hold time at

Table 2.2. Crack Propagation of SMA Type 304/308 Stainless Steel Weldments

Frequency: 30 cpm; Stress Ratio R: 0.05; Temperature: 1100°F; Tension Hold: 1 min at each scribed mark

Test Number	Specimen Number	a_{avg}, 10^{-3} in.	P_{avg}, 10^3 lb	da/dN, 10^{-6}/in.	K, ksi$\sqrt{in.}$	r_p,[a] 10^{-3} in.	K', ksi$\sqrt{in.}$	Remarks
			Base Metal: Aged (1000 hr at 1100°F)					
6C	CE33B5	191.1	7.629	11.49	19.91	45.3	22.14	Fig. 2.4(a), triangles
		247.9	7.629	19.23	25.25	72.9	28.72	
		294.9	7.614	29.27	30.08	103.5	34.96	
		340.1	7.594	38.36	35.69	145.7	42.66	
		386.3	7.599	78.59	42.10	202.8	51.99	
		433.6	7.593	120.11	51.17	299.5	66.54	
		479.6	7.588	209.4	61.77	436.5	85.37	
11C	CE	224.6	5.774	9.295	17.43	34.7	18.73	Fig. 2.4(a), squares
		252.6	5.754	13.117	19.28	42.5	20.84	
		374.9	5.758	32.30	30.58	107.0	34.97	
		433.2	5.753	56.86	38.66	171.0	45.66	
		486.7	5.753	107.88	48.32	267.1	60.13	
14C	CE33B2	226.2	4.740	6.81	14.36	23.6	15.09	Fig. 2.4(a), circles
		256.3	4.740	8.55	16.07	29.5	16.99	
		298.6	4.750	10.60	19.02	41.4	20.30	
		363.6	4.745	21.77	24.27	67.4	26.42	
7C[b]	CE33B1	213.7	7.599	17.69	21.81	54.41	24.33	Fig. 2.4(a), diamonds
		304.9	7.600	39.40	31.31	112.1	36.41	
		356.9	7.590	63.48	37.87	164.1	45.76	
		395.5	7.590	105.0	43.72	218.7	54.48	
		440.1	7.590	163.6	52.37	313.7	68.54	

Table 2.2. Crack Propagation of SMA Type 304/308 Stainless Steel Weldments (Contd.)

Frequency: 30 cpm; Stress Ratio R: 0.05; Temperature: 1100°F; Tension Hold: 1 min at each scribed mark

Test Number	Specimen Number	a_{avg}, 10^{-3} in.	P_{avg}, 10^3 lb	da/dN, 10^{-6}/in.	K, ksi$\sqrt{\text{in.}}$	r_p,[a] 10^{-3} in.	K', ksi$\sqrt{\text{in.}}$	Remarks
			Weld Metal: Aged (1000 hr at 1100°F)					
12C	CE39W1	704.1	7.596	9.61	21.04	56.2	23.76	Fig. 2.4(b), squares
		256.9	7.596	24.33	25.83	84.7	29.79	
		306.5	7.593	37.76	31.66	127.3	37.67	
		348.0	7.596	61.18	36.76	171.6	44.92	
		398.8	7.596	136.2	44.21	248.2	56.31	
		467.9	7.592	294.1	58.46	434.1	81.17	
13C	CE39W2	219.6	5.700	5.61	16.87	36.2	18.21	Fig. 2.4(b), circles
		335.6	5.693	19.40	26.41	88.6	29.69	
		390.7	5.685	33.51	32.06	130.6	37.03	
		454.9	5.690	69.57	41.77	221.6	50.94	
			Weld Metal: As-welded					
10C	CE39W8	189.6	5.695	7.96	14.81	27.9	15.86	Fig. 2.4(c), circles
		231.3	5.690	10.24	17.53	39.0	18.95	
16C	CE41W6	284.8	7.606	31.24	28.90	106.1	33.86	Fig. 2.4(c), squares
		366.3	7.599	52.67	39.14	194.6	48.43	
		426.6	7.604	94.51	49.73	314.1	65.52	

[a]Calculated value based on cyclic yield strength at 1100°F at 37.3 ksi for base metal and 35.8 for weld metal.[2]

[b]No tension hold, lower frequency to 0.3 cpm at each marker cycle.

each scribed mark, except test 7c [diamonds in Fig. 2.4(a)]. Test 7c was conducted by lowering the frequency from 30 to 0.3 cpm for the marker cycle. The results of test 7c are represented by a dashed line drawn parallel to the line for the 1-min tension hold tests. It is postulated that uninterrupted cycling will also show similar parallel behavior, and tests have been planned.

The selection of $\Delta K'$ over ΔK versus da/dN is justified by the linearity of the logarithmic slopes: 1.99 $\pm$ 0.06 (aged base metal); 2.69 $\pm$ 0.10 (aged weld metal); and 1.75 $\pm$ 0.04 (as-welded weld metal) in Figs. 2.4(a)-(c), respectively. ΔK versus da/dN will require arbitrary judgment because of the changing slope for the same range of crack-growth rate, as noted by James[7] and by Shahinian *et al.*[8]

2.2.3 Effects of Surface Roughness on the Low-cycle Fatigue Behavior of Type 304 Stainless Steel -- P. S. Maiya

The great majority of low-cycle fatigue tests on structural materials is being performed on hourglass specimens with surfaces smoothed by final polishing or with a surface finish in the longitudinal direction. The data obtained from such smooth specimens may not reflect the conditions existing in actual structural components. The present report includes results of the influence of surface roughness on the low-cycle fatigue of Type 304 stainless steel (heat 9T2796) at 593°C (1100°F). Also included in this study is how the surface integrity affects the crack-initiation (crack nucleation plus early growth across 1 or 2 grains) and crack-propagation processes.

Several hourglass specimens (0.25-in. minimum diameter) were solution annealed for 30 min at 1092°C (1998°F) and aged for 1000 hr at 593°C (1100°F). Following the heat treatment, the specimens were given different surface treatments, the objective of which was to produce surfaces with different roughness. The specimen was mounted on a lathe and turned. A silicon carbide paper of a chosen grit was applied gently so that circumferential grooves were produced on the entire gauge length of the specimen. The procedure is capable of producing the same degree of surface roughness on several specimens. For longitudinal grooves, the specimen was held stationary while the grinding paper was applied along

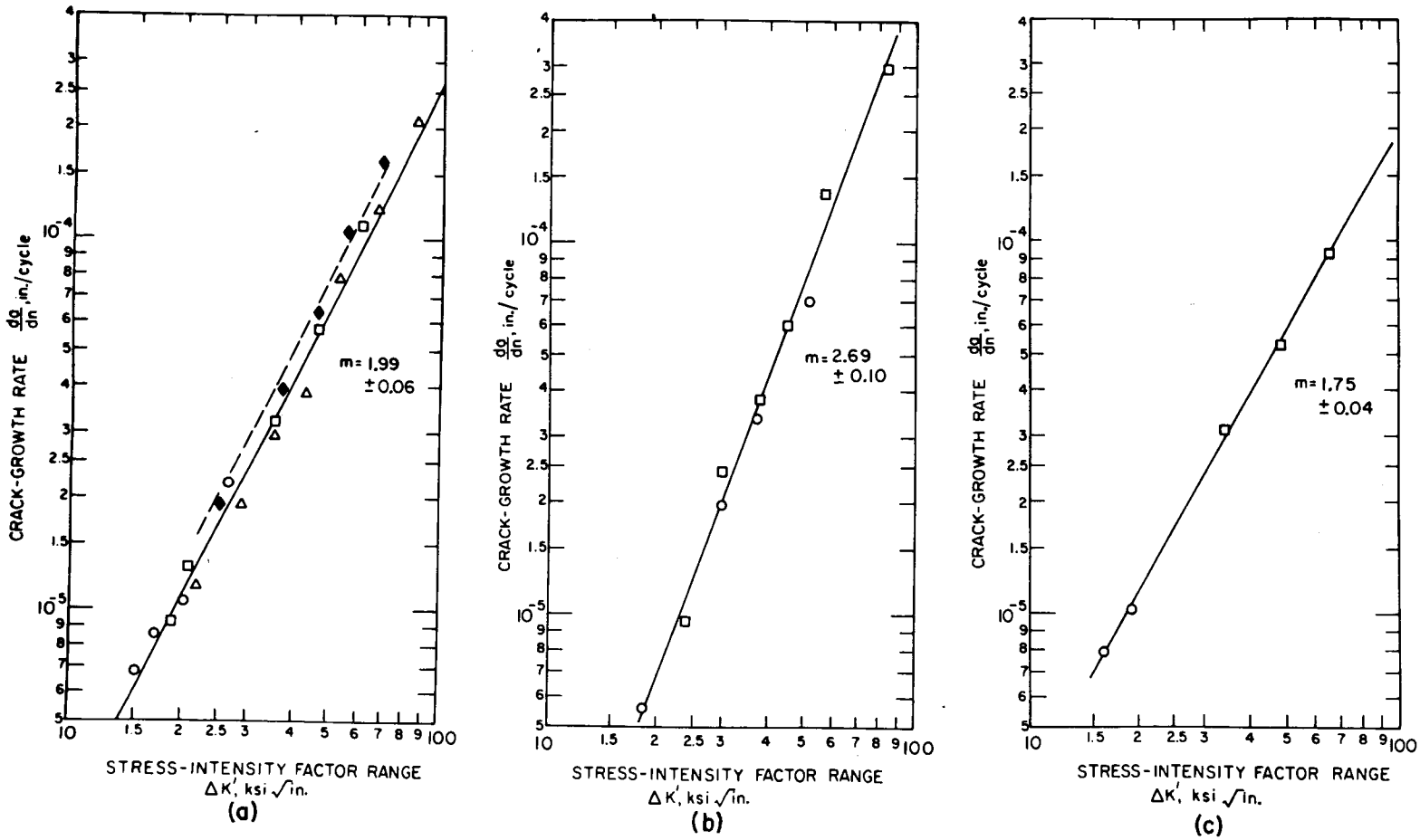

Fig. 2.4. Crack-growth Rate, da/dN, vs Stress-intensity Factor Range, ΔK', at 1100°F in (a) Aged Base Metal, (b) Aged Weld Metal, and (c) As-welded Weld Metal of SMA Type 304/308 Stainless Steel Weldments.

the longitudinal direction. To obtain very smooth surfaces, mechanical polishing and electropolishing techniques were used. The severity of surface roughness produced in various cases is illustrated by a series of scanning electron micrographs shown in Fig. 2.5. The depth of surface roughness R was measured with a Talysurf instrument that traces the profile of the surface irregularities. Typical surface profiles recorded by this instrument for the stainless steel are shown in Fig. 2.6. The surface roughness is described by a root-mean-square (rms) value or a maximum value for the depth of surface grooves. The values for R are obtained from an analysis of surface profiles, such as those displayed in Fig. 2.6. Table 2.3 summarizes the various values of R obtained on the low-cycle fatigue specimens by using the different surface-preparation procedures.

Table 2.3. Surface Roughness Obtained by Various Methods

Surface Preparation	Surface Roughness R, μm (rms)	Maximum Depth of Surface Grooves, μm
Ground on Silicon Carbide Paper		
600 grit	0.045	0.18
240 grit	0.48	1.8
50 grit	2.9	8.9
Polished		
Mechanically polished	∿0.0075	<0.027
Electropolished	∿0.0075	<0.027

The fatigue tests were performed in air in servocontrolled, hydraulically actuated fatigue machines in axial strain control at a strain rate of 4×10^{-3} sec^{-1} and a total strain range of 1%. It is observed that fatigue life depends on the surface roughness, and decreases with an increase in surface roughness for the circumferential grooves. The surface fatigue factor $N_f(R)/N_f(S)$, where $N_f(R)$ = number of cycles to failure

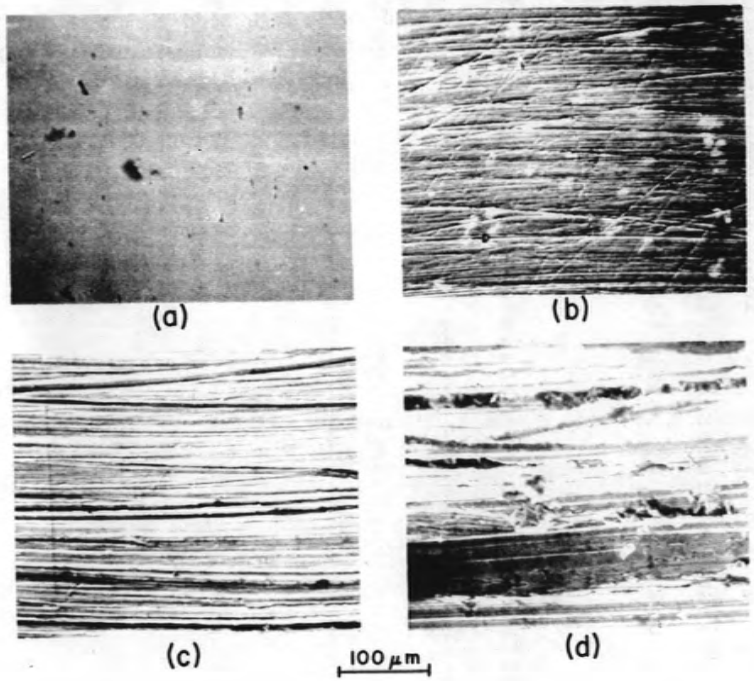

Fig. 2.5. Scanning Electron Micrographs of Specimens with Different Surface Roughness. (a) R < 0.027 μm, (b) R = 0.045 μm, (c) R = 0.48 μm, and (d) R = 2.9 μm.

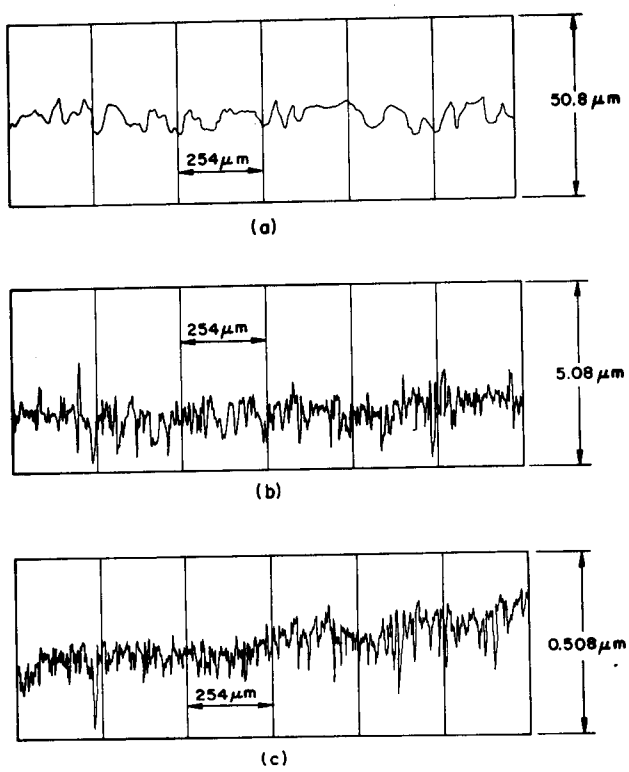

Fig. 2.6. Surface Roughness Profile of Type 304 Stainless Steel. (a) R = 2.9 μm, (b) R = 0.48 μm, and (c) R = 0.045 μm.

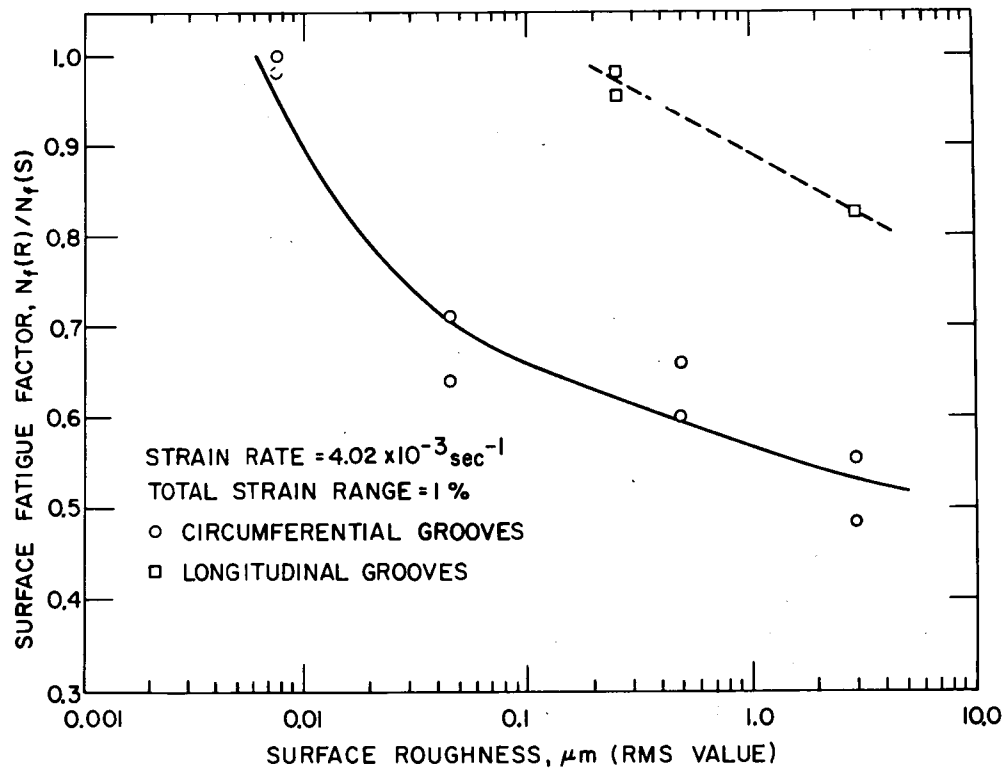

Fig. 2.7. Fatigue Life of Type 304 Stainless Steel as a Function of Surface Roughness at 593°C.

for a specimen with roughness R, and $N_f(S)$ = fatigue life of a specimen with a smooth surface, as a function of R is shown in Fig. 2.7. For the extreme surface roughness R = 2.9 μm, the fatigue life is reduced by a factor of two. This is significant considering the fact that fatigue life for all specimens, under the testing variables described, is reproducible within ± 7-15%. It is also clear that longitudinal grooves have a much less detrimental effect on fatigue life (Fig. 2.7), and therefore will not be discussed further.

The fractured surfaces have been examined by scanning electron microscopy, and all specimens showed fatigue striations. Examples of fatigue striations observed on the fractured surfaces are shown in Fig. 2.8. From striation spacing measurement, it is possible to obtain information on crack length versus strain cycles.[9,10] Plots of crack length, a, versus strain cycles, N, as influenced by R are shown in Fig. 2.9. The trend of these results suggests that the number of cycles to initiate a crack decreases markedly with an increase in R. Some understanding of the effects of R on fatigue life can be achieved by considering crack-initiation and crack-propagation processes separately.

Recently, Solomon[11] has shown that in a notched low-cycle fatigue specimen, ln a (a is the sum of notch depth and crack length) is proportional to N at constant temperature and frequency of loading. The present results indicate that a similar relationship is valid for smooth specimens, but a consistent deviation from the crack-growth law appears to occur after the crack has progressed to a length exceeding 1-2 mm in specimens with R = 0.48 and 2.9 μm. However, the ln a versus a plots shown in Fig. 2.10 offer an approximate method of determining the number of cycles to initiate a crack of length a_o by extrapolation. Inasmuch as the grain diameter of the specimens is of the order of 0.1 mm, it is reasonable to assume a_o equal to 0.1 mm. This assumption is consistent with the observation made by scanning electron microscopy that no fatigue striations were visible in the crack-initiation zone ∿0.1-0.2 mm in length from the crack-nucleation site. Thus, one can determine N_o, which is the number of cycles to initiate a crack of length a_o equal to 0.1 mm. After N_o has been determined, the relation between the crack-

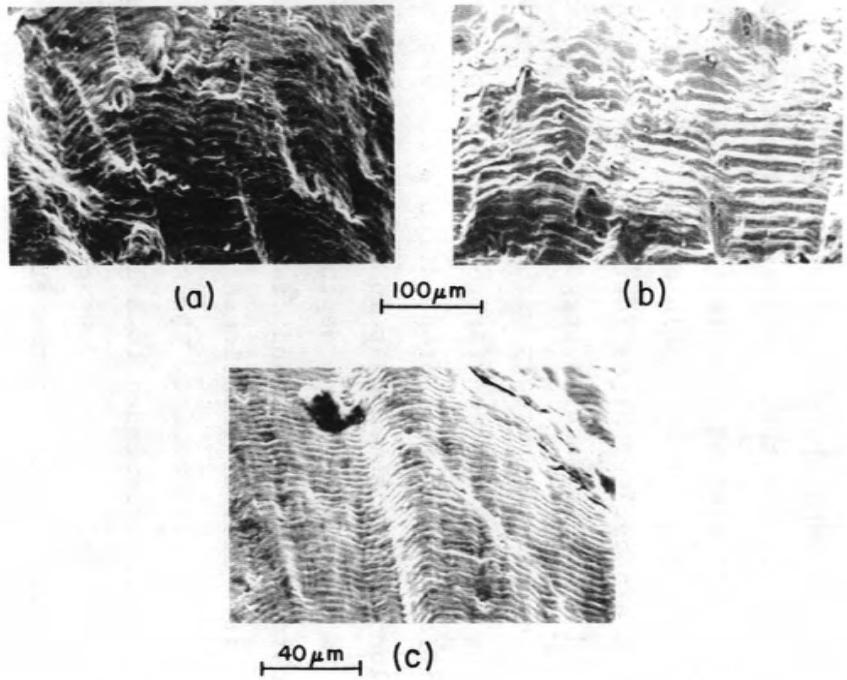

Fig. 2.8. Scanning Electron Micrographs of the Fracture Surfaces of Specimens. (a) R < 0.027 μm, (b) R = 2.9 μm, and (c) R = 0.045 μm.

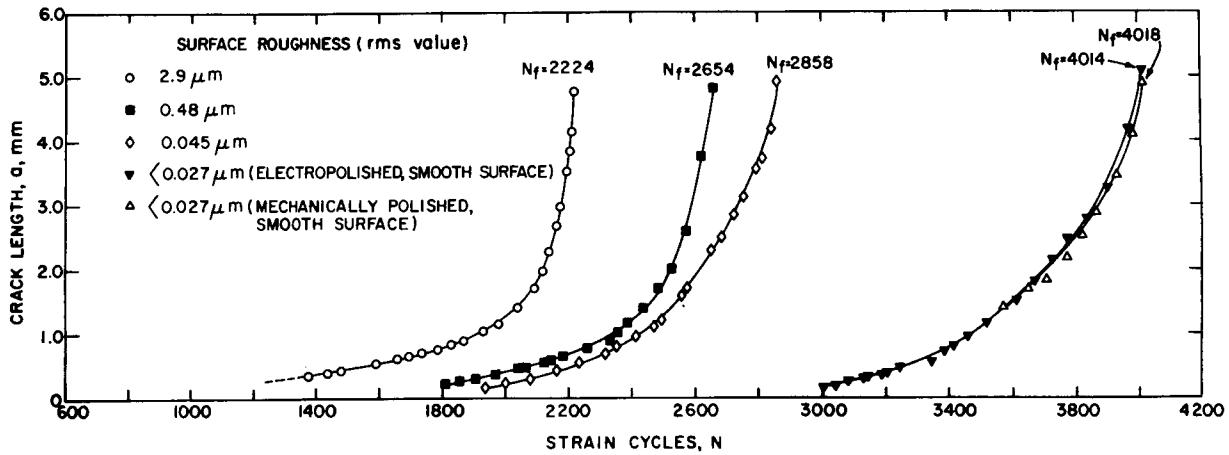

Fig. 2.9. Effect of Surface Roughness on Crack Initiation and Stage I and Stage II Growth.

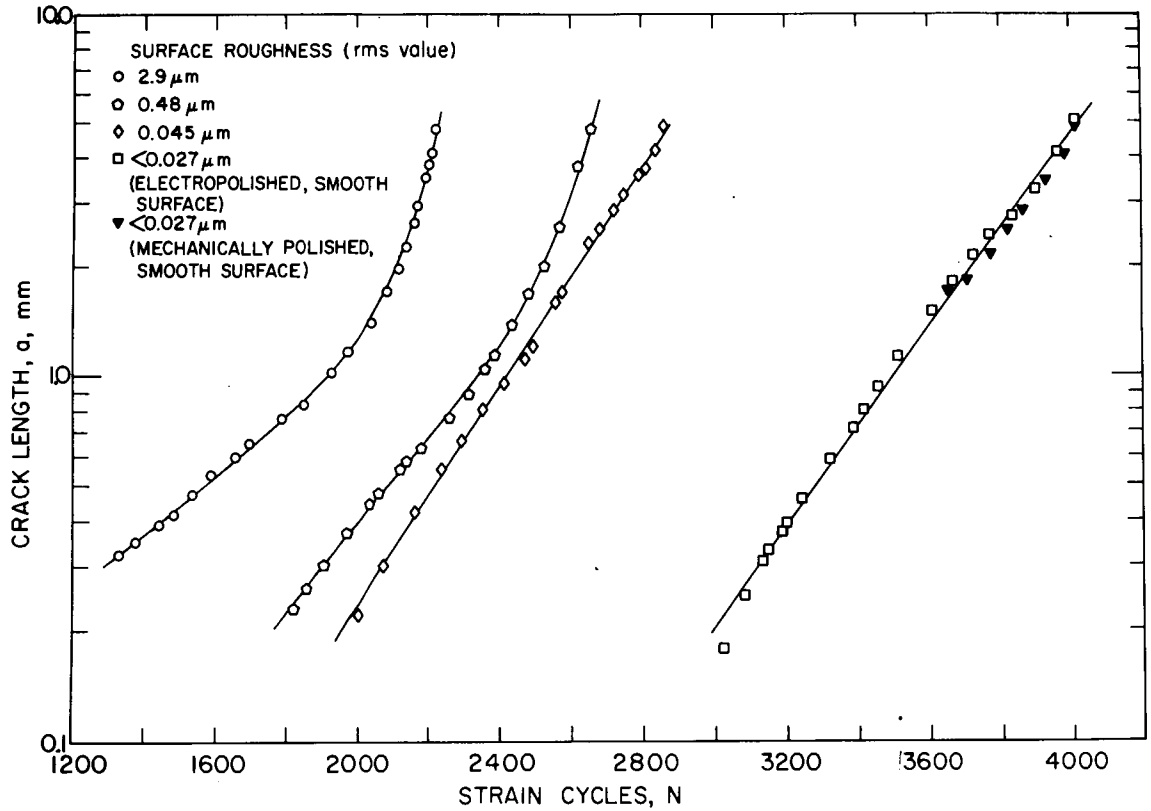

Fig. 2.10. Effect of Surface Roughness on Plots of ln a versus N.

initiation life and the total life (N_f), as influenced by surface effects, can be quantitatively discussed in a manner similar to that outlined by Grosskreutz[12] in his work on the effects of surface coatings on the fatigue life of aluminum.

The total number of cycles to failure, N_f, is the sum of the number of cycles for crack initiation, N_o and the number of cycles for crack propagation, N_p,

$$N_f = N_o + N_p. \tag{1}$$

For a smooth specimen,

$$N_f(S) = N_o(S) + N_p(S). \tag{2}$$

If we assume that surface roughness affects N_o and not N_p, then

$$N_f(R) = N_o(R) + N_p(S). \tag{3}$$

Eliminating $N_p(S)$ from Eqs. (2) and (3) and dividing each term by $N_f(R)$ and representing $N_o(S)/N_f(S)$ by β, we obtain

$$N_f(R)/N_f(S) = 1 + \beta\ [N_o(R)/N_o(S) - 1]. \tag{4}$$

Using the value of β obtained in the present experiments ($\beta = 0.69$) and Eq. (4), the decrease in fatigue life, $N_f(R)$, with a decrease in crack-initiation time can be described by the line shown in Fig. 2.11, and the experimental points follow the prediction within the limits of experimental error.

The decrease in initiation time with an increase in surface roughness, R, may be empirically described by

$$N_o(R) = 1012\ R^{-0.21}. \tag{5}$$

The effect of R on the total fatigue life is

$$N_f(R) = 1012\ R^{-0.21} + N_p(S). \tag{6}$$

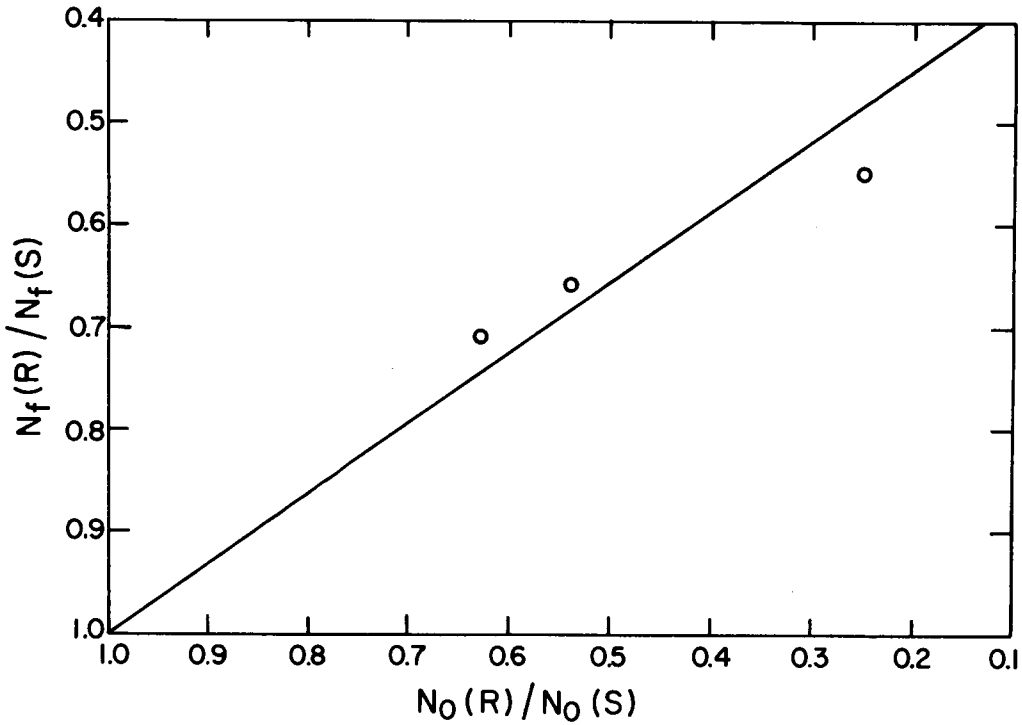

Fig. 2.11. Plot of Decrease in Fatigue Life, $N_f(R)$, with Decrease in Initiation Time, $N_o(R)$, for Type 304 Stainless Steel. Solid line is predicted by Eq. (4), and experimental points are represented by symbols.

Equation (6) thus predicts the fatigue life of a specimen with a roughness R from the smooth specimen data. It is also important to note that surface roughening in a smooth specimen results from strain cycling, which eventually leads to the initiation of a crack.[13] This plastic instability has been modeled by Laird and Krause[14] using simple geometrical assumptions to calculate N_o. Their equation is

$$N_o = C(\Delta\varepsilon_p)^{-m}, \tag{7}$$

where $\Delta\varepsilon_p$ is the plastic strain range, and C and m are constants. The form of Eq. (5) is similar to Eq. (7), if R is assumed to be some function of $\Delta\varepsilon_p$.

Examination of Fig. 2.9 shows that the surface roughness, if it exceeds a certain value ($\geq$ 0.5 μm), appears to influence the crack-propagation rate even though the number of cycles spent in the crack-propagation stage remains unaffected. These results can be rationalized by considering the crack-growth models. The model appropriate to the present discussion is that developed by Tomkins.[15] From Tomkins, the crack extension per cycle, da/dN, is

$$da/dN = \frac{\pi^2}{32}\left(\frac{\sigma_o}{\sigma_y}\right)^2 \Delta\varepsilon_p^{2n'+1}\, a. \tag{8}$$

Here σ_o is defined by the cyclic stress-strain relation, namely, $\Delta\sigma = \sigma_o(\Delta\varepsilon_p)^{n'}$, where n' = cyclic strain-hardening exponent, and σ_y = cyclic flow stress. When $\Delta\varepsilon_p$ is held constant, as in our case, Eq. (8) is rewritten as

$$da/dN = K\, a, \tag{9}$$

where K is a constant that contains cyclic stress-strain parameters. If the crack propagates from the initial length a_o to any length a in $N-N_o$ cycles, the integration of Eq. (9) yields

$$\ln a - \ln a_o = K\,(N-N_o). \tag{10}$$

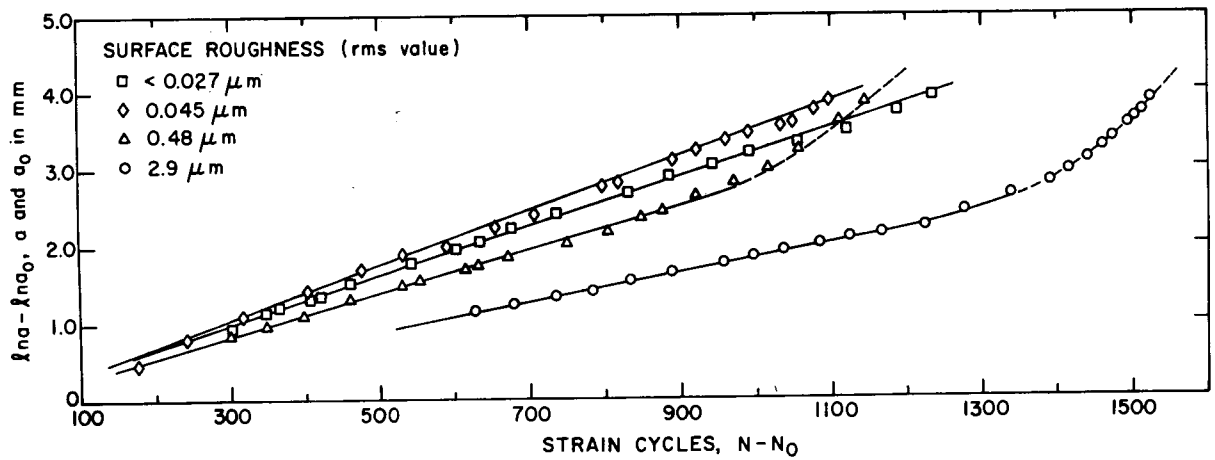

Fig. 2.12. Effect of Surface Roughness on Plot of ln a-ln a_o vs N-N_o for Type 304 Stainless Steel.

Figure 2.12 shows a plot of ln a - ln a_o versus $N-N_o$ for specimens with different surface roughness. It is clear that ln a - ln a_o is proportional to $N - N_o$ for all specimens, as predicted by Eq. (10), although some systematic departure is seen for specimens with $\sim R \geq 0.5$ μm when the crack length a approaches the final crack length a_f. Also, a consistent trend is evident in these plots (see Fig. 2.11) showing that the effect of surface roughness is to slow the crack-propagation rate (i.e., to decrease the value of K), a result which does not become readily apparent from Fig. 2.9. A qualitative understanding of the effect of R on the crack-propagation rate may be achieved by considering crack-growth behavior in the electropolished specimen and in the specimen with R = 2.9 μm. In the former case, the transition in crack growth from stage I to stage II takes place at $N_o(S) \approx 2780$ cycles and, in the latter, $N_o(R) \approx 700$ cycles. Therefore, the crack propagation in the smooth specimen occurs in the material that has accumulated more damage, which results in slight enhancement in crack-growth rate compared with that in the specimen with circumferential grooves. Although this appears to be a reasonable explanation, it should be pointed out that, at present, no crack-propagation models appear to exist which take into account the detailed microstructural changes in the portion of the material ahead of a growing crack. It should also be realized that the shape of the grooves (e.g., root radius/depth ratio), surface stresses, microcracking, and metallurgical changes produced below the strained surface do not enter into the roughness parameter R. Although some of the factors such as surface stresses may not be important in low-cycle fatigue, other factors such as microcracking and linkup of microcracks may well explain the enhanced crack-growth behavior (a systematic deviation in the plot shown in Fig. 2.11) observed in specimens containing circumferential grooves (R > 0.5 μm).

2.2.4 Effect of Environment and Frequency on Low-cycle Fatigue Life of Type 304 Stainless Steel -- P. S. Maiya

In many current applications, structural materials operate under cyclic loads in environments other than air (e.g., sodium containing low levels of oxygen). It is therefore essential to understand the effects of environment and frequency on fatigue life at elevated temperatures,

especially in the regime in which creep-fatigue interaction becomes increasingly important. The present report concerns the frequency effect on low-cycle fatigue behavior of Type 304 stainless steel at 650°C (1202°F) in air as well as in high vacuum (< 10^{-7} torr).

Recently, Sheffler[16] reported the effect of two frequencies (0.39 and 39 cpm) of loading on the fatigue life of Type 304 stainless steel at 650°C in high vacuum (< 10^{-7} torr). (The chemistry and heat treatment of the stainless steel are not known.) The results are shown in Fig. 2.13. It is clear that frequency effects are present and that the effect of lowering the frequency is to reduce the fatigue life. These data obtained in high vacuum were compared with those obtained at ANL in air.

Extensive low-cycle fatigue data have been generated on Type 304 stainless steel (heat 9T276), and the results have been summarized elsewhere.[17] Inasmuch as no data in air are available for the specific frequencies of loading, which are required for comparison with fatigue lives in vacuum, Coffin's[18] high-temperature modification of the low-temperature Coffin-Manson equation has been used

$$\Delta\varepsilon_p = C_2 \left(N_f \, \nu^{k-1}\right)^{-\beta} , \qquad (1)$$

where $\Delta\varepsilon_p$ is the plastic strain range, N_f is the fatigue life, ν is the frequency of cycling, and C_2, k, and β are constants. Using ANL data obtained in air at 1202°F for various strain rates and data with zero hold time and several tension hold times as long as 10 hr, the constants C_2, k, and β have been evaluated by means of a nonlinear regression analysis. For the data with hold times t_H, an effective frequency ν_{eff} $[\nu_{eff} = t_H + 1/\nu)^{-1}]$ was used. The capability of Eq. (1) to predict fatigue lives is quite good (as is clear from Fig. 2.14) and is therefore used for comparing data obtained in air with those obtained in high vacuum at 650°C for the two frequencies. The most significant aspect of the comparison shown in Fig. 2.13 is that, in an air environment, the frequency effects on fatigue life are pronounced, and, for the same frequency, fatigue life in high vacuum is longer. These observations suggest the need for future controlled studies directed toward elucidating the effect of different

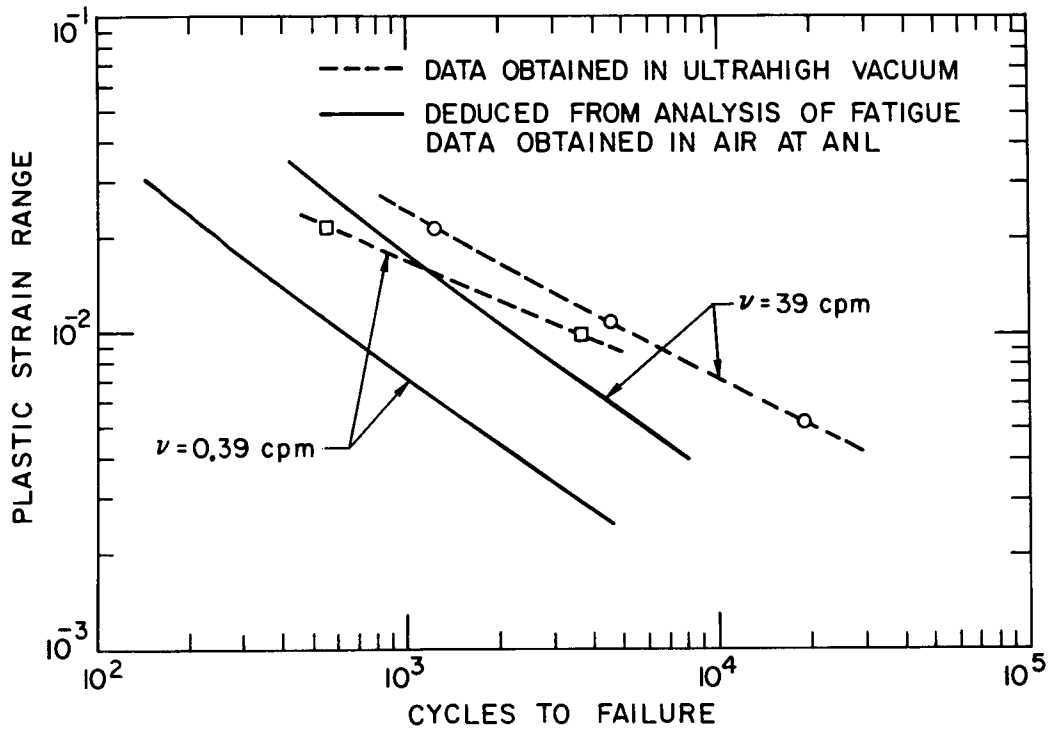

Fig. 2.13. Effects of Environment and Frequency on Fatigue Life of Type 304 Stainless Steel at 650°C.

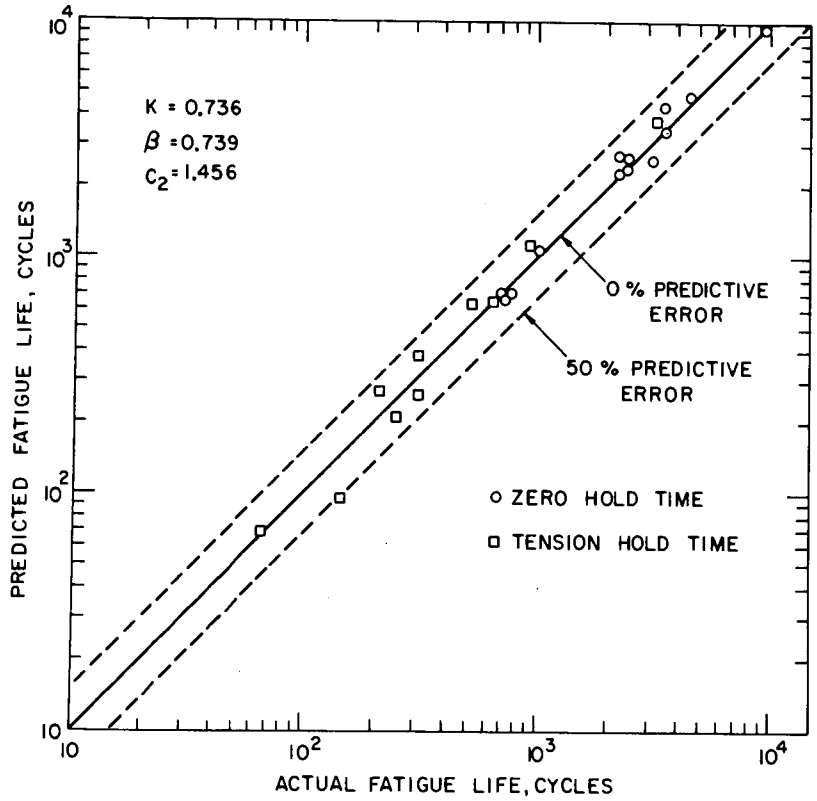

Fig. 2.14. Comparison of Actual and Predicted Fatigue Life for Type 304 Stainless Steel at 650°C. Equation (1) predicts fatigue life within ± 50% error.

environments on fatigue life. It is equally important to determine how different environments affect crack-initiation and crack-propagation processes.

REFERENCES

1. Mechanical Properties Test Data for Structural Materials Quarterly Progress Report for Period Ending October 31, 1973, ORNL-4936, pp. 15-33.

2. J. R. Ellis and E. P. Esztergar, "Considerations of Creep-Fatigue Interaction in Design Analysis," in Design for Elevated Temperature Environment, pp. 29-43, ASME (1971).

3. E. P. Esztergar, "Creep-Fatigue Interaction and Cumulative Damage Evaluations for Type 304 Stainless Steel," ORNL-4757 (1972).

4. J. B. Conway, "Evaluation of Plastic Fatigue Properties of Heat-Resistant Alloys," GEMP-740 (1969).

5. Mechanical Properties Test Data for Structural Materials Quarterly Progress Report for Period Ending January 31, 1974, ORNL-4948, p. 22.

6. G. R. Irwin, Proc. Seventh Sagamore Ordnance Material Research Conf., August 1960, Syracuse University Press, MET. E. 661-611/F.

7. L. A. James, "Effect of Thermal Aging upon the Fatigue-Crack Propagation of Austenitic Stainless Steel," Met. Trans. 5(4), 831 (1974).

8. P. Shahinian, H. H. Smith, and J. R. Hawthorne, "Fatigue Crack Propagation in Stainless Steel Weldments at High Temperature," Welding J., Research Supplement, 51, 527S-532S(Nov 1972).

9. J. C. McMillan and R. M. N. Pelloux, ASTM, Special Tech. Publ. 415 (1967), p. 505.

10. C. Y. Cheng and D. R. Diercks, "Effects of Hold Time on Low-Cycle Fatigue Behavior of AISI Type 304 Stainless Steel at 593°C," Met. Trans. 4, 615 (1973).

11. H. D. Solomon, "Frequency Dependent Low Cycle Fatigue Crack Propagation," Met. Trans. 4, 341 (1973).

12. J. C. Grosskreutz, "The Effect of Surface Films on Fatigue Crack Initiation," Midwest Research Institute, Kansas City, Missouri, Technical Report No. 12 (1972).

13. M. H. Raymond and L. F. Coffin, "Geometrical Effects in Strain Cycled Aluminum," J. Basic Eng., Trans. ASME, Series D, 85, 548 (1963).

14. C. Laird and A. R. Krause, "A Theory of Crack Nucleation in High Strain Fatigue," Intl. J. Fracture Mechanics 4, 219 (1968).

15. B. Tomkins, "Fatigue Crack Propagation - An Analysis," Phil. Mag. 18, 1041 (1968).

16. K. D. Sheffler, "Vacuum Thermal-Mechanical Fatigue Testing of Two Iron Base High Temperature Alloys," Topical Report No. 3, TRW ER-7697, TRW Materials Technology Laboratories, Cleveland, Ohio (Jan 1974).

17. R. W. Weeks, D. R. Diercks, and C. F. Cheng, "ANL Low-cycle Fatigue Studies -- Program, Results, and Analysis," ANL-8009 (Nov 1973).

18. L. F. Coffin, "Predictive Parameters and their Application to High Temperature Low Cycle Fatigue," Proc. Second Intl. Conf. on Fracture, Brighton, 643 (1969).

3. HANFORD ENGINEERING DEVELOPMENT LABORATORY

Contribution not received in time for inclusion in this issue; it will be included in the subsequent report.

4. NAVAL RESEARCH LABORATORY

4.1 INTRODUCTION - L. E. Steele

The research program of the NRL, Metallurgy Division, Reactor Materials Branch, includes the study of the behavior of structural materials useful in reactor construction. Within the scope of the title above much unirradiated data are developed. This report is developed using such data to support the USAEC objective of compiling structural materials properties data for use in national reactor development programs. The NRL program is sponsored by the Office of Naval Research, the U. S. Atomic Energy Commission, and the U. S. Army Engineer Power Group. The unirradiated materials properties data contributed here include that developed in the course of research in the areas of high temperature materials, radiation damage, and fracture mechanics.

4.2 FATIGUE CRACK GROWTH IN TYPE 304 AND 316 STAINLESS STEEL WELDMENTS
H. H. Smith and D. J. Michel

4.2.1 Background

Because of the importance of weld properties to the integrity of nuclear structures, part of the NRL fatigue program includes the study of crack growth in welds. This report reviews and summarizes results comparing the resistance to fatigue crack propagation of weld and base metal in Types 304 and 316 stainless steel weldments by Shahinian, Smith, and Hawthorne.[1] These results will in the future serve as base-line data for current NRL studies of the high temperature fatigue properties of welds.

4.2.2 Test Procedures

The submerged arc weldments, which were 25.4-mm (1-in.) thick, were prepared for the Naval Research Laboratory. Types 308 and 316 filler metals were used for the Types 304 and 316 plates, respectively. The plates were in the solution-annealed condition and the weldments were given a postweld heat treatment of 1 hr at 900 F (482 C). Details of the welding parameters, chemical composition, and flow properties of the weld and plate have been given elsewhere.[1]

Fatigue tests were conducted in air at 77, 800, and 1100 F (25, 427, and 593 C). The single-edge-notched specimens were side grooved and were

cycled at 10 cpm in cantilever bending under zero-to-tension loading (saw-tooth curve) to a constant maximum load. The orientation of the welds in the test specimens were such that the crack advanced through the weld parallel to the welding direction or, in a few cases, perpendicular to the welding direction, passing first through a region containing both base metal and weld and then through the weld. Plate material specimens were oriented such that the plane of crack growth was perpendicular to the rolling direction.

4.2.3 Results

The fatigue crack growth rates in weld metal and in plate are compared as a function of the stress intensity factor range on log-log coordinates in Fig. 4.1-4.6. For the weld, the direction of crack growth is parallel to the welding direction unless specified otherwise.

In both weld and base metal of Types 304 and 316 stainless steel weldments fatigue crack growth rates is seen to be related exponentially to stress intensity factor range (ΔK) at room and elevated temperatures. With an increase in temperature the rate of crack growth for a given ΔK was generally increased. However, the difference between growth rates in the weld metal at 800 and 1100 F (427 and 593 C) was small.

In general, resistance to crack growth by the weld metal appeared about the same as that by the base metal at room temperature, slightly greater at 800 F (427 C), and significantly greater at 1100 F (593 C). An exception was observed at 800 F (427 C) at low ΔK values where the resistance to crack growth of Type 308 weld metal was inferior to that of the Type 304 base metal. Rates of crack growth in directions perpendicular and parallel to the welding direction were approximately equivalent. The greatest superiority in crack growth resistance of weld metal over base metal occurred with the Type 316 weldment; as a result, fatigue life of the weld was longer by about a factor of three. This was because the increase in crack growth rate with increasing temperature was less for the Type 316 stainless steel weld metal than for the base metal. Type 316 weld metal had greater resistance to crack growth than Type 308 weld metal at elevated temperatures.

The superior fatigue resistance of weld metal relative to that of base metal appears to be related to microstructural differences. At elevated temperatures the fine duplex delta ferrite-austenitic microstructure of the weld metal with its many phase boundaries apparently produces better resistance to crack growth than the larger grain, fully austenitic structure of the base metal.

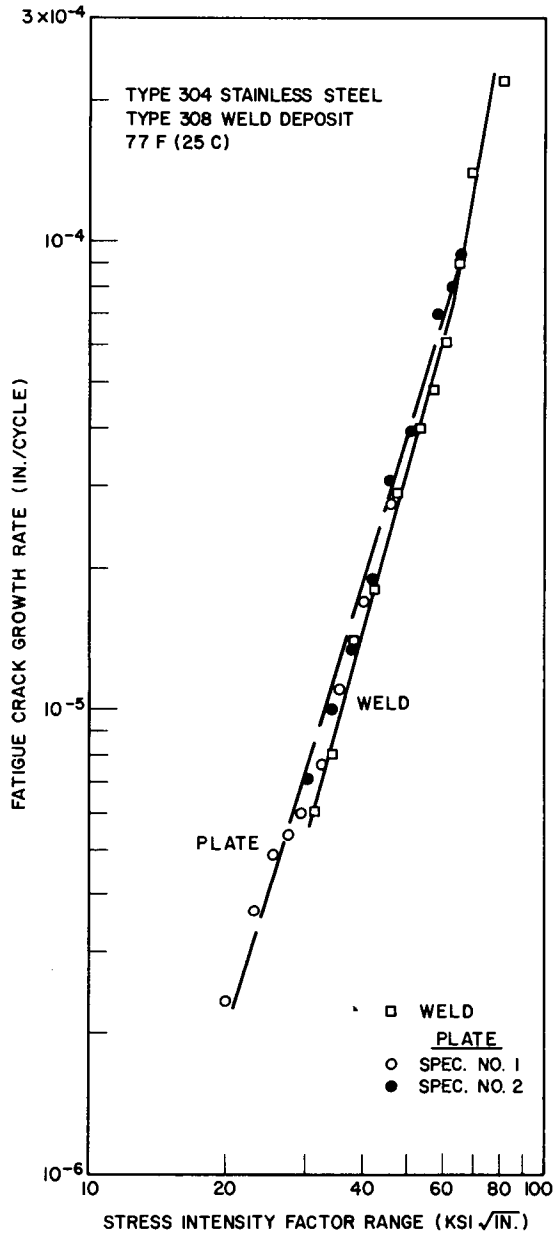

Fig. 4.1 Fatigue Crack Growth Rates in Type 304 Stainless Steel Plate and Type 308 Weld Deposit at 77 F (25 C) as a Function of Stress Intensity Factor Range.

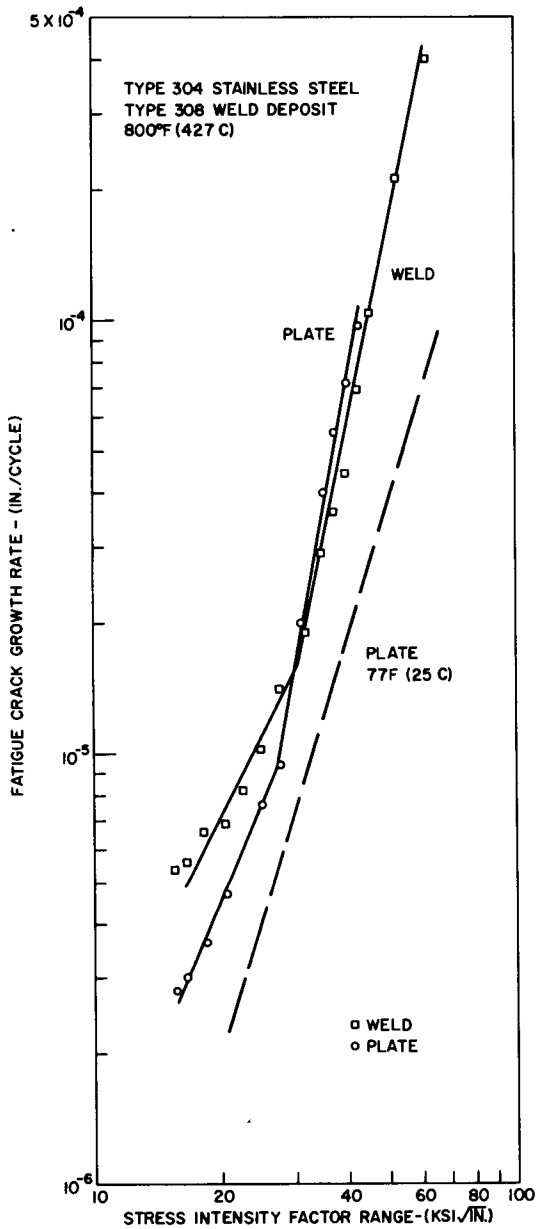

Fig. 4.2 Fatigue Crack Growth Rates in Type 304 Stainless Steel Plate and Type 308 Weld Deposit at 800 F (427 C) as a Function of Stress Intensity Factor Range.

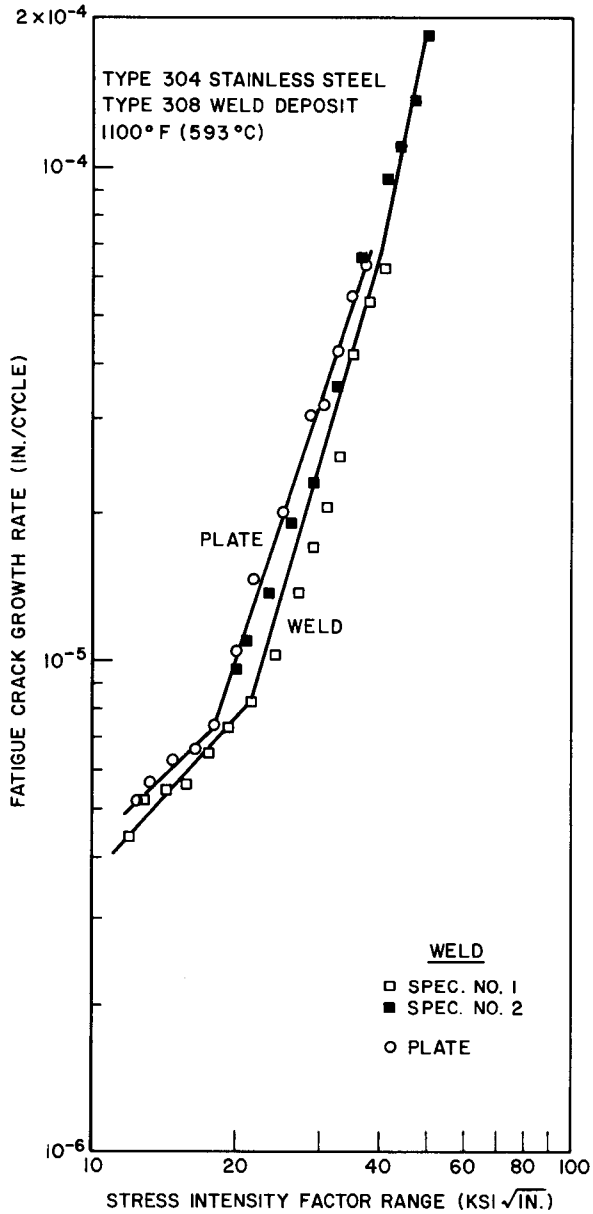

Fig. 4.3 Fatigue Crack Growth Rates in Type 304 Stainless Steel Plate and Type 308 Weld Deposit at 1100 F (593 C) as a Function of Stress Intensity Factor Range.

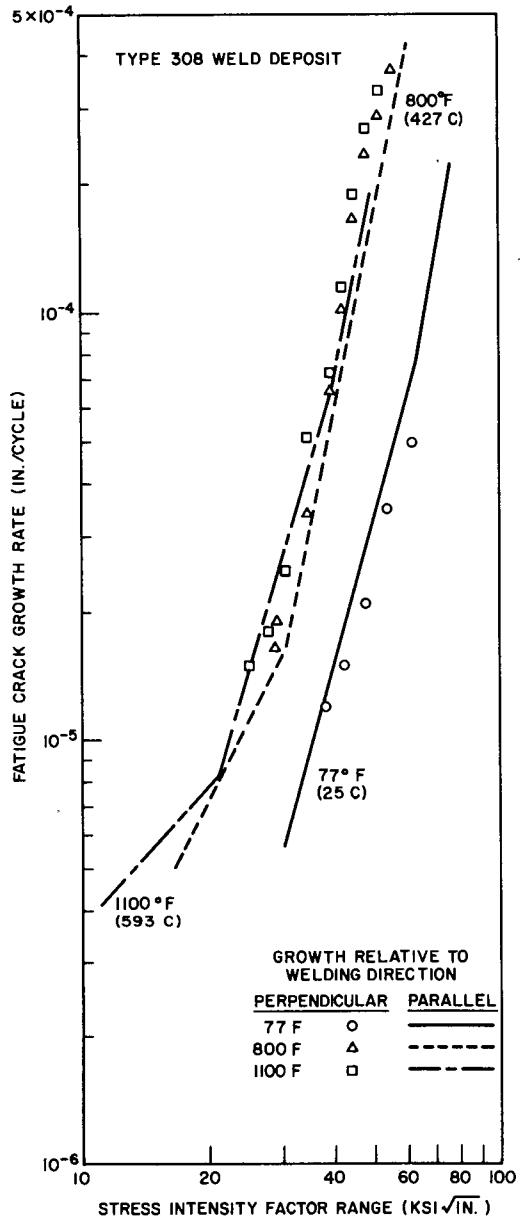

Fig. 4.4 Fatigue Crack Growth Rates in Type 308 Weld Metal in Directions Perpendicular and Parallel to Welding Direction.

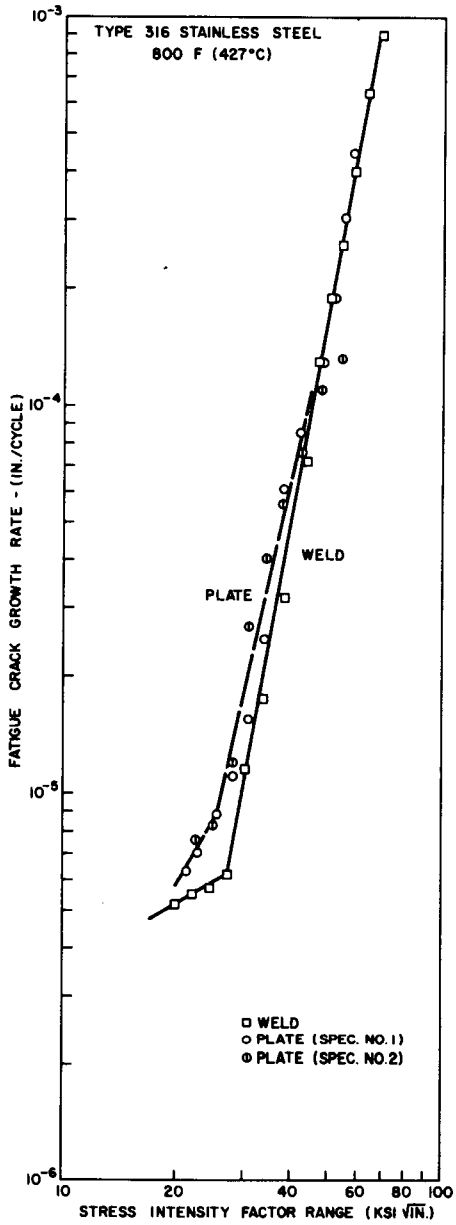

Fig. 4.5 Fatigue Crack Growth Rates in Type 316 Stainless Steel Weld and Base Metals at 800 F (427 C) as a Function of Stress Intensity Factor Range.

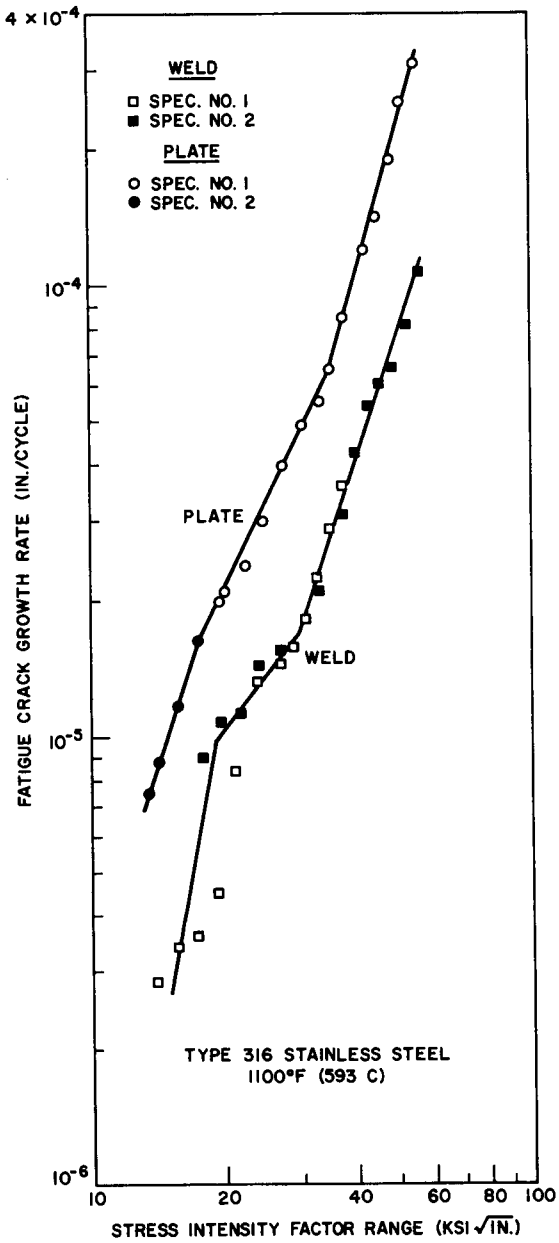

Fig. 4.6 Fatigue Crack Growth Rates in Type 316 Stainless Steel Weld and Base Metals at 1100 F (593 C) as a Function of Stress Intensity Factor Range.

4.3 TOUGHNESS OF TYPE 316 STAINLESS STEEL WELD METAL USING THE J INTEGRAL - F. J. Loss and R. A. Gray, Jr.

4.3.1 Background

The fracture toughness of austenitic stainless steel and nickel-base alloys for advanced fast breeder reactors is being characterized in terms of the J Integral. These alloys, when employed at elevated temperatures, generally exhibit elastic plastic or fully plastic behavior. The J Integral concept provides a means with which to define the initiation of crack extension in the elastic plastic regime and to relate this phenomenon to structural parameters used in design (e.g., critical flaw size and stress level). This procedure is based on a mathematical model for which experimental verification has not het been fully achieved. Nevertheless, the toughness characterization of structural alloys must proceed simultaneously with experimental investigations designed to evolve standard measurement techniques for J and to explore the effects of specimen geometry variations. The subject research explores the toughness of Type 316 stainless steel weld metal at elevated temperature. The J Integral values are defined using a multi-specimen R curve technique that is being evaluated as a measurement method.

4.3.2 EXPERIMENTAL INVESTIGATION

4.3.2.1 Material and Specimen Types

Test specimens were machined from a weldment consisting of 1-in. thick Type 316 stainless steel (SS) plates joined by submerged arc welding, using a Type 316 filler. (See Ref. 2 for detailed description of welding procedures). Notched, three-point bend specimens were cut with the longitudinal dimension of the specimen perpendicular to the welding direction and the plane of the notch perpendicular to the surface of the weldment. The dimensions of the bend specimens were width (W) = 0.394 in., thickness (B) = 0.197 in. and length (L) = 2.165 in. The specimens were fatigue precracked at a ΔK of 25 ksi $\sqrt{in.}$ (27.47 MPa-m$^{1/2}$) using a zero-tension-zero cycle in accordance with ASTM E-399 procedures. Three specimen types were investigated respectively having notch depth (a) to width ratios, a/W, of 0.3, 0.4 and 0.5.

The testing was conducted statically using a three point bend jig having a span of 1.758 in. between supports. All tests were conducted at 500 F (260 C) as achieved with an induction heating coil. The specimen load and mid span deflection were monitored on an X-Y recorder.

4.3.2.2 Results

Specimens of a given a/W ratio were loaded to various fractions of the maximum load as measured from one of the specimens. The specimens were then unloaded and heat tinted at 1100 F (593 C) to delineate the extent of slow stable crack extension that occurred with rising load. The J-Integral value was computed from the total area (A) under the load vs mid span deflection record (i.e., energy) using the approximate equation for a deeply notched beam in pure bending derived simultaneously by Rice[3] and Srawley[4] :

$$J = \frac{2A}{B(W-a)} \qquad \text{Eq. 1}$$

In all cases the deflections of the bend jig are negligible so that the area under the load vs deflection trace represents energy imparted to the specimen.

The values of J, calculated from Eq. 1, are represented in Fig. 4.7 as a function of the average slow crack extension, Δa, at the specimen quarter points. In a strict sense, crack extension is not permitted by the J concept. For this reason, Fig.4.7 includes the variations in J that results when the value of a in Eq. 1 is taken as the original a or as a + Δa.

4.3.3 Discussion

The data in Fig.4.7 illustrate a significant variation in J with crack extension. For example, the value of J associated with the crack extension near the specimen maximum load (i.e., 0.020 to 0.030 in.) can be more than twice as large as that associated with the first few mils of crack extension. In practice, some crack extension must be exhibited in order to define a critical value of J (i.e., J_{Ic}). However, the permissible crack extension has never been standardized. The ASTM standard procedure for crack initiation in a plane strain K_{Ic} test, for example, permits 2% crack extension. A similar criterion for the present

experiments would allow between 2 and 4 mils of growth for specimens having a/W ratios of 0.3 and 0.5 respectively. This criterion is not desirable in that larger crack extensions would be permitted with increasing specimen size (i.e., an artificial size effect).

It has been suggested by Landes and Begley[5] that J_{Ic} be taken as the intersection of the curve of J vs Δa (that is, the R curve) in Fig.4.7 with the line representing the stretch zone at the crack tip. This zone is an apparent crack extension caused by the changing geometry at the crack tip and is arbitrarily taken to be half of the crack opening stretch, COS where COS $\approx J/\sigma_{ys}$. The stretch zone line is plotted in Fig.4.7 using $\sigma_{flow} = \frac{1}{2}(\sigma_{ys} + \sigma_{ult})$* to account for strain hardening.

The J_{Ic} for this material is taken to be 640 in. lb/in.^{2} ($1.12 \times 10^5 \frac{J}{m^2}$) based on data points near the intersection of the R curve and the stretch zone line. Note that the data at zero crack extension should fall along the stretch zone line according to the above assumption. However, measurement techniques used were not able to resolve the crack extensions of 1 mil required to demonstrate this point.

For J_{Ic} data to be considered valid it is reasonable to require the certain minimum dimensions be maintained as in the case of plane strain testing (i.e., ASTM standard E-399). Landes and Begley[5], on the basis of data from ferritic steels, have suggested that a, B, and W-a be greater than 25 J/σ_{flow} or 0.225 in. for the subject material with J_{Ic} = 640 in. lb/in.^{2} In general the present specimens meet this requirement for the a/W = 0.5 notch depth. The a dimension of the other specimens is somewhat less than the proposed requirement. However, the data of Fig.4.7 suggest no effect of the a/W ratio. Additional research is necessary to define more clearly the specimen size limitations for the austenitic stainless steels.

---

*σ_{flow} for this material has been estimated pending completion of the tensile tests. The yield and tensile values at 500 F respectively are assumed to be 65 ksi (448 MPa) and 77 ksi (531 MPa).

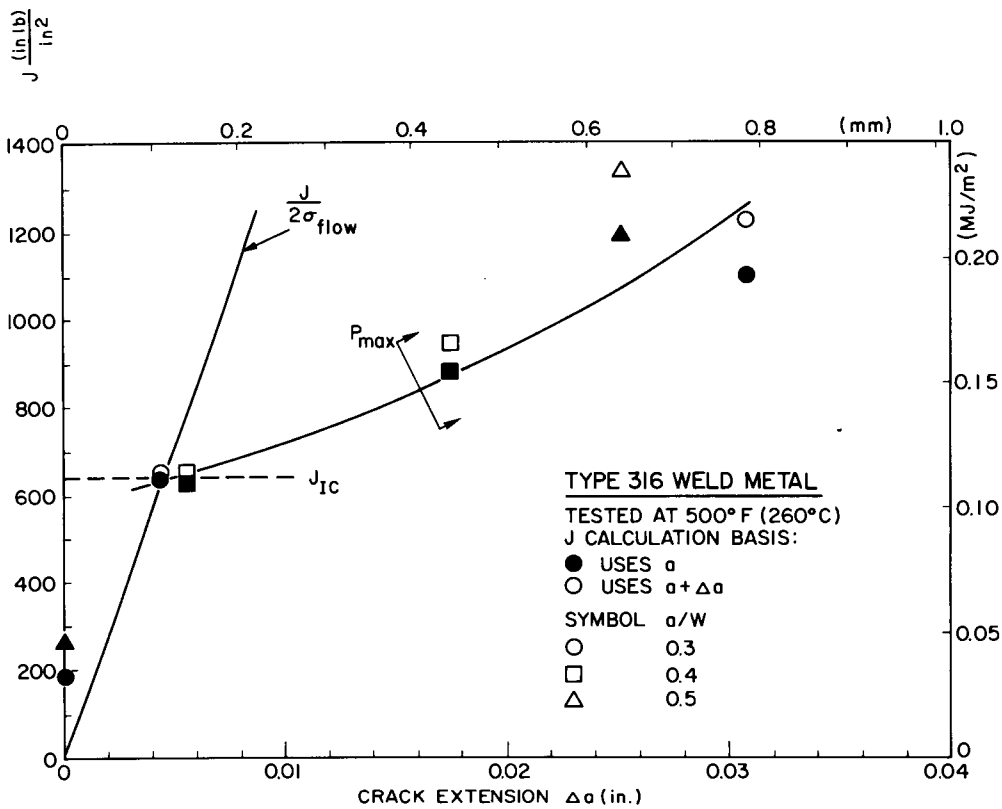

Fig. 4.7 Trend of J Integral Values with Slow Crack Extension. The Critical J, or J_{Ic}, is Defined by the Intersection of the Curve Through the Data (R-curve) and the $J/2\sigma_{flow}$ Line which Denotes the Stretch Zone at the Crack Tip. The J Values Have Been Calculated from Eq. 1; the Shaped Points Were Computed on the Basis of the Original Fatigue-Cracked Notch Length (Δa) Whereas the Open Points Included the Slow Crack Extension (Δa). The Arrows Labeled P_{max} Denotes Those Points Based on J Computed Near Maximum Load.

4.4 REFERENCES

1. P. Shahinian, H. H. Smith, and J. R. Hawthorne, "Fatigue Crack Propagation in Stainless Steel Weldments at High Temperatures," Welding Journal Research Supplement, Vol. 51, Nov. 1972, pp. 527s-532s.
2. J. R. Hawthorne and C. Z. Serpan, Jr., "Postirradiation Notch Toughness Retention of AISI Type 316 Submerged Arc Weld," NRL Memorandum Report 2752, pp. 60-63, March 1974.
3. J. R. Rice, P. C. Paris, and J. G. Merkle, "Some Further Results of J-Integral Analysis and Estimates," ASTM STP 536, Progress in Flaw Growth and Fracture Toughness Testing, 1973, pp. 231-245.
4. J. E. Srawley, "On the Rice J Integral Concept in Fracture Mechanics," lecture notes, NASA-Lewis Research Center, Cleveland, Ohio, July 1972.
5. J. D. Landes and J. A. Begley, "Test Results From J Integral Studies -- An Attempt to Establish a J_{Ic} Testing Procedure," Scientific Paper 73-1E7-FMPWR-P3, Westinghouse Research Laboratories, Pittsburgh, Pa. Oct. 18, 1973.

5. OAK RIDGE NATIONAL LABORATORY

W. R. Martin

5.1 INTRODUCTION

5.2 MECHANICAL PROPERTIES AND BEHAVIOR FOR STRUCTURAL MATERIALS — C. R. Brinkman

The objective of this program is to collect mechanical property data and material behavior for LMFBR structural and component materials. Included in the scope of this effort are the following: (1) basic tensile, creep, creep-rupture, and relaxation base-line data that are directly applicable to design criteria and methods for types 304 and 316 stainless steel reference heats and cyclic stress-strain tests performed with emphasis on loading and history effects, (2) find the variations in properties for several heats of types 304 and 316 stainless steel to allow establishment of minimum and average values of specific properties and the equation parameters required for design purposes. This work will include determination of property variation of samples from different mill products within a given heat of stainless steel.

5.2.1 Base-Line Mechanical Property Testing of Reference Heat of Type 304 Stainless Steel

5.2.1.1 Creep Properties of the 2-in. (51-mm) Plate of Reference Heat — H. E. McCoy

The need for comprehensive mechanical property data on a single heat of type 304 stainless steel for use in developing constitutive equations for design purposes was recognized during the last few years. A large heat of type 304 stainless steel (designated heat 9T2796) was purchased in several product forms, and the testing began in 1972. The test program included creep tests to accurately define the strain-time response. The details of the averaging extensometer and associated electronics for creep testing were described previously.[1] We now have 19 lever-arm creep machines and seven deadload machines equipped to do this caliber of testing.

Some of the test information was summarized in the last three quarterlies[2-4] and will be updated in the current report. The tests that have been completed and those that are in progress are given in Table 5.1. The tests have all been run on the 2-in. thick plate, and samples were taken from the center line in the primary working direction. Test samples have a gage section 0.25 in. in diameter × 2.25 in. long (6.35 × 57.2 mm) and were reannealed 0.5 hr at 1093°C (2000°F) in argon. The test environment was air. The test matrix for long-term tests is given in Table 5.2. The numbers in parentheses are the test numbers and can be used to refer to Table 5.1. All the tests in Table 5.2 have been started.

Some creep tests of about 1000 hr duration are needed to determine the primary creep behavior. The tests of A-1 priority are shown in Table 5.3, and four remain to be started. These tests are in the loading rate series and will be started as soon as a new loading device is completed.

The loading strains were measured for each test, and these are given in Table 5.1. The loading strains were analyzed in terms of the ratio of the creep stress to the yield stress at the test temperature. The correlation between these ratios and the loading strains is shown in Fig. 5.1 in linear coordinates. The same data are shown in Fig. 5.2 in logarithmic coordinates. The latter plot was fitted with two equations — a linear equation when the creep stress was ≤0.7 × the yield stress and a quadratic at higher stress ratios. The equations are, respectively:

$$\log \varepsilon_L = (0.87 \pm 0.11)\log R - (3.02 \pm 0.11),\ 0 \leq \varepsilon_L \leq 0.7\% ,$$

and

$$\log \varepsilon_L = -(1.26 \pm 0.07) + (6.30 \pm 0.26)\log R$$

$$- (2.98 \pm 0.74)\ (\log R)^2,\ 0.7 \leq \varepsilon_L \leq 20 .$$

Where ε_L = loading strain in % and R = creep test stress/yield stress.

Table 5.1. Creep Tests on Type 340 Stainless Steel Reference Heat 9T2796 2-in.-thick (51-mm) Plate[a]

Test	Temperature (°C)	Temperature (°F)	Stress ksi	Stress MPa	Time in Test (hr)	Strain, % Loading	Strain, % Creep	Ratio of Creep Stress To Yield Stress[b]	Comments[c]
11595	427	800	20.0	138	7,270	2.67	0.05	1.57	
12368	427	800	18.0	124	4,240	1.91	0.006	1.42	
12472	427	800	16.0	110	3,370	1.17	0.038	1.26	
12570	427	800	14.0	97	3,040	0.83	0.020	1.10	
11569	482	900	20.0	138	7,390	3.27	0.057	1.70	
12375	482	900	18.0	124	4,170	2.40	0.028	1.53	
11675	482	900	16.0	110	2,451	1.48	0.032	1.36	Discontinued
11693	482	900	14.0	97	2,202	0.92	0.14	1.19	Discontinued
11830	482	900	12.0	83	1,682	0.35	0.04	1.02	Discontinued
13152	482	900	10.0	69	1,200	0.089	0.04	0.85	
13020	482	900	10.0	69	1,900	0.085	0.035	0.85	
10489	538	1000	20.0	138	12,280	3.80	0.53	1.80	
12250	538	1000	18.0	124	4,750	2.62	0.21	1.62	
11625	538	1000	16.0	110	7,150	1.79	0.19	1.44	
10491	538	1000	14.0	97	12,300	1.16	0.22	1.26	
12444	538	1000	14.0	97	3,710	1.18	0.15	1.26	
12445	538	1000	14.0	97	3,740	1.17	0.052	1.26	
11568	538	1000	12.0	83	7,390	0.53	0.078	1.08	
11626	538	1000	10.0	69	7,150	0.071	0.067	0.90	
11641	538	1000	8.0	55	3,170	0.040	0.027	0.72	Discontinued
10853	593	1100	18.0	124	4,545	2.84	5.94	1.65	Ruptured
10852	593	1100	16.0	110	10,540	2.29	1.60	1.47	
10554	593	1100	14.0	97	8.710	1.40	0.65	1.28	Discontinued
11596	593	1100	12.0	83	7,540	0.52	0.31	1.10	
10490	593	1100	10.0	69	12,275	0.22	0.34	0.92	
11227	593	1100	8.0	55	6,103	0.041	0.080	0.73	Discontinued
12459	593	1100	5.0	34	3,550	0.024	0.065	0.46	
10855	649	1200	16.0	110	304	2.41	12.0	1.57	Ruptured
10854	649	1200	14.0	97	791	1.60	13.0	1.37	Ruptured
11563	649	1200	12.0	83	2,674	0.59	13.4	1.18	Ruptured
11226	649	1200	10.0	69	7,279	0.18	7.0	0.98	
10851	649	1200	8.0	55	10,455	0.044	1.03	0.78	
12255	649	1200	5.0	34	992	0.030	0.08	0.49	Discontinued
12443	649	1200	5.0	34	3,500	0.024	0.085	0.49	
12460	649	1200	3.0	21	3,500	0.020	0.15	0.29	
10856	704	1300	10.0	69	568	0.067	15.6	0.90	Ruptured
10562	704	1300	10.0	69	653	0.12	22.5	0.90	Ruptured
11222	704	1300	8.0	55	2,760	0.031	16.4	0.72	Ruptured
12254	704	1300	5.0	34	4,700	0.030	0.66	0.45	
12461	704	1300	3.0	21	3,550	0.018	0.25	0.27	
12462	704	1300	2.0	14	3,500	0.010	0.19	0.18	

[a]Annealed 0.5 hr at 1093°C before testing. All tests loaded at a strain rate of 0.004/min.

[b]Yield stresses used in this ratio were 12,700 psi (88 MPa) at 427°C (800°F), 11,800 psi (81 MPa) at 482°C (900°F), 11,100 psi (77 MPa) at 538°C (1000°F), 10,900 psi (75 MPa) at 593°C (1100°F), 10,200 psi (70 MPa) at 649°C (1200°F), 11,100 psi (77 MPa) at 704°C (1300°F).

[c]Unless otherwise noted, tests in progress.

Table 5.2. Test Matrix for Uniaxial Creep of Type 304 Stainless Steel

Stress		Priority and Test Number[a] for Each Temperature, °F (°C)					
(MPa)	(psi)	800 (427)	900 (482)	1000 (538)	1100 (593)	1200 (649)	1300 (704)
14	2,000						C (12462)
21	3,000					C (12460)	B (12461)
34	5,000				C (12459)	C (12255, 12443)	A-1 (12254)
55	8,000			C (11641)	A-1 (11227)	A-1 (10851)	A-1 (11222)
69	10,000		C (13152, 13020)	C (11626)	A-1 (10490)	A-2 (11226)	A-1 (10856, 11562)
83	12,000		C (11830)	A-2 (11568)	B (11596)	B (11563)	
97	14,000	C (12570)	C (11693)	A-1 (10491)	A-1 (10554)	A-1 (10854)	
110	16,000	C (12472)	C (11675)	B (11625)	A-1 (10852)	A-1 (10855)	
124	18,000	C (12368)	C (12375)	B (12250)	A-1 (10853)		
138	20,000	A-2 (11595)	A-2 (11569)	A-1 (10489)			

[a]Test number refers to Table 5.1.

Table 5.3. Short-Time A-1 Priority Uniaxial Creep Tests of Type 304 Stainless Steel[a]

Stress (ksi)	Stress (MPa)	Loading Strain Rate (min^{-1})	Tests at Each Temperature, °F (°C) 800 (427)	900 (482)	1000(538)	1100 (593)	1200 (649)	1300 (704)
3	21	0.005						12461
5	34	0.005				12459	12255, 12443	12254
8	55	0.005			11641	11227	10851	11222
10	69	0.005		13152, 13020	11626	10490	11226	10856, 11562
		0.0005				b		
		0.25				b		
12	83	0.005		11830	11568	11596	11563	
14	97	0.005	12570	11693	10491, 12444, 12445	10554	10854	
16	110	0.005	12472	11675	11625	10852		
		0.0005				b		
		0.25				b		
20	138	0.005	11595	11569	10489			

[a]Numbers listed refer to test numbers in Table 3.1. Some of the same tests are also part of the long-term test matrix shown in Table 3.2.

[b]Test called for but not yet started.

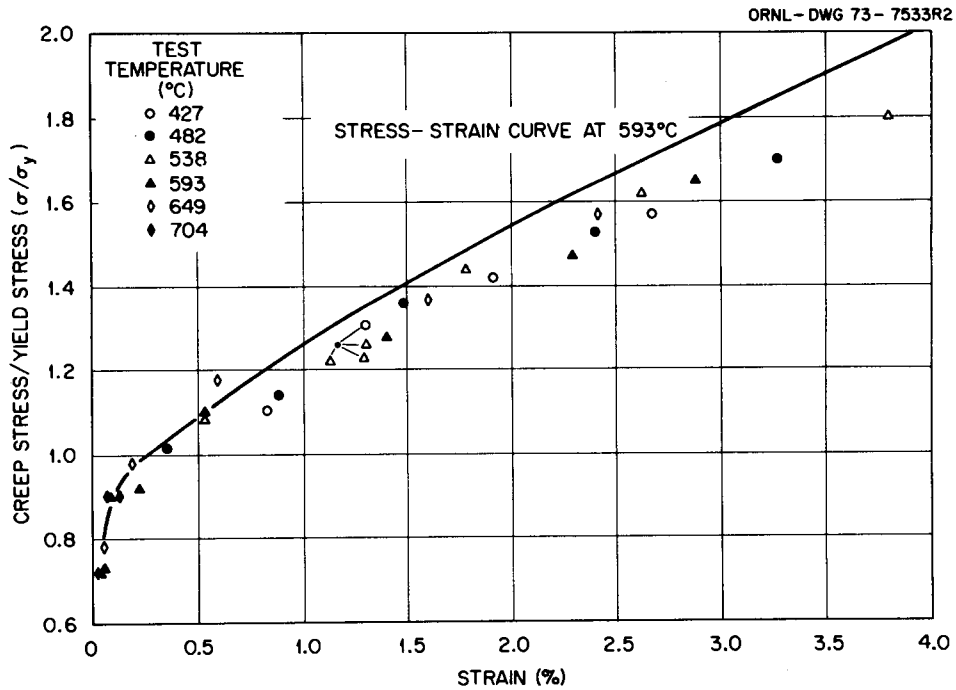

Fig. 5.1. Comparison of Strain on Loading with Stress Ratio for Type 304 Stainless Steel (Heat 9T2796) Annealed 0.5 hr at 1093°C (2000°F).

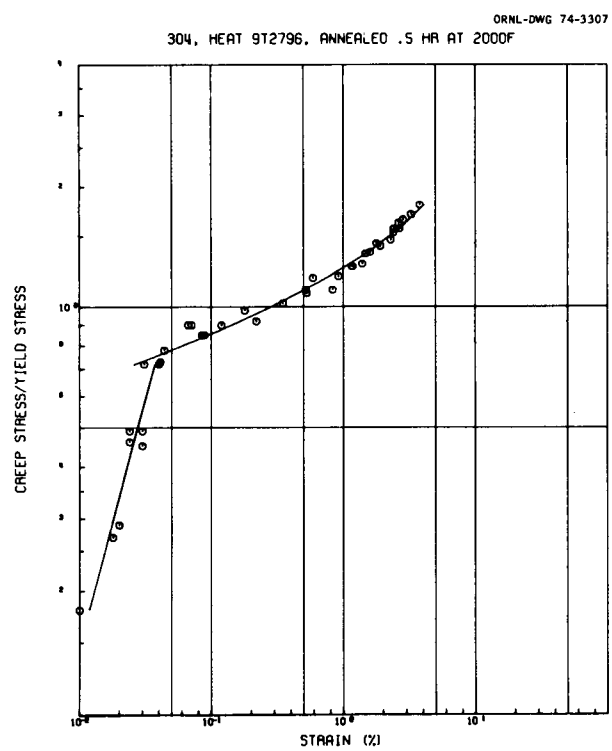

Fig. 5.2. Comparison of Strain on Loading with Stress Ratio in Type 304 Stainless Steel (Heat 9T2796) Annealed 0.5 hr at 1093°C (2000°F).

The loading strains observed for this heat are generally higher than those predicted by the HEDL equations. The agreement is quite good at low stresses where the strain is primarily elastic, but the disagreement is greater at stresses above the proportional limit.

The individual creep curves of most of the tests listed in Table 5.1 have been examined in detail. Several important creep characteristics are summarized in Table 5.4. Several tests were run on this heat as part of another study. They were run with nonaveraging extensometers, but the minimum creep rate and rupture time values should be accurate. The results of these tests are summarized in Table 5.5 and have been included in some of the correlations that follow.

Tests have ruptured thus far at 538, 593, 649, and 704°C (1000, 1100, 1200, and 1300°F). The observed plots of stress against rupture time are compared with the minimum code values in Fig. 5.3. The rupture time at a given stress level was always slightly greater for the reference heat than the specified minimum value. However, the rupture times were considerably less for the reference than for the "average values" taken from Smith's compilation.[5] Thus, the reference heat meets the minimum requirements for rupture strength, but falls short of most heats.

The times required to reach various strains are given in Table 5.4 for all the tests. Although values are tabulated for strains as low as 0.01%, there is obviously too much scatter for the results to be of value. This is not too surprising for such a low strain. At a strain level of 0.1%, the values correlate much better (Fig. 5.4). A similar plot is shown in Fig. 5.5 for a strain level of 1%. Not many tests have reached this strain at the lower temperatures, so the data are sparse.

The time to reach tertiary creep was determined by the intersection of the creep curve with a line displaced 0.2% above the minimum creep rate portion of the curve. The results of the tests that have reached this stage are shown in Fig. 5.6.

The minimum creep rate measurements are shown as a function of stress in Fig. 5.7. Many of the tests are still in primary creep, and the creep rates have not yet reached their true minimum values. Another

Table 5.4. Selected Creep Characteristics

Test	Time to Indicated Creep Strain, hr, for Strain at							Time to Tertiary Creep (hr)	Minimum Creep Rate %/hr	Primary Strain (%)
	0.01%	0.02%	0.05%	0.1%	0.2%	0.5%	1.0%			
11595	250	750	4600						5.4×10^{-6}	>0.05
12368	>1700								4.0×10^{-6}	>0.006
12472	250	800							1.2×10^{-5}	>0.03
12570	800								9.5×10^{-6}	>0.01
11569	50	100	3900						5.8×10^{-6}	0.028
12375	850	1750							1.2×10^{-5}	
11675	25	500							2.0×10^{-6}	0.02
11693	250									
11830	10	50							4.0×10^{-6}	0.032
13152										
13020										
10489	25	50	150	400	1150	~11,000			2.5×10^{-5}	0.22
12250	25	50	240	675	>2200				3.2×10^{-5}	0.11
11625	6	65	400	1200	>4600				1.4×10^{-5}	0.11
10491	3	6	25	600	7700				5.9×10^{-5}	0.16
12444	20	40	440	>1200					1.5×10^{-5}	0.03
12445	400	800	>1800						2.3×10^{-5}	~0
11568	100	1000	4600						9.0×10^{-6}	0.012
11626	~10	75	2600						7.6×10^{-6}	0.030
11641	300	1000								>0.03
10853		3	10	40	160	750	2250	2000	2.4×10^{-4}	0.4
10852	3	5	10	25	100	850	3700		6.0×10^{-5}	0.9
10554	10	20	45	110	550	3,600			2.0×10^{-5}	0.47
11596	6	20	75	300	1500	>4,700			3.2×10^{-5}	0.15
10490	2	30	200	1100	3400	~10,000			1.0×10^{-5}	0.20
11227	200	450	3300	>6000					9.0×10^{-6}	0.020
12459	400	800	>1900						2.0×10^{-5}	0.007
10855					1.4	10	35	120	1.6×10^{-2}	0.4
10854			0.25	1.0	4.0	30	90	220	8.3×10^{-3}	0.3
11563	0.1	1	3	8	25	100	200	2200	3.2×10^{-3}	0.5
11226			17	60	110	300	1000	5600	6.1×10^{-4}	0.45
10851	3	45	150	300	550	2,800	>8500	>8500	5.7×10^{-5}	0.35
12255	60	110	325	>1000					3.2×10^{-5}	0.043
12443	400	620	1500						2.4×10^{-5}	0.014
12460	20	60	250	1500						~0.06
10856						25	45	330	1.9×10^{-2}	~0
11562	0.3	0.6	2	4	7	20	35	450	2.6×10^{-2}	~0
11222						75	175	2300	4.1×10^{-3}	0.7
12254	22	32	60	155	425	3,050		>3000	8.8×10^{-5}	0.23
12461	4	12	45	240	1400				4.3×10^{-5}	0.15
12462	14	20	100	700	>2000				4.1×10^{-5}	0.08

Table 5.5. Creep Tests on Heat 9T2796[a]

Test	Temperature		Stress		Minimum Creep Rate	Rupture Life	Strain, %		Reduction of Area
	(°C)	(°F)	(ksi)	(MPa)	(%/hr)	(hr)	Loading	Creep	(%)
12815	538	1000	460	317	0.034	32.2	21.1	17.9	41.7
10918	593	1100	250	172	0.010	291.2	7.3	7.4	13.8
11339	593	1100	250	172	0.0080	423.3	6.9	4.4	10.3
10917	593	1100	300	207	0.078	92.8	10.4	11.4	20.0
10916	593	1100	350	241	0.37	22.2	14.5	16.2	27.4

[a]Tests with nonaveraging extensometers. All samples annealed 0.5 hr at 1093°C before testing.

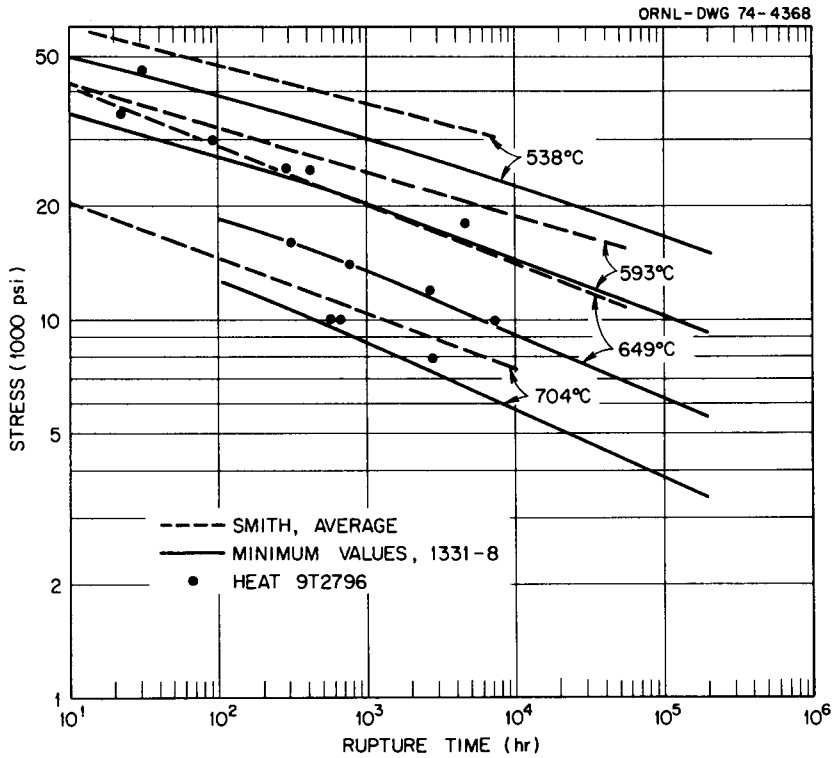

Fig, 5.3. Comparison of Code "Minimum Values" and Observed Values for Heat 9T2796 for Stress-Rupture Time.

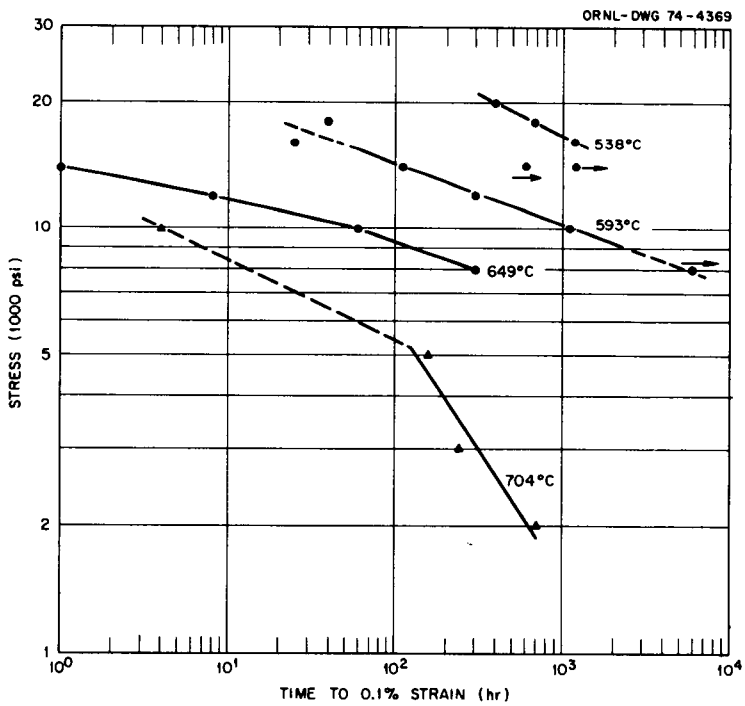

Fig. 5.4. Time to Reach 0.1% Creep Strain as a Function of Stress.

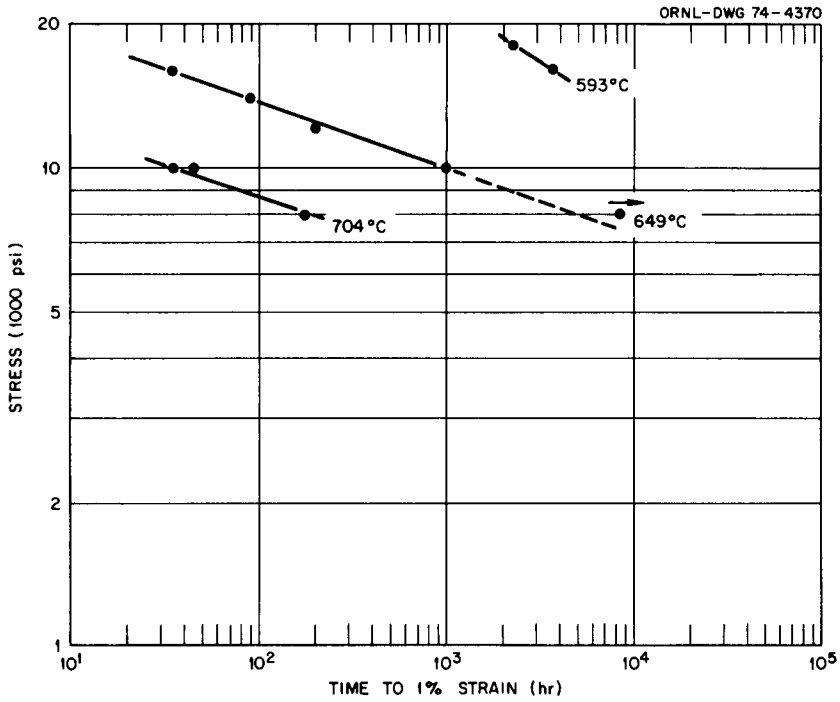

Fig. 5.5. Time to Reach 1% Creep Strain as a Function of Stress.

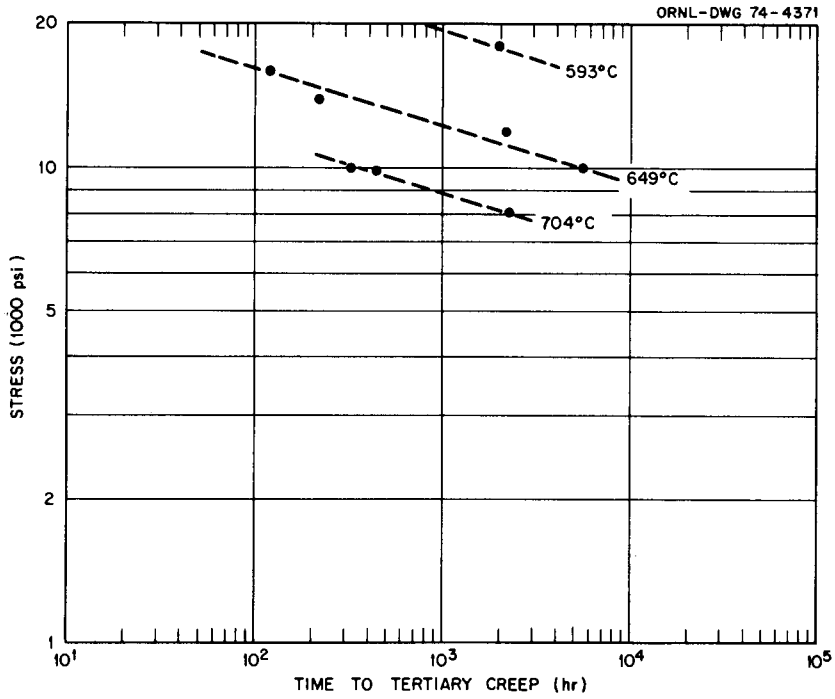

Fig. 5.6. Time to Reach Tertiary Creep as a Function of Stress.

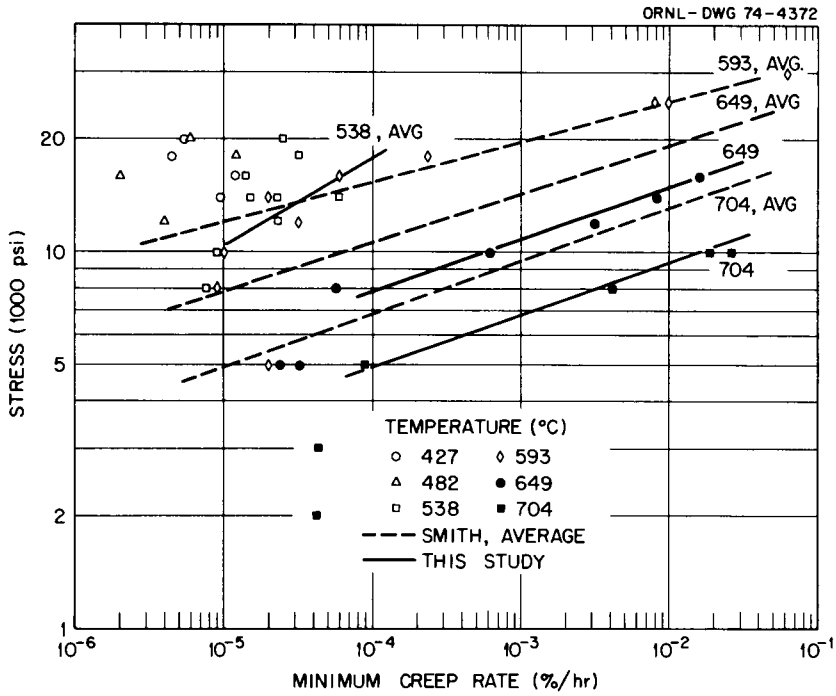

Fig. 5.7. Minimum Creep Rate Data for Heat 9T2796.

problem is that some of the tests have not accumulated enough strain to accurately determine the creep rate. For example, at a creep rate of 10^{-6}%/hr with a gage length of 2.25 in., a specimen will have deformed only 22.5 μin. in 1000 hr. Our estimate of standard error is about 50 μin. Thus, this test will have to run about 10,000 hr (225 μin. strain) to obtain an accurate value of the strain rate. For our test conditions, strain rates of the order of 10^{-5}%/hr are reasonably accurate and rates of the order of 10^{-6}%/hr about the smallest measurable with any accuracy.

The minimum creep rates in Fig. 5.7 for 427, 482, and 538°C (800, 900, and 1000°F) are quite low, and their scatter is such that little information is available about their dependence on stress. The data at 593°C (1100°F) show a systematic dependence on stress level. The tail-off at stress levels of 10,000 and 8000 psi (69 and 55 MPa) is likely due to the creep rate not having reached its minimum value. The creep rates at this temperature agree quite well with the "average" curve taken from Smith.[5] The creep rates at 649 and 704°C (1200 and 1300°F) show a systematic dependence on stress at relatively high stresses but drop off at low stresses. This apparent drop-off is due to the tests still being in the

primary creep stage. The minimum creep rate for the reference heat is higher at these two temperatures than for Smith's "average" heat. From a design standpoint, the stress level to produce a given minimum creep rate is 30 to 40% higher for the "average" heat than for the reference heat.

The primary creep strains are given in Table 5.4 and shown graphically in Fig. 5.8. The values were obtained by back-extrapolation of the minimum creep rate to zero time. Thus, these values depend upon the test actually having reached the minimum creep stage. If the test is still in primary creep, the value for the primary creep strain will be too low. The values at 427 and 482°C (800 and 900°F) are not very accurate, but they are less than 0.1% and show very little variation with stress level. Although there is considerable scatter, the magnitude of the primary strain generally decreased with decreasing stress and the dependence on stress increased with increasing test temperature. Another correlation is that the primary creep strain at a given stress increased with increasing temperature. For example, at 10,000 psi (69 MPa) the primary creep strain would vary from less than 0.01% at 427°C (800°F) to almost 1% at 704°C (1300°F).

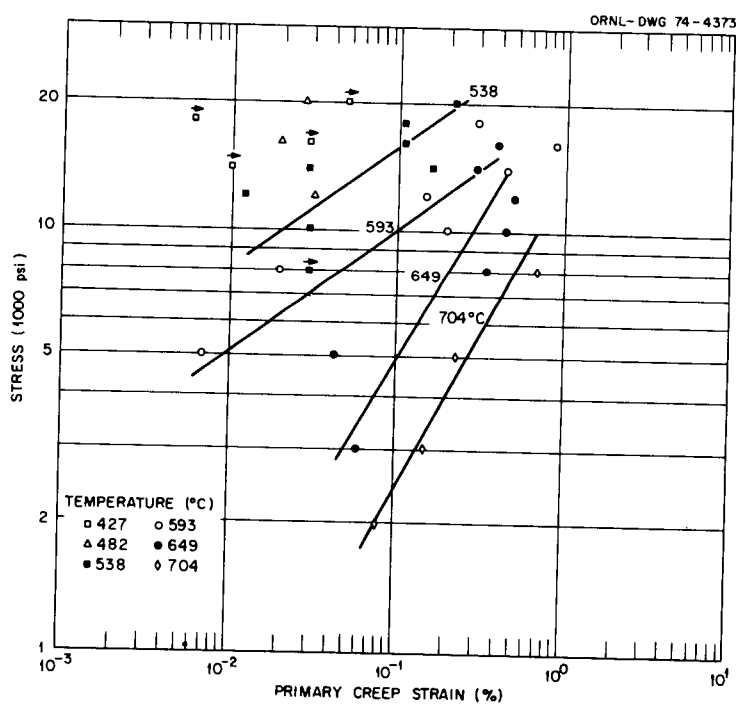

Fig. 5.8. Variation of Primary Creep Strain with Stress and Temperature.

The tests results are complete enough to permit the construction of partial isochronous stress-strain curves. These are shown in Figs. 5.9 through 5.14 and are compared with the stress-strain curve for 1000 hr from Code Case 1331-8. The time intervals used in Code Case 1331-8 are 10, 30, 100, 300, 1000, 3000, 10,000, and 30,000 hr, and we have used these same time intervals as far as our data allow. The data at 427 and 482°C (800 and 900°F, Figs. 5.9 and 5.10, respectively) show very little time dependence. The strain obtained on loading dominated the curves. For a given stress level, the strain is much larger in 1000 hr for heat 9T2796 than predicted by the Code curve. At 538°C (1000°F, Fig. 5.11) the Code and experimental curves agree quite well up to 10,000 psi (69 MPa) but deviate progressively as the stress is increased. At 593°C (1100°F, Fig. 5.12) the strain behavior is noticeably time dependent. The Code and experimental curves agree to about 8000 psi (55 MPa) and deviate

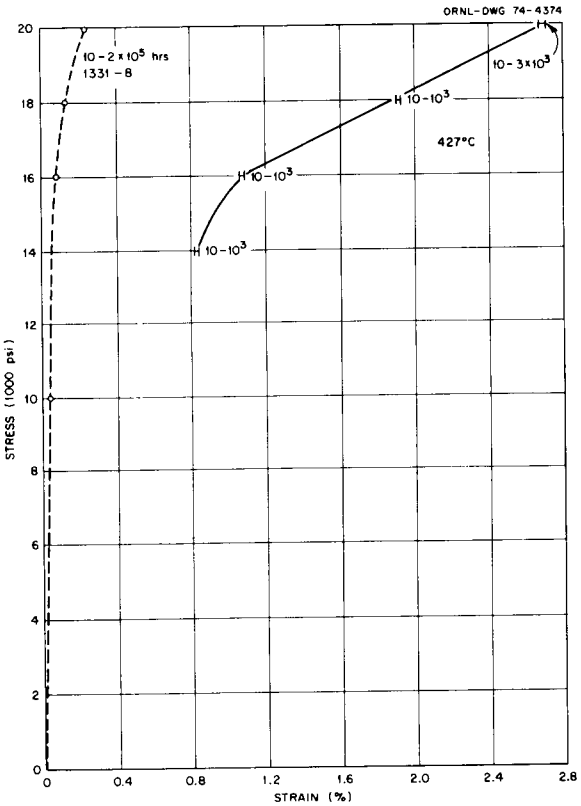

Fig. 5.9. Isochronous Stress-Strain Curve for Heat 9T2796 at 427°C (800°F).

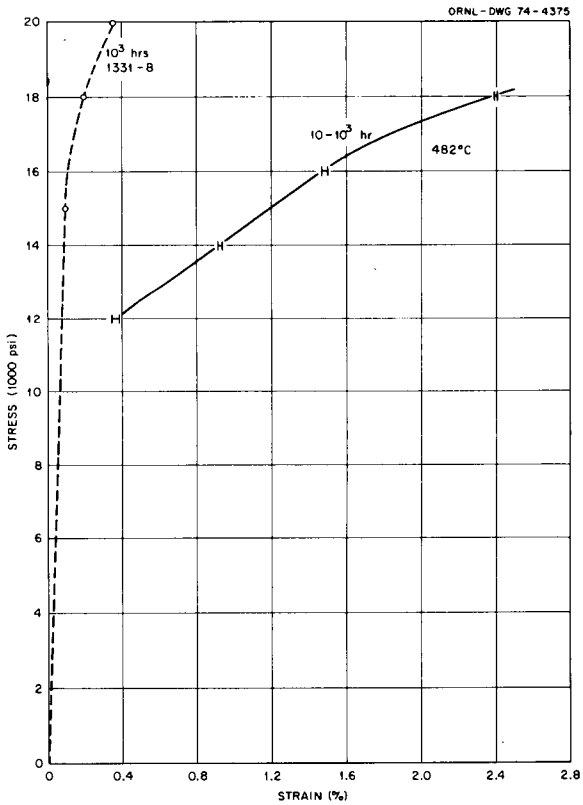

Fig. 5.10. Isochronous Stress-Strain Curve for Heat 9T2796 at 482°C (900°F).

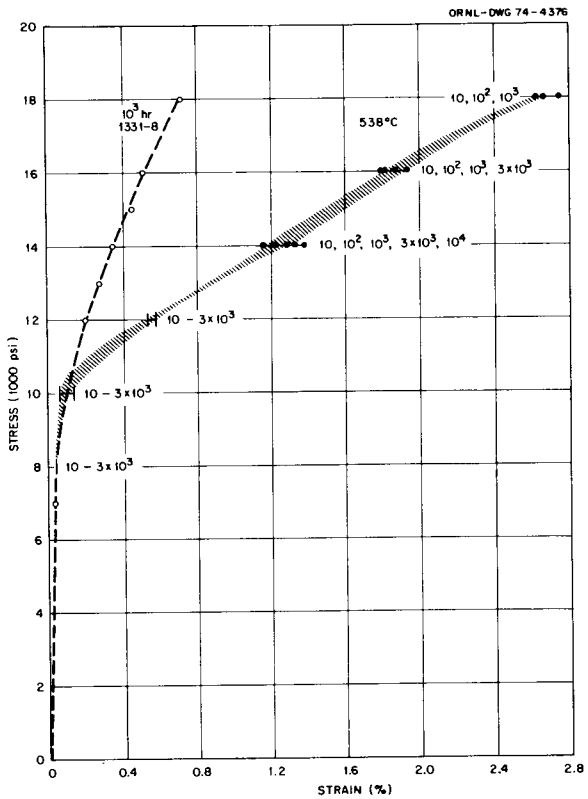

Fig. 5.11. Isochronous Stress-Strain Curve for Heat 9T2796 at 538°C (1000°F).

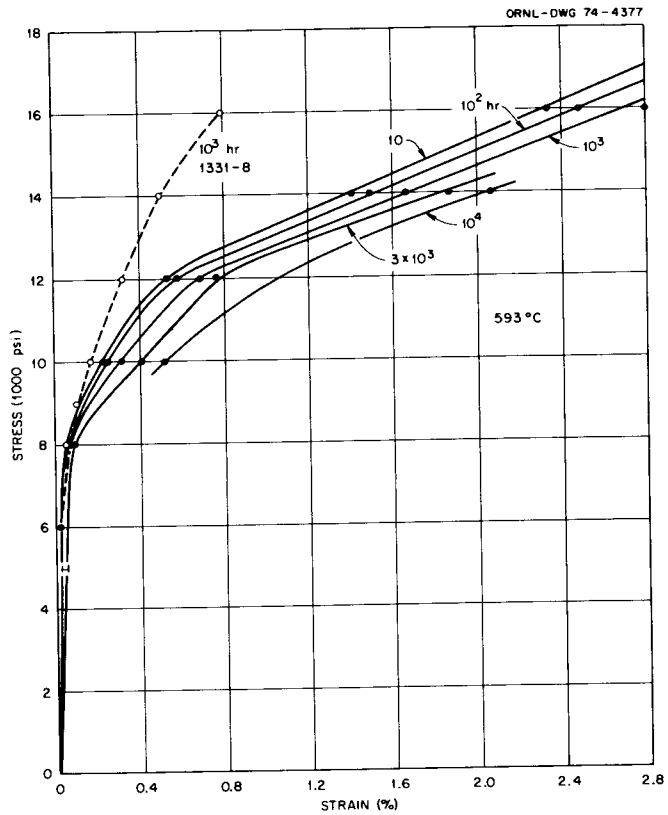

Fig. 5.12. Isochronous Stress-Strain Curves for Heat 9T2796 at 593°C (1100°F).

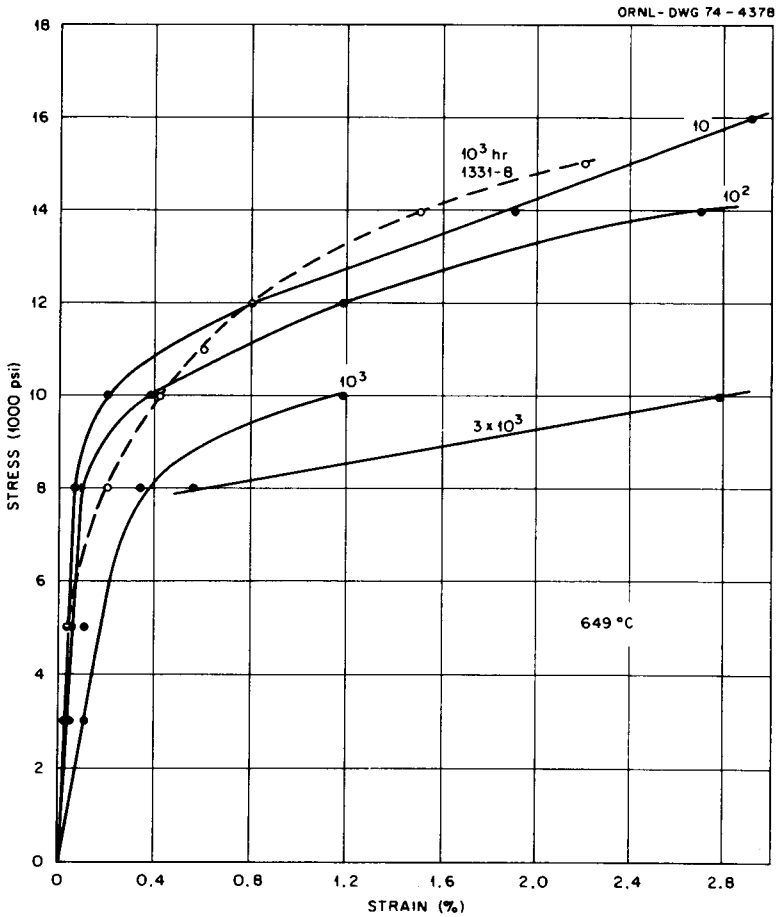

Fig. 5.13. Isochronous Stress-Strain Curves for Heat 9T2796 at 649°C (1200°F).

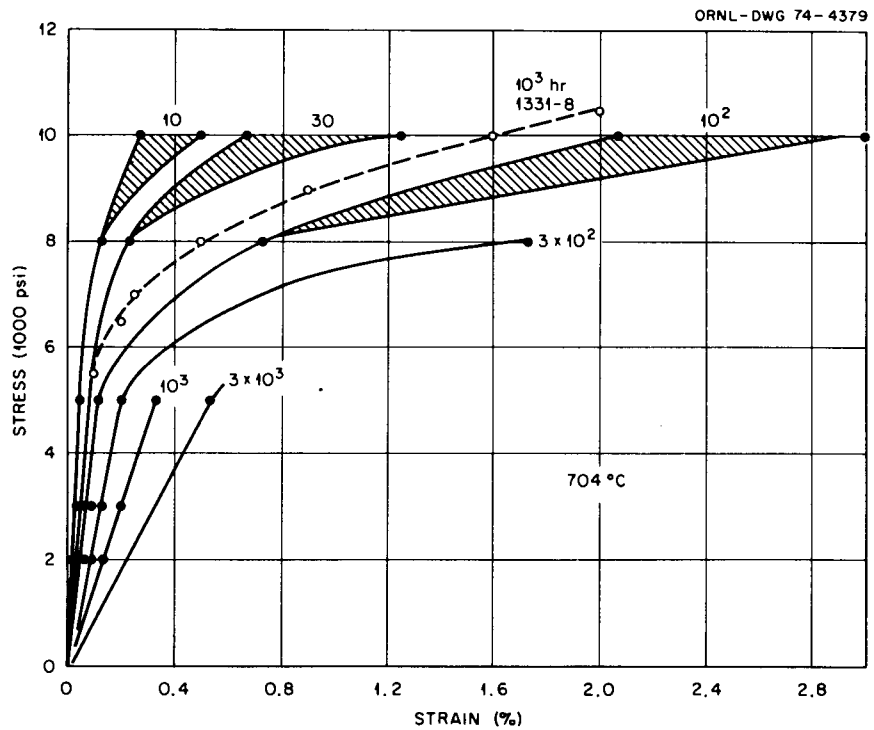

Fig. 5.14. Isochronous Stress-Strain Curves for Heat 9T2796 at 704°C (1300°F).

markedly at higher stresses. The stress-strain behavior at 649°C (1200°F, Fig. 5.13) and 704°C (1300°F, Fig. 5.14) is time dependent even at very low stresses. The experimental strains for heat 9T2796 are higher at a given stress level than predicted by the Code lines.

The creep curves for heat 9T2796 were compared with those predicted by the HEDL two-exponential equation. This equation is of the basic form

$$\varepsilon_T = \varepsilon_L + A(1 - e^{-\alpha t}) + B(1 - e^{-\beta t}) + \dot{\varepsilon}_m t \ ,$$

where

ε_T = total strain
ε_L = loading strain
t = time
$\dot{\varepsilon}_m$ = minimum creep rate
A, B, α, β = constants.

Our comparison is made without the loading strain, ε_L, included. The experimental and calculated curves for 482°C (900°F) are compared in Fig. 5.15. The experimental curve at 18,000 psi (124 MPa) falls out of line with the other tests at 482°C (900°F) because of the uncertainty in the creep behavior during the first 500 hr. However, the calculated curve for 20,000 psi (138 MPa) exhibits less strain than the experimental curve

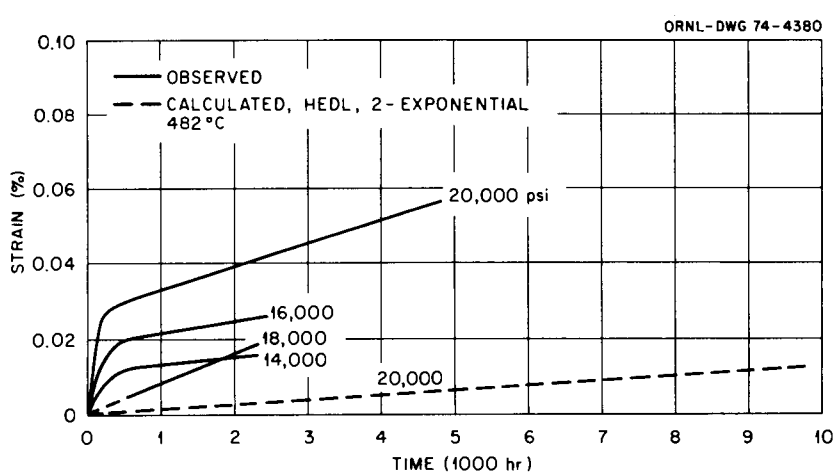

Fig. 5.15. Comparison of Creep Curves for Heat 9T2796 and Calculated Curves at 482°C (900°F).

at 14,000 psi (97 MPa). The main difference is that heat 9T2796 exhibits more primary creep than predicted by the two-exponential equation. However, the minimum creep rate of heat 9T2796 is also higher than predicted by the equation.

The experimental and calculated creep curves at 593°C (1100°F) are compared in Fig. 5.16. The two curves at 18,000 psi (125 MPa) do not agree well. However, the pairs of curves agree quite well at stresses from 16,000 to 5000 psi (110–34 MPa). At 704°C (1300°F, Fig. 5.17) the measured creep curves exhibit higher strain than the calculated curves. The measured curves have larger amounts of primary creep and higher minimum creep rates.

The test results have been fit by regression analysis to several creep models. The first model is an eight-term polynomial of the form

$$\varepsilon = A_0 + A_1 t^{0.14} + A_2 t^{0.28} + A_3 t^{0.43} + A_4 t^{0.58}$$

$$+ A_5 t^{0.71} + A_6 t^{0.86} + A_7 t^{1.01}$$

where

ε = creep strain, % (does not include loading strain),
t = time, hr.

This model obviously cannot fit any portion of the creep curve above the minimum creep stage because the highest power of time is 1.01. This polynomial fits the data quite well, and the estimate of standard error is a good measure of the scatter in the test results. The standard error physically is a band about the fitted curve that is one standard deviation above and below the curve and contains 68% of the data. Although the standard error may depend upon the magnitude of the strain being measured, the reported standard error is an average along the entire fitted curve. The estimates of standard error for the polynomial model are listed in Table 5.6. Tests that went to large strains in a few hundred hours have standard errors of about 100 μin./in. (100 μm/m). Tests with small total strains generally have standard errors of 10 to 50 μin./in. (10–50 μm/m). The average value

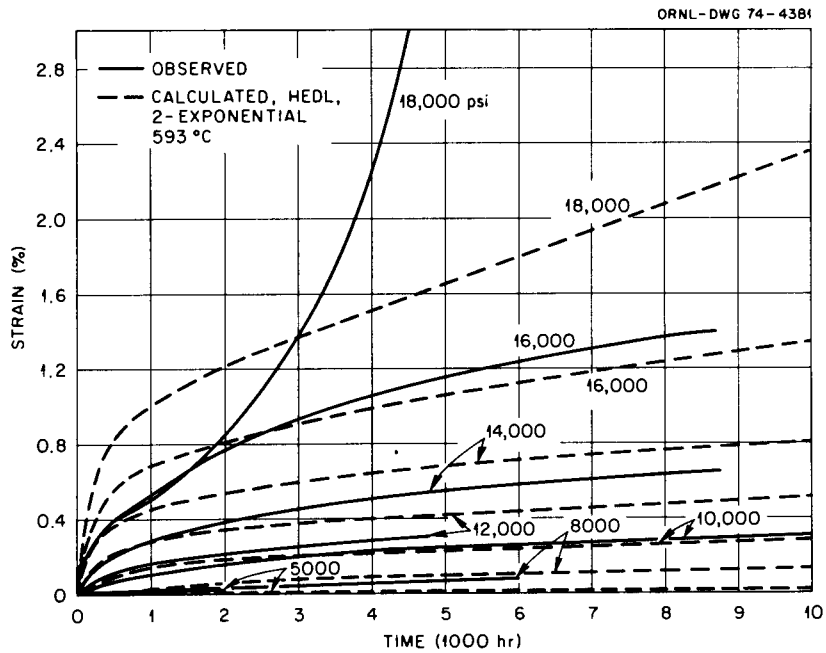

Fig. 5.16. Comparison of Creep Curves for Heat 9T2796 and Calculated Curves at 593°C (1100°F).

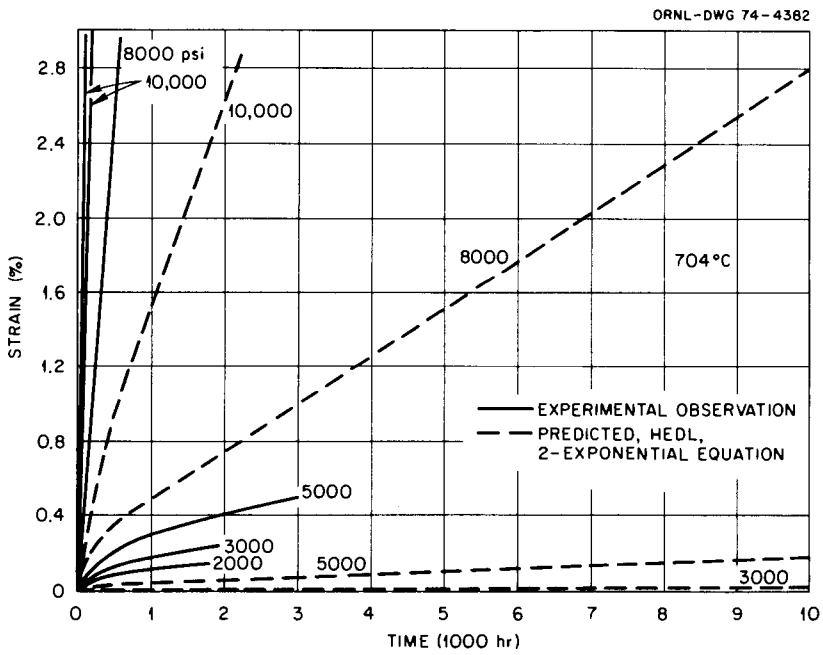

Fig. 5.17. Comparison of Creep Curves for Heat 9T2796 and Calculated Curves at 704°C (1300°F).

Table 5.6. Standard Error Estimates for Various Strain-Time Equations

Test	$At^{3/4} + Bt$	$At^{3/4}$	At	$At^{1/3} + Bt$	$At^{1/3}$	$At^{2/3} + Bt$	$At^{2/3}$	$At^{1/2} + Bt$	$At^{1/2}$	Polynomial
11595	41	57	87	45	64	41	48	43	43	39
12368	20	22	21	20	25	20	23	20	24	20
12472	14	30	49	16	26	14	23	15	15	12
12570	18	20	18	18	28	18	21	18	24	18
11569	66	92	118	53	53	63	82	58	63	39
12375	83	100	95	74	114	82	102	79	107	44
11675	32	85	104	27	44	30	78	28	62	25
11693	31	58	69	31	38	30	55	30	46	30
11830	51	109	133	36	55	48	100	41	79	26
13152										
13020										
10489	176	389	651	123	212	165	300	144	151	44
12250	25	128	235	62	137	28	89	41	42	22
11625	56	230	350	102	118	61	186	78	104	35
10491	80	369	511	48	98	73	318	59	210	40
12444	40	82	128	38	54	38	65	36	38	36
12445	33	39	33	33	80	33	45	33	60	24
11568	47	71	107	35	52	45	59	40	40	33
11626	41	84	117	30	31	39	71	34	46	28
11641	49	66	80	51	51	49	62	49	54	46
10853	288	749	1130	186	321	254	597	195	268	131
10852	286	1543	2452	258	561	209	1196	90	424	80
10554 DG	74	938	1402	265	325	58	754	134	355	41
11596	91	389	582	67	90	74	314	47	148	36
10490 DG	61	333	539	137	228	68	253	96	109	38 DG
11227 DG	38	56	93	31	64	37	44	33	36	29 DG
11227 TR	36	47	83	37	79	37	39	36	45	36 TR
12459	43	52	44	40	87	43	57	42	69	27
10855	1099	1267	2518	528	3,380	1014	1014	802	1698	
10854	671	756	1399	270	2,053	599	599	435	943	61
10563	466	1932	1797	386	9,736	426	3250	365	6224	318
11226 DG	299	300	1868	268	3,973	246	698	184	2182	83
11226 TR	286	287	1785	221	3,876	238	728	168	2169	91
10851	124	596	988	278	434	135	451	189	207	46
12255 DG	35	65	109	55	87	38	51	45	47	24 DG
12255 TR	43	78	122	65	88	47	64	55	55	27 TR
12443	45	65	48	42	124	45	74	43	97	24
12460	79	163	227	77	78	76	140	72	94	43
10856	263	2326	653	289	8,720	262	3429	268	5887	164
11562	472	3880	1051	468	14,778	455	5682	436	9762	159
11222	252	2408	2050	626	12,015	315	4082	459	7781	114
12254	92	444	762	131	313	76	323	77	87	34
12461	75	297	433	64	72	61	243	38	123	26
12462	88	169	253	83	101	84	139	78	86	62

[a]DG indicate data taken with a dial gage, TR transducer.

for all tests is 55 μin./in. (55 μm/m). The data from the dial gages and transducers were fit separately for three tests. In all cases the estimate of standard error was about 10% less for the data from the dial gages.

The data were also fit to several models having one or two terms. These models are shown across the top of Table 5.6, and the estimates of standard errors are shown for each. The fit was much better for the models with two terms. However, the fit generally did not depend upon the power of time in the first term. The two-term models fit the data almost as well as the eight-term polynomial.

5.2.2 Heat-to-Heat Variation Study of Type 304 Stainless Steel

5.2.2.1 Long-Term Creep Tests in Heat-to-Heat Variation Study — H. E. McCoy

Ten long-term creep tests are in progress on several heats of type 304 stainless steel at 593°C (1100°F). The test conditions and status of each test are described in Table 5.7. The creep curves for the tests in progress at 593°C and 17,000 psi (117 MPa) are shown in Fig. 5.18. The creep curves for heats* 330 and 796 in the as-received condition and for heats 414 and 380 after reannealing are quite similar, particularly after 10,000 hr test time. The creep curves for heat 414 in the as-received and reannealed conditions are nearly parallel, although the curve for the as-received material is displaced downward by about 0.2% strain. All these tests are creeping less than predicted by the HEDL two-exponential equation. Heat 187 exhibits creep behavior that is well described by the HEDL equation. Heat 544 creeps similar to the prediction of the HEDL equation for the first few thousand hours, the creep rate remains at a steady value for the next few thousand hours, and then the creep rate begins to accelerate. Heat 697 does not exhibit much primary creep and crept at a relatively high rate for about 18,000 hr.

The wide range of creep curves exhibited by these tests is quite striking. The basic shapes of the curves vary markedly. The strain

---

*Heats listed in Table 5.7 are identified in text by the last three digits of their numbers.

Table 5.7. Status of Several Long-Term Creep Tests of Type 304 Stainless Steel at 593°C (1100°F)

Test	Heat	Condition[a]	Stress, (ksi)	Stress, (MPa)	Test Time (hr)	Strain, % Loading	Strain, % Creep	Minimum Creep Rate (%/hr)	Time to Onset of Tertiary Creep (hr)	Data Used for Analysis (hr)	Estimate of Std. Error-Polynomial Fit (μin./in.)
10396	60551	A 479	25.0	172	12,732	1.81	3.60	1.4×10^{-4}	>12,732	All	97
10395	346845	A 240	25.0	172	12,733	1.37	4.83	1.4×10^{-4}	9,800	8,000	275
9499	300380	Reannealed	17.0	117	18,878	0.72	0.91	~0	>18,878	All	76
9483	600414	Reannealed	17.0	117	18,999.4	1.49	0.92	1.1×10^{-5}	>18,999	All	155
9464	337330	A 240	17.0	117	19,212	−0.20	0.95	5.5×10^{-6}	>19,212	All	198
9446	9T2796	A 479	17.0	117	19,262	0.13	1.00	2.1×10^{-5}	>19,262	All	445
9443	337187	A 240	17.0	117	19,171	0.47	3.20	9.7×10^{-5}	17,000	12,000	183
9371	55697	A 479	17.0	117	19,458	0.62	2.95	1.4×10^{-4}	15,500	17,000	383
9221	600414	A 240	17.0	117	21,398	0.18	0.71	1.0×10^{-5}	>21,398	All	282
9508	346544	A 240	17.0	117	18,776	0.22	2.13	3.5×10^{-5}	17,300	12,000	97

[a]As received per indicated specification or reannealed 0.5 hr at 1065°C (1950°F).

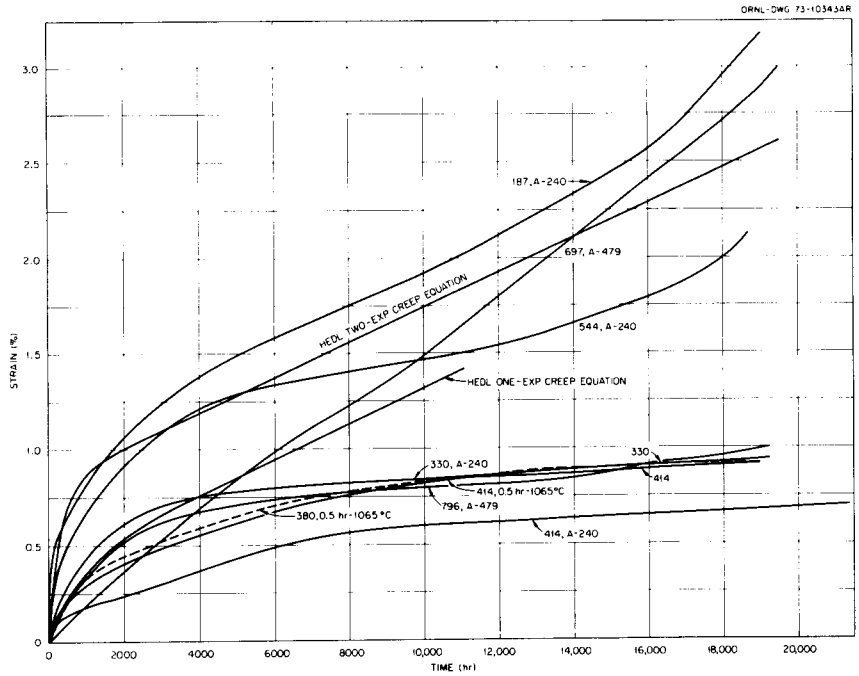

Fig. 5.18. Creep Curves for Type 304 Stainless Steel Tested at 593°C (1100°F) and 17,000 psi (117 MPa).

observed after 19,000 hr varied from 0.68 to 3.16%. The minimum creep rates varied from 5.5×10^{-6} to 1.4×10^{-4}%/hr (Table 5.7). The time to tertiary creep will likely vary by more than the current spread of 15,500 hr to above 21,398 hr. However, all these tests have exceeded the minimum rupture time of about 3000 hr specified by Code Case 1331-8.

Two creep curves for tests at 25,000 psi (172 MPa) and 593°C (1100°F) are shown in Fig. 5.19. Although the strains are reasonably close over the duration of the test, the creep rate of one test is decreasing and the other increasing. Thus the two curves will likely become more divergent. Both tests have far exceeded the minimum rupture time of about 300 hr specified by Code Case 1331-8.

These tests were fit by regression analysis to several models. The estimates of standard error given in Table 5.8 are indicative of how well the models fit the data. None of the models had time exponents over 1.01, so data above the steady-state creep portion of the curve were not used. The polynominal fit the data quite well, with estimates of standard error ranging from 76 to 445 μin./in. (μm/m). The two-term equations of the form $\varepsilon = At^n + B$ do not fit the data as well as the polynomial; however,

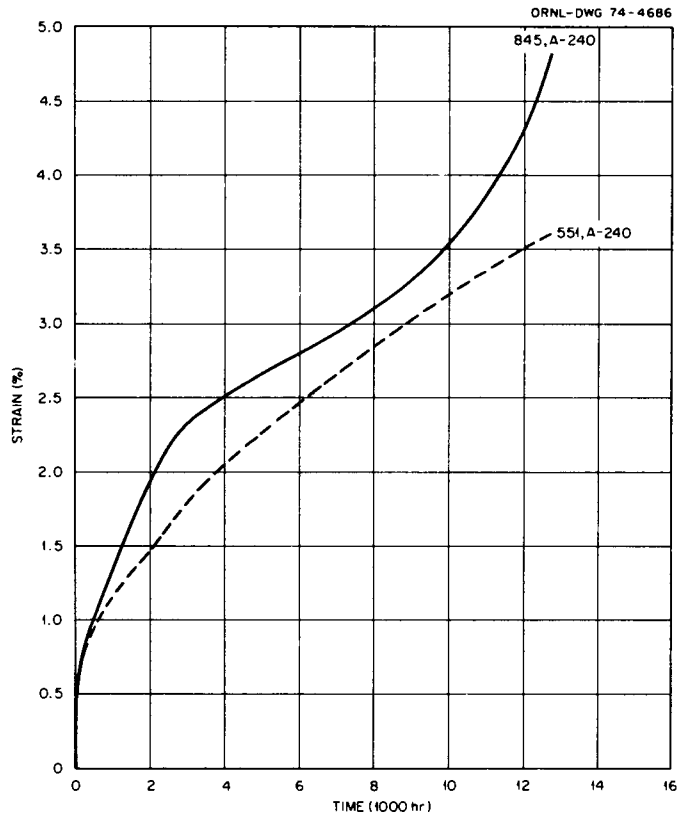

Fig. 5.19. Creep Behavior of Two Heats of Type 304 Stainless Steel at 593°C (1100°F) and 25,000 psi (172 MPa).

the estimate of standard error is generally within a factor of 2. The fit is generally equally good with n equal to 1/3, 1/2, or 2/3, although in some instances the fit is significantly better for one value of n than for another. The models with only a single term do not fit well except for test 9371 (heat 697, Fig. 5.18), where the creep behavior is described reasonably well by a linear mode.

5.2.2.2 Effect of Aging on the Tensile Properties — V. K. Sikka

The aim of the present program is to determine the influence of aging on the mechanical properties of various heats of type 304 stainless steel. The aging program involved nine heats of type 304 stainless steel and various combinations of aging time and temperature. The scope of the aging program is shown in Fig. 5.20(a). The chemical analysis and the grain size of nine heats in the as-received condition were included in a previous listing.[6] The aging program involves aging times as long as 10,000 hr

Table 5.8. Estimates of Standard Error for Various Models Fit to Creep Data[a] for Type 304 Stainless Steel at 593°C (1100°F)

	Standard Error, μin./in. (μm/m), for Each Model									
Test	$At^{3/4} + Bt$	$At^{3/4}$	At	$At^{1/3} + Bt$	$At^{1/3}$	$At^{2/3} + Bt$	$At^{2/3}$	$At^{1/2} + Bt$	$At^{1/2}$	Polynomial[b]
10396	1413	3893	6284	289	2179	1204	2934	740	879	97
10395	840	4808	7285	965	1133	677	3865	571	1840	275
9499	226	1696	2466	333	333	149	1404	122	768	76
9483	223	1500	2248	386	412	187	1218	221	621	155
9464	693	2535	3342	448	807	590	2223	420	1532	198
9446	828	2154	2892	559	667	748	1872	607	1254	445
9443	930	2879	4201	230	345	788	2365	477	1201	183
9371	500	986	674	538	3568	505	1423	518	2425	383
9221	366	934	1461	478	577	376	751	414	457	282
9508	693	2767	3763	489	499	534	2358	245	1384	97

[a]See Table 5.7 for more details on test conditions.

[b]Equation of the form $\varepsilon = A_0 + A_1 t^{0.14} + A_2 t^{0.28} + A_3 t^{0.43} + A_4 t^{0.58} + A_5 t^{0.71} + A_6 t^{0.86} + A_7 t^{1.01}$, where ε = strain, t = time.

and is still continuing. The present status of the aging program is shown in Fig. 5.20(b). Each aged block is large enough to make six test samples for tensile and creep testing.

(a)

X-22807	Aging Program	
600414		
300380	Time (hr)	Temperature (°F)
9T2796K		
R22926		
346845	1,000	900
8043813	2,000	1100
346544	4,000	1200
3121	10,000	

(1) Microstructure
(2) Tensile Properties, RT, 1100°F
(3) Creep Behavior at
1100°F – 30 ksi (100 to 2000 hr)
1100°F – 17 ksi (Disc. 2000 hr)
1200°F – 14 ksi (Disc. 2000 hr)
900°F – 20 ksi (Disc. 2000 hr)

(b)

ORNL-DWG 73-11407R2

AGING TIME (hr)	482	593	649
10,000	121 □ 414 ○,□ 380 ○,□ 796 ○,□ 845 ○,■ 807 ○,□ 813 ○,□ 926 ■ 544 ○,□	414 ○,□ 380 ○,□ 796 ○,□ 845 ○,■ 807 ○,□ 813 ○,□ 926 ■ 544 ○,□	121 □ 414 ○,□ 380 ○,□ 796 ○,□ 845 ○,■ 807 ○,□ 813 ○,□ 926 ■ 544 ○,□
4000	414 ●,■ 380 ●,■ 796 ●,■ 845 ●,■ 807 ●,■ 813 ■ 926 ■ 544 ○,□	414 ●,■ 380 ●,■ 796 ●,■ 845 ●,■ 807 ■ 813 ■ 926 ■ 544 ○,□	414 ●,■ 380 ●,■ 796 ●,■ 845 ●,■ 807 ●,■ 813 ■ 926 ■ 544 ○,□
2000	121 ■	845 ■ 807 ■ 813 ■ 544 ●,■	121 ■ 414 ● 380 ● 796 ●,■ 845 ●,■ 807 ●,■ 813 ■ 544 ●,■
1000			414 ● 380 ● 796 ●,■ 845 ●,■ 807 ●,■ 813 ■ 544 ●,■

AGING TEMPERATURE (°C)

○ ANNEALED 0.5 hr AT 1065°C PRIOR TO AGING
□ AGED IN AS-RECEIVED CONDITION
OPEN SYMBOLS – AGING IN PROGRESS
CLOSED SYMBOLS – COMPLETED

Fig. 5.20. Creep Aging Program for Type 304 Stainless Steel. (a) Scope. (b) Status.

Several of the aged samples have been tensile tested. The results for heats R22926 and 3121 were reported earlier.[7] The results for other heats have been updated and are presented in Tables 5.9 through 5.14. The tensile tests on heat 346544 are still in progress. The effect of aging treatment on the yield strength of eight heats of type 304 stainless steel is summarized in Table 5.15.

Table 5.9. Tensile Properties of Type 304 Stainless Steel Heat 346845 at a Strain Rate of 0.04/min

Condition	Treatment			Stress, ksi (MPa)		Strain, %		Reduction of Area (%)
	Time (hr)	Temperature (°C)	Temperature (°F)	Yield	Ultimate Tensile	Uniform	Total	
				Tested at 25°C (77°F)				
A240				35.9(248)	88.7(612)	69.7	79.0	76.0
A240, aged	4000	482	900	32.7(225)	86.7(598)	78.4	86.8	83.0
				34.4(237)	89.0(614)	76.0	86.4	81.4
A240, aged	2000	593	1100	34.6(239)	87.6(604)	72.0	78.0	62.2
A240, aged	4000	593	1100	40.4(279)	93.3(643)	68.0	75.4	71.4
A240, aged	1000	649	1200	36.2(250)	91.5(632)	66.4	74.0	68.5
A240, aged	2000	649	1200	34.3(236)	91.3(629)	64.8	70.8	68.3
A240, aged	4000	649	1200	34.9(241)	91.4(630)	62.4	69.8	68.4
Reannealed	0.5	1065	1900	29.7(205)	87.1(601)	76.7	89.0	84.5
Reannealed, aged	4000	482	900	32.3(223)	88.1(607)	73.6	86.6	84.0
Reannealed, aged	4000	593	1100	31.5(217)	88.8(612)	74.4	84.5	76.9
Reannealed, aged	1000	649	1200	33.5(231)	90.0(621)	68.8	77.4	72.8
Reannealed, aged	2000	649	1200	31.0(214)	90.6(625)	67.2	72.1	68.3
Reannealed, aged	4000	649	1200	31.6(218)	90.5(624)	61.6	70.8	67.2
				Tested at 593°C (1100°F)				
A240				20.3(140)	51.8(357)	39.2	48.8	68.1
A240, aged	4000	482	900	15.5(107)	51.2(353)	40.0	52.6	71.6
				17.1(118)	51.5(355)	40.0	50.9	72.4
A240, aged	2000	593	1100	21.5(148)	51.0(352)	36.0	45.8	70.9
A240, aged	4000	593	1100	23.0(159)	50.5(348)	32.0	34.5	69.4
A240, aged	1000	649	1200	21.5(148)	50.2(346)	31.2	38.0	66.6
A240, aged	2000	649	1200	20.4(141)	48.4(334)	28.8	39.9	64.3
A240, aged	4000	649	1200	20.0(138)	48.3(333)	28.0	40.1	68.2
Reannealed	0.5	1065	1900	13.8(95)	52.2(360)	36.8	50.5	73.6
Reannealed, aged	4000	482	900	15.4(106)	50.8(350)	36.0	46.2	74.3
Reannealed, aged	4000	593	1100	16.7(115)	50.6(349)	40.0	54.4	71.4
Reannealed, aged	1000	649	1200	16.5(114)	50.5(348)	34.4	45.1	67.4
Reannealed, aged	2000	649	1200	17.2(119)	48.8(336)	31.2	40.4	59.7
Reannealed, aged	4000	649	1200	17.4(120)	48.7(336)	29.6	38.8	57.9

Table 5.10 Tensile Properties of Type 304 Stainless Steel Heat 8043813 at a Strain Rate of 0.040/min

Condition	Treatment			Stress, ksi (MPa)		Strain, %		Reduction of Area (%)
	Time (hr)	Temperature (°C)	Temperature (°F)	Yield	Ultimate Tensile	Uniform	Total	
Tested at 25°C (77°F)								
A240				31.0(214)	92.4(637)	74.6	87.2	—
Reannealed	0.5	1065	1950	29.6(204)	87.8(605)	80.0	87.3	84.0
A240, aged	4000	482	900	35.1(242)	89.4(616)	73.6	85.8	81.4
A240, aged	2000	593	1100	33.9(234)	88.6(611)	73.6	81.4	72.1
A240, aged	4000	593	1100	37.2(256)	91.1(628)	71.2	81.4	69.4
A240, aged	1000	649	1200	35.8(247)	91.9(634)	68.0	73.8	67.2
A240, aged	2000	649	1200	30.4(210)	92.0(634)	67.2	73.0	65.2
A240, aged	4000	649	1200	39.6(273)	93.9(647)	61.6	71.1	63.4
Tested at 593°C (1100°F)								
A240				15.2(105)	50.1(345)	39.8	47.4	70.3
Reannealed	0.5	1065	1950	11.9(82)	51.3(354)	43.4	51.6	71.9
A240, aged	4000	482	900	15.8(109)	52.8(364)	40.0	52.0	72.8
A240, aged	2000	593	1100	14.8(102)	52.4(361)	40.0	45.8	68.6
A240, aged	4000	593	1100	18.8(130)	51.9(358)	36.0	47.0	67.5
A240, aged	1000	649	1200	19.3(133)	51.7(356)	34.4	41.8	65.0
A240, aged	2000	649	1200	16.3(112)	50.1(345)	32.0	43.5	63.1
A240, aged	4000	649	1200	20.9(144)	49.4(341)	30.4	40.0	62.8

Table 5.11. Tensile Properties of Type 304 Stainless Steel Heat 9T2796K at a Strain Rate of 0.040/min

Condition[a]	Treatment			Stress, ksi (MPa)		Strain, %		Reduction of Area (%)
	Time (hr)	Temperature (°C)	Temperature (°F)	Yield	Ultimate Tensile	Uniform	Total	
Tested at 25°C (77°F)								
A240[b,c]				29.5(203)	79.4(547)	66.7	69.8	81.9
A240[c,d]				31.5(217)	79.5(548)	66.2	68.7	78.3
A240[d]				32.7(225)	80.8(557)	62.2	65.7	82.1
A240, aged	4000	482	900	31.8(219)	79.9(551)	81.6	97.0	83.9
A240, aged	1000	649	1200	32.6(225)	86.4(596)	64.0	72.0	66.6
A240, aged	2000	649	1200	33.9(234)	86.7(598)	62.4	72.0	69.6
A240, aged	4000	649	1200	31.0(214)	85.3(595)	64.0	73.2	68.1
Reannealed	0.5	1093	2000	25.8(178)	78.1(538)	85.6	91.4	83.0
Reannealed	0.5	1093	2000	27.7(191)	78.6(542)	76.3	89.0	83.3
Reannealed, aged	1000	649	1200	29.2(201)	83.0(572)	73.6	77.5	65.2
Reannealed, aged	2000	649	1200	27.9(192)	83.0(572)	73.6	74.2	64.3
Reannealed, aged	4000	649	1200	28.8(199)	86.0(593)	69.6	78.2	64.3
Tested at 593°C (1100°F)								
A240				14.9(103)	48.4(334)	33.3	35.4	70.8
A240, aged	4000	482	900	8.2(57)	47.3(326)	40.0	49.4	63.3
A240, aged	1000	649	1200	16.7(115)	46.3(319)	32.0	39.8	60.1
A240, aged	2000	649	1200	19.4(134)	44.6(308)	28.0	37.2	58.1
A240, aged	4000	649	1200	16.2(112)	44.9(310)	28.8	36.0	54.5
Reannealed	0.5	1093	2000	10.1(70)	46.7(322)	48.0	49.6	63.3
Reannealed, aged	1000	649	1200	13.9(96)	47.0(324)	36.0	41.2	58.9
Reannealed, aged	2000	649	1200	13.5(93)	46.5(321)	36.8	43.9	58.3
Reannealed, aged	4000	649	1200	15.2(105)	46.6(321)	32.0	39.2	52.5

[a]All specimens were taken along the rolling direction of the 2-in. plate and, except where indicated, were from the center of the plate.

[b]Taken from the top of the plate.

[c]Tested at a strain rate of 0.044/min.

[d]Taken from the bottom of the plate.

Table 5.12. Tensile Properties of Type 304 Stainless Steel Heat 600414 at a Strain Rate of 0.040/min

Condition	Treatment			Stress, ksi (MPa)		Strain, %		Reduction of Area (%)
	Time (hr)	Temperature (°C)	Temperature (°F)	Yield	Ultimate Tensile	Uniform	Total	
				Tested at 25°C (77°F)				
A240[a]				34.0(234)	88.7(612)	62.5	69.7	
A240, aged	4000	482	900	33.6(232)	85.8(592)	77.6	91.4	82.9
A240, aged	4000	593	1100	39.0(269)	90.1(621)	67.2	78.8	72.4
A240, aged	4000	649	1200	38.0(262)	92.7(639)	56.8	68.2	65.9
Reannealed[b]	0.5	1065	1900	30.3(209)	86.5(596)	49.8	72.0	76.4
Reannealed, aged	4000	482	900	36.6(252)	86.3(595)	72.8	85.6	80.2
Reannealed, aged	4000	593	1100	35.2(243)	90.3(623)	67.2	79.0	71.4
Reannealed, aged	1000	649	1200	33.8(233)	89.0(614)	68.8	80.0	68.1
Reannealed, aged	2000	649	1200	36.9(254)	91.1(628)	63.2	71.0	64.0
Reannealed, aged	4000	649	1200	33.8(233)	89.5(617)	64.0	75.3	60.2
				Tested at 593°C (1100°F)				
A240[b]				15.4(106)	50.5(348)	35.6	37.4	66.5
A240, aged	4000	482	900	15.2(105)	53.4(368)	41.6	54.5	68.1
A240, aged	4000	593	1100	17.9(123)	54.6(376)	36.6	50.4	68.8
A240, aged	4000	649	1200	19.8(137)	51.1(352)	28.8	37.0	57.3
Reannealed	0.5	1065	1900	13.2(91)	52.5(362)	38.4	41.3	64.6
Reannealed, aged	4000	482	900	15.6(108)	54.5(376)	39.8	48.3	66.3
Reannealed, aged	4000	593	1100	15.5(107)	53.7(370)	36.8	45.3	62.9
Reannealed, aged	1000	649	1200	15.9(110)	53.0(365)	40.0	46.4	62.9
Reannealed, aged	2000	649	1200	16.9(117)	51.9(358)	34.4	41.5	60.4
Reannealed, aged	4000	649	1200	16.1(111)	50.8(350)	31.6	42.6	55.2

[a]Strain rate 0.044/min.

[b]Strain rate 0.050/min.

Table 5.13. Tensile Properties of Type 304 Stainless Steel Heat 300380 at a Strain Rate of 0.040/min

Condition	Treatment			Stress, ksi (MPa)		Strain, %		Reduction of Area (%)
	Time (hr)	Temperature (°C)	Temperature (°F)	Yield	Ultimate Tensile	Uniform	Total	
				Tested at 25°C (77°F)				
A240[a]				40.7(281)	90.2(622)	60.0	67.7	78.4
A240, aged	4000	482	900	39.8(274)	91.2(629)	72.0	85.0	83.1
A240, aged	4000	593	1100	39.7(274)	94.1(649)	70.4	82.2	74.3
A240, aged	4000	649	1200	40.8(281)	97.7(674)	60.0	69.1	66.5
Reannealed[a]	0.5	1065	1900	35.4(244)	88.1(607)	66.4	69.9	80.8
Reannealed, aged	4000	482	900	38.5(265)	91.5(631)	70.4	85.4	82.7
Reannealed, aged	4000	593	1100	37.0(255)	94.9(654)	71.2	80.0	70.7
Reannealed, aged	1000	649	1200	37.7(260)	96.2(663)	66.4	72.4	64.6
Reannealed, aged	2000	649	1200	37.4(258)	97.1(669)	64.0	70.8	64.3
Reannealed, aged	4000	649	1200	36.4(251)	95.4(658)	64.0	74.2	65.6
				Tested at 593°C (1100°F)				
A240[a]				18.1(125)	54.5(376)	33.3	37.8	61.3
A240, aged	4000	482	900	18.0(124)	54.9(379)	39.0	49.6	69.2
A240, aged	4000	593	1100	19.0(131)	54.6(376)	37.6	47.2	68.0
A240, aged	4000	649	1200	21.4(148)	51.5(355)	28.0	36.5	59.1
Reannealed[b]	0.5	1065	1900	14.1(97)	52.8(364)	39.1	44.5	66.2
Reannealed, aged	4000	482	900	17.1(118)	54.6(376)	38.4	48.0	69.4
Reannealed, aged	4000	593	1100	16.2(112)	53.5(369)	36.0	44.0	62.9
Reannealed, aged	1000	649	1200	17.3(119)	52.0(359)	34.4	42.6	60.5
Reannealed, aged	2000	649	1200	17.8(123)	51.4(354)	31.2	39.4	54.7
Reannealed, aged	4000	649	1200	19.8(137)	51.7(356)	31.2	39.0	58.8

[a]Strain rate 0.044/min.

[b]Strain rate 0.050/min.

Table 5.14. Tensile Properties of Type 304 Stainless Steel Heat X22807 at a Strain Rate of 0.040/min

Condition	Treatment			Stress, ksi (MPa)		Strain, %		Reduction of Area (%)
	Time (hr)	Temperature (°C)	Temperature (°F)	Yield	Ultimate Tensile	Uniform	Total	
Tested at 25°C (77°F)								
A240				33.2(229)	83.4(575)	67.2	82.0	75.7
A240, aged	4000	482	900	47.9(330)	86.8(598)	61.2	73.4	77.1
A240, aged	2000	593	1100	32.1(221)	78.9(544)	66.4	74.1	68.9
A240, aged	4000	593	1100	32.5(224)	79.4(547)	64.0	74.8	69.7
A240, aged	1000	649	1200	30.7(212)	79.5(548)	65.6	73.5	62.8
A240, aged	2000	649	1200	29.3(202)	79.6(549)	64.0	72.2	63.8
A240, aged	4000	649	1200	31.0(214)	80.6(556)	61.6	70.4	54.0
Reannealed	0.5	1065	1900	27.0(186)	81.1(559)	72.8	83.0	78.3
Reannealed, aged	4000	482	900	29.7(205)	84.1(580)	69.6	80.1	73.9
Reannealed, aged	1000	649	1200	28.0(193)	79.2(546)	68.8	74.0	60.7
Reannealed, aged	2000	649	1200	27.9(192)	80.0(552)	64.0	70.4	56.5
Reannealed, aged	4000	649	1200	33.6(232)	80.9(558)	60.8	67.9	57.9
Tested at 593°C (1100°F)								
A240				17.9(123)	45.2(312)	33.6	45.3	68.0
A240, aged	4000	482	900	16.7(115)	47.0(324)	34.4	44.4	51.7
A240, aged	2000	593	1100	16.7(115)	42.7(294)	30.4	38.4	53.8
A240, aged	4000	593	1100	17.5(121)	42.7(294)	32.0	41.0	52.6
A240, aged	1000	649	1200	16.8(116)	43.5(300)	32.8	39.6	57.3
A240, aged	2000	649	1200	15.5(107)	43.3(249)	33.6	40.1	49.7
A240, aged	4000	649	1200	20.6(142)	44.6(308)	28.8	37.8	43.9
Reannealed	0.5	1065	1900	13.0(90)	47.9(330)	36.0	45.7	74.9
Reannealed, aged	4000	482	900	14.3(99)	47.0(324)	36.0	45.4	67.2
Reannealed, aged	1000	649	1200	13.4(92)	43.3(299)	32.0	41.3	51.7
Reannealed, aged	2000	649	1200	14.0(97)	44.0(303)	32.0	36.5	44.3
Reannealed, aged	4000	649	1200	16.3(112)	44.3(305)	31.2	38.6	50.4

Table 5.15. Effect of Aging Treatment on the Yield Strength of Various Heats of Type 304 Stainless Steel

Heat	Condition Before Aging	Test Temperature (°C)	Test Temperature (°F)	Change in Yield Strength (0.2% Offset), ksi[a] for Various Aging Conditions: 482°C (900°F) 4000 hr	593°C (1100°F) 4000 hr	649°C (1200°F) 4000 hr	649°C (1200°F) 1000 hr	649°C (1200°F) 2000 hr
346845	A240	25	77	−2.4	+4.4	−1.0	+0.3	−1.6
	A240	593	1100	−4.0	+2.7	−0.3	+1.2	+0.1
	Reannealed	25	77	+2.6	+1.8	+1.9	+3.8	+1.3
	Reannealed	593	1100	+1.6	+2.9	+3.6	+2.7	+3.4
X22807	A240	25	77	+14.7	−0.7	−2.2	−2.5	−3.9
	A240	593	1100	−1.2	−0.4	+2.7	−1.1	−2.4
	Reannealed	25	77	+2.7		+6.6	+1.0	+0.9
	Reannealed	593	1100	+1.3		+3.3	+0.4	+1.0
300380	A240	25	77	−0.9	−1.0	+0.1		
	A240	593	1100	−0.1	+0.9	+3.3		
	Reannealed	25	77	+3.1	+1.6	+1.0	+2.3	+2.0
	Reannealed	593	1100	+3.0	+2.1	+5.7	+3.2	+3.7
80043813	A240	25	77	+4.1	+6.2	+8.6	+4.8	−0.6
	A240	593	1100	+0.6	+3.6	+5.7	+4.1	+1.1
9T2796K	A240	25	77	+0.6		−0.2	+1.4	+2.7
	A240	593	1100	−6.7		+1.3	+1.8	+4.5
	Reannealed	25	77			+3.0	+3.4	+2.1
	Reannealed	593	1100			+5.1	+3.8	+3.4
600414	A240	25	77	−0.4	+5.0	+4.0		
	A240	593	1100	−0.2	+2.5	+4.4		
	Reannealed	25	77	+6.3	+4.9	+3.5	+3.5	+6.6
	Reannealed	593	1100	+2.4	+2.3	+2.9	+2.7	+3.7
R22926	A240	25	77	+2.7	+0.7	+0.8		
	A240	593	1100	−2.0	−0.6	+1.2		
3121	A312	25	77					+0.7
	A312	593	1100					+2.2

[a] 1 ksi = 6.895 MPa.

Tensile results in Tables 5.9 through 5.14 suggest that aging affects the yield strength and tensile ductility. The amount of change due to aging is a function of (a) pretreatment, (b) aging temperature, and (c) aging time. The present results are described below only for material reannealed before aging in terms of effect of aging temperature and effect of aging time.

5.2.2.2.1 Effect of Aging Temperature. The results on increase in yield strength in Fig. 5.21 for a test temperature of 25°C (77°F) show the following:

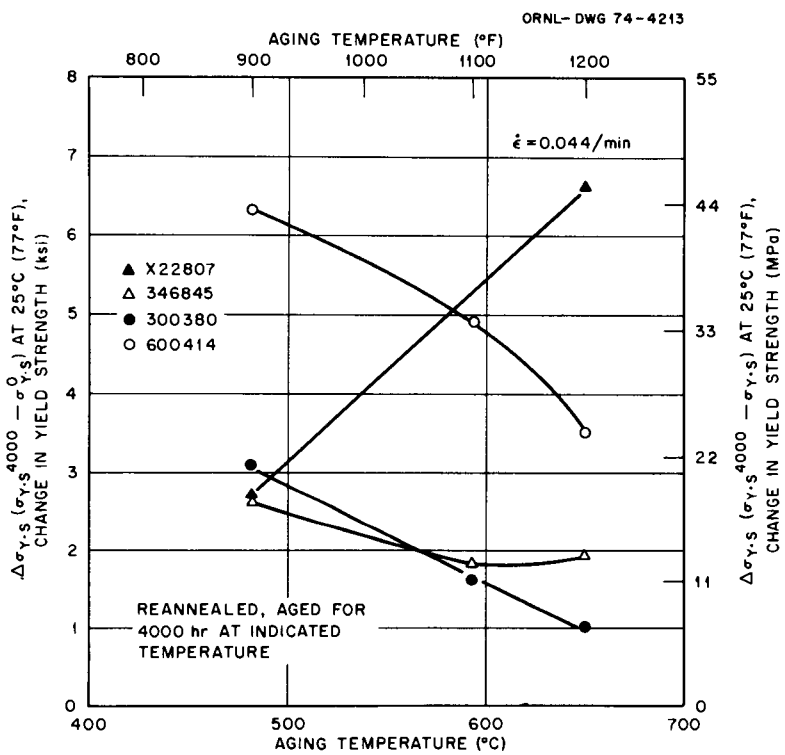

Fig. 5.21. Change in Yield Strength at 25°C (77°F) as a Function of Aging Temperature for Various Heats of Type 304 Stainless Steel.

1. Heats 346845, 300380, and 600414 show a maximum increase in yield strength at an aging temperature of 482°C (900°F). The higher aging temperatures show no change or reduce the increase in yield strength.

2. Heat X22807 in contrast to the other three heats shows a minimum increase in yield strength at 482°C (900°F). The higher aging temperatures further increase the yield strength.

The results on increase in yield strength in Fig. 5.22 for a test temperature of 593°C (1100°F) show the following:

1. All four heats show a minimum increase in yield strength at an aging temperature of 482°C (900°F).

2. Heats 300380 and 600414 show no further increase in yield strength up to 593°C (1100°F) and then increase linearly.

3. Heats 346845 and X22807 show a linear increase in yield strength with increasing aging temperature from 482 to 649°C (900–1200°F).

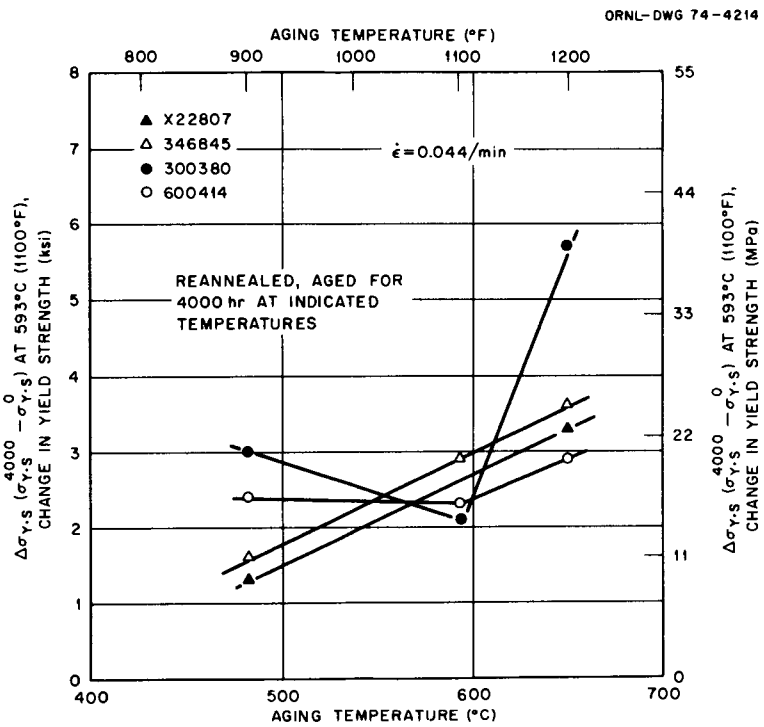

Fig. 5.22. Change in Yield Strength at 593°C (1100°F) as a Function of Aging Temperature for Various Heats of Type 304 Stainless Steel.

The results on change in total elongation in Figs. 5.23 and 5.24 for the test temperatures of 25 and 593°C (77 and 1100°F) show the following:

1. Heats 300380 and 600414 show a maximum increase in total elongation at an aging temperature of 482°C (900°F). It decreases with increasing aging temperature and still remains positive for the test temperature of 25°C (77°F). For the test temperature of 593°C (1100°F), it decreases with increasing temperature and still remains positive for heat 600414, but becomes negative for heat 300380 even at 593°C (1100°F).

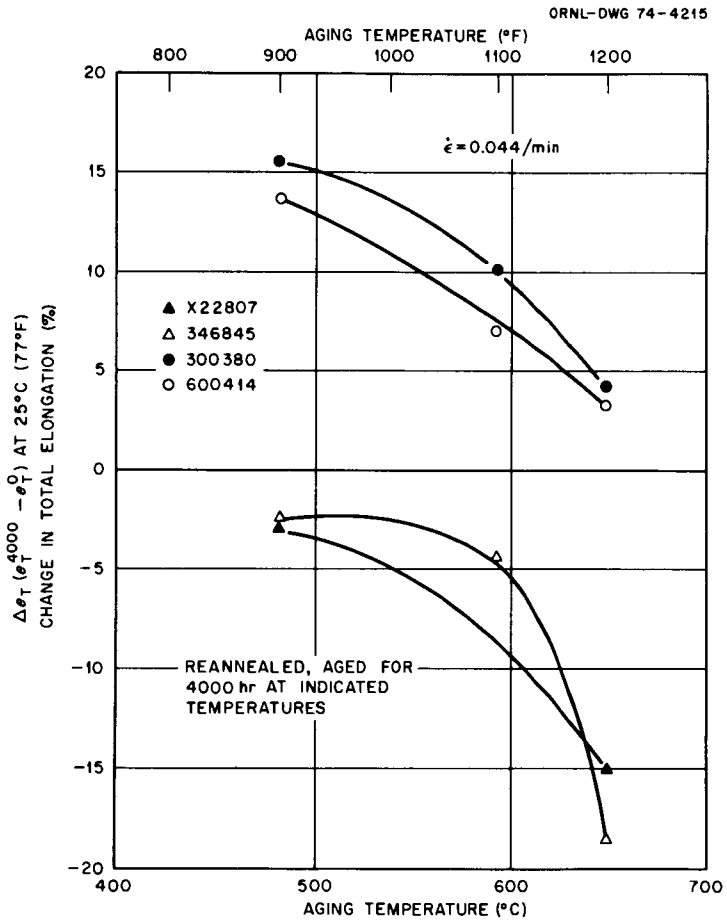

Fig. 5.23. Change in Total Elongation at 25°C (77°F) as a Function of Aging Temperature for Various Heats of Type 304 Stainless Steel.

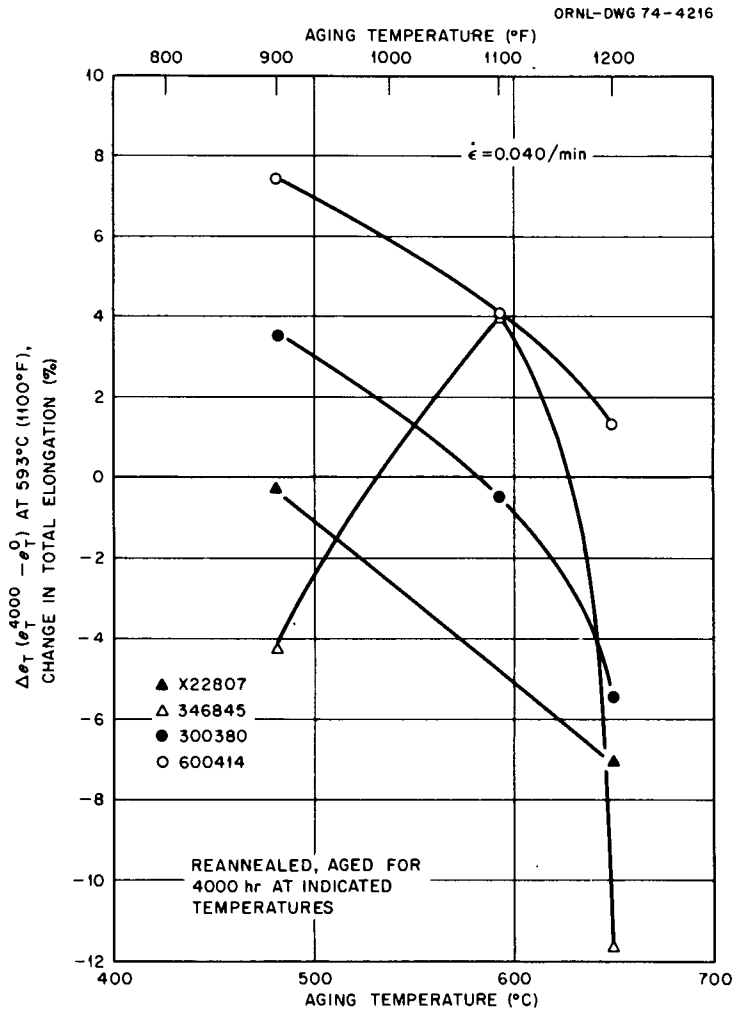

Fig. 5.24. Change in Total Elongation at 593°C (1100°F) as a Function of Aging Temperature for Various Heats of Type 304 Stainless Steel.

2. Heat X22807 shows a decrease in total elongation at an aging temperature of 482°C (900°F), and a further decrease with increasing aging temperature.

3. Heat 346845 shows a behavior similar to X22807 for a test temperature of 25°C (77°F), but behaves abnormally (Fig. 5.24) at a test temperature of 593°C (1100°F).

The results of change in reduction of area in Figs. 5.25 and 5.26 for the test temperatures of 25°C (77°F) and 593°C (1100°F) show the following:

1. Heats 300380 and 600414 show a maximum increase in reduction of area (similar to total elongation) at an aging temperature of 482°C (900°F). It decreases with increasing aging temperature and becomes negative for both higher temperatures.

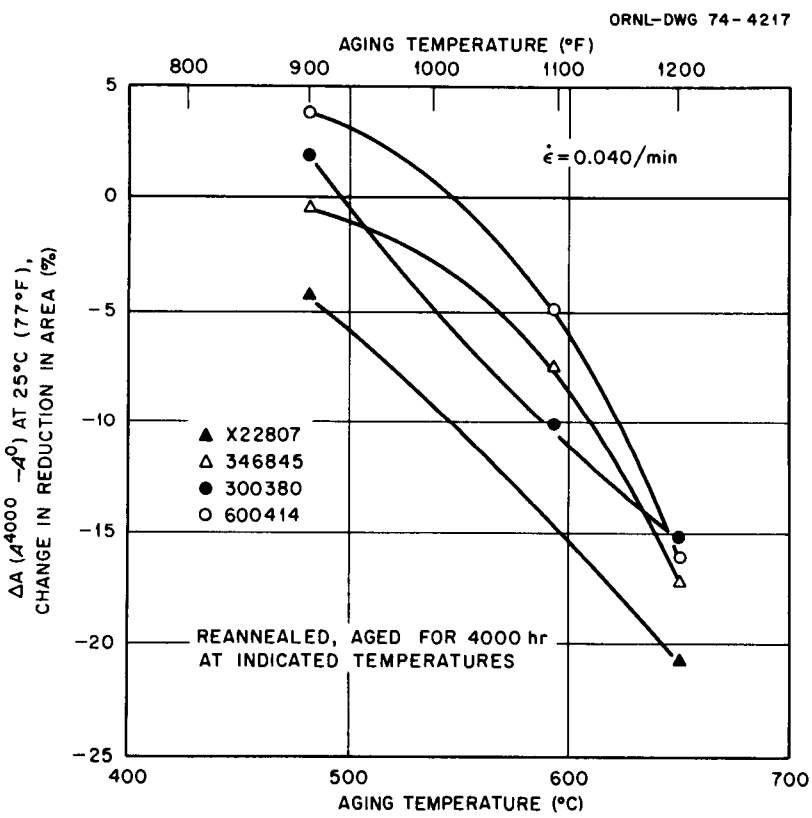

Fig. 5.25. Change in Reduction of Area at 25°C (77°F) as a Function of Aging Temperature for Various Heats of Type 304 Stainless Steel.

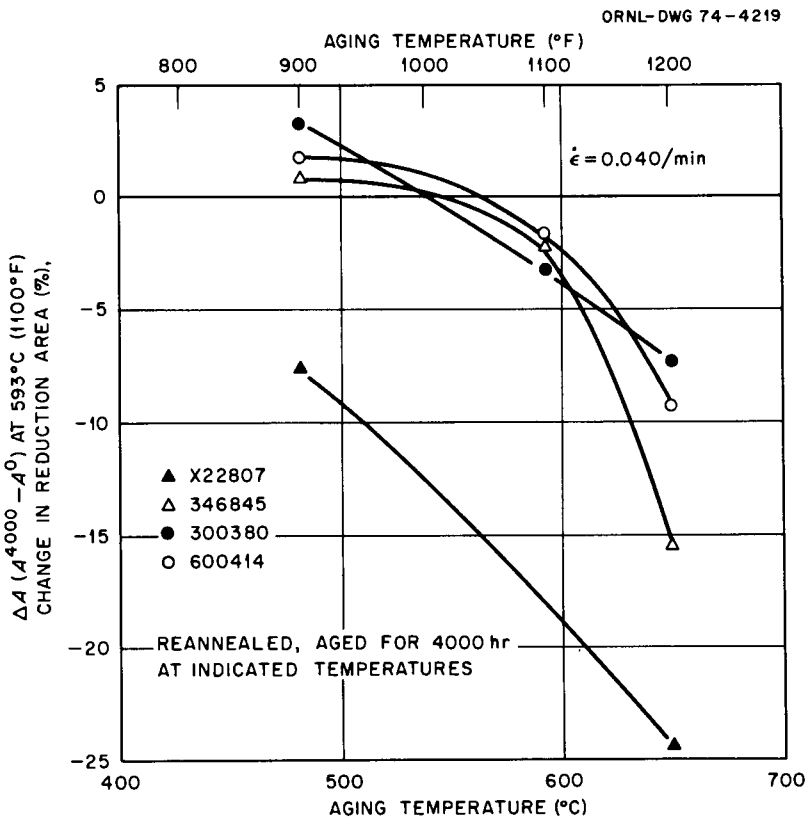

Fig. 5.26. Change in Reduction of Area at 593°C (1100°F) as a Function of Aging Temperature for Various Heats of Type 304 Stainless Steel.

2. Heats 346845 and X22807 show a decrease in reduction of area at an aging temperature of 482°C (900°F), and a further decrease with increasing aging temperature.

One of most significant observation is that, while aging at 482°C (900°F) produces a maximum increase in yield strength for a test temperature of 25°C (77°F), it produces a minimum increase for a test temperature of 593°C (1100°F). Furthermore, for heats 300380 and 600414, aging produces a significant increase in ductility with increase in yield strength for test temperatures of both 25 and 593°C (77 and 1100°F) and all three aging temperatures.

5.2.2.2.2 Effect of Aging Time. The results on increase in yield strength in Fig. 5.27 for a test temperature of 25°C (77°F) show the following:

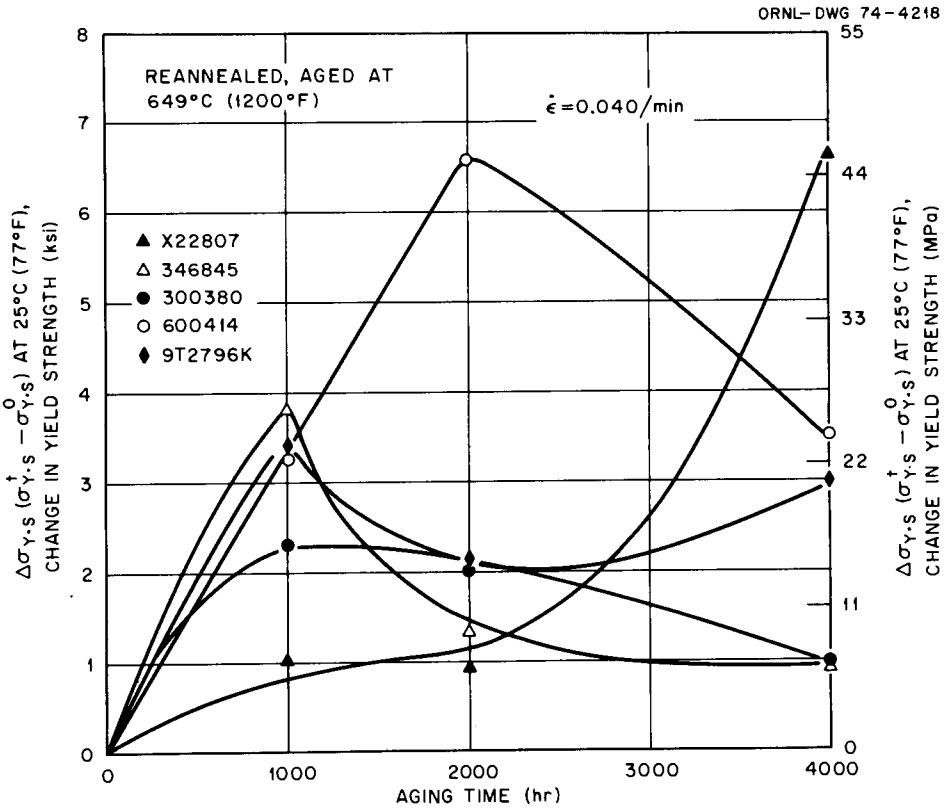

Fig. 5.27. Change in Yield Strength at 25°C (77°F) as a Function of Aging Time at 649°C (1200°F) for Various Heats of Type 304 Stainless Steel.

1. Heats 346845, 300380, and 9T2796K show a peak increase in yield strength for an aging time of 1000 hr, while heat 600414 shows the maximum at 2000 hr.

2. Heat X22807 shows a small increase in yield strength for aging times up to 2000 hr and then a sharp increase.

3. In general, all heats seem to show precipitation hardening, with some heats showing overaging even at aging times of only 1000 to 2000 hr.

The results on increase in yield strength in Fig. 5.28 for a test temperature of 593°C (1100°F) show the following:

1. Heat 600414 shows a peak increase in yield strength for an aging time of 2000 hr, similar to that observed for a test temperature of 25°C (77°F).

2. Heat 9T2796K shows a peak increase in yield strength at 1000 hr, followed by overaging and further increase in yield strength at 4000 hr.

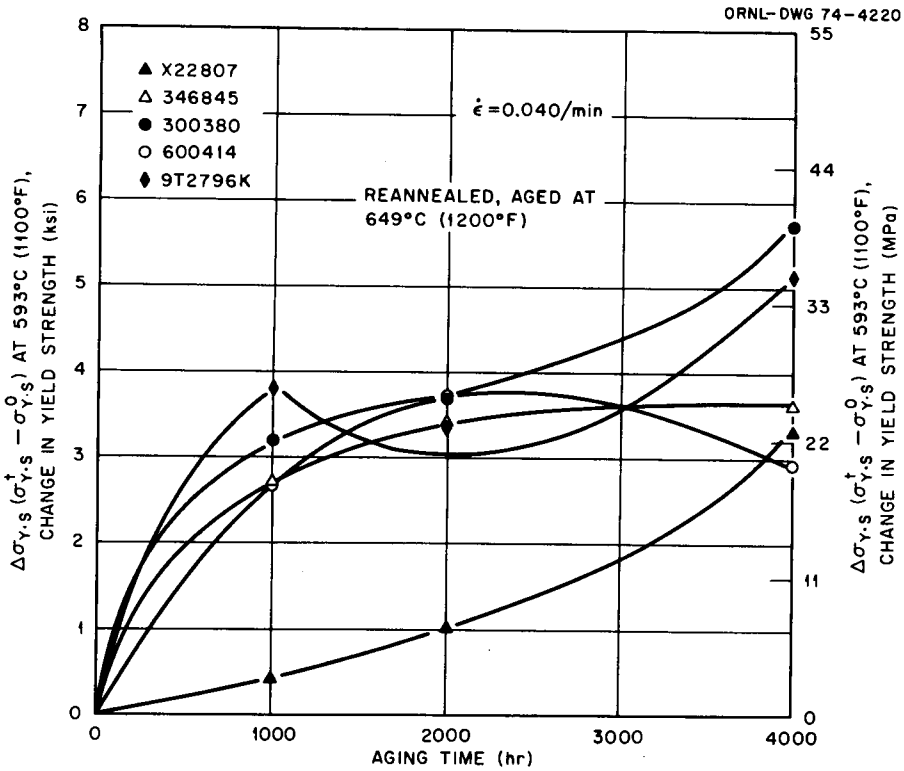

Fig. 5.28. Change in Yield Strength at 593°C (1100°F) as a Function of Aging Time at 649°C (1200°F) for Various Heats of Type 304 Stainless Steel.

3. Heats X22807, 346845, and 300380 show increases in yield strength, which increase with increasing aging time.

The results on change in total elongation, in Figs. 5.29 and 5.30, for the test temperatures of 25 and 593°C (77 and 1100°F) show the following:

1. Heat 600414 shows a peak increase in total elongation for an aging time of 1000 hr for both test temperatures. Longer aging produces a small negative ductility change for a test temperature of 25°C (77°F) and a small positive ductility for 593°C (1100°F).

2. Heat 300380 for all aging times shows an increase in ductility for the test temperature of 25°C (77°F) and a decrease in ductility for 593°C (1100°F).

3. Heats X22807, 346845, and 9T2796K all show a decrease in ductility for an aging time of 1000 hr and an even greater decrease for the longer aging times.

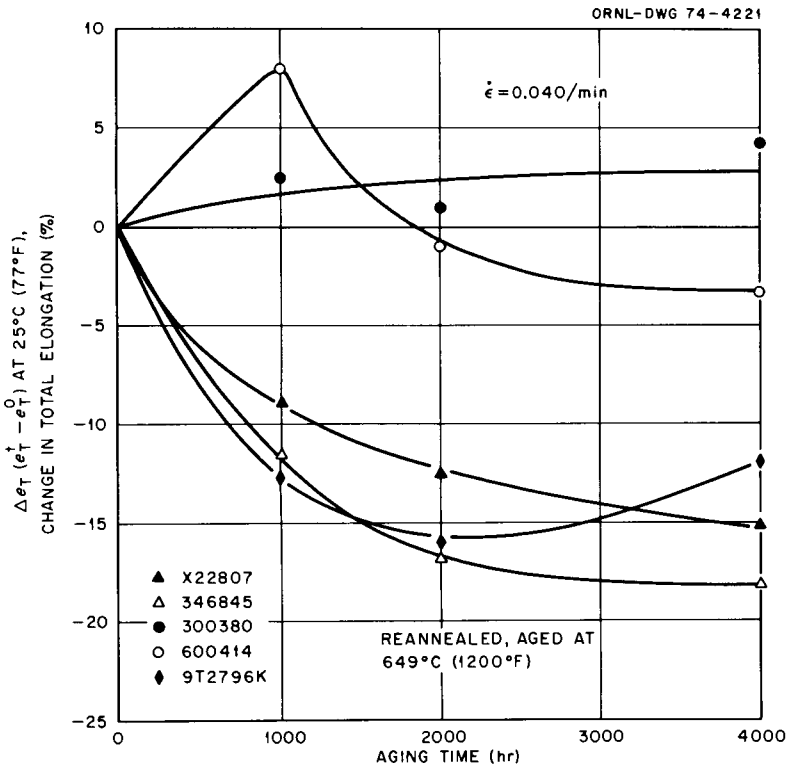

Fig. 5.29. Change in Total Elongation at 25°C (77°F) as a Function of Aging Time for Various Heats of Type 304 Stainless Steel Aged at 649°C (1200°F).

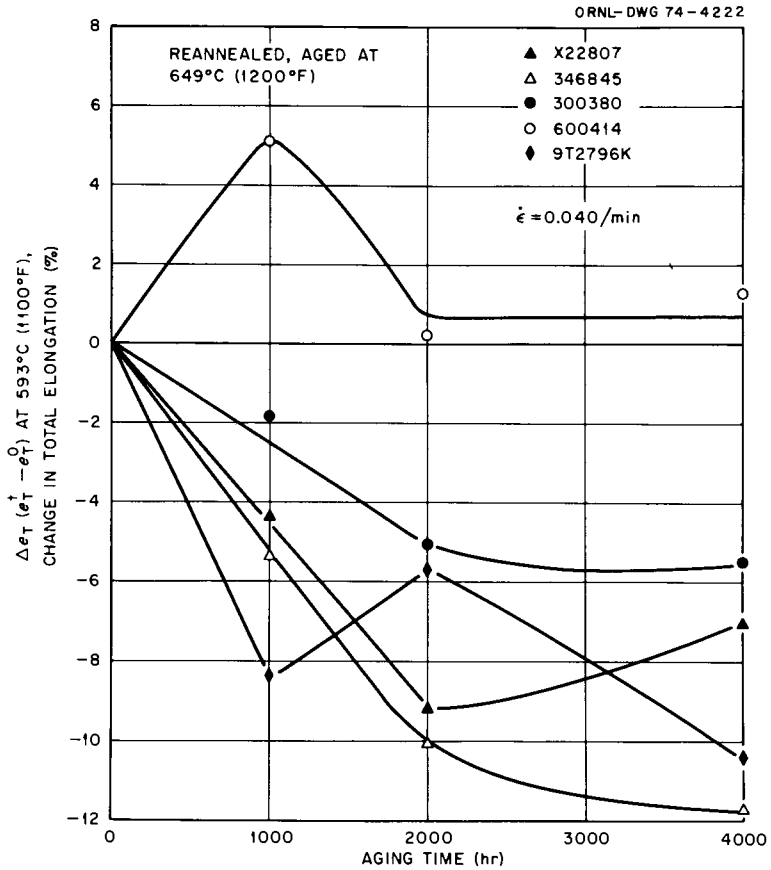

Fig. 5.30. Change in Total Elongation at 593°C (1100°F) as a Function of Aging Time for Various Heats of Type 304 Stainless Steel Aged at 649°C (1200°F).

4. For heat 9T2796K, the ductility curve is a mirror image of the increase in yield strength curve for a test temperature of 593°C (1100°F) (i.e., maximum decrease in ductility for a maximum increase in yield strength and vice versa).

The results on change in ductility, based on reduction of area, in Figs. 5.31 and 5.32 for the test temperatures of 25 and 593°C (77 and 1100°F) show the following:

1. All heats show a decrease in reduction of area for all aging times.

2. Trends in decrease in reduction in area as a function of time are quite similar for both test temperatures.

The significant observations of results on the effect of aging time are that overaging effects are observed for a test temperature of 25°C (77°F), while they are not well pronounced for 593°C (1100°F). Heat 600414 shows a peak increase in total elongation for aging time of 1000 hr at 649°C (1200°F) for both test temperatures.

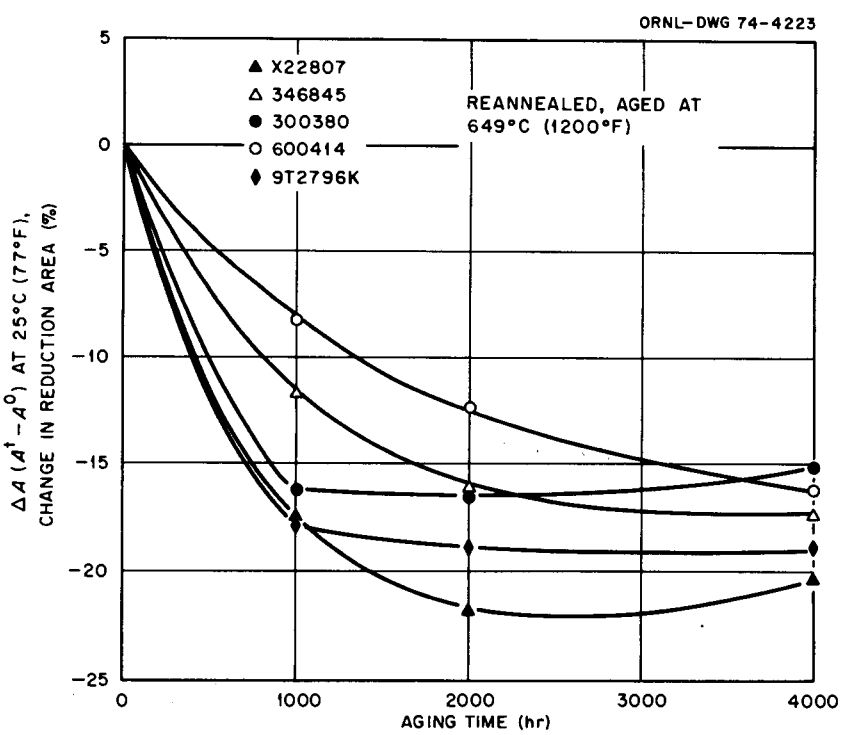

Fig. 5.31. Change in Reduction of Area at 25°C (77°F) as a Function of Aging Time at 649°C (1200°F) for Various Heats of Type 304 Stainless Steel.

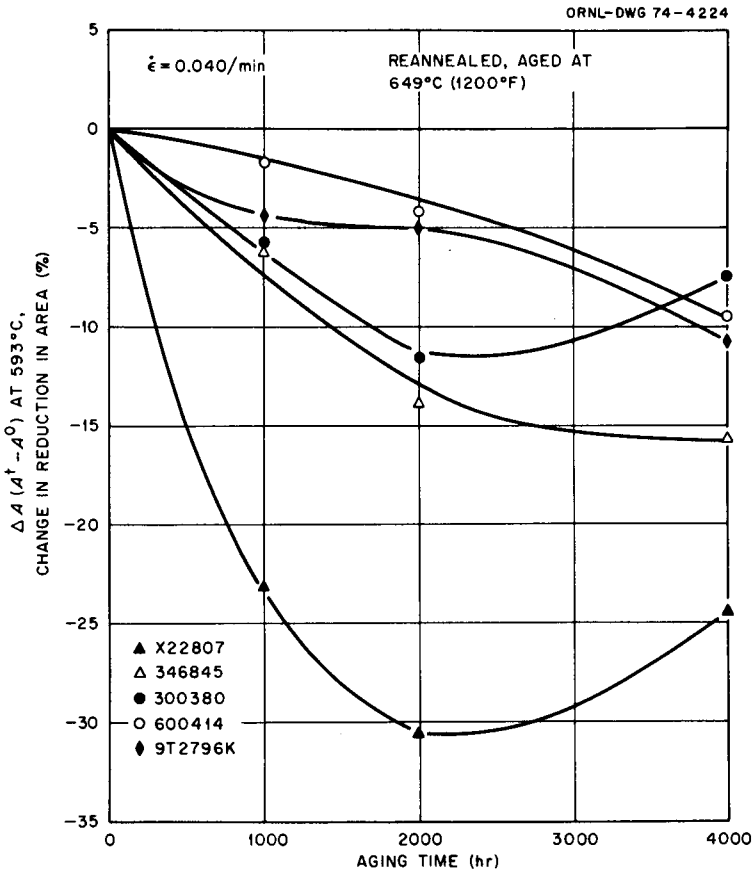

Fig. 5.32. Change in Reduction of Area at 593°C (1100°F) as a Function of Aging Time at 649°C (1200°F) for Various Heats of Type 304 Stainless Steel.

In general, aging for 4000 hr at all temperatures increases the yield strength, both at 25 and 593°C (77 and 1100°F). The increase in yield strength results in a corresponding decrease in ductility except in heat 600414, where there is an increase or no change in ductility. The room-temperature strength shows a maximum increase for an aging temperature of 482°C (900°F), whereas 593°C (1100°F) strength shows a maximum for an aging temperature of 649°C (1200°F). Aging for different times at 649°C (1200°F) shows overaging for strength at 25°C (77°F); the effect is not well pronounced for strength at 593°C (1100°F).

Work will be initiated on room-temperature hardness, metallography, and transmission electron microscopy to explain the observed aging effects.

5.2.2.3 Transmission Electron Microscopy of Heat-to-Heat Variations of Type 304 Stainless Steel — V. K. Sikka

Transmission electron microscopic observation of various heats of type 304 stainless steels, in the as-received condition, has been initiated. Some preliminary results are presented here.

Typical micrographs of the reference heat 9T2796 are shown in Figs. 5.33 and 5.34. The characteristic microstructural features include low dislocation line density, low density of extended nodes (Figs. 5.33 and 5.34) and large intrinsic-extrinsic stacking fault ribbons near the grain boundary (Fig. 5.34).

Typical micrographs of heat 346845 are shown in Figs. 5.35 and 5.36. The microstructure includes slip bands filled with array of extended nodes (Fig. 5.35), intrinsic-extrinsic stacking fault ribbons (Fig. 5.36), and a low dislocation line density. It is interesting to note (Fig. 5.35) that heat 346845 shows the presence of some coherent precipitate, which was not observed in the reference heat. In addition to coherent precipitate at least one area showed the presence of a large precipitate particle marked by "A" in Fig. 5.36.

Typical micrographs of heat 8043813 are shown in Figs. 5.37 and 5.38. The microstructure includes a relatively large dislocation line density, low density of extended nodes, and intrinsic-extrinsic stacking fault ribbons. Most of the dislocations in Fig. 5.37 show the formation of junctions, which seem to have pinched off a large number of dislocation loops. The presence of some extremely small coherent precipitate particles can also be observed in both Figs. 5.37 and 5.38.

Work will continue to examine the other heats and to characterize the microstructure quantitatively.

Fig. 5.33. Typical Micrograph of Heat 9T2796K As Received.

Fig. 5.34. Typical Electron Micrograph of Heat 9T2796K As Received, Showing Intrinsic-Extrinsic Stacking Fault Ribbons.

Fig. 5.35. Typical Electron Micrograph of Heat 346845 As Received, Showing Extended Nodes in a Slip Band and Coherent Precipitate.

Fig. 5.36. Typical Electron Micrograph of Heat 346845 As Received, Showing Intrinsic-Extrinsic Stacking Fault Ribbons.

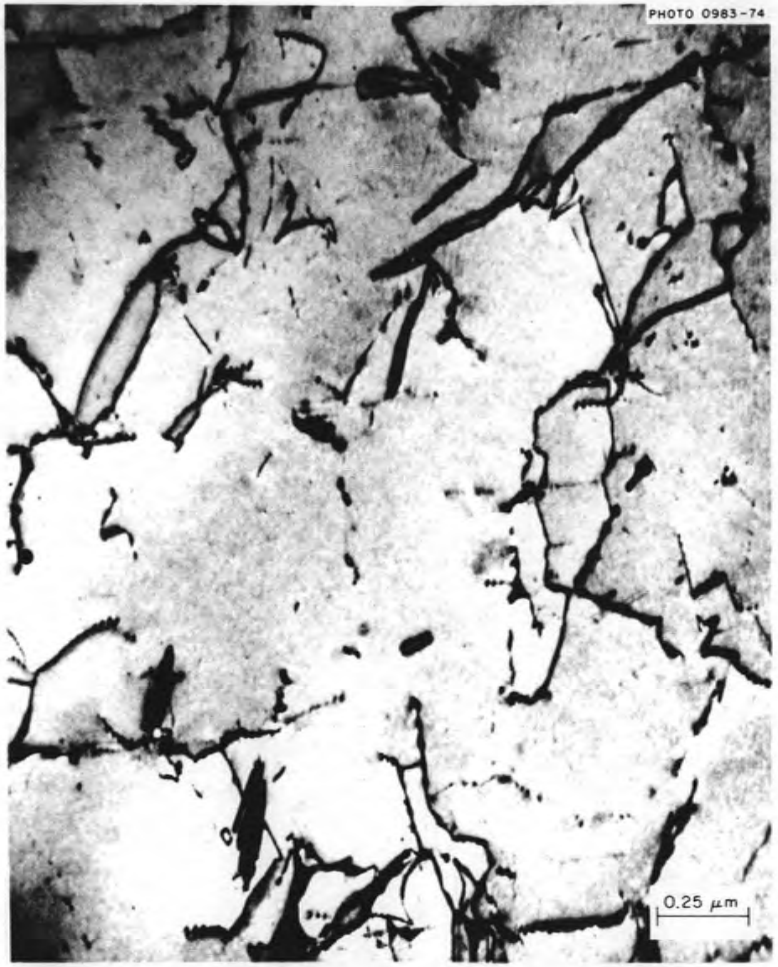

Fig. 5.37. Typical Electron Micrograph of Heat 8043813 As Received, Showing Intrinsic-Extrinsic Stacking Fault Ribbons and Dislocation Loops.

Fig. 5.38. Typical Electron Micrograph of Heat 8043813 As Received.

5.2.2.4 Influence of Aging on the Creep Properties of Type 304 Stainless Steel — H. E. McCoy

Several heats of type 304 stainless steel are being aged at 482, 593, and 649°C (900, 1100, and 1200°F). In addition to the tensile tests already discussed, creep tests have been run on several of the materials at 30,000 psi (207 MPa) and 593°C. The results will be reported in more detail when more of the tests are completed, but the creep curves in Fig. 5.39 and 5.40 illustrate the trends that have been observed.

Heat 807, shown in Fig. 5.39, contained only 0.029% C and 0.021% N, but the creep behavior changes as a result of aging. For the 4000-hr aging condition studied, the minimum creep rate increased about 40%. Aging at 482°C (900°F) increased the rupture life, but aging at 649°C (1200°F) had little effect. Heat 845, shown in Fig. 5.40, contained 0.057% C and 0.024% N, and the effects of aging were greater than those noted for heat 807. The rupture life decreased progressively with increasing aging temperature, so that the rupture life after aging for 4000 hr

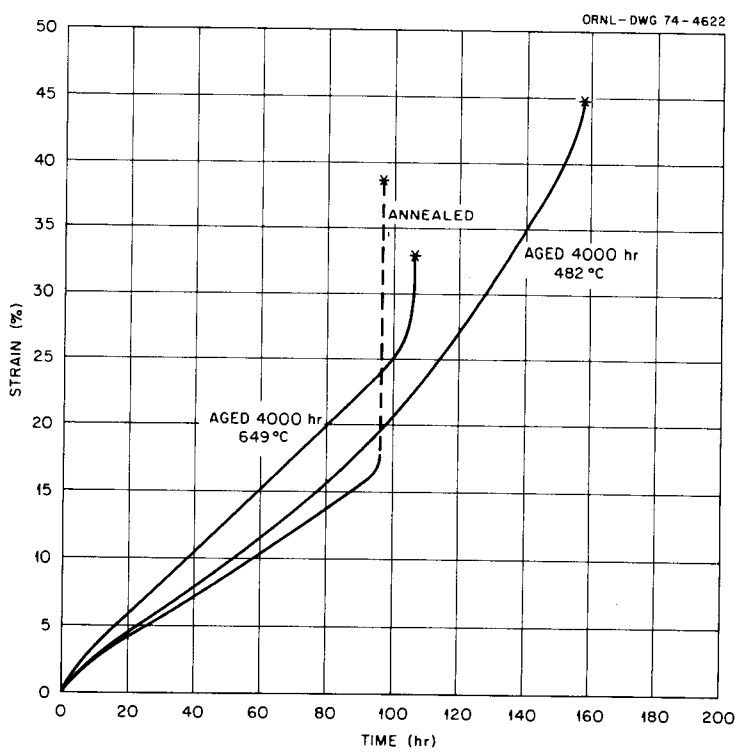

Fig. 5.39. Effect of Aging on the Creep Behavior of Type 304 Stainless Steel (Heat 807) at 30,000 psi (207 MPa) and 593°C (1100°F).

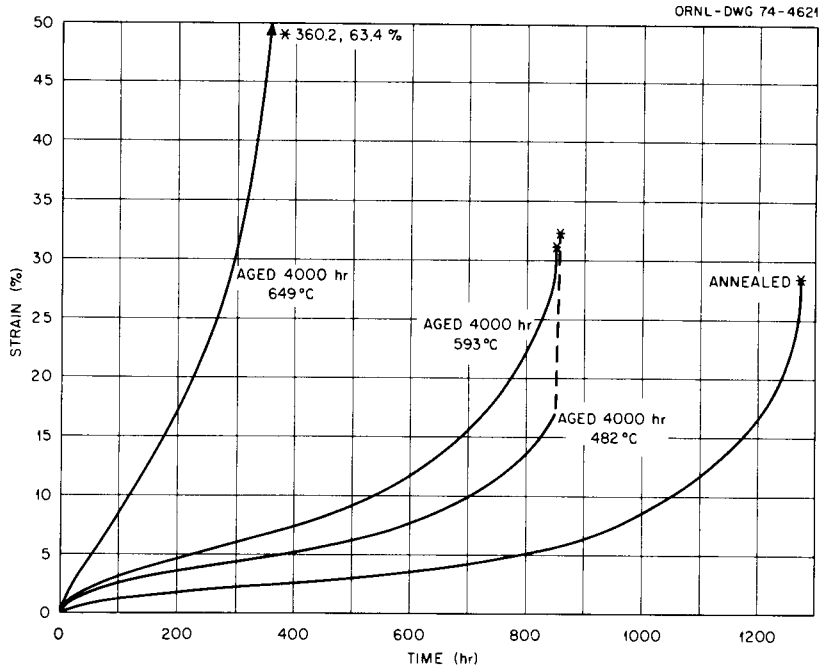

Fig. 5.40. Effect of Aging on the Creep Behavior of Type 304 Stainless Steel (Heat 845) at 30,000 psi (207 MPa) and 593°C (1100°F).

at 649°C was only about one-fourth that of the annealed material. The minimum creep rate increased with aging from 0.0044%/hr for the annealed material to 0.077%/hr for material aged 4000 hr at 649°C. Aging doubled the fracture strain.

Other tests are in progress. These tests show that thermal aging can have large effects on the creep properties and indicate that the effects are much larger in heats with higher carbon and nitrogen concentrations.

5.2.3 Mechanical Properties of Type 316 Stainless Steel

5.2.3.1 Procurement of Type 316 Stainless Steel Reference Heat — R. J. Beaver

The type 316 stainless steel reference heat was melted in late January, and all ingots except a spare ingot have been processed into semifinished products. The ladle analyses and subsequent checks of the semifinished products have shown compliance to the composition requirements, with semifinished product uniformity (based on 38 samples) as follows:

Element	Range (wt %)
C	0.056 to 0.066
Cr	17.13 to 17.30
Ni	13.40 to 13.55
Mo	2.32 to 2.35
Mn	1.86 to 1.88
Si	0.58 to 0.60
P	0.023 to 0.025
S	0.017 to 0.019
Cu	0.09 to 0.10
Co	0.02
N	0.031 to 0.034
Ti	0.01
B	0.0005 to 0.0006
Nb plus Ta	0.00

A surveillance of Republic Steel's production was made in mid-March. The program is intensively pursued by the metallurgical personnel in overseeing this procurement, and the aircraft identity system imposed by our specification is efficiently controlled. Although no recent formal completion date has been established by Republic Steel, we anticipate that all fabrication will be completed by mid-June, with the plate and most of the forging product available for delivery to us early in June. Delivery of pipe, to be produced by U.S. Steel, subcontractor to Republic Steel, is not expected until mid-September, the contract scheduled delivery date.

A contract has been negotiated with Rollmet, Inc., for production of the 16- and 28-in.-diam (405 and 710 mm) pipe. We estimate delivery of these items for November, based on present status.

5.2.3.2 Heat-to-Heat Variation Studies of Type 316 Stainless Steel — H. E. McCoy

Seven wrought heats of material and one as-cast heat are currently included in this program. The chemical composition and other pertinent data are given in Table 5.16. Three heats were in the form of 1/2-in.-thick (12.7-mm) plate (A 240 condition), three heats in the form of 2 1/16-in.-diam × 24-in.-long (52.4 × 610 mm) bars (A 479 condition), one heat in the form of 28-in.-OD × 0.375-in.-wall (710 × 9.5 mm) welded pipe (A 312), and one heat in the form of a 1475-lb (670 kg) casting (A 351). Tensile and creep tests were run on these materials in the as-received and reannealed (0.5 hr at 1065°C, 1950°F) conditions.

Table 5.16. Type 316 Stainless Steel Being Studied in the Heat-to-Heat Variation Program[a]

	Heat						
	327686	500613	2P3212	30160	91694	91695	915509
Heat Symbol	686	613	212	160	694	695	509
Vendor	Allegheny Ludlum	Carlson	USS				
As-Received Form	Plate	Plate	Plate	Bar	Bar	Bar	Pipe
Dimensions, in.(mm)	1/2(12.7)	1/2(12.7)	1/2(12.7)	2 1/16(52.4) Diameter	2 1/16(52.4) Diameter	2 1/16(52.4) Diameter	28 OD×3/8 wall (710×9.5)
Grain Size, ASTM							
As-Received	8	6.0	6.5	9	7.4	7.5	4.0
Reannealed[b]	8	6.4	4.8	6.8	5.4	5.3	4.8
Chemical Composition, %							
Carbon	0.053	0.063	0.055	0.041	0.043	0.039	0.053
Nitrogen	0.079	0.042	0.053	0.021	0.021	0.019	0.074
Phosphorus	0.023	0.023	0.026	0.019	0.018	0.019	0.022
Boron	0.010	0.0002	0.0002	0.0001	0.0001	0.0001	0.00005
Oxygen	0.0066	0.015	0.0076	0.0032	0.0088	0.0036	0.0010
Hydrogen	0.0005	0.0002	0.0008	0.0004	0.0007	0.0006	0.0025
Nickel	13.3	12.9	13.4	13.6	13.5	13.7	13.5
Manganese	1.60	1.65	1.41	1.63	1.63	1.38	1.54
Chromium	17.2	16.4	17.3	17.4	17.4	17.3	16.9
Silicon	0.55	0.72	0.55				0.60
Molybdenum	2.2	2.2	2.4	2.2	2.2	2.2	2.5
Sulfur	0.007	0.024	0.012	0.013	0.014	0.014	0.015
Titanium	0.037	0.041	0.035	0.030	0.030	0.030	<0.001
Copper	0.13	0.19	0.09	0.10	0.10	0.10	0.07
Cobalt	0.03	0.08	0.07	0.03	0.03	0.03	0.15
Lead	0.0007	0.007	0.0007				<0.0003
Niobium	0.15	0.005	0.002	0.0020	0.0020	0.0020	<0.002
Tin	<0.01	<0.01	<0.01	0.0010	0.0030	0.0030	0.001
Tantalum	<0.001	<0.001	<0.001	0.0003	0.0001	0.0001	<0.001
Vanadium				0.030	0.030	0.030	
Tungsten				0.010	0.010	0.010	

[a]Also, heat 30173 (symbol 173) has been received in the form of a 1475-lb (670-kg) ingot.

[b]0.5 hr at 1065°C (1950°F).

The results of tensile tests on the first three heats were reported previously.[8] The results obtained on the four additional wrought heats are given in Table 5.17, and those for the cast heat are given in

Table 5.17. Tensile Properties of Type 316 Stainless Steel[a]

Heat, Condition	Test Temperature (°C)	Test Temperature (°F)	Stress, ksi(MPa) Yield	Stress, ksi(MPa) Ultimate Tensile	Strain, % Uniform	Strain, % Total	Reduction in Area (%)
30160	25	77	44.8(309)	85.0(586)	48.8	61.4	75.9
A 479	427	800	34.2(236)	68.0(409)	35.2	42.6	68.1
	593	1100	27.3(188)	59.1(407)	36.0	45.6	71.9
	649	1200	27.0(186)	47.6(328)	29.6	56.5	75.7
91694	25	77	45.6(314)	86.5(596)	47.2	58.9	74.9
A 479	427	800	31.9(220)	67.9(468)	35.2	41.8	68.0
	593	1100	28.7(198)	59.2(408)	36.0	44.8	71.2
	649	1200	29.0(200)	50.2(346)	28.0	57.4	72.0
91695	25	77	46.7(322)	86.7(598)	47.2	61.4	75.9
A 479	427	800	33.9(234)	68.9(475)	33.6	42.1	66.9
	593	1100	30.2(208)	59.6(411)	36.0	45.8	72.5
	649	1200	30.2(208)	49.9(344)	27.2	56.8	80.9
915509[b]	25	77	36.1(249)	81.7(563)	48.9	57.0	70.8
A 312	427	800	20.9(144)	69.4(478)	39.6	41.4	59.4
	593	1100	18.2(125)	60.6(418)	40.9	43.3	59.3
	649	1200	17.0(117)	50.7(350)	34.7	44.8	63.5
30160	25	77	29.7(205)	79.7(550)	64.0	76.0	81.8
Reannealed[c]	427	800	16.7(115)	65.3(450)	47.2	55.4	75.6
	593	1100	12.9(89)	57.0(393)	44.0	55.2	74.8
	649	1200	13.9(96)	48.8(336)	36.0	61.6	76.9
91694	25	77	27.7(191)	78.8(543)	64.8	76.8	82.1
Reannealed[c]	593	1100	11.4(79)	55.0(379)	46.4	56.0	73.3
	649	1200	11.3(78)	48.0(331)	37.6	65.5	75.0
91695	25	77	27.8(192)	78.0(538)	65.2	78.4	83.8
Reannealed[c]	427	800	13.7(94)	63.5(438)	47.2	56.2	75.8
	593	1100	10.8(74)	54.3(374)	46.4	56.0	72.6
	649	1200	11.3(78)	47.4(327)	38.4	62.4	77.3
915509	25	77	34.7(239)	81.7(563)	53.3	60.3	71.1
Reannealed[c]	427	800	17.8(123)	67.6(466)	42.2	42.4	62.5
	593	1100	15.8(109)	60.0(414)	40.0	44.0	60.8
	649	1200	14.8(102)	50.7(350)	40.0	49.5	60.3

[a]Strain rate of 0.04/min except where noted.

[b]Strain rate of $0.044/min^{-1}$.

[c]0.5 hr at 1065°C (1950°F).

Table 5.18. The 2 1/16-in.-diam bars were quartered, and samples were made parallel to the bar axis. Samples were made from the pipe wall with the specimen axis parallel to the pipe axis. A horizontal section 4 in. thick was cut from the center of the ingot. The section was 12 in. square, and samples were cut along the two diagonals with their axes

Table 5.18. Tensile Properties of Type 316 Stainless Steel Casting, Heat 173[a]

Condition	Specimen	Stress, ksi (MPa)		Strain, %		Reduction of Area (%)
		Yield	Ultimate Tensile	Uniform	Total	
		Tested at 25°C (77°F)				
As cast	1	26.7(184)	62.7(432)	52.9	62.5	76.6
	3	27.1(187)	60.5(417)	37.0	47.7	68.7
	5	27.1(187)	56.2(387)	40.1	49.7	77.9
	7	25.4(175)	58.5(403)	58.4	70.8	71.6
	9	26.4(182)	63.2(436)	48.9	39.1	64.8
	11	26.6(183)	60.5(417)	33.9	37.4	43.4
	21	26.4(182)	62.0(427)	55.7	61.3	63.2
Reannealed[b]	2	24.0(165)	61.2(422)	54.1	68.6	73.6
	4	23.6(163)	60.4(416)	50.2	59.8	75.2
	6	23.0(199)	53.9(372)	44.2	51.3	66.5
	8	24.4(168)	61.9(427)	47.8	55.9	74.1
	10	24.1(166)	61.5(424)	43.5	53.1	66.0
	12	21.6(149)	33.8(233)	12.1	19.7	22.4
		Tested at 593°C (1100°F)				
As cast	17	17.1(118)	43.5(300)	38.2	48.1	49.0
	19	12.7(88)	41.6(287)	41.2	44.4	54.4
	23	13.0(90)	41.3(285)	36.3	44.0	61.1
	25	12.7(88)	44.7(308)	43.7	50.7	58.3
Reannealed[b]	14	10.0(69)	44.0(303)	40.6	44.2	52.3
	16	9.9(68)	43.0(296)	41.8	39.9	47.7
	18	11.9(82)	37.4(258)	24.8	36.1	56.2
	20	9.5(66)	39.0(269)	43.1	40.3	59.5
	22	10.1(70)	40.9(282)	35.9	42.9	60.1
	24	10.6(73)	44.0(303)	43.8	45.9	66.1

[a]Strain rate of 0.04/min.

[b]0.5 hr at 1065°C (1950°F).

vertical. Samples numbered 1 through 25 ran along one diagonal and those numbered 26 through 50 ran along the other.

The yield stresses of all eight heats as received are compared in Fig. 5.41. All heats except the casting had yield stresses above the minimum expected values given in ASME Pressure Vessel Code 1331-8. After reannealing, many of the heats have yield stresses below the minimum expected values. The number of heats falling below the line increases progressively with increasing temperature. The extremes in Fig. 5.42 are occupied on the high side by heat 686 and on the low side by the casting, heat 173.

The ultimate tensile stresses of six of the wrought heats are quite close, e.g. at 25°C (77°F) the range is from 78.0 to 86.7 ksi (538–598 MPa), at 649°C (1200°F) from 47.4 to 54.1 ksi (327–373 MPa). Wrought heat 686 had an ultimate tensile stress of 100 ksi (689 MPa) at 25°C and 62.3 to 64.8 ksi (429–447 MPa) at 649°C. The ultimate tensile stresses of cast heat 173 (Table 5.18) varied from 53.9 to 63.2 ksi (372–436 MPa) at 25°C and from 37.4 to 44.7 ksi (258–308 MPa) at 593°C.

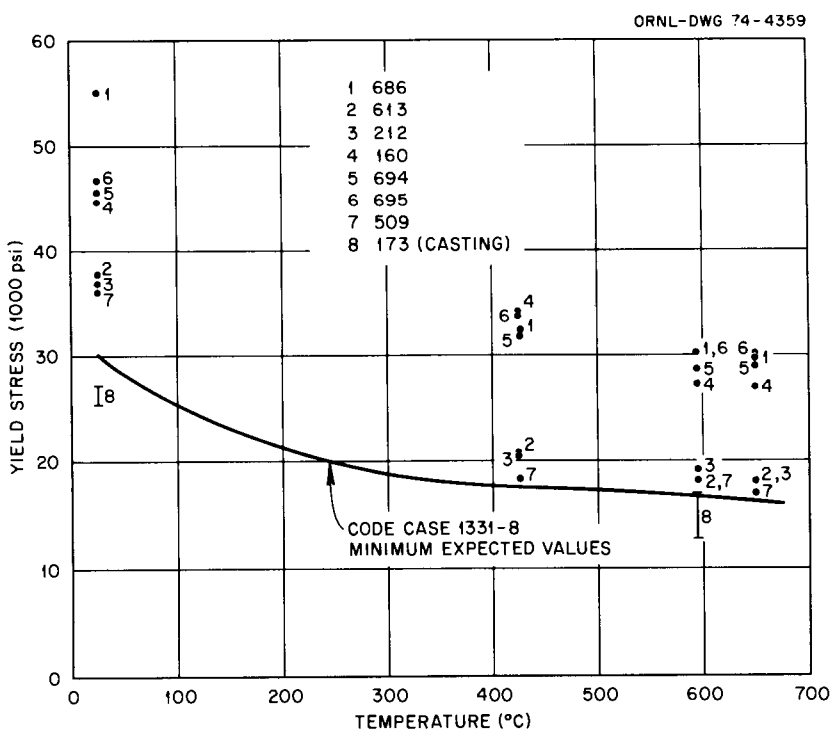

Fig. 5.41. Comparison of the Yield Stresses of Several Heats of Type 316 Stainless Steel As Received.

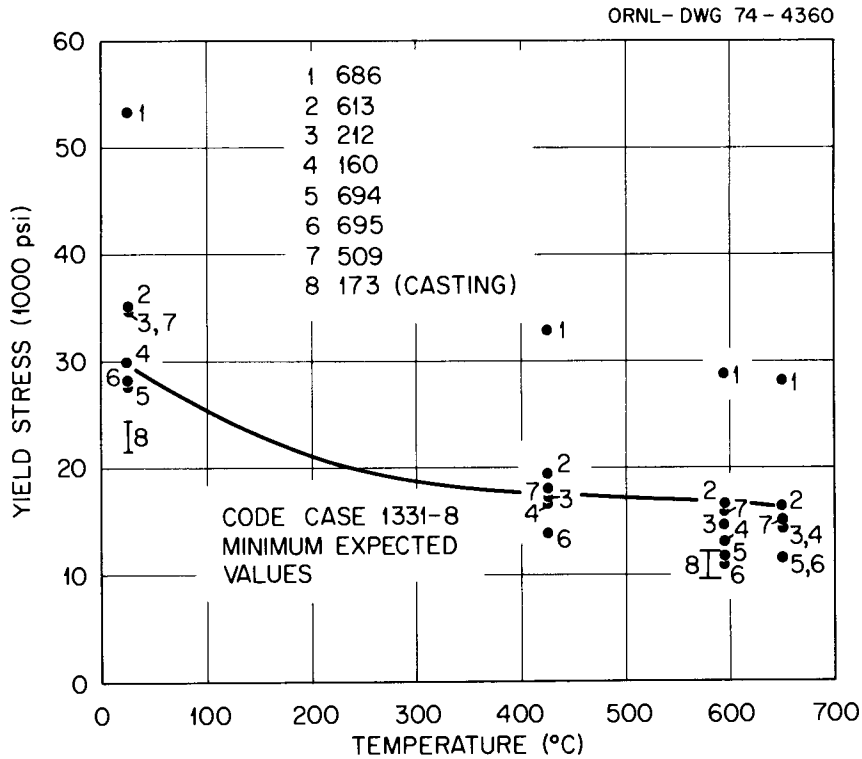

Fig. 5.42. Comparison of the Yield Stresses of Several Heats of Type 316 Stainless Steel Reannealed 0.5 hr at 1065°C (1900°F).

The ultimate tensile strength of heat 686 was significantly above that of the other heats and that of heat 173 significantly below.

The ductility measures (uniform strain, total strain, and reduction of area) were quite high for all heats. The heats differ slightly, but the values are all so high that the differences have no immediate significance.

The tensile results in Table 5.18 give some indications of the variation of properties across the casting. Sample 1 was located at the outer edge and sample 11 was located near the center of the ingot, where the cooling rate should have been less. There is no detectable effect of specimen location on the strength measures, but the ductility appears to decrease from edge to center. Reannealing the samples for 0.5 hr at 1065°C (1950°F) reduced the yield stress 10 to 20%. The ultimate tensile stress and the ductility measures remained unchanged. The tensile properties at 593°C (1100°F) show no detectable effect of sample location.

Reannealing reduced the yield stress but did not alter the other properties. The castings had a large grain size, and the fractures were characterized by anisotropic cross sections.

Limited creep tests have been run on these heats, and the results are summarized in Table 5.19. Five of the heats have very similar properties but heat 686 has far superior strength. The tests on cast heat 173 are given in Table 5.20. The scatter in results overshadows any possible effect of specimen location. The cast material was characterized by very high loading strains — e.g., at 35,000 psi (241 MPa) the casting

Table 5.19. Creep Properties of Type 316 Stainless Steel at 593°C (1100°F)

Heat	Condition[a]	Stress (ksi)	Stress (MPa)	Rupture Life (hr)	Minimum Creep Rate (%/hr)	Strain, % Loading	Strain, % Creep	Reduction of Area (%)
160	A479	40	276	245.1	0.071	8.6	44.3	62.4
160	Reannealed	40	276	220.0	0.066	9.8	36.2	39.1
212	Reannealed	35	241	1520.1	0.0076	8.0	25.3	38.3
212	A240	40	276	163.1	0.068	9.1	22.3	26.1
212	Reannealed	40	276	149.1	0.059	12.1	16.9	27.0
509	A312	40	276	186.0	0.031	9.4	9.6	23.8
509	Reannealed	40	276	142.0	0.041	11.0	10.3	22.5
613	A240	35	241	465.4	0.0080	5.9	7.7	15.3
613	Reannealed	35	241	460.7	0.0074	6.6	8.3	14.5
613	A240	40	276	197.9	0.013	6.1	8.3	13.4
613	Reannealed	40	276	122.8	0.034	8.9	7.4	17.4
686	A240	35	241	5260.2[b]		0.88	3.2	3.4
686	Reannealed	35	241	1007.4[b]		1.88	0.9	2.5
686	A240	40	276	3186.4[b]	5.0×10^{-5}	2.5	3.7	5.4
686	Reannealed	40	276	3161.9[b]	6.4×10^{-4}	2.9	6.9	7.7
686	A240	50	345	531.4	0.0011	5.2	6.9	12.7
694	A240	40	276	250.8	0.073	3.5	49.1	60.9
694	Reannealed	40	276	89.5	0.12	15.0	26.0	41.5
695	A429	40	276	195.3	0.099	3.6	46.7	71.2
695	Reannealed	40	276	223.6	0.067	12.5	40.4	59.2

[a]ASTM specification for as-received condition or reannealed 0.5 hr at 1065°C (1950°F).

[b]Discontinued before rupture.

Table 5.20. Creep Properties of Type 316 Stainless Steel Casting (Heat 173) at 593°C (1100°F)

Specimen	Stress (ksi)	Stress (MPa)	Rupture Life (hr)	Minimum Creep Rate (%/hr)	Strain, % Loading	Strain, % Creep	Reduction of Area (%)
			Tested As Cast				
26	40	276	17.3	0.24	26.7	17.9	55.2
27	35	241	47.1	0.051	19.3	14.9	43.0
28	35	241	28.1	0.14	20.2	14.5	35.0
29	35	241	42.1	0.20	22.4	14.4	33.5
30	25	172	266.9	0.0032	12.1	7.2	29.0
32	35	241	14.4	0.13	20.0	14.6	36.6
34	35	241	1.5	1.5	29.8	15.1	58.8
36	35	241	68.7	0.067	17.1	14.3	30.6
38	35	241	19.1	0.11	18.7	8.9	26.6
			Reannealed 0.5 hr at 1065°C (1950°F)				
39	35	241	6.0	0.15	19.5	7.2	45.7
41	35	241	41.8	0.10	18.6	16.6	25.3
44	35	241	18.2	0.26	25.5	13.7	35.4
47	35	241	28.0	0.12	26.1	10.6	39.6
49	35	241	63.6	0.043	19.1	11.4	27.5
50	35	241	66.6	0.040	21.2	7.8	21.9

deformed about 20%, compared with 6 to 8% for the wrought heats. The rupture lives of the casting fall far short of those for the wrought heats.

The rupture lives of these heats of material are compared in Fig. 5.43 with those from Smith's compilation[5] and from Code Case 1331-8. The properties of the casting fall below those from all other sources, and the properties of heat 686 fall above. The other heats have rupture lives above the minimum expected values. The minimum creep rates are compared in Fig. 5.44. Heat 686 has a very low creep rate, and the other

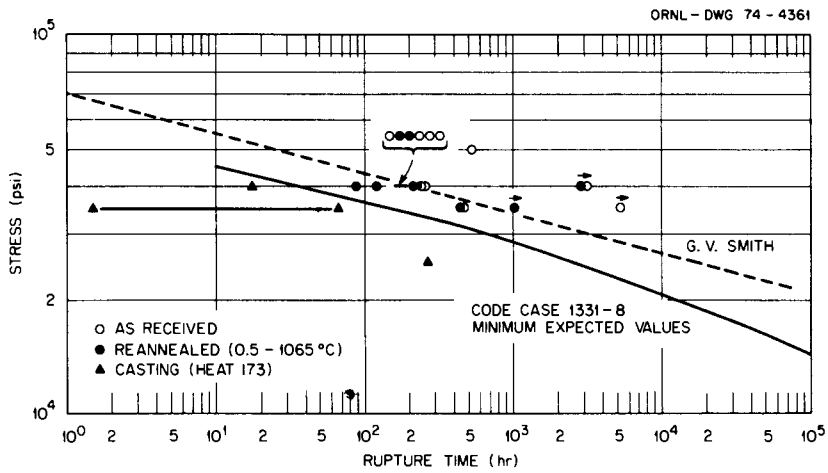

Fig. 5.43. Stress-Rupture Properties of Type 316 Stainless Steel at 593 (1100°F).

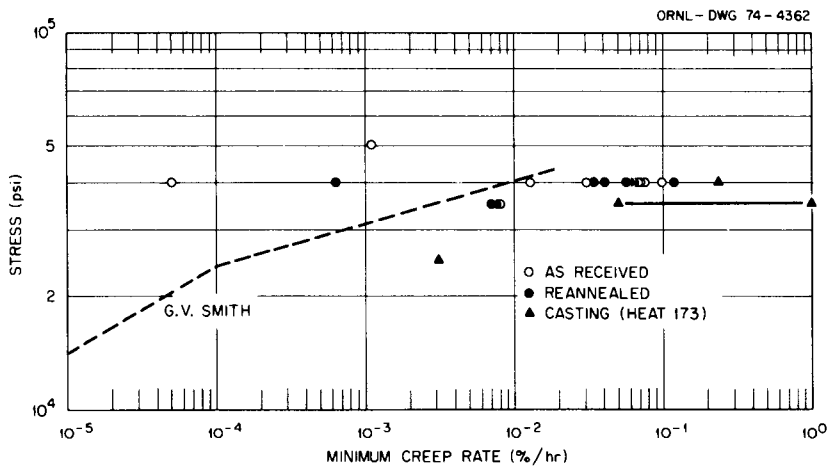

Fig. 5.44. Creep Properties of Type 316 Stainless Steel at 593°C (1100°F).

heats creep faster than those in Smith's compilation. The casting (heat 173) has the highest creep rate.

Some of the details of the creep behavior are illustrated in Fig. 5.45. Heat 686 consistently showed a very low creep rate over a small segment of the creep curve. The length of this low-creep-rate region increased as the stress level was decreased. The creep curves for the casting (heat 173) had numerous discontinuities. The particular test shown in Fig. 5.45 was read quite frequently, so there is no doubt about the steps actually occurring. The creep curve for heat 694 is typical of the other five heats.

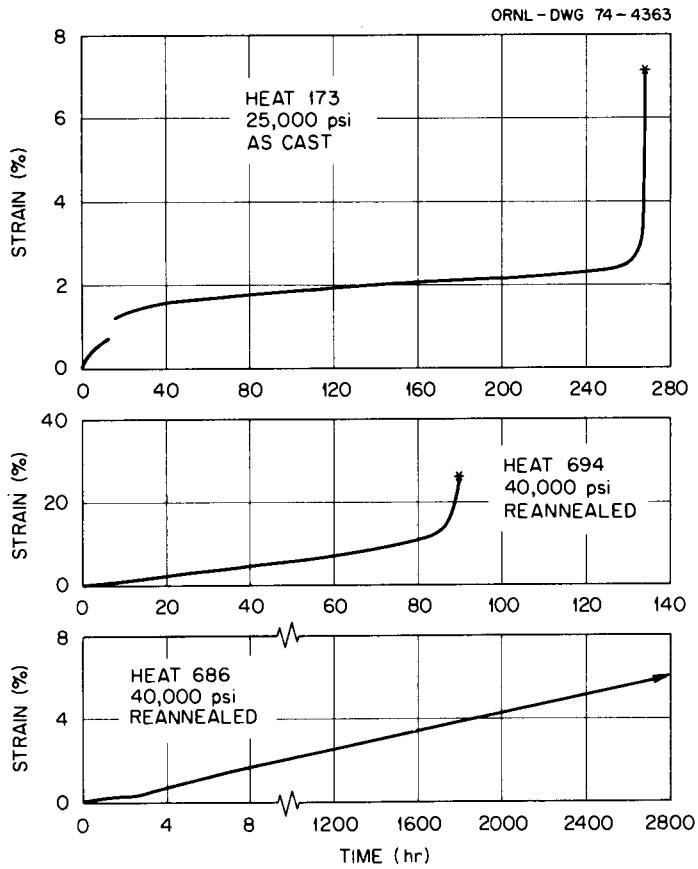

Fig. 5.45. Creep Curves for Type 316 Stainless Steel at 593°C (1100°F).

Four of these heats are being studied in an aging program, and the status of the program is summarized in Fig. 5.46. The results of tensile tests after 1000 hr aging at 649°C (1200°F) are summarized in Tables 5.21, 5.22, and 5.23. Generally, aging increased the yield stress and decreased all ductility measures (uniform and total elongations and reduction of area). The ultimate tensile stress was affected both ways, but in most cases aging caused the ultimate tensile stress to increase at 25°C (77°F) and to decrease at 593°C (1100°F).

5.2.4 Failure Criteria — Strain Limits — C. R. Brinkman

A workable strain limit for design applications should reflect material "ductility," which can be a function of many variables including state of strain, load or strain history, and the failure mechanism. However, definition of a precise "ductility" limit or limits that would be

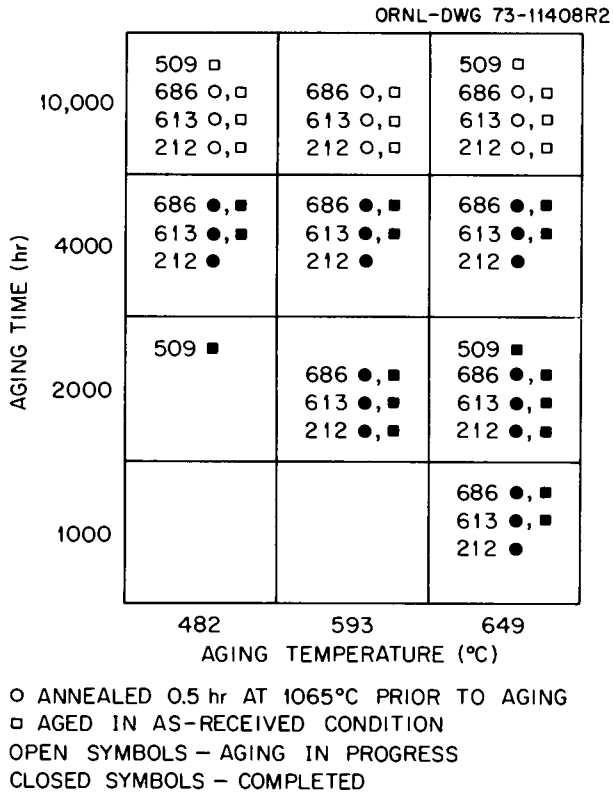

Fig. 5.46. Aging Program for Type 316 Stainless Steel.

meaningful for the combinations of static and dynamic elevated-temperature loading envisioned for reactor components throughout their design lifetimes is difficult to establish because of (1) the paucity of relevant long-term cyclic and monotonic creep data, and (2) the inherent scatter in available data.

Ideally, the strain limit should be based on a measurable material "ductility" indicator that not only would preclude actual failure, but also would eliminate the instability (i.e., nonuniform deformation and tertiary creep), thereby minimizing excessive voidage and cracking. One might simply conclude, therefore, that the onset of tertiary creep be employed as this criterion; however, the onset of tertiary creep is a poor indicator in that it is not always well defined. It has also been suggested that the product of minimum creep rate and time to rupture be used, as this criterion is based on the observation that this product may remain constant over a fairly broad temperature and stress range.[9]

Table 5.21. Tensile Properties of Type 316 Stainless Steel Heat 212 at a Strain Rate of 0.040/min

Condition	Treatment			Stress, ksi(MPa)		Strain, %		Reduction of Area (%)
	Time (hr)	Temperature (°C)	Temperature (°F)	Yield	Ultimate Tensile	Uniform	Total	
				Tested at 25°C (77°F)				
A 240				36.8(254)	86.6(597)	60.7	72.0	73.0
Reannealed	0.5	1065	1950	34.8(240)	85.0(586)	56.8	72.0	72.9
Reannealed, aged	1000	649	1200	35.9(218)	87.1(601)	53.6	65.7	61.6
				Tested at 593°C (1100°F)				
A 240				19.2(132)	66.3(457)	44.0	49.0	60.4
Reannealed	0.5	1065	1950	14.5(100)	60.6(418)	49.6	51.0	60.7
Reannealed, aged	1000	649	1200	18.4(127)	61.5(424)	37.6	51.4	57.2

Table 5.22. Tensile Properties of Type 316 Stainless Steel Heat 613 at a Strain Rate of 0.040/min

Condition	Treatment			Stress, ksi(MPa)		Strain, %		Reduction of Area (%)
	Time (hr)	Temperature (°C)	Temperature (°F)	Yield	Ultimate Tensile	Uniform	Total	
				Tested at 25°C (77°F)				
A 240				37.8(261)	86.5(596)	54.4	69.0	67.0
A 240, aged	1000	649	1200	41.9(289)	92.9(641)	44.0	55.1	57.1
Reannealed	0.5	1065	1950	35.1(242)	85.7(591)	64.0	72.4	65.8
Reannealed, aged	1000	649	1200	35.5(245)	89.4(616)	48.8	60.3	58.5
				Tested at 593°C (1100°F)				
A 240				18.1(125)	63.2(436)	45.6	45.5	53.9
A 240, aged	1000	649	1200	22.0(152)	62.7(432)	33.6	41.9	49.9
Reannealed	0.5	1065	1950	16.3(712)	63.5(438)	45.6	53.9	53.9
Reannealed, aged	1000	649	1200	20.2(139)	60.0(414)	33.6	42.4	51.9

Table 5.23. Tensile Properties of Type 316 Stainless Steel Heat 686 at a Strain Rate of 0.040/min

Condition	Treatment			Stress, ksi(MPa)		Strain, %		Reduction of Area (%)
	Time (hr)	Temperature (°C)	Temperature (°F)	Yield	Ultimate Tensile	Uniform	Total	
				Tested at 25°C (77°F)				
A 240				53.4(368)	100.3(698)	38.8	57.0	69.0
A 240, aged	1000	649	1200	55.6(383)	105.2(725)	36.0	45.9	59.3
Reannealed	0.5	1065	1950	52.2(360)	98.5(679)	39.8	57.0	70.7
Reannealed, aged	1000	649	1200	50.3(347)	103.1(711)	39.2	48.4	58.5
				Tested at 593°C (1100°F)				
A 240				30.2(208)	75.0(517)	35.2	46.5	59.5
A 240, aged	1000	649	1200	35.5(245)	68.2(470)	27.2	35.7	49.5
Reannealed	0.5	1065	1950	28.8(199)	72.6(501)	38.4	48.8	60.5
Reannealed, aged	1000	649	1200	30.0(207)	67.8(467)	28.8	36.0	47.5

The strain at the end of secondary creep (ε_s), the product of the minimum strain rate ($\dot{\varepsilon}_m$), and the time to rupture (t_r), and the total elongation at failure are compared for several sets of data from the literature for two temperatures in Figs. 5.47 and 5.48. The onset of tertiary creep was defined by the investigators for these particular sets of data. Code numbers refer to heat treatments and data sources reported previously.[10] The point to be made in comparing these ductility indices is that (1) scatter is inherent regardless of the index chosen, and (2) the product of the minimum strain rate and rupture time may not be a constant over either broad temperature, stress, or time intervals, and, therefore, suggested use of such a criterion as a strain limit may be speculative until additional long-term data are available.

An average strain rate method employing average strain rates to failure (i.e., total elongation divided by rupture time), as discussed

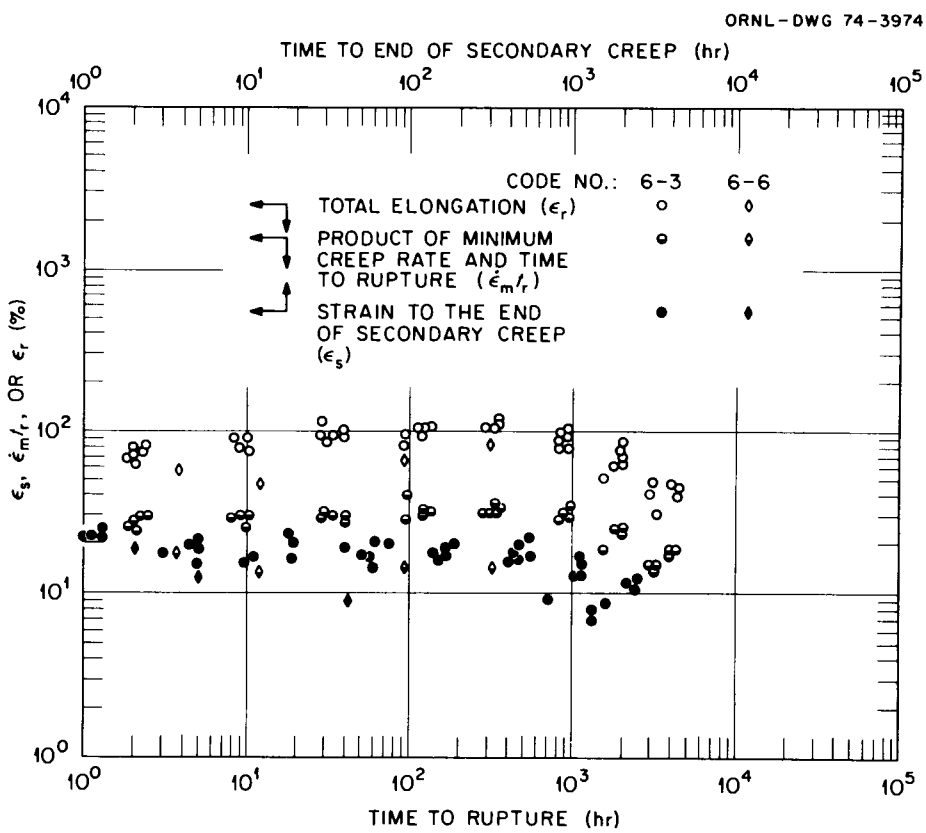

Fig. 5.47. Comparison of Several End-of-Life Criteria for Two Heats of Type 316 Stainless Steel Tested in Uniaxial Tension at 704°C (1300°F).

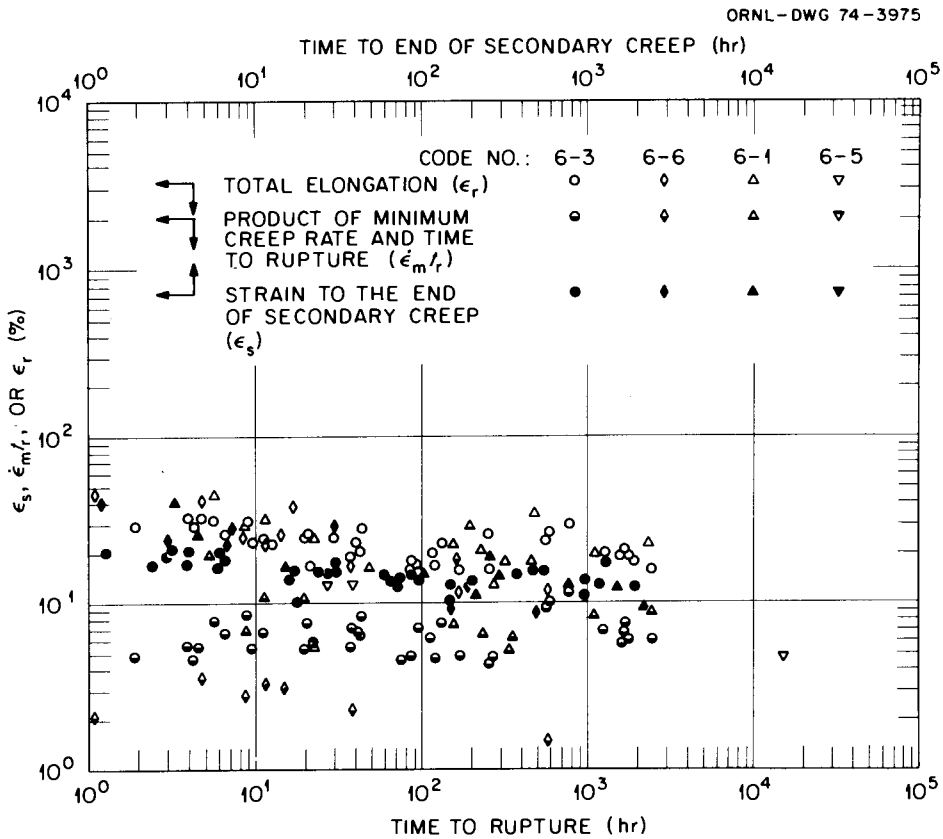

Fig. 5.48. Comparison of Several End-of-Life Criteria for Four Heats of Type 316 Stainless Steel Tested in Uniaxial Tension at 593°C (1100°F).

previously,[10] was employed to estimate the 10^5-hr total elongation and onset of tertiary creep for type 308 CRE stainless steel weld metal. The extrapolations shown in Fig. 5.49 give estimated elongations, which fall within the range of similar extrapolations performed on type 304 stainless base material.[10] However, it should be pointed out that the creep-rupture tests were performed on all-weld-metal specimens taken from heavy section weldments in the longitudinal orientation, where the amount of strain anisotropy is minimal in comparison with the transverse direction. It should again be stated that the concept of an average strain rate is only a crude measure of the actual material flow rates due to the several mechanisms involved (i.e., hardening, softening, intergranular flow, void formation, etc.).

Future experimental efforts need to be directed at complex multiple load studies involving inelastic strain accumulation by several mechanisms

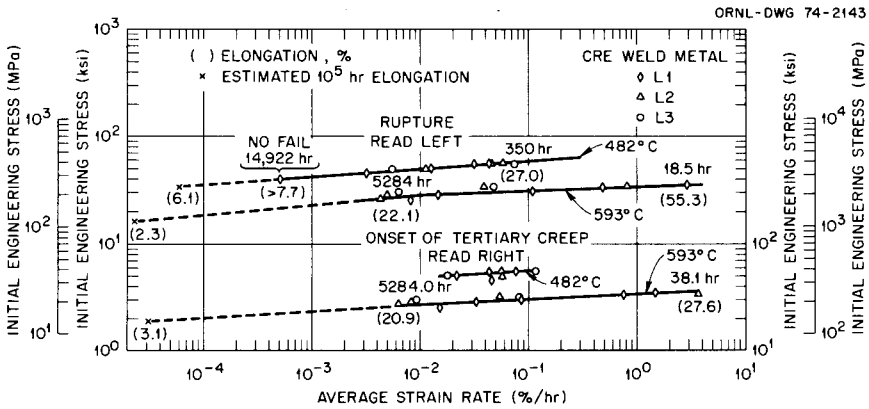

Fig. 5.49. Initial Engineering Stress as a Function of Average Strain Rate to Rupture or Onset of Tertiary Creep, Showing Estimated 10^5-hr Stress-Rupture Elongation and Strain to the Onset of Tertiary Creep for Type 308 CRE Stainless Steel Weld Metal at 482 and 593°C (900 and 1100°F).

over as long a test period as is practical to achieve. Presently planned programs will involve these types of tests. Additional efforts will also be directed at understanding the importance of metallurgical variability in determining long-term ductility for reactor structural materials.

5.2.5 Measurement of Elastic Constants of 2 1/4 Cr-1 Mo Steel by the Dynamic Method — J. P. Hammond and M. W. Moyer*

The Young's and shear moduli and Poisson's ratio were determined for 2 1/4 Cr-1 Mo steel by measuring sonic velocities at temperatures ranging from 24 to at least 760°C (75–1400°F). Measurements were made by two methods: (1) a double-pulse contact pulse-echo technique, which gives better resolution at room temperature with bulk samples, and (2) a magnetostrictive method for generating ultrasound in thin wires. The bulk samples were plates 1 in. square × 1/4 and 1/2 in. thick (25.4 × 6.4 and 12.7 mm), and the wire specimens were 1/16 in. in diameter × about 6 ft (1.6 mm × 1.8 m). These were fabricated from annealed 1-in.-thick commercial plate that had a carbon content of 0.135%. The experimental techniques and relationships between moduli and experimentally measured quantities were reported previously.[11]

*Laboratory Development, Y-12.

The results obtained on bulk samples of 2 1/4 Cr-1 Mo steel are as follows:

Velocities: longitudinal V_L = 5966, shear V_S = 3277, extensional V_E = 4622 m/sec;

Poisson's ratio: $\nu = 0.2840$;

Young's modulus: $E = 2.162 \times 10^{11}$ Pa = 3.135×10^7 psi;

Shear modulus: $G = 8.42 \times 10^{10}$ Pa = 1.221×10^7 psi;

Density: $\rho = 7839$ kg/m^3.

Measurements made at temperatures higher than 24°C (75°F) were normalized to data taken at 24°C by the more accurate block-sample method. The wire samples were heated at 10°C/min (18°F/min) to 788°C (1450°F); the tests were made in argon to prevent oxidation of the 2 1/4 Cr-1 Mo steel.

Data were gathered over two complete cycles of heating and cooling. Lower velocities and moduli were obtained on some of the determinations for decreasing temperatures below 150°C (300°F). This was because the sample was removed from the furnace to hurry cooling, causing the surface of the wire to cool off faster than the interior. Because these data points were suspect, they were given smaller weights in the analysis. The results of a typical run are shown graphically in Fig. 5.50.

The data from all four cycles (two heating and two cooling) were combined into a single set and fitted to cubic equations by regression analysis. Figure 5.51 presents the combined data for Young's modulus as a function of temperature with the curve for the best-fit equation superimposed. The individual sets of four data points are represented as mean and standard deviation values.

The equation is:

$$E(T) = E(T_0)[1 + A_E(T - T_0) + B_E(T - T_0)^2 + C_E(T - T_0)^3] \quad ,$$

where

T = temperature in °F,

T_0 = (75°F),

$E(T_0) = 31.35 \times 10^6$,

$A_E = (-2.64 \pm 0.08) \times 10^{-4}$,

$$B_E = (1.8 \pm 0.2) \times 10^{-7},$$
$$C_E = (-1.26 \pm 0.08) \times 10^{-10}.$$

The root mean square (rms) of the deviations of the calculated values from the experimental ones was 0.4%, and the maximum difference was 1.1%.

Note the modulus decreased characteristically with temperature. Also shown in Fig. 5.51 for comparison is Young's modulus determined by the static method (Pressure Vessel Code, Case 1331-8). The static values are only slightly lower than the dynamic ones to about 427°C (800°F) and then depart more and more at higher temperatures. This difference may be attributed in part to small plastic strain accompanying the elastic in the static measurements. Factors influencing the extent of plastic strain include level and duration of stressing and temperature. The first two factors, of course, would be negligible in the case of

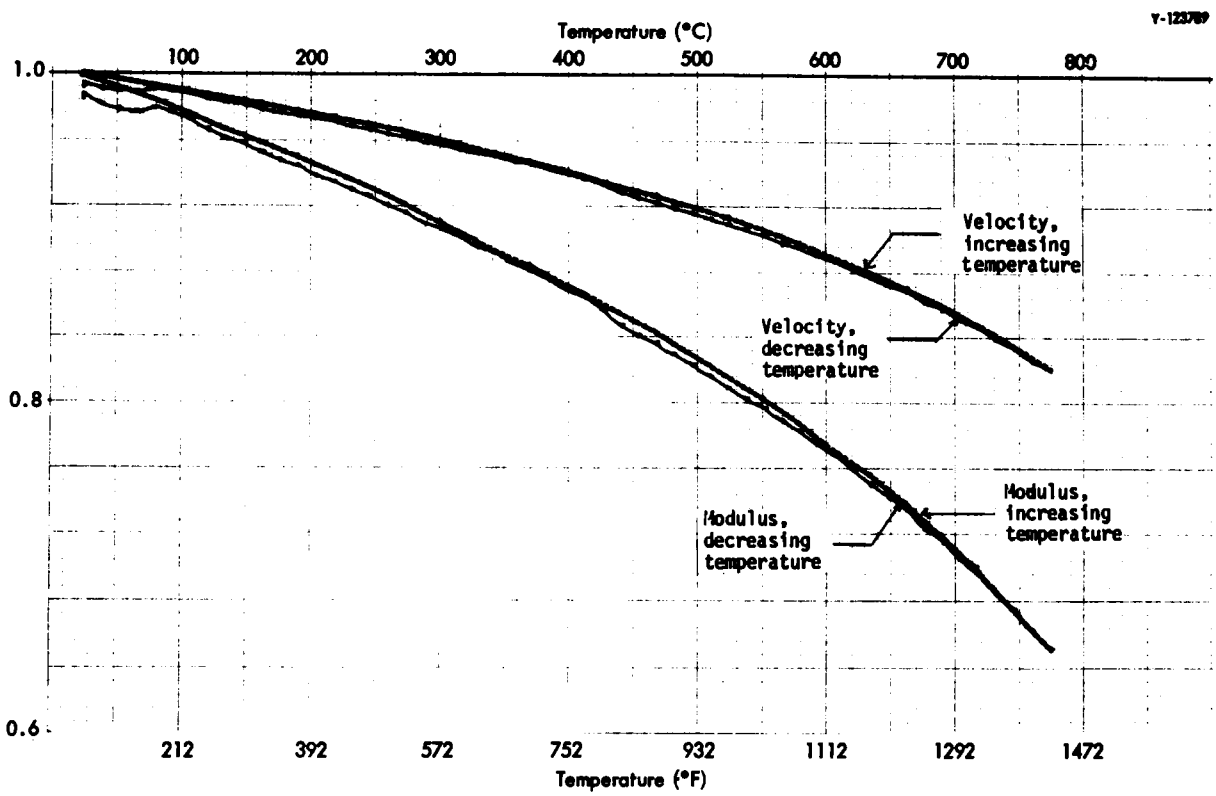

Fig. 5.50. Velocity and Young's Modulus Determinations for a Typical Run. Determinations are in ratios of elevated-temperature values to room temperature ones.

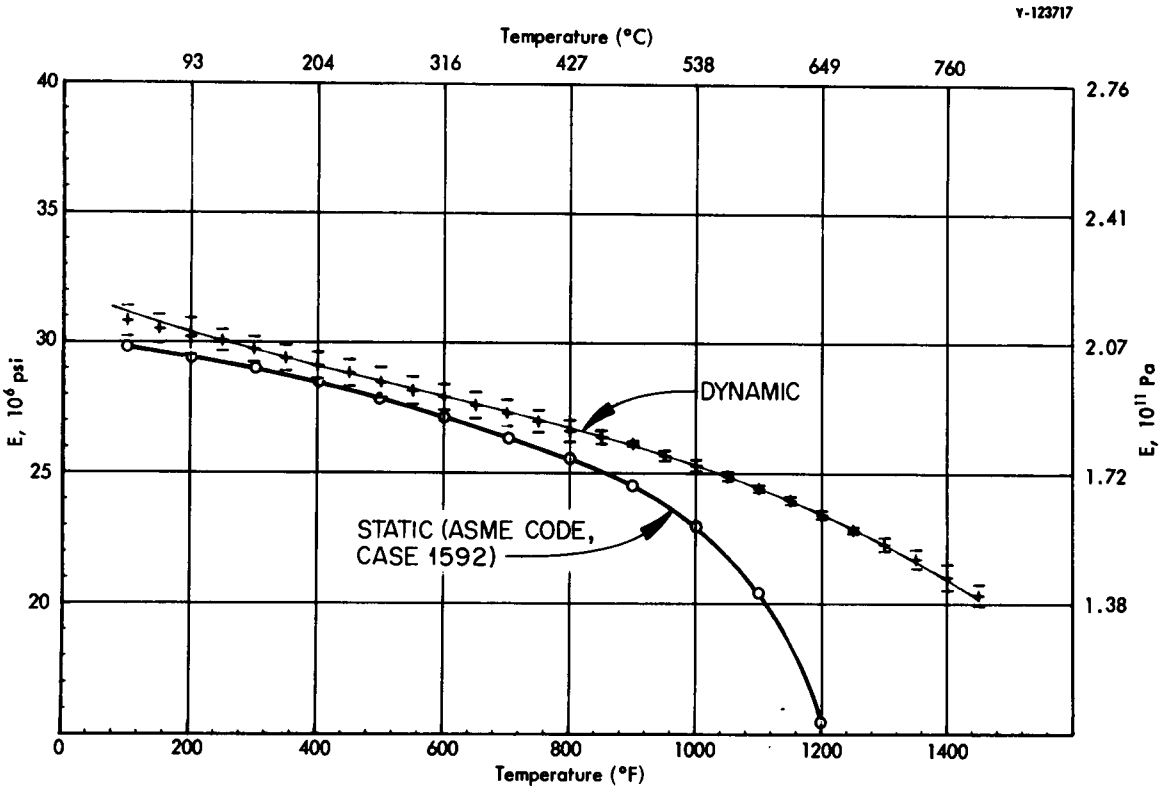

Fig. 5.51. Young's Modulus of 2 1/4 Cr-1 Mo Steel.

the dynamic (sonic) method, where wave frequency was high and the stress level never exceeded 1 psi. With negligible stress level and duration, raising temperature would not be expected to influence plastic strain (lowering of modulus) as much for measurements made by the dynamic method as with the static.

The experimental data for the dynamic shear modulus (two runs) were examined similarly by regression analysis. The mean and standard deviation values are shown in Fig. 5.52 with the curve for the best-fit equation superimposed. The equation is:

$$G(T) = G(T_0)[1 + A_G(T - T_0) + B_G(T - T_0)^2 + C_G(T - T_0)^3] \quad ,$$

where

$$G(T_0) = 12.21 \times 10^6$$

$$A_G = (-9.2 \pm 0.7) \times 10^{-5},$$

$$B_G = (-2.1 \pm 0.2) \times 10^{-7},$$

$$C_G = (7 \pm 1) \times 10^{-11}.$$

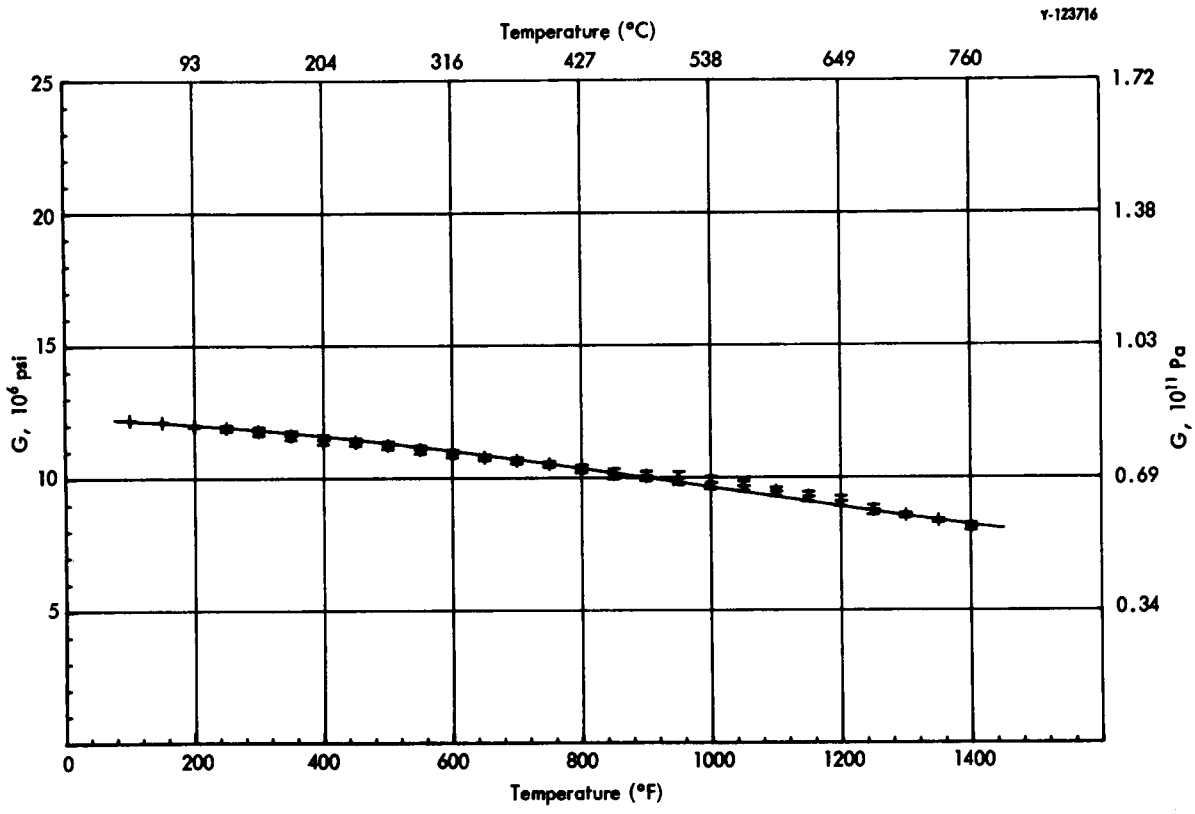

Fig. 5.52. Shear Modulus of 2 1/4 Cr-1 Mo Steel.

The rms of the deviations of the calculated values from the experimental ones was 1.0%, and the maximum difference was 2.1%. Again the modulus decreased with temperature but not as much as for Young's modulus.

Values of Poisson's ratio were determined from the preceding dynamic moduli data by the relationship:

$$\nu = E/2G - 1 \quad .$$

These data are represented graphically in Fig. 5.53, and the best-fit equation is:

$$\nu(T) = A_\nu + B_\nu T + C_\nu T^2 + D_\nu T^3 \quad ,$$

where

$A_\nu = 0.259 \pm 0.005,$

$B_\nu = (0.2 \pm 2.9) \times 10^{-5},$

$C_\nu = (7 \pm 5) \times 10^{-8},$

$D_\nu = (-3.5 \pm 2.1) \times 10^{-11}.$

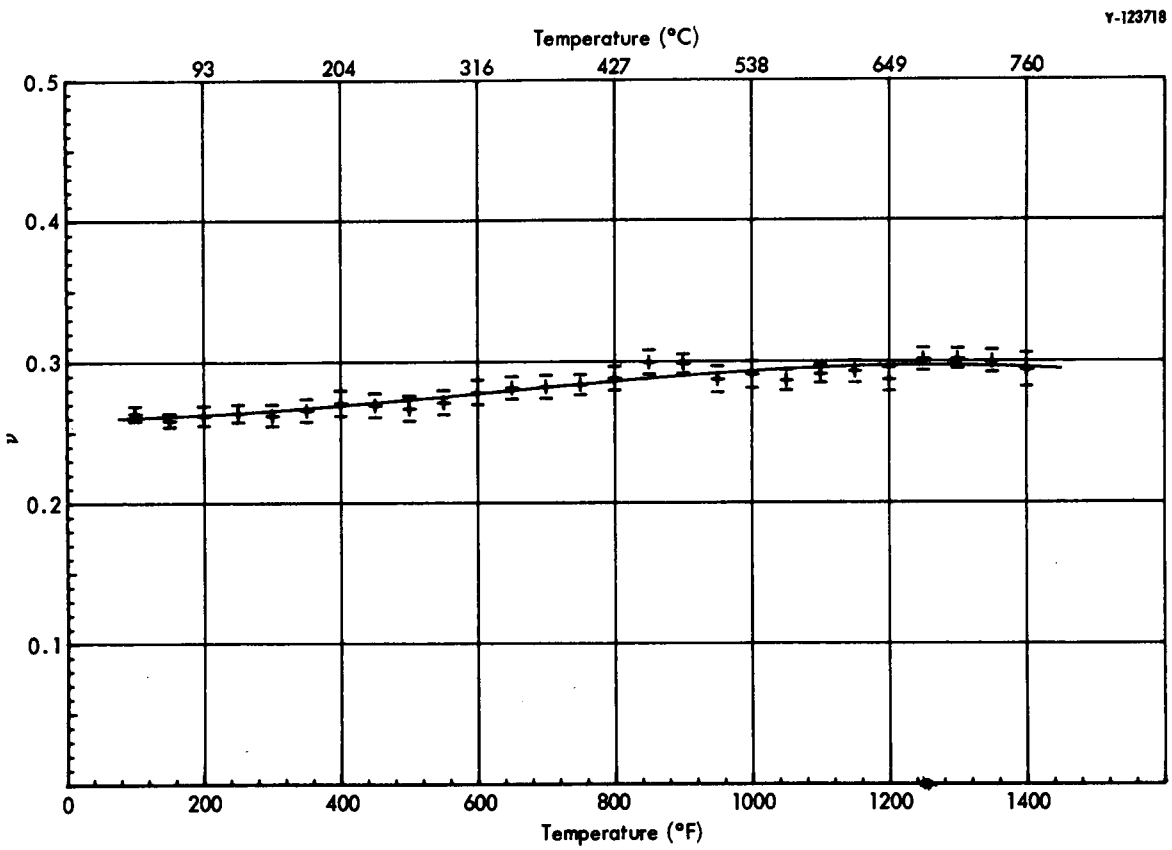

Fig. 5.53. Poisson's Ratio of 2 1/4 Cr-1 Mo Steel.

The rms of the deviations of the calculated values from the experimental ones was 1.6%, and the maximum difference was 3.9%.

Values of the dynamic Young's and shear moduli and Poisson's ratio calculated at 28°C (50°F) intervals are given in Table 5.24. Values of the static Young's modulus as a function of temperature, taken from the ASME Code, Case 1592, are given in Table 5.25.

5.2.6 Analytical Studies of Mechanical Properties Testing — B. R. Dewey*

We have commenced mechanics investigations pertaining to several facets of mechanical properties testing. Our goal is to provide support in (1) the design of specimens and instrumentation, (2) the interpretation of test results, and (3) the development of data in forms useful for subsequent application in design. To this end, we are engaged in a number of diverse projects.

---

*Subcontractor from Department of Engineering Science and Mechanics, University of Tennessee, Knoxville.

Table 5.24. Elastic Constants of 2 1/4 Cr-1 Mo Steel Calculated at 50°F (28°C) Intervals

Temperature		Young's Modulus, E		Shear Modulus, G		Poisson's Ratio, ν
(°C)	(°F)	(psi)	(GPa)	(psi)	(GPa)	
24	75	31.35×10^6	216.2	12.21×10^6	84.2	0.284
38	100	31.15	214.8	12.18	84.0	0.260
66	150	30.76	212.1	12.11	83.5	0.261
93	200	30.39	209.5	12.03	82.9	0.262
121	250	30.05	207.2	11.94	82.3	0.263
149	300	29.72	204.9	11.84	81.6	0.265
177	350	29.41	202.8	11.72	80.8	0.267
204	400	29.11	200.7	11.60	80.0	0.268
232	450	28.81	198.6	11.47	79.1	0.270
260	500	28.52	196.6	11.33	78.1	0.273
288	550	28.24	194.7	11.19	77.2	0.275
316	600	27.95	192.7	11.03	76.0	0.277
343	650	27.67	190.8	10.87	74.9	0.279
371	700	27.37	188.7	10.71	73.8	0.281
399	760	27.07	186.6	10.54	72.7	0.283
427	800	26.75	18.44	10.37	76.5	0.285
454	850	26.42	182.2	10.19	70.3	0.287
482	900	26.07	179.7	10.01	69.0	0.289
510	950	25.70	177.2	9.83	67.8	0.291
538	1000	25.31	174.5	9.65	66.5	0.293
566	1050	24.89	171.6	9.47	65.3	0.294
593	1100	24.44	168.5	9.28	64.0	0.295
621	1150	23.95	165.1	9.10	62.7	0.296
649	1200	23.43	161.5	8.92	61.5	0.297
677	1250	22.87	157.7	8.74	60.3	0.297
704	1300	22.27	153.5	8.57	59.1	0.297
732	1350	21.63	149.1	8.39	57.8	0.296
760	1400	20.94	144.4	8.23	56.7	0.296
788	1450	20.20	139.3			

Table 5.25. Static Young's Modulus of 2 1/4 Cr-1 Mo Steel (ASME Code, Case 1592)

Temperature		*E*, Young's Modulus	
(°C)	(°F)	(psi)	(GPa)
24	75	29.9×10^6	206
93	200	29.5	203
149	300	29.0	200
204	400	28.6	197
260	500	28.0	193
316	600	27.4	189
371	700	26.6	183
427	800	25.7	177
482	900	24.5	169
538	1000	23.0	159
593	1100	20.4	141
649	1200	15.6	108

5.2.6.1 Investigation of Bending in an Axially Loaded Specimen

Some evidence has been seen from time to time that suggests that bending strain is present in axially loaded specimens such as those in creep tests. That bending strain causes scatter in the results of a tensile test has been recognized for a long time.[12] Apparently bending is induced by nonsymmetry in the load train and by imperfection in the specimen. Measured bending strains also may be influenced by inaccuracy in the strain gaging.

From the following analysis it will be apparent that at least two strain gages are needed to determine the nominal strain when bending is present, that at least three strain gages are needed to determine the maximum and minimum bending strains, and that four strain gages are recommended to give a check against strain-gaging errors.

We assume that the four gages are mounted at 90° stations around the circumference at a given plane section. With the four gages designated 1, 2, 3, 4 and arranged counterclockwise, the average strain ε_{av}

is given by

$$\varepsilon_{av} = \frac{\varepsilon_1 + \varepsilon_2 + \varepsilon_3 + \varepsilon_4}{4} = \frac{\varepsilon_1 + \varepsilon_3}{2} = \frac{\varepsilon_2 + \varepsilon_4}{2} \quad , \tag{1}$$

where ε_1, ε_2, ε_3, ε_4 are the strain readings from the four gages. As seen from Eq. (1), two gages at opposite ends of a diameter are necessary to determine the average strain; an additional two gages give a check of this result. Of course, if all four readings are subject to random error, the result would be more accurate if all four were averaged.

Three of the four gage readings may also be used to determine the maximum and minimum strains developed on the surface of the specimen, and the location of these extrema. If we let the extrema be located on a diameter making an angle θ (positive counterclockwise) with the 1-axis,

$$\varepsilon_{max,min} = \varepsilon_{av} \pm (\varepsilon_1 - \varepsilon_{av})\cos\theta \pm (\varepsilon_2 - \varepsilon_{av})\sin\theta \quad , \tag{2}$$

where

$$\theta = \tan^{-1} \frac{\varepsilon_2 - \varepsilon_{av}}{\varepsilon_1 - \varepsilon_{av}} \quad . \tag{3}$$

Thus, of course, it would only be in exceptional circumstances that the strain gage readings would give the maximum and minimum strains directly. To reduce bending, we suggest (1) that screw threads be replaced by more positive locating surfaces and (2) that universal centering joints be located as close as possible to the specimen itself.

5.2.6.2 Stress Analysis of the Hourglass Fatigue Specimen

A study of the stress and strain distributions in the hourglass-shaped fatigue specimen of 2 1/4 Cr-1 Mo steel is now in progress. An elastic finite-element analysis shows that the stress at the surface at the smallest section is some 3.3% higher than the nominal stress at that section or some 5.2% higher than the stress at the center of the specimen. Preliminary inelastic calculations for a nominal 0.5% strain show a favorable stress redistribution, whereby the stress on the outer surface is not more than 1.9% higher than that at the center of the specimen.

To check these inelastic results and to incorporate the effects of creep and relaxation we have begun to use the ORNL CREEP-PLAST code.[13] A complete report will be written when this study is completed.

5.2.6.3 Buckling Analysis of a Hollow Tubular Biaxial Specimen

A stability analysis of a hollow tubular specimen which can be subjected to simultaneous torsion and compression is presently in progress. The decrease of Young's Modulus, E, with temperature proportionally lowers the buckling load. Our preliminary findings show about equal chances for the specimen to buckle as a column (in the Engesser range) or to buckle locally as a shell. It also appears that the applied torsion also increases the likelihood of buckling.

5.3 MECHANICAL AND METALLURGICAL BEHAVIOR OF WELDMENTS FOR LMFBR — P. Patriarca, G. M. Slaughter, W. R. Martin, and C. R. Brinkman

5.3.1 Effect of Postweld Heat Treatment on the Tensile Properties of Type 308 Stainless Steel Weld Metal with Controlled Residual Elements — R. T. King and E. Bolling

Postweld heat treatments have been applied to austenitic stainless steel weldments to reduce residual stresses, to improve ductility, and to reduce susceptibility to sensitization.[14,15] Although the FFTF vessel weldments were not subjected to postweld heat treatment, the possibility was considered, and it may be considered for later LMFBR systems. We have, therefore, begun to investigate the effects of postweld heat treatment on the type 308 CRE stainless steel weld metal from welds that are prototypic of the longitudinal seam and girth welds of the FFTF. The mechanical properties results reported here are from a limited exploratory test series in which weld metal specimens of one type were annealed for 2 hr in the range from 982 to 1204°C (1800–2200°F). Metallographic examination of the failed specimens will be performed next.

The weld metal was taken from 1:1–1 welds,* and only L1 (longitudinal, all-weld-metal specimens from the surface region of the weld)[16] were used.

---

*Electrode batch 6 was used to join two plates of Heat 1, see R. T. King and G. M. Goodwin, *Fuels and Materials Development Program Quart. Progr. Rep. Sept. 30, 1972*, ORNL-TM-4055 pp. 5.14–5.16.

The tensile specimens had 0.25-in.-diam × 1.25-in.-long (6.4 × 31.8 mm) gage sections.[16] The postweld heat treatment was performed on individual specimens rather than on whole sections of the weldment. Specimens were annealed in air for 2 hr at 982, 1038, 1093, 1149, and 1204°C (1800, 1900, 2000, 2100, 2200°F) and then air-cooled. No significant distortion of the specimens occurred during heat treatment.

The specimens were tensile tested in air at room temperature at 0.004/min nominal strain rate on an Instron tensile testing machine. An averaging extensometer was attached to the center inch of the gage length, and the data from both the extensometer and Instron load-elongation curves were reduced by techniques that have been described previously.[17]

The tensile test data are in Table 5.26. The highest and lowest values measured[17] for as-welded specimens made with all the combinations of type 304 stainless steel base metal heats and type 308 CRE stainless steel electrodes are given for comparison. Data for postweld heat-treated specimens that fall outside the range of values for as-welded specimens are shown in italics. Unmarked italics designate values below the range for as-welded specimens, and an asterisk(*) denotes values above the range for as-welded specimens.

The engineering stress-strain curves of the as-welded[17] and post-weld-heat-treated 1:1—1 weld metal are compared in Fig. 5.54. The effects of postweld heat treatment on some strength and ductility measures are given in Figs. 5.55 and 5.56, respectively.

The following observations were made concerning the effects of postweld heat treatment in the range 982 to 1204°C (1800—2200°F) on room-temperature tensile properties of type 308 CRE stainless steel all-weld-metal specimens:

1. The elastic limit measured by averaging extensometers was greatly reduced from the 135 to 220 MPa (20—30 ksi) range to as low as 47 MPa (6.8 ksi).

2. The 0.2% offset yield stress was also greatly reduced, from the 310 to 345 MPa (45—50 ksi) range, to as low as 178 MPa (25.8 ksi).

3. The ultimate tensile strength decreased slightly.

4. All measures of ductility — the uniform strain, total elongation, and reduction of area — tended to increase.

Table 5.26. Room-Temperature Tensile Stress-Strain Properties of Type 308 CRE Stainless Steel Weld Metal After Various Post-Weld Heat Treatments[a]

Post-Weld Heat Treating Temperature		Instron Chart Measurements							Reduction of Area (%)	Diametral Strain						Extensometer Measurements, ksi[b]	
			Strength, ksi[b]				Strain, %			At Fracture			Away From Fracture				
(°C)	(°F)	Valve Type	Apparent Elastic Limit	0.2% Offset Yield	Ultimate	Fracture	Uniform	Total		Maximum (%)	Minimum (%)	Ratio[c]	Maximum (%)	Minimum (%)	Ratio[c]	Elastic Limit	0.2% Offset Yield Strength
As Welded	(high value)	Engineering	51.4	51.3	88.0	83.3	54.7	65.5	57.1	43.0	27.0	2.6	30.9	13.6	3.2	32.1	50.6
		True		51.4	136.1	185.2	0.44	0.85									
As Welded	(low value)	Engineering	33.8	45.1	82.8	79.4	40.8	41.3	31.8	22.8	10.6	1.5	21.4	6.7	2.0	19.6	45.6
		True		45.2	116.5	120.4	0.34	0.38									
982	1800	Engineering	*29.0*	*36.6*	84.0	*77.2*	*57.8**	*68.1*	51.3	42.3	19.9	2.1	27.5	11.9	2.3	*12.4*	*36.9*
		True		*36.9*	132.6	158.6	*0.46**	0.72									
1038	1900	Engineering	*29.6*	*34.5*	*81.6*	*72.1*	*58.9**	*66.0**	*61.8**	*43.8**	*33.1**	*1.3*	23.9	12.6	*1.9*	*18.3*	*34.3*
		True		*34.6*	129.7	*188.9**	*0.46**	*0.96**									
1093	2000	Engineering	*28.1*	*33.4*	*81.1*	*72.9*	*65.6**	*76.8**	*62.9**	*44.4**	*34.3**	*1.3*	23.8	10.5	2.3	*17.6*	*33.5*
		True		*33.4*	134.3	*194.0**	*0.50**	*0.99**									
1149	2100	Engineering	*22.8*	*26.9*	84.4	*66.6*	*74.6**	*84.2**	*71.0**	*51.2**	*41.5**	*1.2*	27.0	*18.9**	*1.4*	*13.0*	*26.8*
		True		*27.0*	*147.4**	*236.7**	*0.56**	*1.24**									
1204	2200	Engineering	*22.8*	*25.9*	*79.5*	*72.2*	*58.9**	64.2	*59.8**	39.5	*33.8**	*1.2*	22.6	11.3	2.0	*6.8*	*25.8*
		True		*25.9*	126.3	179.9	*0.46**	*0.91**									

[a]Values for aged specimens below the range for as-welded specimens are shown in italics. Values above the range are in italics and marked with *.

[b]1 ksi = 6.895 MPa.

[c]Where data are available from more than one specimen, the low and high extreme values are given. The diametral strain ratios are the extremes for ratios for individual specimens, not ratios of the extreme values for all specimens.

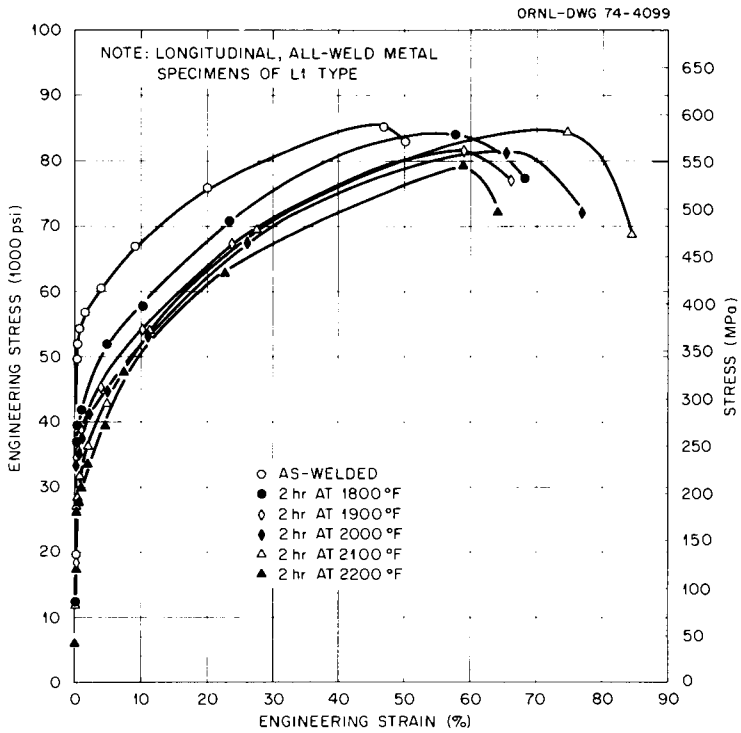

Fig. 5.54. Engineering Room-Temperature Tensile Stress-Strain Behavior of Type 308 CRE Stainless Steel After Various Postweld Heat Treatments.

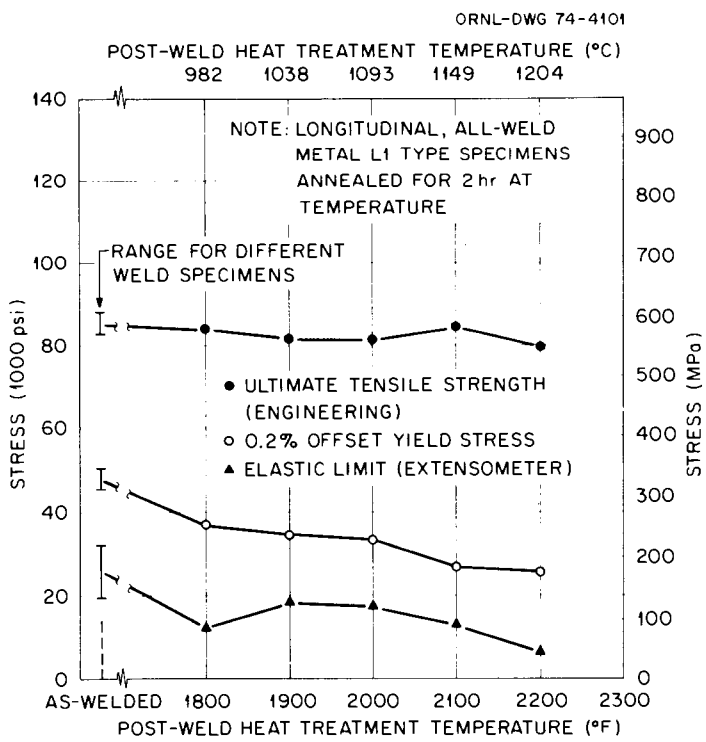

Fig. 5.55. Effect of Postweld Heat Treatment Temperature on the Room-Temperature Strength Properties of Type 308 CRE Stainless Steel Weld Metal.

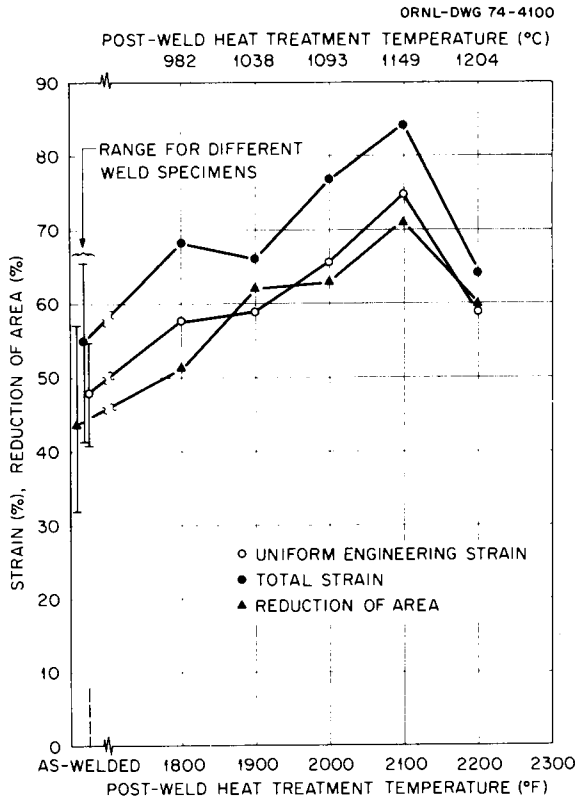

Fig. 5.56. Effect of Postweld Heat Treatment Temperature on the Room-Temperature Strain Measures of Type 308 CRE Stainless Steel Weld Metal.

5. The ratio of maximum to minimum diametral strain at the point of fracture is a measure of anisotropy that was reduced by postweld heat treatment. However, the same ratio measured away from the necked region is a measure of anisotropy of plastic deformation at somewhat lower strains; the decrease in this value after postweld heat treatments is not as great as that at fracture.

The decrease in the room-temperature yield strength for postweld heat treatment above 1093°C (2000°F) is important for engineering code purposes. ASME Boiler and Pressure Vessel Committee Code Case 1331-8 and present drafts of proposed ASME Code Case 1592 give the minimum yield strength at room temperature for type 304 stainless steel base metal as 207 MPa (30 ksi). Postweld heat-treating the type 308 CRE stainless steel weld metal for 2 hr at 1149 or 1204°C (2100 or 2200°F) reduced the weld metal yield strength to or below 178 MPa (25.8 ksi), or below the allowable stress for base metal. This information should be considered

in setting the allowable range of postweld heat treatment temperatures for this weld metal.

5.3.2 Creep and Creep-Rupture Properties of Type 308 CRE Stainless Steel Weld Metal From the FFTF Vessel Test Welds — R. T. King and E. Bolling

Long-time creep tests are in progress for as-deposited longitudinal all-weld metal specimens of type 308 stainless steel with controlled residual elements (CRE). These tests are the backbone of a design data matrix aimed at elevated-temperature applications. The welds are prototypic of the longitudinal seam and girth welds in the FFTF vessel. This portion of the data matrix was reviewed at an earlier stage in detail in a previous report.[18]

The data are aimed at two fundamental problem areas:

1. ASME engineering codes for design and construction of nuclear components and systems to operate in the creep range do not refer specifically to the properties of weldments. These data will form part of a data base for the material, and they are necessary for analyzing time-dependent deformation in these weldments.

2. Conventional type 308 stainless steel weld metal has low long-time creep ductility in the temperature range where sigma phase forms. These results demonstrate that the addition of controlled amounts of the residual elements B, P, and Ti lead to improved ductility.[18]

The specimen preparation and test methods have already been described in detail.[16,19] The weld metal exhibits (1) variation in properties through the thickness of the weld test plate, and (2) directionality or anisotropy of deformation behavior. The results are, therefore, organized to facilitate identification of specimen location and orientation in the weld. The longitudinal L1, L2, and L3 all-weld-metal specimens are from the surface passes, intermediate locations in the weld metal, and the root pass regions, respectively.

A number of fundamental results are summarized in Table 5.27, including the strains during loading ($\varepsilon_{loading}$), primary ($\varepsilon_{Stage\ I}$), secondary, and tertiary creep (both by departure from linearity and the 0.2% strain offset method, $\varepsilon_{Stage\ II(real)}$, $\varepsilon_{Stage\ III(real)}$, $\varepsilon_{Stage\ II(offset)}$,

Table 5.27. Creep Behavior of Type 308 CRE Stainless Steel Weld Metal

Test Temperature (°C)	Test Temperature (°F)	Specimen Type	Stress (ksi)	Stress (MPa)	Strain, % Loading ε_L	Strain, % $\varepsilon_{Stage\ I}$	Strain, % $\varepsilon_{Stage\ II}$ Real	Strain, % $\varepsilon_{Stage\ II}$ Offset	Strain, % $\varepsilon_{Stage\ III}$ Real	Strain, % $\varepsilon_{Stage\ III}$ Offset	Strain, % Rupture ε_r	Strain Rate, %/hr $\dot{\varepsilon}_{Stage\ II}$ Real	Strain Rate, %/hr $\dot{\varepsilon}_{Stage\ II}$ Offset	Strain Rate, %/hr ε_r/t_r	Reduction of Area (%)	Rupture Time, t_r (hr)	t_{III}/t_r[a]
482	900	L1	57.5	396							39.45				46.2	~0	
			55.0	379	14.965	~0	0.021	0.049	14.61	14.59	29.6	1.5×10^{-4}	2.6×10^{-4}	0.032	41.5	913.8	0.36
			55.0	379	12.16	~0	0.11	0.365	23.74	23.54	36.16	5.53×10^{-4}	1.22×10^{-3}	0.0414	57.7	873.0	0.34
			50.0	345	5.84	0.01	0.26	0.367	18.17	18.06	24.28	4.33×10^{-4}	4.59×10^{-4}	0.0126	52.3	1,921.9	0.42
			45.0	310	1.65	0.08	0.17	0.581	19.2	18.79	21.6	9.19×10^{-4}	1.4×10^{-3}	0.00319	31.7	6,764.7	0.06
			40.0[b]	276	1.05	0.05	0.05	0.285			>9.12	2.17×10^{-4}	7.31×10^{-4}			>18,448.7	<0.04
		L2	57.5	396	6.915	~0	0.745	1.094	12.66	12.3	20.32	5.96×10^{-3}	7.29×10^{-3}	0.0596	15.7	341.1	0.44
			55.0	379	3.2	~0	0.22	0.438	18.66	18.44	22.08	7.33×10^{-4}	1.34×10^{-3}	0.0448	28.2	492.4	0.66
			50.0	345	2.8	~0	0.5	0.767	24.62	24.35	27.92	1.33×10^{-3}	1.80×10^{-3}	0.0117	c	2,394.6	0.18
			45.0	310												>1,008.2	
		L3	60.0	414							31.32				43.4	~0	
			57.5	396	8.003	0.097	0.72	1.07	16.0	15.7	24.84	7.58×10^{-3}	9.3×10^{-3}	0.082	48.7	303.2	<0,40
			55.0	379	9.24	0.05	0.78	1.00	16.97	16.75	27.04	7.28×10^{-3}	9.34×10^{-3}	0.076	35.9	353.9	0.40
			50.0	345	0.66	0.12	0.47	0.97	10.93	10.43	12.2	1.67×10^{-3}	3.23×10^{-3}	0.00505	63.6	2,416.8	0.25
			45.0	310							>5.8					>9,162.2	
			40.0	276	0.185	0.26						$\sim 1.06 \times 10^{-5}$				>10,000.0[d]	
566	1050	L1	37.0	255	3.5	8.0	6.8	7.66	14.58	13.72	32.88	3.3×10^{-1}	3.44×10^{-1}	0.484	65.3	67.9	0.57
			35.0	241	2.0	5.8	10.2	12.2	18.04	16.04	30.24	1.5×10^{-1}	1.52×10^{-1}	0.217	53.7	139.6	0.75
		L2	37.0	255	0.25	1.35	1.7	2.43	15.5	14.77	18.8	7.08×10^{-3}	7.72×10^{-3}	0.0267	49.2	703.8	0.53
			35.0[e]	241		<0.9	1.6	2.12	11.38	10.86	14.08	2.91×10^{-3}	3.21×10^{-3}	0.0107	49.5	1,311.3	0.57
					~2	~2.0	~1.2	1.56	17.72	17.36	21.92	1.6×10^{-3}	1.84×10^{-3}	0.00789	c	2,779.7	0.49
		L3	37.0	255	~0.25	9.95	1.5	2.15	25.54	24.89	28.24	3.75×10^{-3}	4.13×10^{-3}	0.0236	49.6	1,195.4	0.52
			35.0	241	~0.30	0.6	0.3	0.554	12.64	12.39	13.84	9.84×10^{-5}	1.54×10^{-4}	0.00187	32.0	7,417.9	0.64

Table 5.27. (Continued)

Test Temperature (°C)	Test Temperature (°F)	Specimen Type	Stress (ksi)	Stress (MPa)	Strain, % Loading ε_L	Strain, % $\varepsilon_{Stage\ I}$	Strain, % $\varepsilon_{Stage\ II}$ Real	Strain, % $\varepsilon_{Stage\ II}$ Offset	Strain, % $\varepsilon_{Stage\ III}$ Real	Strain, % $\varepsilon_{Stage\ III}$ Offset	Strain, % Rupture ε_r	Strain Rate, %/hr $\dot{\varepsilon}_{Stage\ II}$ Real	Strain Rate, %/hr $\dot{\varepsilon}_{Stage\ II}$ Offset	ε_r/t_r	Reduction of Area (%)	Rupture Time, t_r (hr)	t_{III}/t_r [a]
593	1100	L1	35.0	241	3.17	1.33	31.5	32.73	19.32	18.09	55.32	2.58	2.60	2.99	65.6	18.5	0.70
			33.0	228	0.69	1.46	7.05	8.36	26.56	25.1	35.76	2.47×10^{-1}	2.53×10^{-1}	0.488	49.9	73.3	0.52
			30.0	207	~2.0	8.25	3.75	4.53	12.24	11.46	26.24	5.77×10^{-2}	6.04×10^{-2}	0.111	54.6	236.4	0.59
			28.0	193	0.291	1.37	0.84	1.08	25.18	24.9	27.68	1.5×10^{-3}	1.95×10^{-3}	0.0148	58.1	1,873.9	0.40
			25.0	172	0.1	0.5	0.4	0.816	25.22	24.8	26.12	392×10^{-4}	5.20×10^{-4}	0.00829	64.0	3,152.5	0.52
			22.5	155	<0.20						>0.684					>11,104.0	
		L2	35.0	241	0.44	0.31	4.25	6.81	27.64	25.08	30.64	9.4×10^{-1}	9.7×10^{-1}	0.804	60.3	38.1	0.20
			33.0	228	0.34	1.46	2.2	2.93	19.92	19.19	23.92	8.8×10^{-3}	9.44×10^{-3}	0.0392	35.5	610.2	0.59
			30.0	207	0.249	0.28	0.69	0.91	20.48	20.26	21.7	3.7×10^{-4}	4.9×10^{-4}	0.0049	53.1	4,446.3	0.54
			28.0	193	0.251	0.219	0.695	1.11	20.9	20.5	22.08	2.8×10^{-4}	3.5×10^{-4}	0.0042	54.8	5,284.0	0.61
		L3	35.0	241	0.335	0.26	0.694	1.02	23.75	23.6	25.04	0.0191	0.024	0.291	48.1	86.0	0.55
			33.0	228	0.4	0.35	1.25	1.81	19.44	18.88	21.44	8.06×10^{-3}	9.06×10^{-3}	0.0485	52.2	441.9	0.51
			30.0	207	0.2	0.17	0.85	1.08	16.86	16.63	18.08	5.15×10^{-4}	6.35×10^{-4}	0.00648	47.9	2,791.2	0.63
			28.0	193	0.12	0.15					>0.738	$\sim 2.8 \times 10^{-5}$				>16,770.6	
649	1200	L1	28.0	193	<0.2	0.05	0.25	0.46	37.58	37.38	38.08	1.67×10^{-2}	2.92×10^{-2}	1.614	54.4	23.6	0.68
			22.0	152	0.197	1.111	0.26	0.53	44.03	43.76	43.30	8.11×10^{-4}	1.30×10^{-3}	0.0552	c	785.0	0.52
			20.0	138	0.18	0.24	0.37	0.69	19.7	19.6	20.5	2.47×10^{-4}	3.5×10^{-4}	0.0079	60.5	3,249.4	0.68
		L2	28.0	193	0.25	0.15	0.6	0.95	19.79	19.19	20.79	1.24×10^{-2}	1.56×10^{-2}	0.213	59.6	97.5	0.64
			22.0	152	0.005	0.112	0.161	0.43	15.3	15.1	15.6	4.05×10^{-5}	7.6×10^{-5}	3.03×10^{-3}	45.8	6,425.1	0.88

[a] t_{III} = time to third-stage creep.

[b] Curve shape irregular.

[c] Not available for measurement.

[d] Test terminated before rupture.

[e] Two analyses of results.

$\varepsilon_{\text{Stage III(offset)}}$, respectively, the minimum creep rate [$\dot{\varepsilon}_{\text{Stage II(real)}}$], the creep rate averaged between the end of primary and onset of 0.2% offset teritary creep [$\dot{\varepsilon}_{\text{Stage II(offset)}}$], the average creep rate for the test (ε_r/t_r, or rupture strain/time to rupture), the reduction of area, and the fraction of the total rupture time before tertiary creep ($t_{\text{III, offset}}/t_r$). Interpretation of the data is in progress.

5.3.3 Deformation Characteristics of Whole Weldment Cross Sections — R. G. Berggren and R. T. King

An important goal of the Welding Development Program is to define the nature and magnitude of stress and strain concentrations that occur in weldments over temperatures ranging from room temperature to the upper temperature limits for pressure boundaries in Liquid Metal Fast Breeder Reactors. This information should be factored into engineering codes for design and construction of nuclear systems. We believe that modern technology is not capable of analyzing these stress and strain concentrations on strictly theoretical grounds, nor are there means for accurate experimental monitoring of the stress and strain distributions within a thick weldment during a test at elevated temperatures. However, limited computation and certain complementary types of experimental measurements can provide at least some of the desired information.

We are now performing preliminary tensile tests on whole-weld cross sections cut from the test shielded metal-arc welds made with type 308 CRE stainless steel electrodes. The welds are prototypical of the longitudinal girth and seam welds of the FFTF. The tests have been limited to room temperature, but elevated-temperature tests will be initiated soon. Several qualitative or semiquantitative techniques for determining local stress and strain concentrations in these specimens have been used at room temperature, including brittle lacquer coatings, the birefringent Photostress plastic overlay, and extensometry techniques. The qualitative information will be used to select critical areas of stress and strain concentration, where strain gages will be mounted in a final room-temperature tensile test. This report covers the results of the qualitative or semiquantitative tests.

Two preliminary tests were run using a specimen design that has been improved for later tests. The specimens were made by cutting a 0.63 cm × 6.0 cm (0.25 in. × 2.375 in.) cross-section slab from the test weld with the weld in the center of the slab. End pieces for gripping were then welded to the slab, and a 15.2-cm (6.0-in.) gage length was machined into the assembly. The specimens were then tested on a 60,000-lb Tinius Olson machine under load control at room temperature. The tests were stopped at multiples of 1000-lb load for observations. The first specimen had a brittle lacquer coating, while the second had brittle lacquer on one side of the gage section and Photostress plastic on the other side. The Photostress plastic provided results that were more readily interpreted than did the brittle lacquer. These results are sufficiently similar to those obtained from the test on the third specimen, which had an improved design, that they will not be discussed.

Some post-test measurements are of interest, though. The second test specimen was subjected to a maximum nominal stress of 502 MPa (72.8 ksi) during the test. The measured 0.2% yield stress for longitudinal all-weld-metal specimens is 234–470 MPa (34–68 ksi), and the ultimate stress is 570–680 MPa (83–99 ksi), while the appropriate as-received type 304 stainless steel base metal yield and ultimate tensile strengths are 280 and 620 MPa (40.7 and 90 ksi). Thus, the specimen experienced gross plastic straining during the test. After the test, a grid was marked on the specimen, and a micrometer with 5.1-mm-diam (0.20-in.) ball heads was used to measure the final specimen thickness at the grid intersections. The changes in thickness that occurred were converted to linear strains in the thickness direction for the assumption that the original specimen thickness was uniformly 6.4 mm (0.250 in.). These strains are indicated at each grid point in Fig. 5.57. The width of the specimen was also measured, and the overall width strains are also indicated in Fig. 5.57 for each column of the grid.

The gage section of the specimen had a uniform machined surface before the test. After the test, the weld metal region and weld metal

(Y-123864)

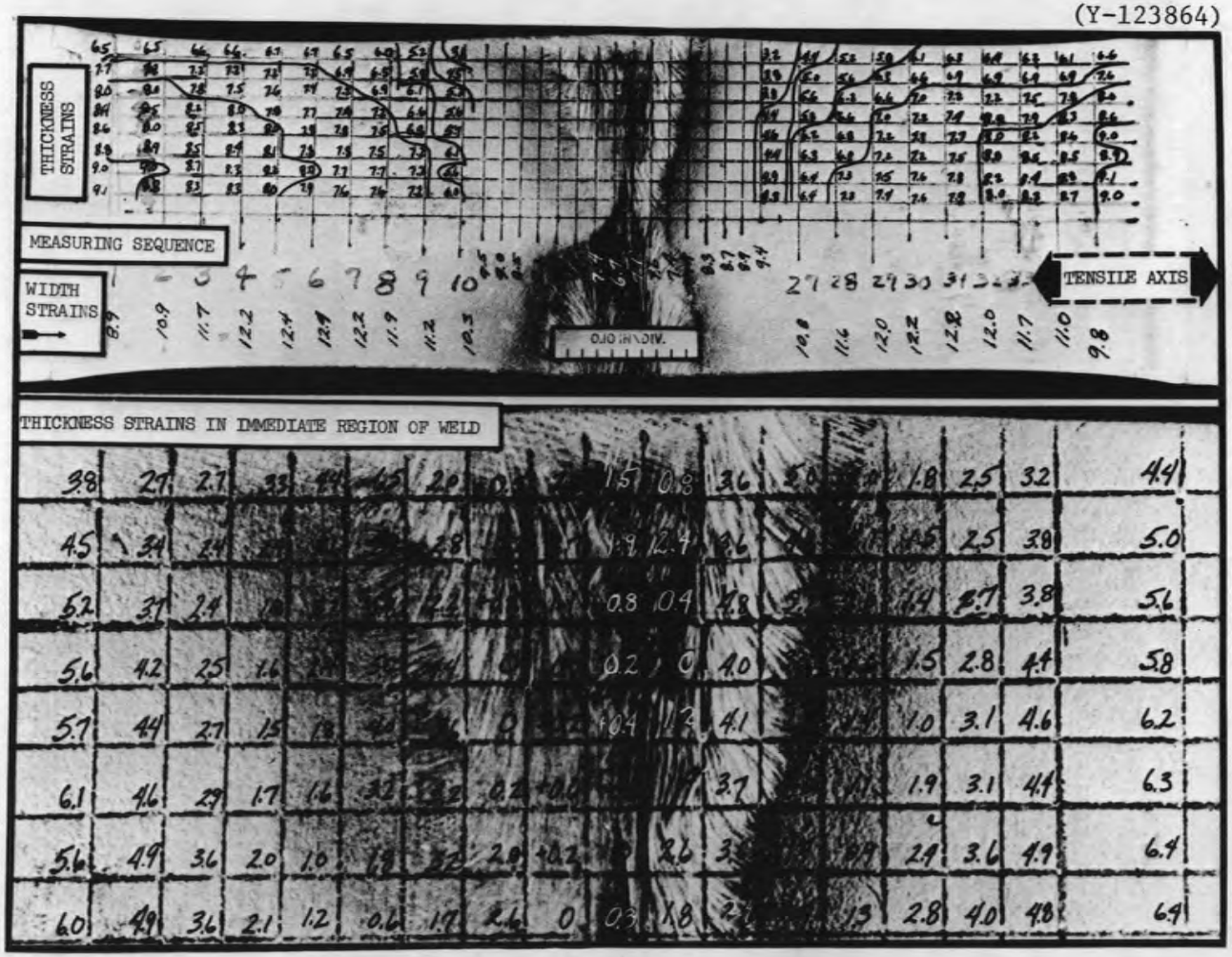

Fig. 5.57. Macrograph of Weldment Tensile Tested at Room Temperature, with Grid Points where Thickness Strains (%) and Grid Lines where Width Strains (%) were Measured. All strains are negative (reduction of dimension) except those specifically marked with a (+). Surface was machined finish before testing, not retouched after testing. Upper figure shows entire gage length; lower figure shows enlargement of immediate weld area.

substructure were clearly defined by the nonhomogeneous anisotropic plastic flow that occurred. The specimen surface shown in Fig. 5.57 has not been etched or otherwise altered after the test.

The following observations may be made from the data:

1. The as-received base metal away from the weld strained about 7 to 8% through the thickness, and about 12% in the width direction. The region near the grip was subjected to both a stress concentration effect near the fillet radius that is probably responsible for local thickness strains as large as 9%, and to the stiffening effects of the larger grip area that caused width strains to decrease near the grip.

2. The base metal strains near the weld were influenced by the stiffening effect of the stronger weld metal, and by the changes in properties (mainly an increase in the dislocation line density of the base metal and an increase in the yield strength)[20,21] that occurred in the "heat-affected zone."

3. Strains in the weld metal were nonuniform and highly directional, reflecting the heterogeneous and anisotropic flow behavior of the weld metal. Generally, the greatest strains through the width occurred in regions where the solidification direction in the plane of the specimen had a large component (treated as a vector) parallel to the tensile axis; strains as large as 5% occurred there. Where the solidification direction was essentially perpendicular to the tensile axis, the thickness strains were zero within the limits of uncertainty of about ±0.5%. The surface contour indicates that the width strains had a sharp maximum where the substructure was perpendicular to the weld surface.

4. The strains through the width exhibited sharp discontinuities at those interpass boundary regions where the substructure orientation changed sharply.

The third test was performed on a specimen of improved design, which had a pin-type grip to minimize bending. The gage and weld cross-section configuration remained the same. An extensometer was attached to each side of the specimen, spanning the middle 127 mm (5 in.) of the gage length. A 3.2 mm-thick (1/8-in.) sheet of Photostress plastic was applied to one side of the gage section, and brittle lacquer was applied to the other side. A camera was positioned to view the Photostress plastic.

The tensile load was applied to the specimen incrementally on the 60,000-lb Tinius Olson machine, with periodic halts in loading to photograph the Photostress plastic under polarized light, and to examine the lacquer. The maximum load applied produced an averaged cross-section stress of 313 MPa (45,500 psi).

The nominal stress is plotted against the strain measured on each extensometer in Fig. 5.58. At nominal stresses below about 172 MPa (25 ksi), no time-dependent deformation of the specimen was observed during the periods when the load was held constant and data were being acquired. Above 172 MPa, noticeable deformation occurred while the load was held constant, causing "plateaus" in the stress-strain curve. Most of the time-dependent deformation occurred in the base metal.

At stresses below about 172 MPa, the deformation measured with the extensometers was essentially linear with stress. The calculated elastic

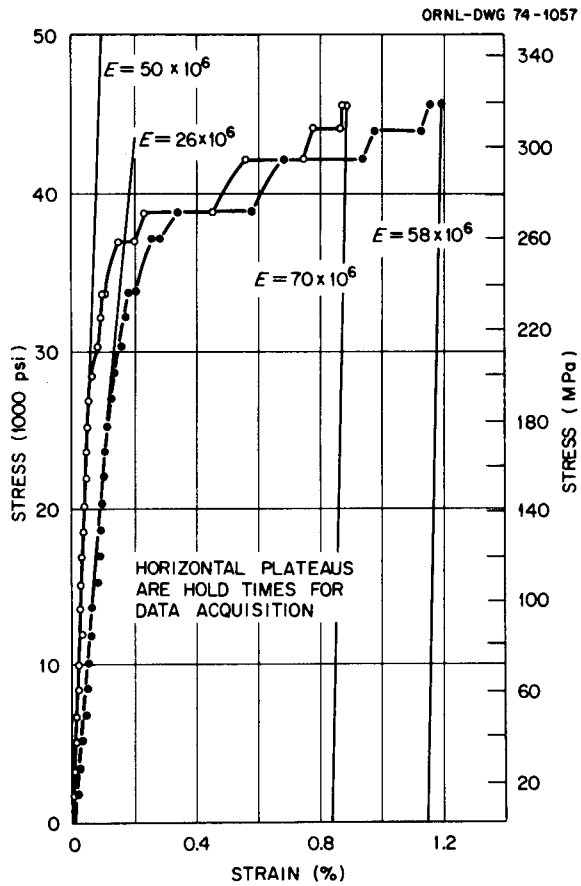

Fig. 5.58. Stress-Elongation Data from Extensometers on Full-Cross-Section FFTF Vessel Test Weld, Tensile Tested at Room Temperature.

moduli from the two extensometers were about 179 and 345 GPa (26×10^6 and 50×10^6 psi). The room-temperature modulus expected for type 304 stainless steel base metal[22] is about 193 GPa (28×10^6 psi). The results from the full weld cross section are difficult to interpret because of the composite nature of the specimen. We are now performing experiments to determine the static and dynamic elastic properties of the weld metal.

The Photostress plastic, viewed under appropriate conditions with polarized light, exhibits colors that are related to the maximum shear stress (or the difference between the maximum principal tensile stresses) in the plane of the surface to which it is attached. Figure 5.59 shows photographs of the Photostress plastic when the nominal stress in the specimens was 232 MPa (33.7 ksi), slightly above the yield stress for the base metal but probably not above the yield stress of the weld metal; 255 MPa (37 ksi), the stress at which time-dependent plastic deformation was first noticed during a holding period; and 290 MPa (42.1 ksi), a stress at which much time-dependent deformation occurred during the deformation period. The grid and outline of the weld were drawn on the plastic before the test to serve as reference marks; the springs holding the extensometers to the specimens can be seen.

At 232 MPa (33.7 ksi) in Fig. 5.59(a), the maximum shear strain distribution is clearly nonuniform throughout the weldment. Isoshear strain contours of the same magnitude exist at about reference marks 3 and 8 and in the weld metal at points near reference marks 5 and 6. The highest strains occurred in the base metal near the grips, in agreement with the earlier observations of thickness and width plastic strains on a highly deformed specimen. The lowest local shear strains occurred in an "X"-shaped region near the center of the weld. The difference in magnitude between the peak and local minimum shear strain values is about 0.07% at an overall gage strain of 0.1 to 0.2%.

At higher stresses [Fig. 5.59(b) and (c)], the local shear strain concentrations in the weld metal are less evident. The dominant feature is a minimum in the shear strain pattern near the center of the weld. This behavior is consistent with the results of room-temperature tensile tests on small samples of weld metal, which showed the root passes of the weld metal to have higher yield and ultimate tensile strengths than the surface passes.

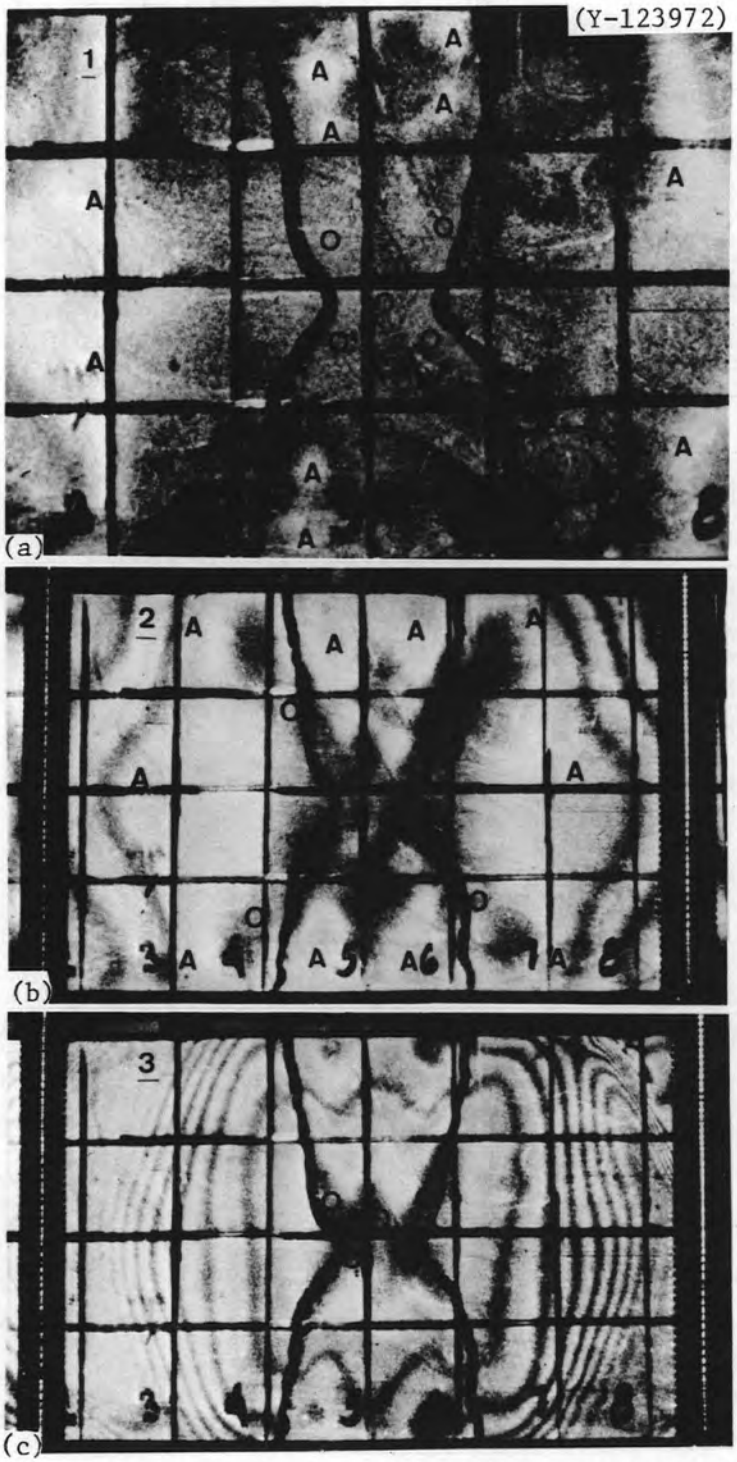

Fig. 5.59. Black and White Reproductions of Color Photographs of Photoelastic Plastic on Weldment Specimens. See text for details of test conditions. Contours labeled "O" are minimum shear strain within weld metal, contours labelled "A" are maximum shear strain within weld metal and the same strain in base metal. Maximum shear strain tends to increase going away from the weld in base metal regions shown.

Another important observation was made by changing the polarized light and viewing filters to reveal the axes of principal strain. These deviated from the tensile axis by as much as 6 to 12° at high stresses, probably because of the anisotropic flow characteristics of the weld metal.

We suspect that the discontinuities in weld substructure and solidification direction that occur at some parts of the interpass boundaries play and important role in creating stress and strain concentrations within the weld metal. At such discontinuities, the principal axes of anisotropy of the weld metal change suddenly, terminating certain "easy flow" directions. The discontinuity stresses that arise are somewhat analogous to those that occur at grain boundaries, where the Burgers' vector suddenly changes. The severity of this effect is shown in Fig. 5.60, taken of the second specimen (which had large width and thickness strains) under lighting conditions that highlighted the surface contours caused by anisotropic deformation. At some points near the fusion line, the substructure in a given pass is rotated nearly 90° relative to the substructure of an adjacent pass. Severe discontinuities in the strain distribution occurred near such points.

These results must be contrasted with the stress and strain distribution predicted by a simple finite-element analysis model that assumed the weld metal and base metal to be two homogeneous, isotropic regions.[23] The simple model was not expected to predict the behavior of the real weldment accurately, and it did not do so even qualitatively. The need for more realistic models is clearly indicated, and such models are now being developed.

While this test demonstrated that at room temperature one heat of the base metal of the FFTF vessel deforms more readily than the weld metal, it does not indicate what deformation pattern might be expected at elevated temperatures. This test should be considered only a step toward developing experimental and analytical techniques that can be applied to other weldments in the process of examining the adequacy of present engineering codes for design and construction of nuclear containment systems.

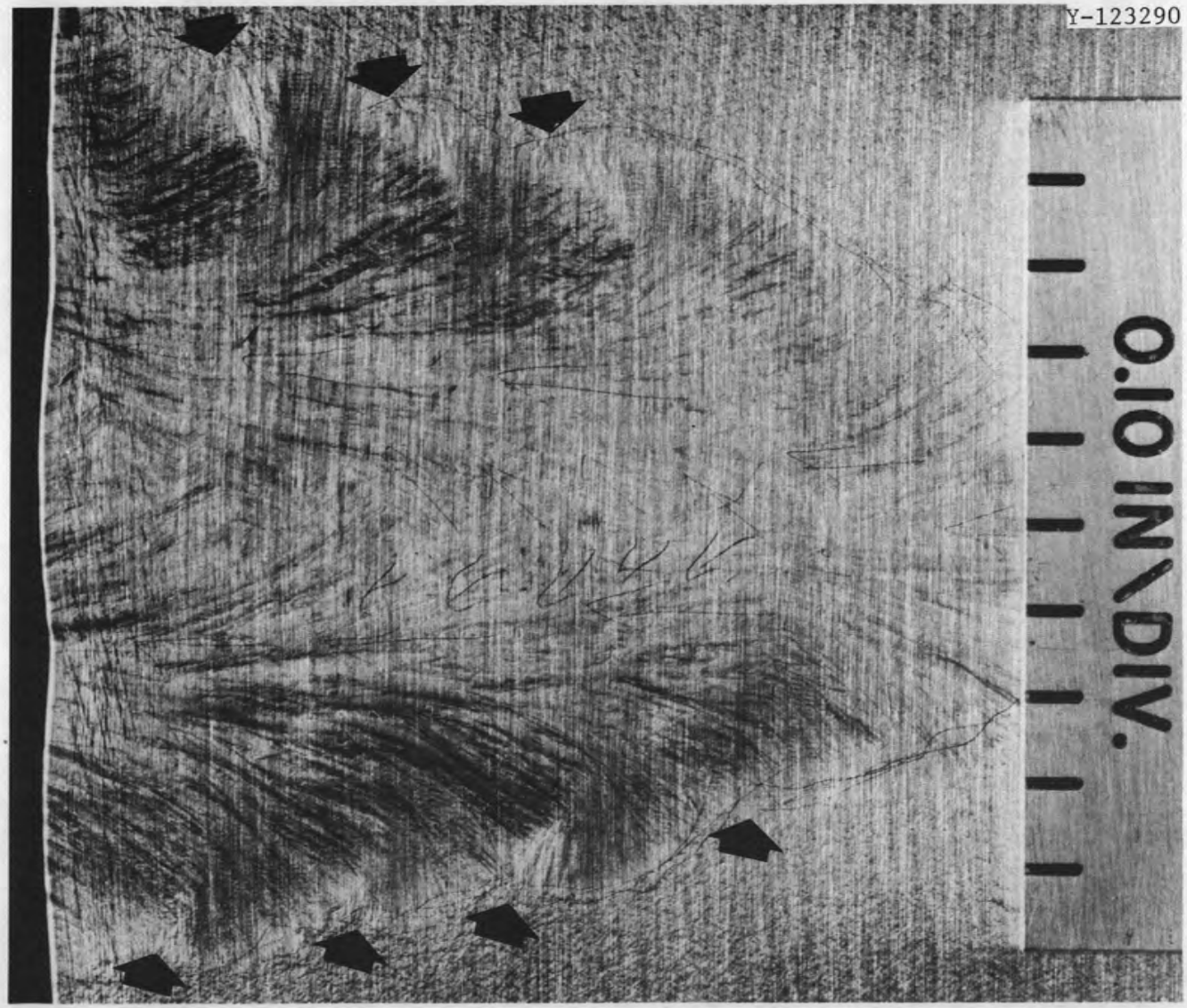

Fig. 5.60. Closeup of Unretouched, Unetched Surface of Type 308 CRE Whole-Weld Cross Section Stressed to 502 MPa (72.8 ksi) Nominal, Illuminated to Highlight Discontinuity in Substructure and Solidification Direction at Certain Interpass Boundary Regions That Are Indicated by Arrows. Some surface scratches from tracing operations appear as black lines.

5.4 MECHANICAL PROPERTIES OF STEAM GENERATOR MATERIALS

5.4.1 Tensile Properties of 2 1/4 Cr-1 Mo Steel — R. L. Klueh

We continued to determine exact tensile properties of 2 1/4 Cr-1 Mo steel from 25 to 593°C (77–1100°F). During this quarter we tested annealed material at nominal strain rates of 0.4, 0.04, 0.004, and 0.0004/min (crosshead speeds of 0.5, 0.05, 0.005, and 0.0005 in./min, 12.7 mm to 12.7 μm/min); only high-temperature tests were completed at the slowest speed. The results of these tests are given in Table 5.28 and shown graphically below along with those reported last quarter[24] (0.04/min strain rate).

In all cases the properties determined in these tests fell within the scatter band for annealed 2 1/4 Cr-1 Mo steel given by Smith[25] in his compilation of elevated-temperature properties of 2 1/4 Cr-1 Mo steel. Figure 5.61 shows that the 0.2% yield stress is little affected by strain rate. Only the 565°C (1050°F) test at the lowest strain rate (0.0004/min) shows any indication of an effect. The ultimate tensile stress, however, is affected by strain rate, the effect increasing as the temperature increases. The ultimate tensile stress shows a strain aging peak in Fig. 5.62. At 371 and 454°C (700 and 850°F), temperatures very near the strain aging peak, a decrease in strain rate respectively increases and has no effect on the ultimate tensile stress. That is, strain aging has offset the normal rate sensitivity, as evidenced at the higher temperatures, where a decrease in strain rate leads to a decrease in the ultimate tensile stress.

The change in ductility with temperature is shown in Fig. 5.63. For a given strain rate, the total elongation and reduction of area go through a minimum that corresponds roughly with the ultimate tensile stress maximum, while the uniform elongation shows a rather steady decrease with temperature. When the strain rate is decreased, the total elongation and reduction of area increase, while the uniform elongation continued to decrease.

Using a regression analysis, we have fitted the portion of the true stress–true strain data between the 0.2% yield strength and the ultimate tensile strength to the Hollomon (modified Ludwik) equation,[26]

Table 5.28. Tensile Properties of Annealed 2 1/4 Cr-1 Mo Steel

Temperature °C(°F)	Estimated Static Modulus, [psi(KPa)]	Proportional Limit, [ksi(MPa)]	Strength, ksi(MPa)		Fracture Stress [ksi(MPa)]	Elongation, %		Reduction of Area (%)
			0.2% Yield	Ultimate Tensile		Uniform	Total	
			0.4/min					
	$\times 10^6$							
25(77)	29.6(204)	18.3(126)	37.7(260)	76.4(527)	44.8(309)	12.0	28.2	69.9
204(400)	29.5(203)	19.3(133)	31.7(219)	64.2(443)	40.9(282)	11.8	24.6	70.9
371(700)	34.1(235)	14.3(99)	33.0(228)	72.4(499)	52.0(359)	9.0	19.0	57.4
454(850)	30.0(207)	17.2(119)	31.3(216)	67.9(468)	41.6(287)	10.2	22.9	64.2
510(950)	22.0(152)	14.3(99)	30.2(208)	62.1(428)	31.6(217)	8.5	24.7	70.9
538(1000)	23.1(159)	15.8(109)	30.6(211)	61.5(424)	29.6(204)	8.5	23.3	72.5
565(1050)	24.0(165)	14.3(99)	28.4(196)	53.2(367)	21.4(148)	9.1	28.3	80.3
593(1100)	25.0(172)	15.3(106)	29.1(201)	51.3(354)	20.0(138)	7.6	27.8	81.7
			0.04/min					
25(77)	33.2(229)	17.3(119)	37.4(258)	76.1(525)	45.8(316)	12.8	28.3	67.3
204(400)	29.9(206)	21.1(145)	32.0(221)	65.2(450)	42.6(294)	11.0	23.7	66.2
371(700)	34.1(235)	13.9(95.8)	32.9(227)	74.5(514)	51.0(352)	9.5	20.1	56.9
454(850)	32.8(226)	14.3(99)	33.3(230)	72.4(499)	44.9(310)	8.7	21.0	61.5
510(950)	23.7(163)	15.2(105)	32.5(224)	66.5(459)	33.5(231)	8.9	23.6	69.2
538(1000)	26.4(182)	14.2(98)	31.5(217)	61.3(423)	17.3(119)	8.4	26.3	73.9
565(1050)	23.5(162)	15.2(105)	30.2(208)	54.3(374)	9.1(63)	7.7	25.9	79.3
593(1100)	25.0(172)	14.2(98)	29.5(203)	47.5(328)	5.1(35)	6.8	36.5	84.7
			0.004/min					
25(77)	23.4(161)	18.3(126)	36.8(254)	74.6(514)	44.8(309)	13.3	28.7	69.5
204(400)	27.2(188)	17.3(119)	34.3(237)	68.8(474)	45.7(315)	10.9	22.9	66.0
371(700)	19.7(136)	21.3(147)	33.2(229)	74.8(516)	49.8(343)	10.4	21.3	58.6
454(850)	26.5(183)	15.3(106)	32.1(221)	71.7(494)	40.7(281)	8.7	21.8	64.5
510(950)	23.4(161)	15.7(108)	31.2(215)	60.3(416)	30.5(210)	7.4	29.4	76.2
538(1000)	25.0(172)	16.4(113)	29.5(203)	51.3(354)	30.8(212)	7.4	36.4	82.6
565(1050)	25.5(176)	14.3(99)	29.5(203)	48.3(333)	7.1(49)	6.8	37.0	84.0
593(1100)	24.9(172)	15.3(106)	26.8(185)	36.2(250)	2.5(17)	5.8	37.2	89.0
			0.0004/min					
371(700)	31.5(217)	18.3(126)	33.5(231)	78.1(538)	48.8(337)	10.7	22.4	61.7
454(850)	20.5(141)	14.9(103)	32.2(222)	69.5(479)	29.7(205)	9.1	24.8	69.3
510(950)	22.8(157)	15.2(105)	29.1(201)	51.0(352)	7.1(49)	7.0	31.8	84.7
565(1050)	26.3(181)	11.3(78)	26.1(180)	33.0(228)	2.4(17)	3.9	53.0	91.1

$$\sigma = K\varepsilon_p^n \quad , \tag{1}$$

where σ is the true stress, ε_p the true plastic strain, and K and n are material constants (K is known as the "strength coefficient" and n as the "strain-hardening coefficient"). The curves were also fit by the Ludwik equation[27]

$$\sigma = K_1\varepsilon_p^{n_1} + \sigma_0 \quad , \tag{2}$$

where K_1, n_1, and σ_0 are material constants; starting with σ_0 = 500 psi and increasing σ_0 at 500 psi intervals up to the yield stress, the best $\sigma_0 \neq 0$ was determined.

In all cases, Eq. (1) gave the best fit. The results are shown in Table 5.29. Figures 5.64 and 5.65 show n and K of Eq. (1) as functions of temperature, and both parameters reflect the strain-aging peak

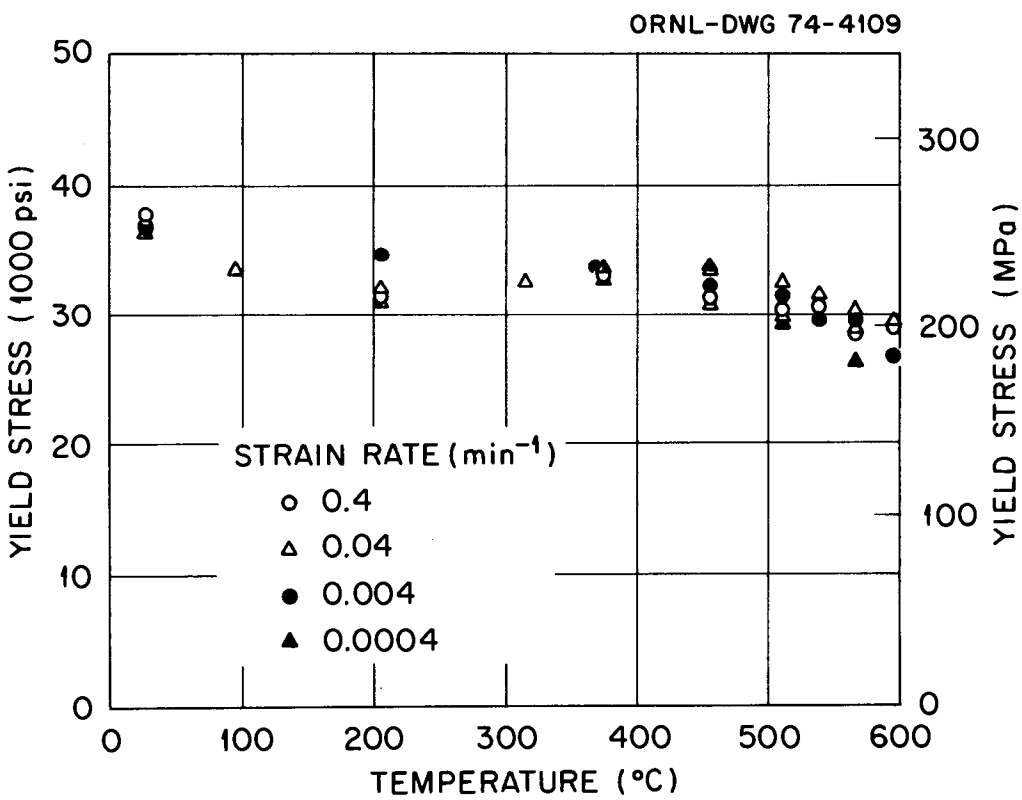

Fig. 5.61. Yield Strength as a Function of Temperature and Strain Rate for Annealed 2 1/4 Cr-1 Mo Steel.

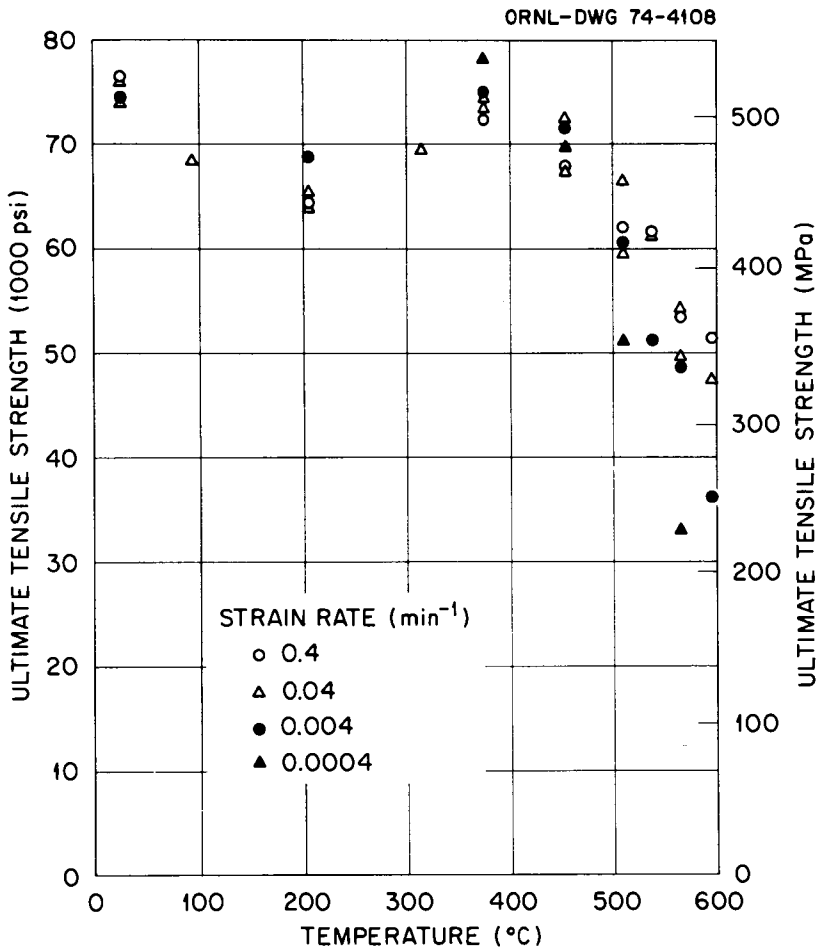

Fig. 5.62. Ultimate Tensile Strength as a Function of Temperature and Strain Rate for Annealed 2 1/4 Cr-1 Mo Steel.

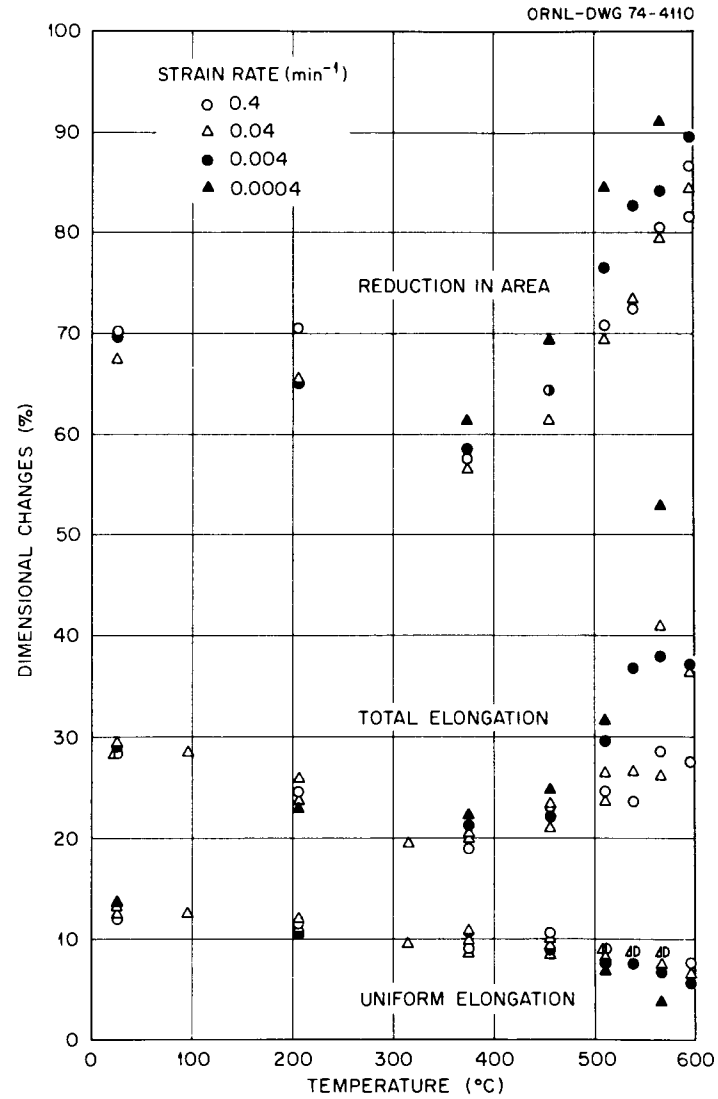

Fig. 5.63. Total and Uniform Elongation and Reduction of Area as Functions of Temperature and Strain Rate for Annealed 2 1/4 Cr-1 Mo Steel.

observed for the ultimate tensile strength. The strain-hardening coefficient, n, is rather well behaved. For strain rates down to 0.004/min, n is unaffected by strain rate below 510°C (950°F) and decreases with decreasing strain rate as temperature is increased above 510°C. At a strain rate of 0.0004/min, the behavior of n follows the behavior of the ultimate tensile stress shown in Fig. 5.62. The strength coefficient, K, although showing a similar behavior, shows somewhat more scatter with strain rate at the lower temperatures.

Table 5.29. Constants for Curve-Fitting Tensile Data for Annealed 2 1/4 Cr—1 Mo Steel

Strain Rate (min^{-1})	Temperature °C(°F)	$\sigma = K\varepsilon_p^n$		Variance
		K (ksi)	n	
0.4	25(77)	129	0.21	2.7×10^{-3}
	204(400)	116	0.21	1.5×10^{-4}
	371(700)	141	0.23	3.2×10^{-4}
	454(850)	131	0.23	4.4×10^{-4}
	510(950)	116	0.21	3.6×10^{-4}
	538(1000)	111	0.20	6.6×10^{-4}
	566(1050)	92	0.18	4.0×10^{-4}
	593(1100)	85	0.17	4.1×10^{-4}
0.04	25(77)	131	0.21	1.0×10^{-3}
	204(400)	117	0.21	1.1×10^{-3}
	371(700)	140	0.23	6.3×10^{-4}
	454(850)	140	0.23	6.8×10^{-4}
	510(950)	124	0.21	5.3×10^{-4}
	538(1000)	111	0.20	3.9×10^{-4}
	565(1050)	97	0.18	2.3×10^{-4}
	593(1100)	70	0.12	3.7×10^{-5}
0.004	25(77)	127	0.21	4.0×10^{-3}
	204(400)	122	0.21	5.2×10^{-4}
	371(700)	143	0.23	6.8×10^{-4}
	454(850)	136	0.23	1.1×10^{-3}
	510(950)	112	0.21	5.8×10^{-4}
	538(1000)	87	0.19	2.3×10^{-4}
	566(1050)	75	0.14	2.6×10^{-4}
	593(1100)	52	0.10	4.5×10^{-5}
0.0004	371(700)	156	0.26	9.6×10^{-4}
	454(850)	129	0.21	8.8×10^{-4}
	510(950)	86	0.16	3.6×10^{-4}
	566(1050)	45	0.083	1.1×10^{-5}

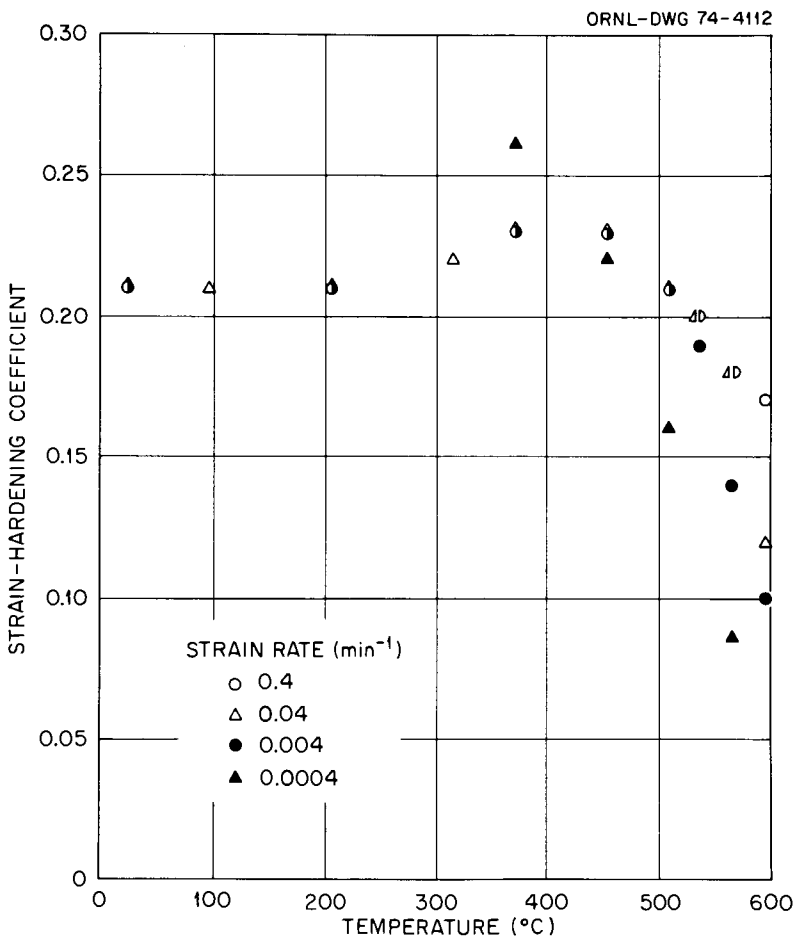

Fig. 5.64. Strain-Hardening Coefficient for the Hollomon Equation as a Function of Temperature and Strain Rate for Annealed 2 1/4 Cr-1 Mo Steel.

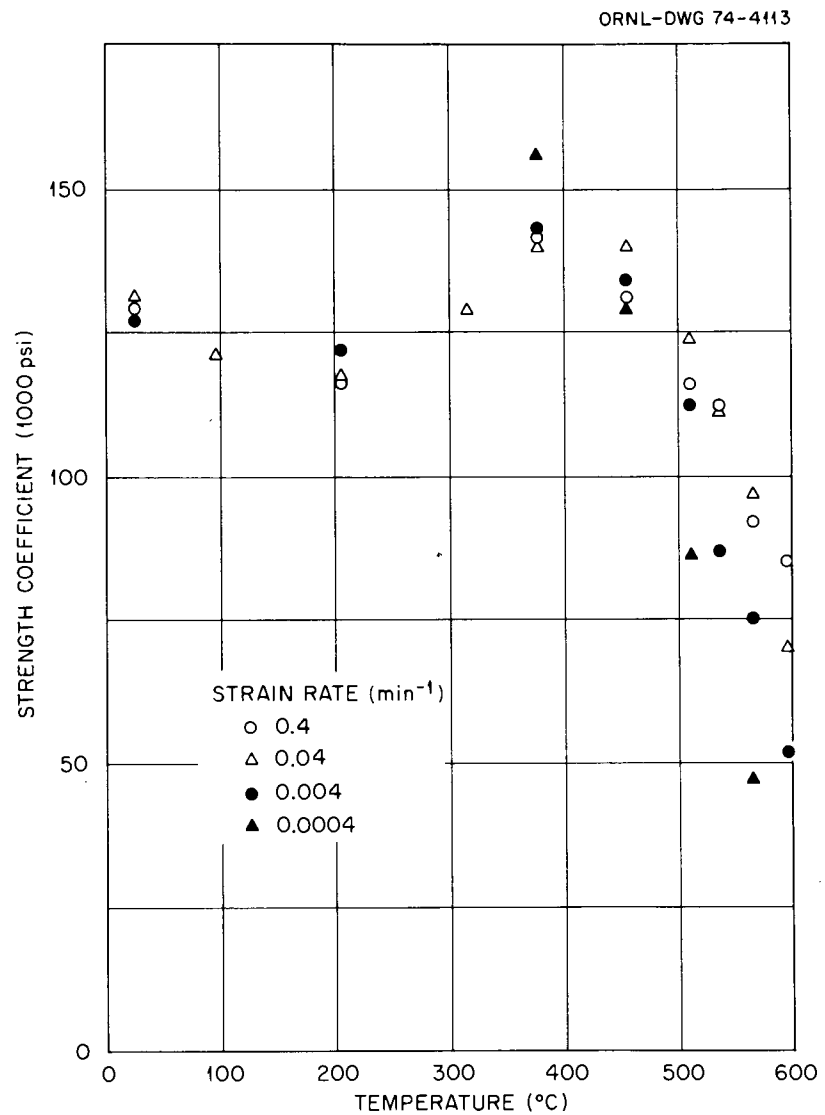

Fig. 5.65. Strength Coefficient for the Hollomon Equation as a Function of Temperature and Strain Rate for Annealed 2 1/4 Cr-1 Mo Steel.

During this quarter we also began to extend our tensile studies to much higher strain rates. By using an MTS Electro-Hydraulic test machine, we will be able to conduct tests over the strain-rate range of approximately 10 to 10,000/min. The results of these studies will be reported next quarter.

5.4.2 Cyclic Creep of Decarburized 2 1/4 Cr-1 Mo Steel Tubes — R. L. Klueh

In a steam generator of 2 1/4 Cr-1 Mo steel, decarburization by sodium is possible. It could result in a surface layer that is weaker than the remainder of the tube wall. Although we feel that the effect of a carbon loss on the creep strength under sustained loads can be designed for, the effect of cyclical loads on the creep of a steam generator tube is uncertain.

To determine the effect of decarburization and the resulting low-carbon surface layer on cyclic creep, a series of comparative tests are being planned for 510°C (950°F). To establish the carbon gradient, the specimens are being annealed in a wet hydrogen atmosphere at 704°C (1300°F). After such a heat treatment, a hardness gradient is detected, an indication that decarburization has occurred. The amount of decarburization and the type of gradient achieved can be varied by varying the time in the hydrogen. The hardness variations achieved through the wall of a 2 1/4 Cr-1 Mo steel tube after 24, 93, and 147 hr in the wet hydrogen atmosphere is shown in Fig. 5.66 (decarburization, in this case, was from both sides). When these specimens were examined metallographically, a difference in precipitate density near the surface and center of the specimen was evident. This is shown in Fig. 5.67 for the specimen decarburized for 93 hr.

Although 704°C is well above any temperatures to be encountered in a steam generator, these temperatures allow rapid decarburization and were used because we are interested in comparative studies of decarburized and nondecarburized specimens, not absolute creep data. In all cases, the decarburized specimen will be compared with one annealed in an inert atmosphere at 704°C for the same time.

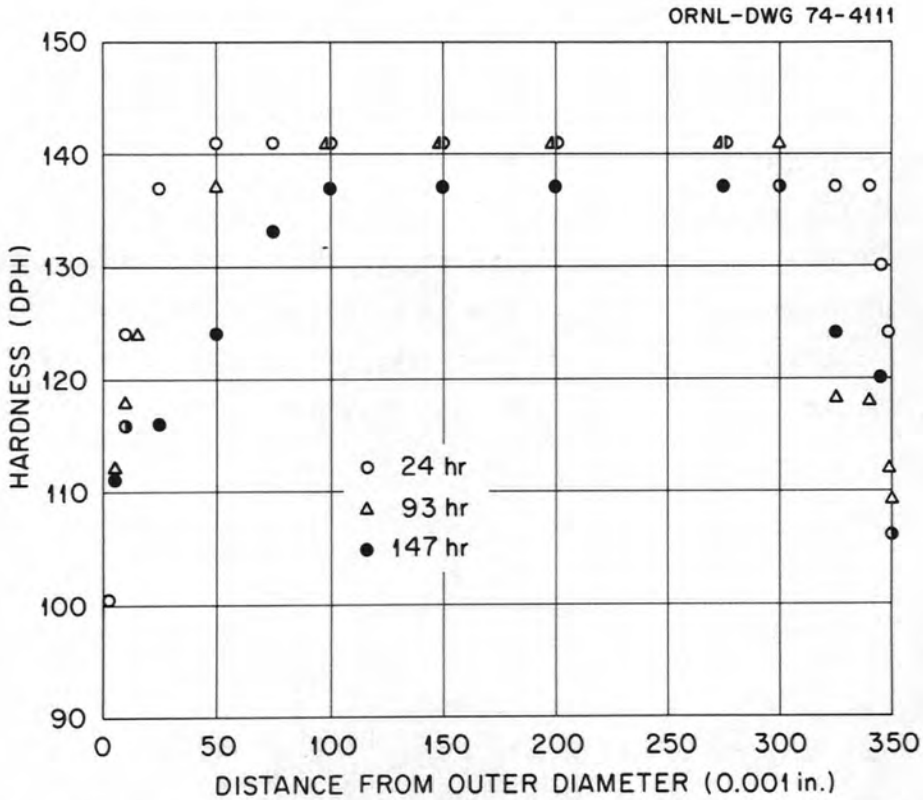

Fig. 5.66. Hardness Variation in a 2 1/4 Cr-1 Mo Steel Tube Decarburized in Wet Hydrogen at 704°C (1300°F) for 24, 93, and 147 hr.

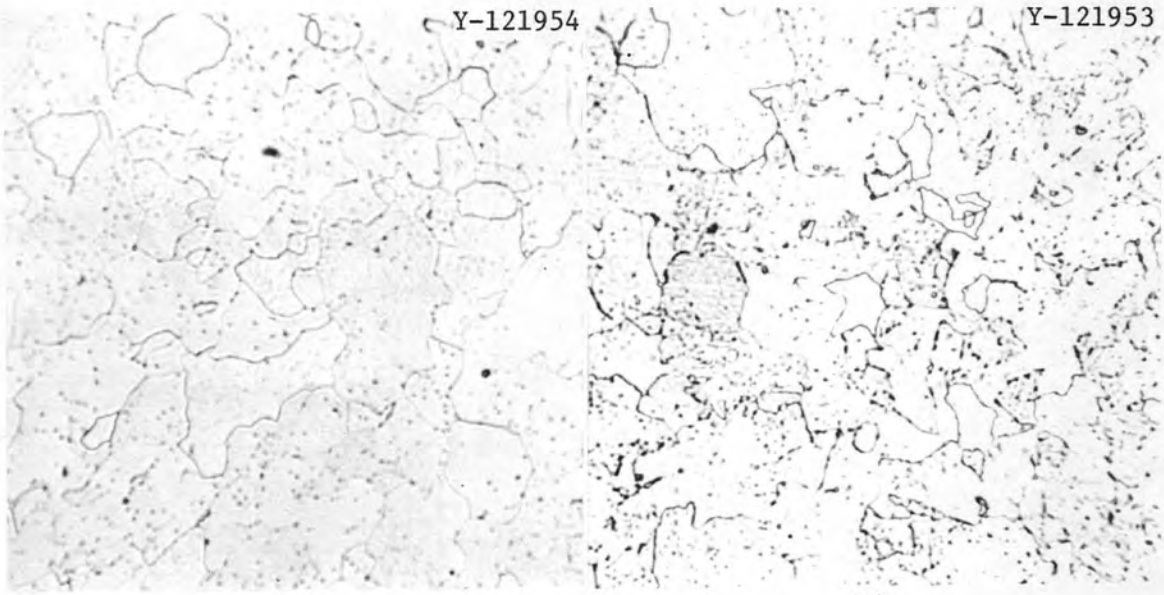

(a) (b)

Fig. 5.67. Microstructure of 2 1/4 Cr-1 Mo Steel after Decarburization for 93 hr at 704°C (1300°F). (a) Edge. (b) Center. 500×.

Figure 5.68 shows the cyclic creep equipment that is being used for these tests. This system is a slight modification of that used previously by McCoy.[28] The test sample is tubular and was machined from a 1.5-in.-diam tube with a 0.385-in. wall thickness (38 × 9.8 mm). The specimen has a 1-in. (25 mm) gage section, where the wall thickness has been reduced to 0.070 in. (1.78 mm). The top of the test specimen is welded to a tubular support, and the bottom is welded to a rod that passes to the piston through the sample and support. To generate the force for cycling, either side of the piston can be pressurized; the magnitude of

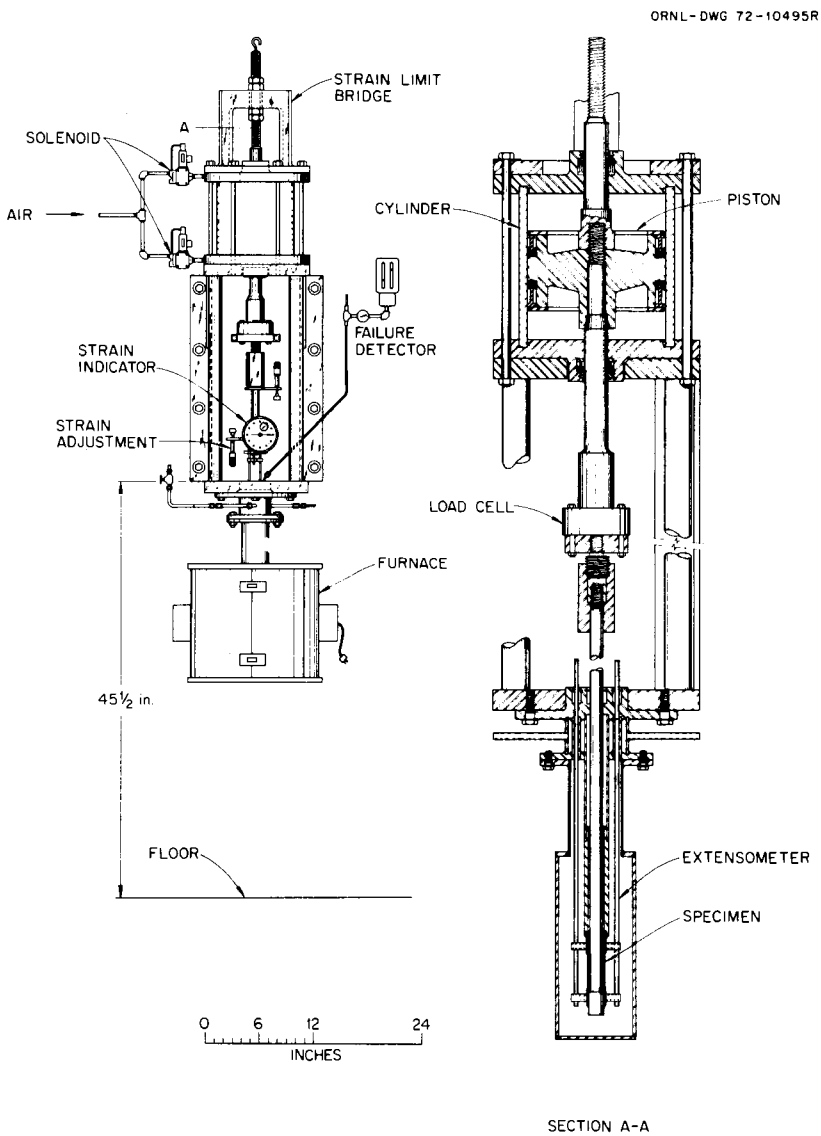

Fig. 5.68. Schematic Drawing of Cyclic Creep Equipment.

the force is controlled by the air pressure and measured by the load cell. Strain, tensile and compressive, is measured by a four-rod extensometer. The first tests are being run at 510°C (950°F) and 20,000 psi (138 MPa).

5.4.3 Mechanical Properties of Weld-Overlaid Stainless Steel Forgings — R. L. Klueh

5.4.3.1 Tensile Properties

During the last two quarters we reported on the tensile properties of the type 304 stainless forging that was unaffected by the overlay process[29] and of the type 308 stainless steel weld overlay.[30] In a previous report,[31] we showed that the hardness of the type 304 stainless steel forging immediately adjacent to the overlay-forging interface was significantly greater than the constant hardness at some distance from the fusion line, an indication that the overlay process had affected the forging.

We have now completed tensile tests on specimens taken from the region adjacent to the overlay-forging interface. Three types of specimens were tested: radial and tangential specimens machined from immediately adjacent (parallel) to the weld metal—forging interface and an axial specimen taken across the interface and containing both weld metal and forging. To obtain material from as near the interface as possible, we fabricated the radial and tangential specimens by joining gage blanks of the forging to type 304 stainless steel specimen end pieces, using a low-heat-input welding process. A similar procedure was used for the axial specimens, but because of the limited amount of weld metal, 1-in.-gage-length (25 mm) specimens were tested.

Table 5.30 gives the tensile test results for the type 304 stainless steel immediately adjacent to the interface. Duplicate tests were run at the 0.04/min strain rate. Figure 5.69 shows the yield strength and ultimate tensile strength as functions of temperature for one data set, while Fig. 5.70 shows the elongation and reduction of area. As was true for the forging and weld metal, no effect of orientation was apparent, and the only effect of strain rate was observed on the ultimate tensile

Table 5.30. Tensile Properties of Type 304 Stainless Steel Adjacent to Fusion Line

Temperature (°C)	Temperature (°F)	Nominal Strain Rate (min^{-1})	0.2% Offset Yield Stress (ksi)	0.2% Offset Yield Stress (MPa)	Ultimate Tensile Stress (ksi)	Ultimate Tensile Stress (MPa)	Total Elongation (%)	Reduction of Area (%)
			Radial Orientation					
25	75	0.04	66.3	457	96.1	663	53.2	54.6
			62.1	428	87.7	604	36.7	46.2
427	800	0.04	44.5	307	64.7	446	24.3	37.1
			44.3	305	71.4	492	37.8	50.5
482	900	0.04	41.0	283	60.4	416	24.5	48.6
			43.7	301	68.6	473	36.2	41.7
538	1000	0.04	40.4	279	60.8	419	27.7	57.0
			42.3	292	65.7	453	35.8	45.9
593	1100	0.04	37.7	260	56.4	389	24.8	54.1
			37.2	256	59.6	411	34.9	43.2
649	1200	0.04	38.3	264	51.9	358	27.8	51.5
			37.7	260	51.9	358	31.0	36.0
482	900	0.004	44.0	303	70.9	489	35.3	53.8
593	1100	0.004	40.0	276	58.9	406	36.4	45.8
649	1200	0.004	36.2	250	45.5	314	28.5	42.3
482	900	0.0004	43.1	297	69.1	476	32.6	50.5
593	1100	0.0004[a]	38.2	263	54.2	374	24.1	23.0
649	1200	0.0004[a]	34.4	237	41.4	285	31.4	30.8
			Tangential Orientation					
25	75	0.04	67.1	463	92.3	636	47.2	42.7
			68.1	470	99.2	683	57.7	47.1
427	800	0.04	46.8	323	68.0	469	25.4	40.9
			44.9	310	71.7	494	38.0	46.6
482	900	0.04	43.5	300	61.3	423	19.4	51.1
			42.6	294	70.0	483	36.0	42.5
538	1000	0.04	43.2	298	63.7	439	25.1	48.9
			41.8	288	66.1	456	37.0	47.3
593	1100	0.04	38.7	267	57.8	399	25.3	51.3
			39.3	271	60.9	420	39.8	50.6
649	1200	0.04	36.9	255	50.6	349	21.9	36.5
			36.6	252	52.1	359	39.8	53.7

[a]Fractured at gage mark.

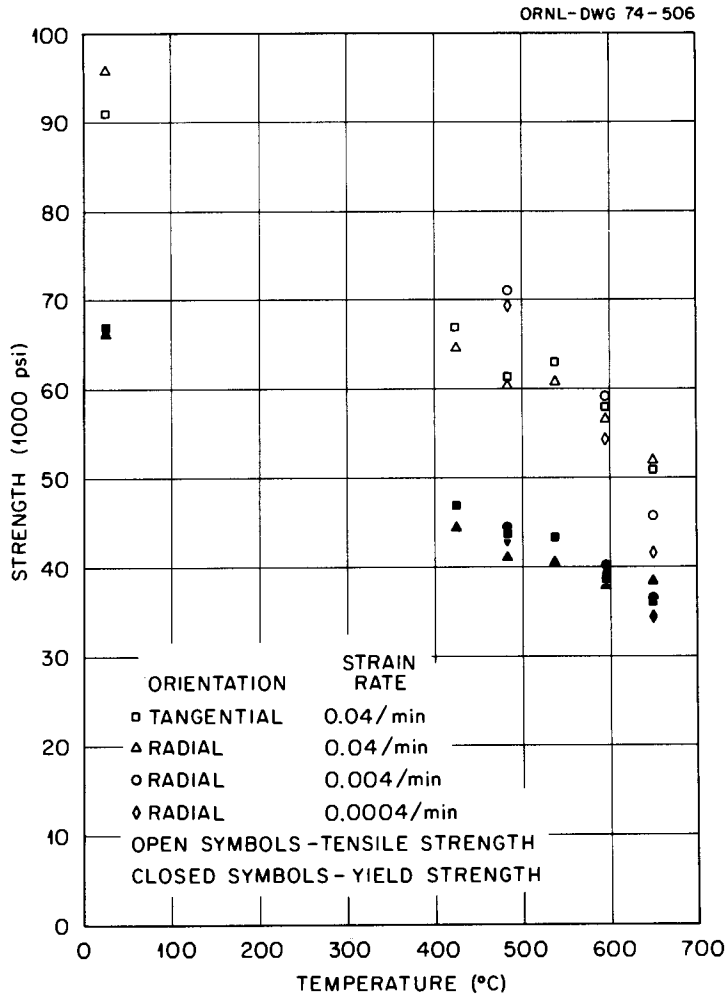

Fig. 5.69. Yield and Ultimate Tensile Strengths of Type 304 Stainless Steel Adjacent to the Fusion Line for Two Orientations and Three Strain Rates as Functions of Temperature.

strength and reduction of area at 593 and 649°C (1100 and 1200°F) (the reduction of area measurements are probably extra low because the fracture occurred where the extensometer was attached).

Visual and metallographic observations indicated that all specimens tested at 0.04/min showed transgranular failures, as did those at the two lower strain rates at 482°C (900°F) and the test at 593°C (1100°F) at 0.004/min. However, the tests at 0.0004/min at 593°C and both low strain rates at 649°C (1200°F) displayed an intergranular fracture.

Table 5.31 shows the results for the composite specimens with both weld metal and forging in the gage section. A comparison with the results previously obtained for the forging and the weld metal indicates

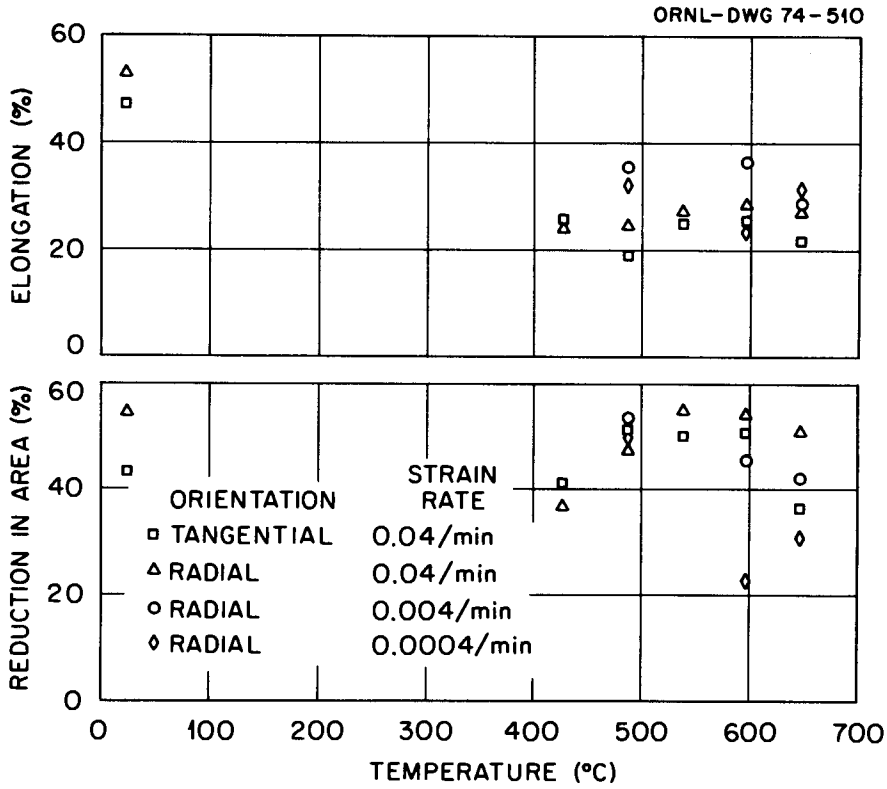

Fig. 5.70. Elongation and Reduction of Area of Type 304 Stainless Steel Adjacent to the Fusion Line for Two Orientations and Three Strain Rates as Functions of Temperature.

that the yield strength of the composite specimen is always slightly below that for the weld metal and for the forging adjacent to the fusion line. The ultimate tensile strengths of the weld metal and the composite specimens are comparable at all temperatures and somewhat below those for specimens taken from adjacent to the fusion line. Above room temperature, the failures occurred in the weld metal; however, at room temperature failure occurred in the forging.

With the completion of these tests, it is of interest to compare the behavior of the three materials (i.e., forging, weld metal, and forging adjacent to the fusion line). Table 5.32 compares sets of data for radial specimens from each location in the overlaid forging; Fig. 5.71 shows the strength data graphically. At all temperatures, the yield strengths of the weld metal and interface region are quite similar and considerably greater than those of the unaffected forging. It should be noted, however, that the relative difference between the yield strengths

Table 5.31. Tensile Properties of Weld-Overlaid Forging Specimens Containing Both Type 304 Stainless Steel and Type 308 Stainless Steel Weld Metal[a]

Temperature		0.2% Offset Yield Stress		Ultimate Tensile Stress		Total Elongation	Reduction of Area
(°C)	(°F)	(ksi)	(MPa)	(ksi)	(MPa)	(%)	(%)
25	75	59.6	411	88.6	611	42.4	68.1
		56.7	391	89.3	616	56.1	73.5
427	800	42.2	291	64.2	443	30.0	52.5
		40.2	277	65.2	450	31.0	51.0
482	900	39.8	274	61.2	422	30.8	52.6
		36.3	250	59.5	410	31.9	61.7
538	1000	35.1	242	58.2	401	29.7	46.9
		38.6	266	56.5	390	31.7	56.9
593	1100	35.5	245	50.7	350	32.4	58.0
		33.2	229	53.6	370	27.7	63.5
649	1200	31.6	218	44.1	304	31.7	67.2
		32.2	222	44.6	308	31.1	67.4

[a]Tested at a nominal strain rate of 0.04/min; axially oriented specimens.

of the weld metal and interface region and those of the forging decreases somewhat with temperature. In addition to the effect of temperature on yield strength, temperature dramatically affects the relative behavior of the early part of the stress-strain curve, as illustrated in Figs. 5.72 and 5.73, where the first 5% of the stress-strain curves for 25 and 649°C (77 and 1200°F) are shown. There is much less difference between the three materials at 649°C than at 25°C.

It is also of interest to note the relative ultimate tensile strengths, shown in Fig. 5.71. Except at room temperature, where the ultimate tensile strengths parallel the yield strengths, there is relatively little difference in ultimate tensile strength for specimens taken from forging, weld metal, or forging adjacent to the fusion line (even at room temperature, the difference is not nearly as large as that for the yield strengths). Of further interest is the fact that the

Table 5.32. Comparison of Tensile Properties of Radial Specimens at Various Locations in the Weld-Overlaid Forging at 0.04/min

Temperature (°C)	Temperature (°F)	Specimen Type	Strength, ksi[a] Yield	Strength, ksi[a] Ultimate Tensile	Total Elongation (%)	Reduction of Area (%)
25	77	Forging	42.0	85.7	63.4	74.0
		Weld Metal	63.3	90.6	39.3	43.3
		Forging-Interface	66.3	96.1	53.2	54.6
427	800	Forging	28.3	64.0	39.3	56.2
		Weld Metal	43.4	64.7	33.0	46.5
		Forging-Interface	44.5	64.7	24.3	37.1
482	900	Forging	33.1	65.5	42.8	60.9
		Weld Metal	44.9	61.8	21.4	45.7
		Forging-Interface	41.0	60.4	24.5	48.6
538	1000	Forging	32.2	62.8	39.5	64.6
		Weld Metal	43.6	56.6	20.8	43.7
		Forging-Interface	40.4	60.8	27.7	57.0
593	1100	Forging	30.8	58.4	41.3	62.5
		Weld Metal	37.9	50.3	24.6	53.2
		Forging-Interface	37.7	56.4	24.8	54.1
649	1200	Forging	29.2	49.4	46.2	60.8
		Weld Metal	35.6	44.6	27.3	43.1
		Forging-Interface	38.3	51.9	27.8	51.5

[a]1 ksi = 6,895 MPa.

ultimate tensile strength of the weld metal drops off relative to the other two, and at the higher temperatures it is consistently below that for the other two materials.

The elongation and reduction of area of the forging are always considerably above that for the other two locations. Except at 25 and 427°C (77 and 800°F), the ductilities of weld metal and the forging adjacent to the fusion line differ little. The effect of strain rate is very nearly the same for all locations. In all cases there was little effect on yield strength. For all locations, above 482°C (900°F) the ultimate tensile strength and ductility decreased with decreasing strain rate, the relative effect increasing with temperature.

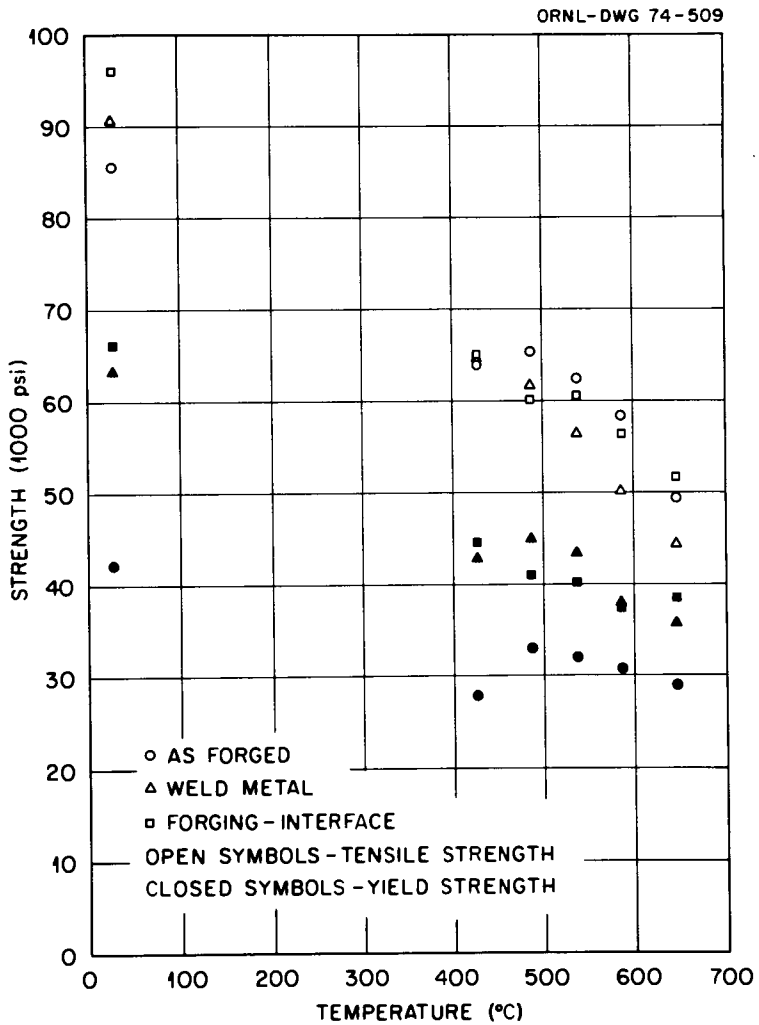

Fig. 5.71. A Comparison of Yield and Ultimate Tensile Strengths at 0.04/min for Radial Specimens Taken from the Forging, Weld Metal, and Forging Adjacent to the Interface. 1000 psi = 6.895 MPa.

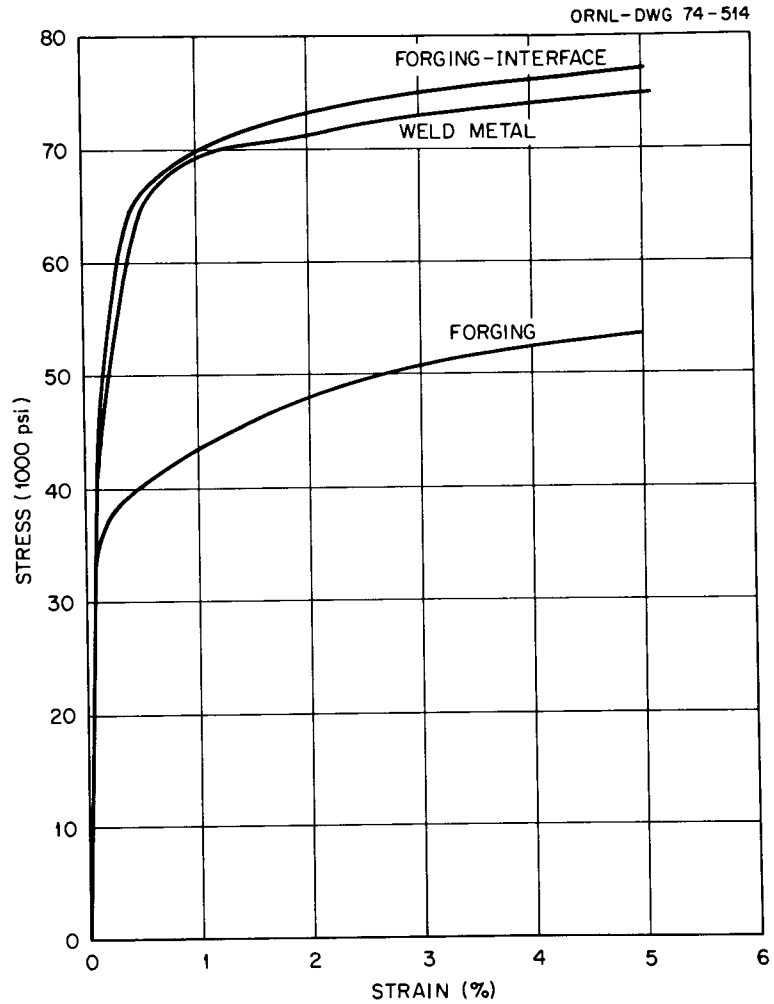

Fig. 5.72. A Comparison of the Tensile Curves for the Forging, Weld Metal, and Forging Adjacent to the Fusion Line at 25°C (77°F). 1000 psi = 6.895 MPa.

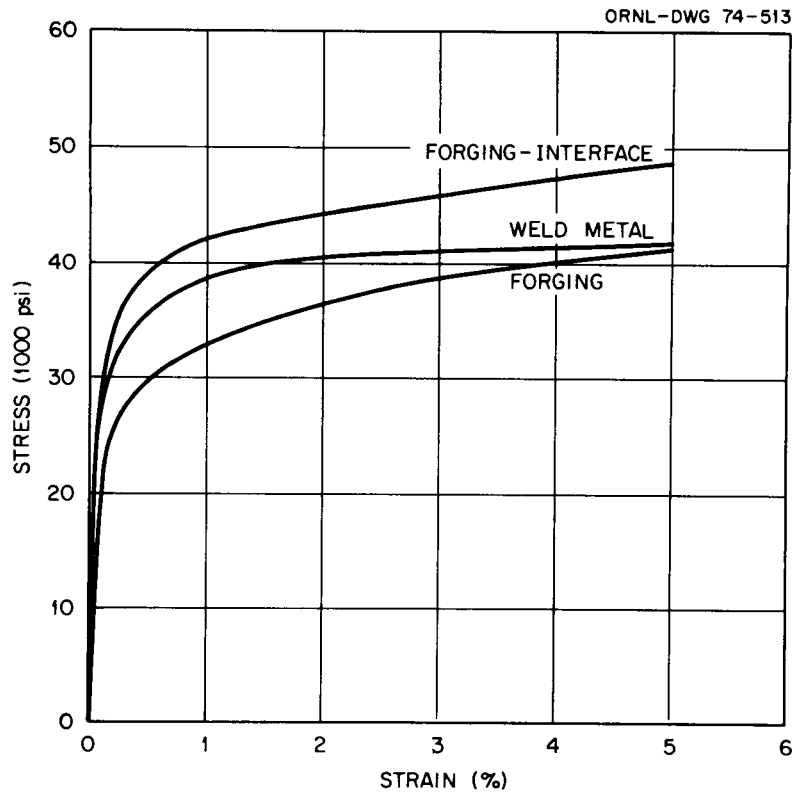

Fig. 5.73. A Comparison of the Tensile Curves for the Forging, Weld Metal, and Forging Adjacent to the Fusion Line at 649°C (1200°F). 1000 psi = 6.895 MPa.

5.4.3.2 Creep-Rupture Properties

The creep-rupture properties of specimens taken from the weld-overlaid type 304 stainless steel forging are being determined at 482 and 593°C (900 and 1100°F). Tests are to be made as a function of orientation and position in the forging in the same way as the tensile properties were determined.

In Table 5.33, the creep-rupture properties of axial, radial, and tangential specimens taken from the type 304 stainless steel forging (unaffected by the overlay process) at 593°C (1100°F) are given. Figure 5.74 gives the creep-rupture curves and minimum creep rate as functions of stress. Specimen orientation appears to have little or no effect. In addition to a similarity of creep-rupture properties, creep curves for the different orientations are also similar. This is illustrated in Fig. 5.75, where the creep curves for axial, radial, and tangential specimens tested at 37.5 ksi (258 MPa) are shown.

Table 5.33. Creep-Rupture Properties of Type 304 Stainless Steel Forging at 593°C (1100°F)

Stress ksi	Stress MPa	Rupture Life (hr)	Elongation (%)	Reduction of Area (%)	Minimum Creep Rate (%/hr)
			Axial Specimens		
45	310	77.4	20.7	22.8	0.058
40	276	515.9	20.3	19.7	0.0079
37.5	259	1125.0	23.6	27.1	0.0036
35	241	2420.0	31.4	34.1	0.0018
30	207	a			0.00087
			Tangential Specimens		
45	310	78.1	19.4	16.6	0.047
40	276	427.0	15.2	15.7	0.0061
37.5	259	1208.3	17.4	19.9	0.0030
35	241	2246.3	26.9	31.2	0.0015
			Radial Specimens		
45	310	69.0	21.6	19.9	0.066
40	276	457.1	16.5	13.7	0.0050
37.5	241	1275.2	23.8	26.9	0.0030

[a]Test discontinued after 2662 hr.

5.4.4 Minimum Creep Rate of 2 1/4 Cr-1 Mo Steel — D. O. Hobson and T. L. Hebble*

One of the inputs to the Nuclear Systems Materials Handbook (NSMH) is to comprise pages that show an equation for calculating the expected values of the minimum creep rate (MCR) for 2 1/4 Cr-1 Mo steel, an equation or equations for calculating the tolerance limits on those expected values, and a page or pages that show graphs or tables to illustrate the results.

We have examined a data base of approximately 200 creep tests for which minimum creep rates were given. Usual practice for austenitic steels is to correlate the MCR with creep stress and test temperature.

*Mathematics Research Staff.

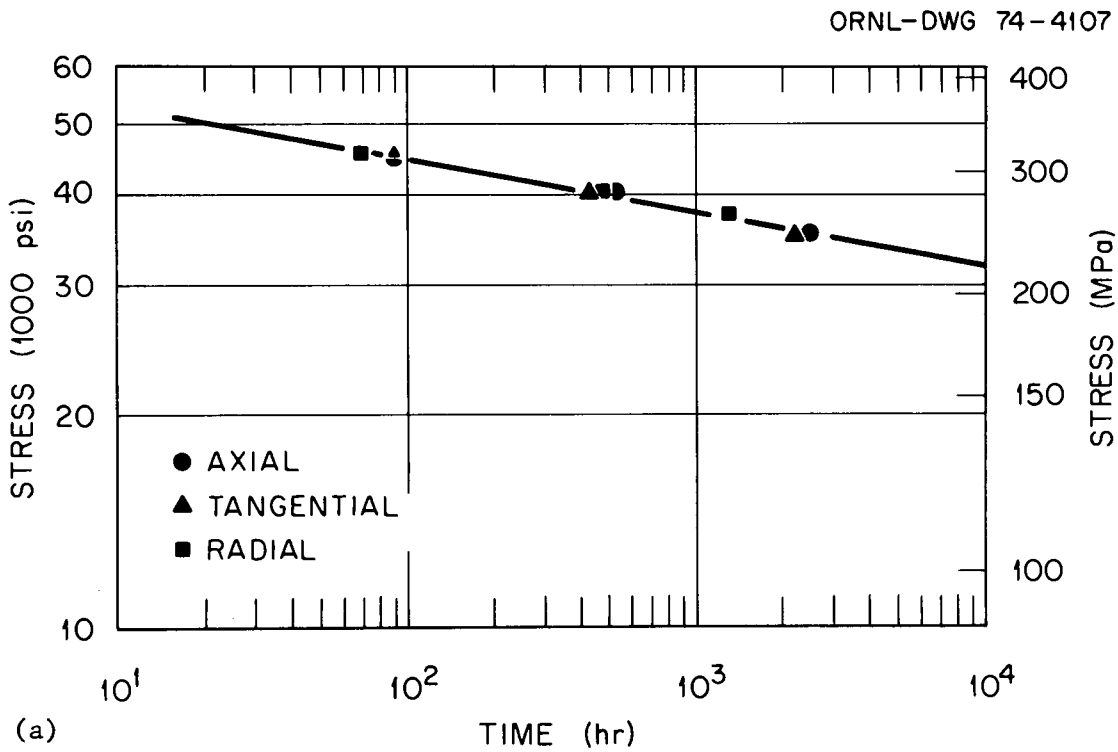

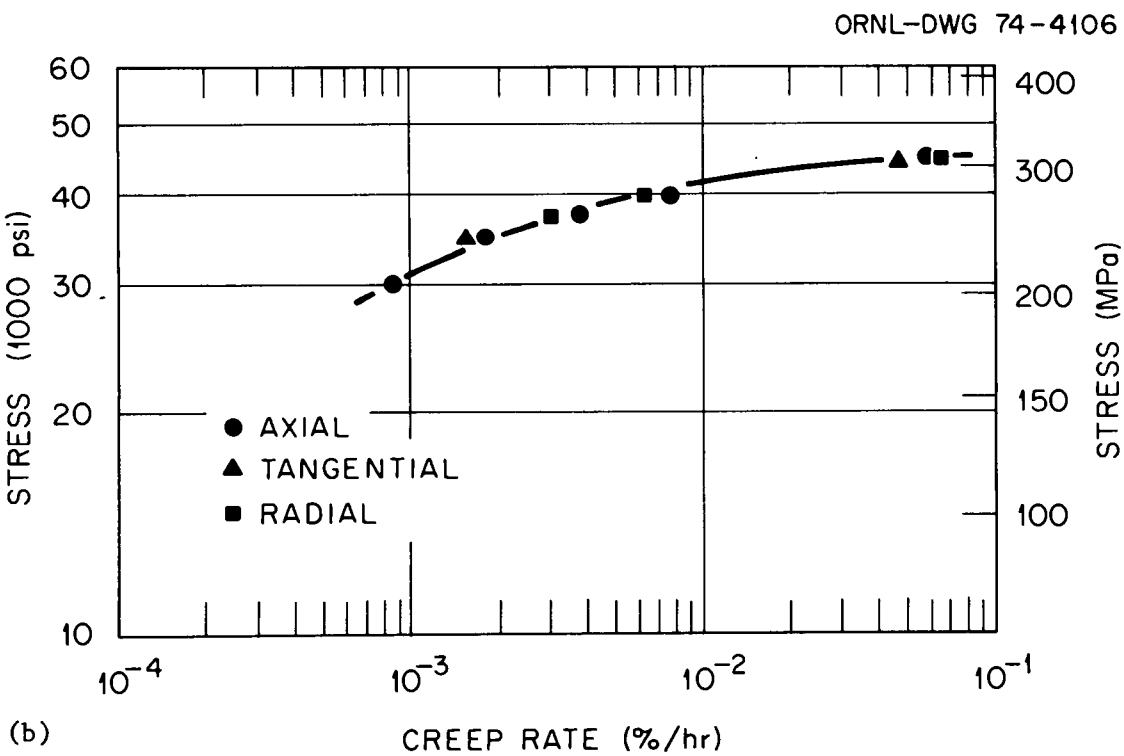

Fig. 5.74. Creep-Rupture Properties of Type 304 Stainless Steel Forging. (a) Rupture life. (b) Minimum creep rate.

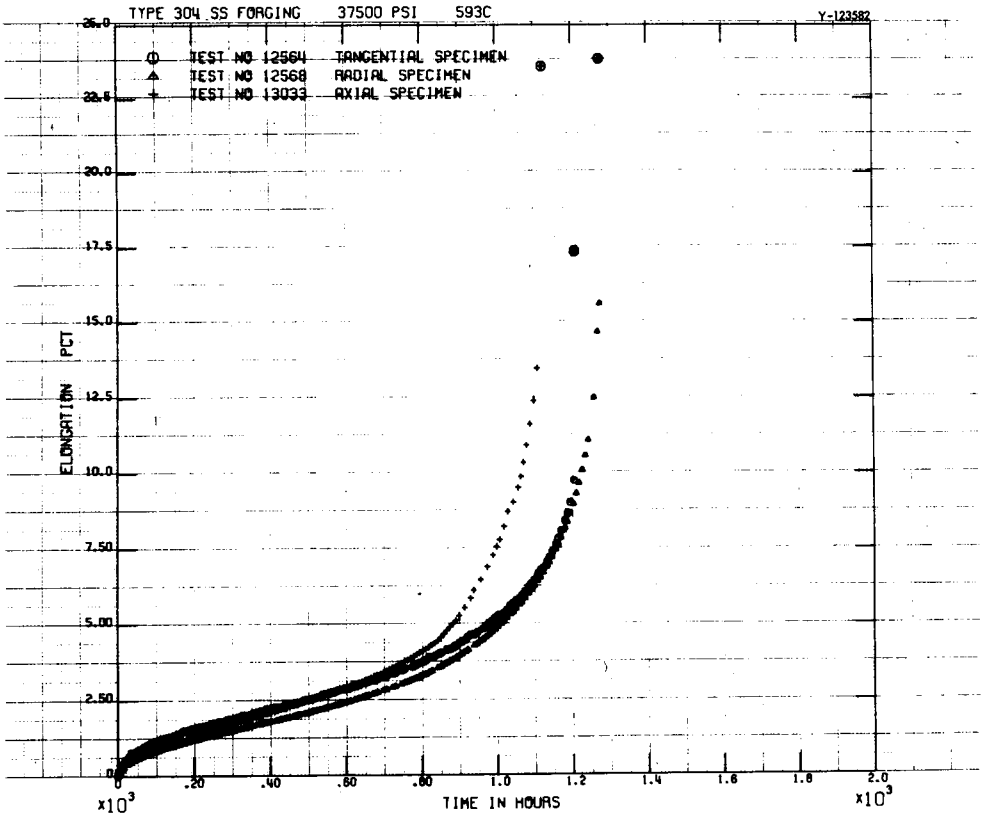

Fig. 5.75. Creep Curves for Type 304 Stainless Steel Forging Specimens Taken in the Axial, Radial, and Tangential Orientations Tested at 37.5 ksi (258 MPa).

We have found that the ferritic 2 1/4 Cr-1 Mo steels require an additional correlation variable to handle the effects of heat treatment on strength and creep behavior. In general, we found that MCR was inversely related to room-temperature ultimate tensile strength, $(UTS)_{RT}$, as long as the heat treatment that produced the strength level resulted in a relatively stable microstructure.

An interim model of the form $\log MCR = \alpha_0 + \alpha_1\sigma + \alpha_2\sigma T + \alpha_3\sigma T^2 + \alpha_4\tau^2 + \alpha_5 T\tau^2$, with MCR in units of %/hr and σ = creep stress (ksi) or (MPa), T = test temperature (°F ± 460) or (°C ± 273), and $\tau = (UTS)_{RT}$ (ksi) or (MPa), generated a 0.79 coefficient of variation. That is, 79% of the variability is accounted for by this model. Least squares estimates of the coefficients are given in Table 5.34.

A portion of the variability of the data that is not adequately explained by the equation can probably be attributed to either a heat

Table 5.34. Coefficient With Standard Deviations of the Interim MCR Equation

Coefficient	English Units	SI Units
α_0	-3.24 ± 0.17	-3.24 ± 0.17
α_1	3.17 ± 0.55	0.460 ± 0.080
α_2	$-4.80 \times 10^{-3} \pm 8.0 \times 10^{-4}$	$-1.25 \times 10^{-3} \pm 2.1 \times 10^{-4}$
α_3	$1.87 \times 10^{-6} \pm 2.9 \times 10^{-7}$	$8.80 \times 10^{-7} \pm 1.4 \times 10^{-7}$
α_4	$-9.16 \times 10^{-4} \pm 3.3 \times 10^{-4}$	$-1.93 \times 10^{-5} \pm 6.9 \times 10^{-6}$
α_5	$3.05 \times 10^{-7} \pm 2.1 \times 10^{-7}$	$1.15 \times 10^{-8} \pm 8.0 \times 10^{-9}$

treatment or a cold-working operation that provided a high or low $(UTS)_{RT}$ that did not reflect the subsequent creep behavior of the material because of an unstable microstructure. We are presently examining this phenomenon, and preliminary observations suggest that heat treatments that consist of a 1- or 2-hr hold at temperatures from 899 to 969°C (1650–1775°F), followed by a slow cooldown to the 649 to 719°C (1200–1325°F) range, followed by an air- or furnace-cooldown produce the requisite stable structure. Such observations also suggest that a correlation with carbon content may be appropriate. The above heat treatment closely resembles the ORNL-recommended heat treatment for 2 1/4 Cr-1 Mo steels.

5.4.5 Subcritical Crack Growth and Fatigue of 2 1/4 Cr-1 Mo Steel — C. R. Brinkman

Subcritical crack growth studies are presently under way on a single heat of 2 1/4 Cr-1 Mo steel. Test parameters and material heat treatment were reported previously.[10] Results from three elevated-temperature tests are compared in Fig. 5.76. Work is continuing.

A test matrix was further defined for the fatigue testing of this material in air, steam, sodium, and helium. Specific details concerning

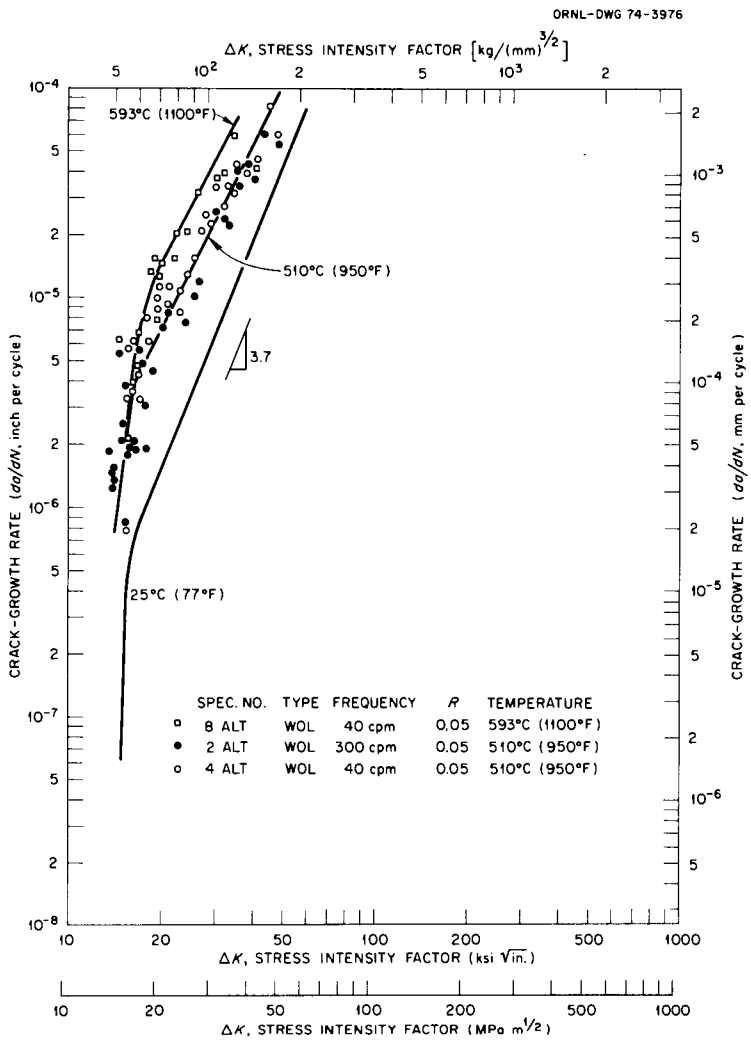

Fig. 5.76. Crack Growth Rate as a Function of the Change in Stress Intensity for Annealed 2 1/4 Cr-1 Mo Steel for Several Temperatures and Frequencies.

test parameters are available upon request. Types of tests identified were as follows:

- Low-cycle fatigue
- High-cycle fatigue ($\leq 10^7$ cycles)
- Fatigue, strain-rate sensitivity
- Creep-fatigue
  - Short term
  - Long term
- Tensile
  - Constant strain rate to failure
  - Cyclic stress-strain curve
  - Interrupted fatigue
- Block or multiple-step fatigue
- Combined-mode fatigue
- Mixed-mode fatigue
- Mean-strain fatigue
- Fatigue of weld metal and weldments
- Notched fatigue
- Stable crack growth
- Combined push-pull axial and torsion
- Aging and test environment

5.5 HIGH-TEMPERATURE DESIGN — W. L. Greenstreet, J. M. Corum, and C. E. Pugh

5.5.1 Exploratory Testing to Identify Behavioral Features — R. W. Swindeman

5.5.1.1 Development of Laboratory Facilities

Two cyclic creep testing machines, in addition to the two currently in use, are being installed. This will increase the machine allocation on the exploratory work to eight uniaxial machines, four cyclic creep machines, one creep-plasticity testing machine, one 100-hr relaxation testing machine, and one 50,000-lb MTS machine.

5.5.1.2 Stress-Strain Testing

During the past quarter efforts were made to develop representations for the monotonic stress-strain behavior of type 304 stainless steel (heat 9T2796) 1-in. (25.4-mm) plate. The tensile test matrix for recommended material, reported previously,[32] was completed, and all tests were processed to produce stress-strain datum pairs over the plastic strain range from 5×10^{-5} to the rupture elongation. About 25 to 30 pairs were obtained from each test. The surface generated by plotting the 0.2% yield strength data against the temperature and strain rate is shown in Fig.5.77. At low temperatures the yield exhibited a pronounced temperature sensitivity and a slight strain-rate sensitivity, while at temperatures of interest to the LMFBR, 300 to 600°C (572–1112°F), the yield for this reannealed material was relatively insensitive to either temperature or strain rate. The surface generated by plotting the ultimate tensile strength against temperature and strain rate is shown in Fig. 5.78. We observed a pronounced decrease in strength with temperature between 25 and 200°C (77 and 392°F) and then a leveling off or even rise in the

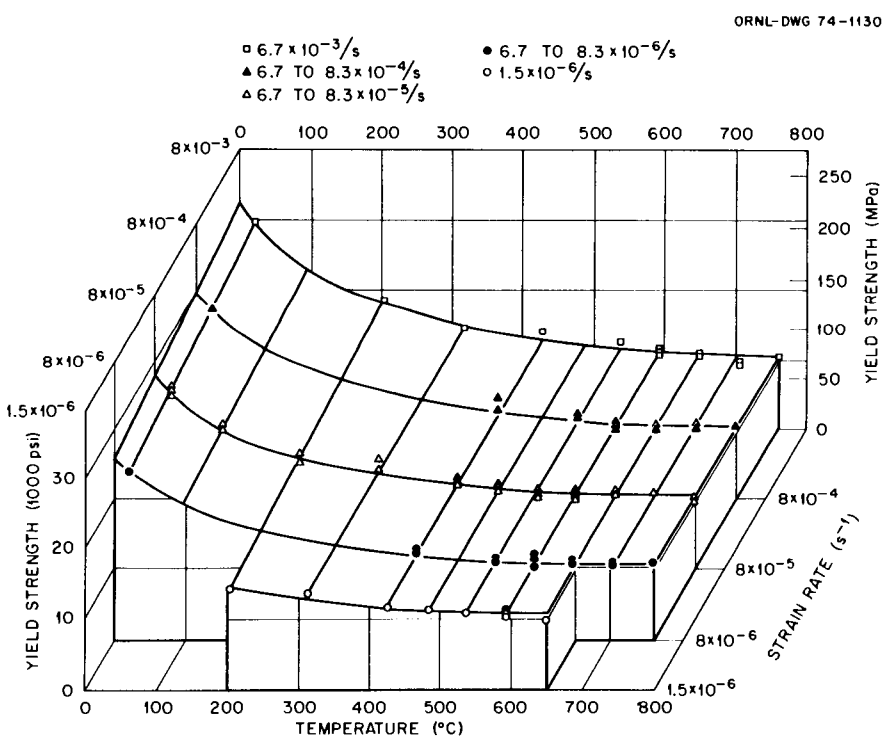

Fig. 5.77. Variation of the 0.2% Offset Yield Strength with Temperature and Strain Rate for Reannealed Type 304 Stainless Steel (Heat 9T2796).

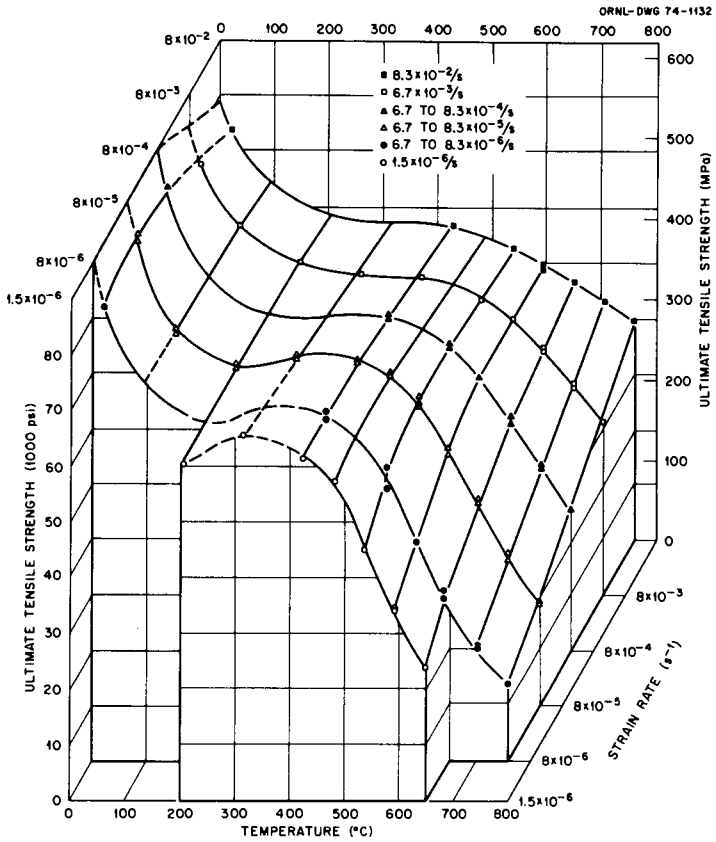

Fig. 5.78. Variation of Ultimate Tensile Strength with Temperature and Strain Rate for Reannealed Type 304 Stainless Steel (Heat 9T2796).

range 200 to 500°C (392—932°F) and finally a decrease, at a rate dependent on the strain rate, at temperatures above 500°C. The slight maximum in the 200 to 500°C range is possibly a manifestation of strain aging, while the high sensitivity to strain rate above 500°C is clearly associated with creep effects. The surface generated by plotting the uniform strain at the ultimate strength is shown in Fig. 5.79. In many respects the surface is similar to that exhibited by the ultimate strength. Again we observed a sharp decrease between room temperature and 200°C, a plateau at intermediate temperatures, and a strong dependence on temperature and strain rate above 500°C.

In developing a representation for these tensile data, three ranges of plastic strains were of interest. The first range covered the region of plastic deformation between the elastic limit and the knee of the yield curve. The strain data corresponded to stresses below the surface shown in Fig. 5.77.

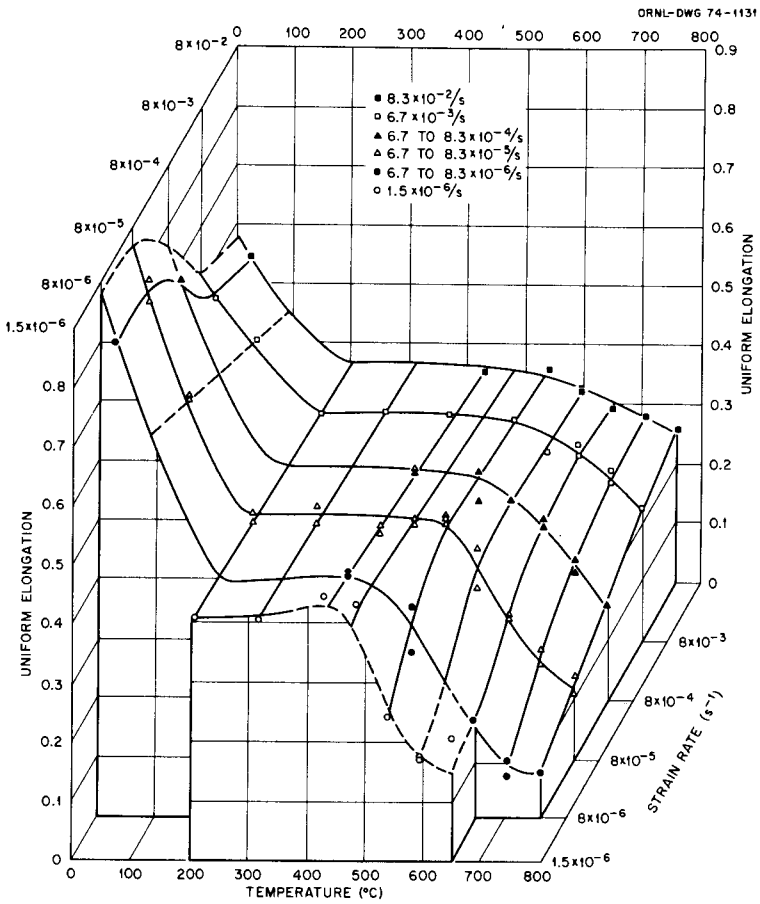

Fig. 5.79. Variation of the Uniform Elongation with Temperature and Strain Rate for Reannealed Type 304 Stainless Steel (Heat 9T2796).

The stress data were taken from about 80 extensometer traces at four plastic strain values: 5×10^{-5}, 1×10^{-4}, 2×10^{-4}, and 5×10^{-4}. We examined the data, qualitatively, in regard to temperature and strain-rate sensitivity and concluded that the stresses corresponding to specific plastic strains were insensitive to strain rate within our accuracy of measurement. We examined several temperature functions, including those which involve modulus compensation of the stresses, and concluded that the following representation was fairly descriptive:

$$f(\varepsilon_{acc}) = T(S - S_{acc}) \ , \qquad (1)$$

where ε_{acc} refers to the engineering strain values in the accomodation strain range, T is absolute temperature (K), S is engineering stress, and

S_{acc} is a constant having a value near 3000 psi (20.7 MPa). Data are plotted in Fig. 5.80. As implied by the linear trend in log-log coordinates, $f(\varepsilon_{acc})$ could be approximated by a power relation.

The second strain range of investigation covered engineering stress-strain data between the knee of the flow curve (approximately 0.1%) and 5%. A Ludwik-type[27] expression was quite successful in this region, and we found:

$$S = C\varepsilon_p^{3/4} + S_0 \ , \tag{2}$$

where S is engineering stress, ε_p is engineering plastic strain, C is a material constant independent of temperature and strain rate, within certain restrictions, and S_0 is a material constant sensitive to both temperature and strain rate. The restriction on C was that temperature could not exceed 593°C except at high strain rates. The value for C was found to be near 1.53×10^5 psi (1055 MPa). We found that S_0 could be represented by a relation similar to Eq. (1) by replacing strain by strain rate. Thus:

$$f(\dot{\varepsilon}) = T(S_0 - \alpha) \ , \tag{3}$$

where $\dot{\varepsilon}$ is engineering strain rate and α is a material constant whose value

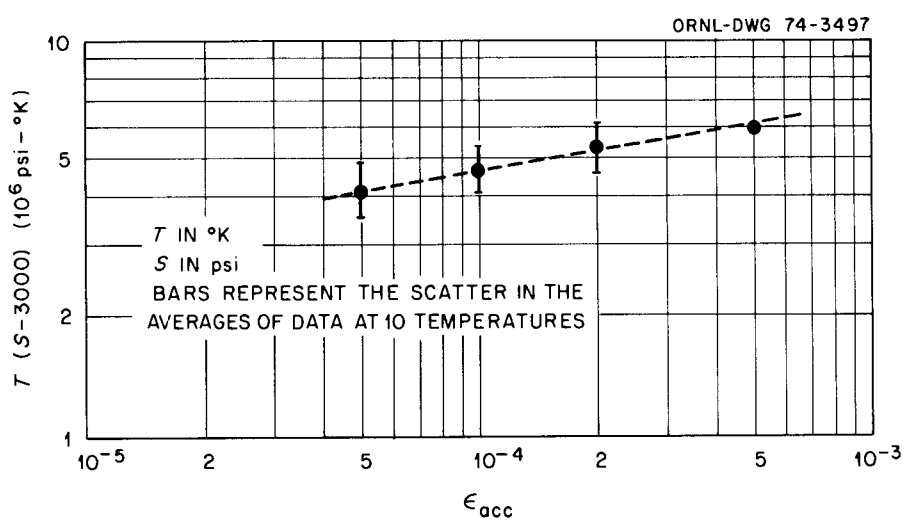

Fig. 5.80. Dependence of Temperature-Compensated Stress on the Plastic Strain Below the Knee of the Flow Curve.

is near 1500 psi (10.34 MPa). The temperature-compensated parameter involving S_0 is shown plotted against strain rate in Fig. 5.81. Although plotted in semi-log coordinates with the log axis being strain rate, an equally good fit was observed when the parameter was plotted on log-log coordinates.

The quantities plotted in Figs. 5.80 and 5.81, or analytical expressions representing them, can be used in conjunction with the known elastic modulus data for type 304 stainless steel to construct monotonic tensile curves valid in the strain range from 0 to about 5%. We are currently examining analytical expressions for representing the quantities and hope to develop a monotonic flow model in the next quarter.

The third range of plastic strain data, which was of interest in regard to developing representation, covered the region from 0.1% to the uniform strain at the ultimate. This range, of course, overlapped the strain range used to develop Eq. (2), but the stress-strain datum pairs used in the third range were obtained from the tensile machine load-cross-head displacement charts rather than from extensometers. Further, data were processed on the basis of true-stress vs true-strain rather than

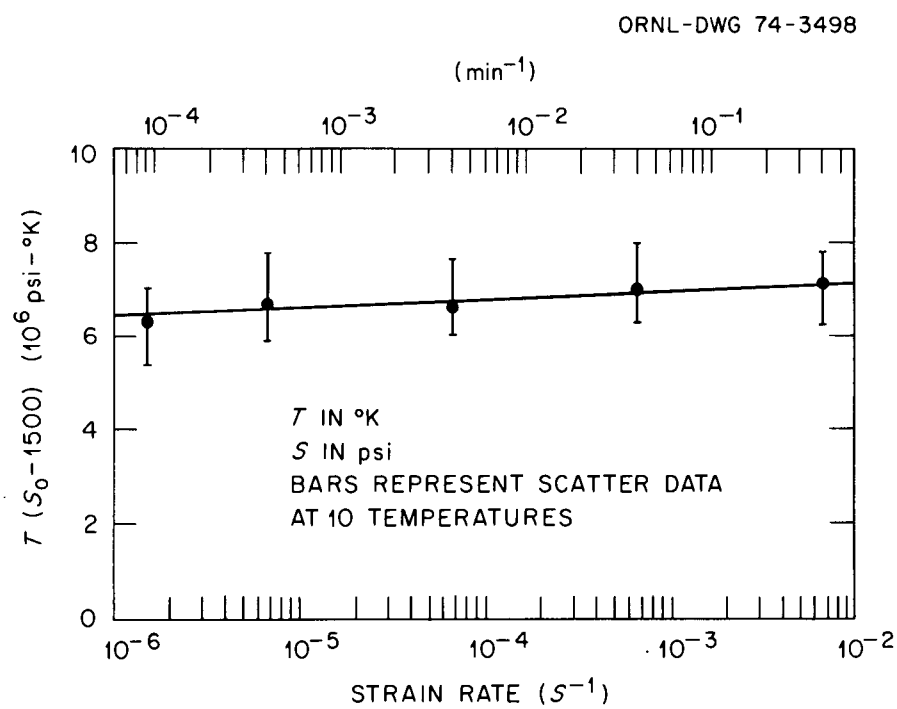

Fig. 5.81. Dependence of Temperature-Compensated Yield Stress, S_0, on Strain Rate.

Table 5.35. Values for the Strain Hardening Exponent, m, and Strength Coefficient, k, for Reannealed Type 304 Stainless Steel

Temperature		Strain Rate	Hollomon Equation			Ludwik Equation			
(°c)	(°F)	(Sec^{-1})	m	ln k	Variance	m'	ln k'	σ_0	Variance
25	77	6.7×10^{-6}	0.35	11.9	2.6×10^{-2}	0.76	12.1	2.2×10^{4}	2.2×10^{-4}
		6.7×10^{-5}	0.33	11.9	2.8×10^{-2}	0.78	12.1	2.4	1.3×10^{-4}
		8.3×10^{-5}	0.31	11.8	2.3×10^{-2}	0.76	12.1	2.5	4.7×10^{-4}
		6.7×10^{-4}	0.31	11.9	2.5×10^{-2}	0.77	12.1	2.6	1.3×10^{-4}
		6.7×10^{-3}	0.29	11.7	2.2×10^{-2}	0.77	12.0	2.8	3.6×10^{-4}
		8.3×10^{-2}	0.35	11.8	5.3×10^{-3}	0.73	12.0	2.8	7.2×10^{-5}
93	200	6.7×10^{-5}	0.33	11.7	1.6×10^{-2}	0.72	12.0	1.9	6.6×10^{-4}
		6.7×10^{-5}	0.35	11.7	2.0×10^{-2}	0.75	12.0	1.8	1.1×10^{-3}
		6.7×10^{-3}	0.31	11.7	1.8×10^{-2}	0.75	12.0	2.1	7.7×10^{-4}
204	400	1.5×10^{-6}	0.40	11.6	2.7×10^{-2}	0.85	12.1	1.3	1.0×10^{-3}
		6.7×10^{-5}	0.36	11.6	2.0×10^{-2}	0.77	12.1	1.5	5.7×10^{-4}
		6.7×10^{-5}	0.37	11.6	2.3×10^{-2}	0.78	12.1	1.4	9.1×10^{-4}
		6.7×10^{-3}	0.32	11.5	2.1×10^{-2}	0.81	12.1	1.7	1.1×10^{-3}
316	600	1.5×10^{-6}	0.41	11.7	2.9×10^{-2}	0.87	12.3	1.3	5.8×10^{-4}
		6.7×10^{-5}	0.37	11.7	2.2×10^{-2}	0.80	12.1	1.5	7.0×10^{-4}
		8.3×10^{-5}	0.37	11.6	2.7×10^{-2}	0.82	12.2	1.3	1.6×10^{-3}
		6.7×10^{-3}	0.37	11.5	2.7×10^{-2}	0.88	12.2	1.4	1.5×10^{-3}
427	800	1.5×10^{-6}	0.44	11.7	3.6×10^{-2}	0.90	12.2	1.1	2.7×10^{-3}
		6.7×10^{-6}	0.42	11.8	0.93×10^{-3}	0.60	11.9	0.82	4.9×10^{-3}
		6.7×10^{-6}	0.43	11.7	2.2×10^{-2}	0.79	12.1	1.1	7.5×10^{-4}
		6.7×10^{-5}	0.42	11.7	2.1×10^{-2}	0.79	12.1	1.2	5.5×10^{-4}
		8.3×10^{-5}	0.40	11.6	2.2×10^{-2}	0.79	12.2	1.2	8.1×10^{-4}
		6.7×10^{-4}	0.38	11.7	1.8×10^{-2}	0.77	12.1	1.3	5.6×10^{-4}
		6.7×10^{-4}	0.40	11.6	2.2×10^{-2}	0.82	12.1	1.2	4.4×10^{-4}
		6.7×10^{-3}	0.37	11.6	2.2×10^{-2}	0.81	12.1	1.3×10^{4}	9.4×10^{-4}
		8.3×10^{-2}	0.42	11.7	$1.0 \quad 10^{-2}$	0.80	12.1	1.4	1.3×10^{-3}
482	900	1.5×10^{-6}	0.43	11.6	$2.2 \quad 10^{-2}$	0.80	12.1	1.0	1.1×10^{-3}
		6.7×10^{-5}	0.42	11.7	$2.2 \quad 10^{-2}$	0.79	12.1	1.0	5.3×10^{-4}
		8.3×10^{-5}	0.40	11.6	$2.1 \quad 10^{-2}$	0.76	12.1	1.1	1.2×10^{-3}
538	1000	1.5×10^{-6}	0.37	11.4	$1.6 \quad 10^{-2}$	0.77	12.0	0.96	6.1×10^{-4}
		6.7×10^{-6}	0.38	11.5	$1.5 \quad 10^{-2}$	0.73	11.9	1.0	4.9×10^{-4}
		6.7×10^{-5}	0.43	11.6	$1.9 \quad 10^{-2}$	0.76	12.0	0.90	9.1×10^{-4}
		6.7×10^{-5}	0.42	11.6	$2.1 \quad 10^{-2}$	0.75	12.0	0.88	7.8×10^{-4}
		8.3×10^{-5}	0.41	11.6	$2.3 \quad 10^{-2}$	0.77	12.1	1.0	1.3×10^{-3}
		6.7×10^{-4}	0.40	11.5	$2.2 \quad 10^{-2}$	0.80	12.0	1.1	5.2×10^{-4}
		6.7×10^{-3}	0.38	11.5	$1.9 \quad 10^{-2}$	0.79	12.0	1.1	7.6×10^{-4}
		8.3×10^{-2}	0.45	11.6	5.4×10^{-3}	0.69	11.9	0.93	9.2×10^{-4}

Table 5.35. (Continued)

Temperature (°C)	Temperature (°F)	Strain Rate (Sec^{-1})	Hollomon Equation m	Hollomon Equation $\ln k$	Hollomon Equation Variance	Ludwik Equation m'	Ludwik Equation $\ln k'$	Ludwik Equation σ_0	Ludwik Equation Variance
593	1100	1.5×10^{-6}	0.33	11.2	3.7×10^{-3}	0.51	11.4	0.66×10^{4}	3.3×10^{-3}
		1.5×10^{-6}	0.35	11.2	6.1×10^{-3}	0.63	11.6	0.76	4.4×10^{-3}
		6.7×10^{-6}	0.33	11.3	5.3×10^{-3}	0.56	11.5	0.88	2.7×10^{-3}
		6.7×10^{-5}	0.39	11.4	1.3×10^{-2}	0.70	11.8	0.88	2.3×10^{-3}
		8.3×10^{-5}	0.38	11.4	1.1×10^{-2}	0.69	11.9	0.91	2.1×10^{-3}
		6.7×10^{-4}	0.39	11.5	1.5×10^{-2}	0.72	11.9	0.96	1.5×10^{-3}
		6.7×10^{-3}	0.39	11.5	1.3×10^{-2}	0.71	11.9	0.94	1.6×10^{-3}
		6.7×10^{-2}	0.50	11.7	1.5×10^{-4}	0.52	11.7	0.96	1.3×10^{-4}
		8.3×10^{-2}	0.51	11.7	1.1×10^{-3}	0.64	11.8	0.62	6.9×10^{-4}
649	1200	1.5×10^{-6}	0.27	10.7	5.8×10^{-3}	0.63	11.1	0.84	7.9×10^{-3}
		6.7×10^{-6}	0.29	11.0	2.8×10^{-3}				
		6.7×10^{-5}	0.31	11.2	3.5×10^{-3}	0.45	11.3	0.66	3.0×10^{-3}
		8.3×10^{-5}	0.35	11.3	8.0×10^{-3}	0.64	11.7	0.81×10^{4}	5.8×10^{-3}
		6.7×10^{-4}	0.38	11.3	9.2×10^{-3}	0.67	11.7	0.78	2.6×10^{-3}
		6.7×10^{-3}	0.38	11.4	1.2×10^{-2}	0.68	11.8	0.86	2.2×10^{-3}
		6.7×10^{-3}	0.37	11.4	1.0×10^{-2}	0.69	11.8	0.92	2.3×10^{-3}
		8.3×10^{-2}	0.37	11.5	1.3×10^{-3}	0.57	11.6	1.2	5.2×10^{-4}
704	1300	6.7×10^{-6}	0.19	10.5	9.8×10^{-4}				
		6.7×10^{-6}	0.21	10.5	6.3×10^{-4}				
		6.7×10^{-5}	0.26	10.8	1.0×10^{-3}				
		8.3×10^{-5}	0.28	11.0	2.7×10^{-3}				
		6.7×10^{-4}	0.32	11.1	3.3×10^{-3}	0.45	11.2	0.53	2.9×10^{-3}
		6.7×10^{-4}	0.32	11.1	5.6×10^{-3}	0.55	11.3	0.74	5.1×10^{-3}
		6.7×10^{-3}	0.36	11.3	6.9×10^{-3}	0.60	11.5	0.73	2.5×10^{-3}
		6.7×10^{-3}	0.37	11.3	8.9×10^{-3}	0.64	11.6	0.79	3.6×10^{-3}
		8.3×10^{-2}	0.40	11.4	3.6×10^{-3}	0.58	11.6	0.73	1.9×10^{-3}
760	1400	6.7×10^{-6}	0.065	9.74	3.9×10^{-4}				
		6.7×10^{-5}	0.17	10.3	1.1×10^{-3}				
		6.7×10^{-5}	0.21	10.5	1.0×10^{-3}				
		6.7×10^{-4}	0.26	10.8	1.3×10^{-3}				
		6.7×10^{-4}	0.30	11.0	3.2×10^{-3}	0.44	11.1	0.55	2.6×10^{-3}
		8.3×10^{-2}	0.36	11.3	1.1×10^{-3}	0.48	11.4	0.62	4.3×10^{-4}

Hollomon: $\ln \sigma = \ln k + m \ln \varepsilon_p$

Ludwik: $\ln (\sigma - \sigma_0) = \ln k' + m' \ln \varepsilon_p$
σ, σ_0, k, k' in psi (1 psi = 6.895 kPa), Variance given by
$\{\Sigma[\ln \sigma(\text{observed}) - \ln \sigma(\text{calculated})]^2\}/(\text{number of data})$

engineering stress vs engineering strain values. Approximately 60 sets of tensile data were fitted to the Hollomon[26] expression, and the results are given in Table 5.35 in terms of the strain-hardening exponent, m, and the strength coefficient, k, defined in the Hollomon equation:

$$\sigma = k\varepsilon_p^{\,m} , \tag{4}$$

where σ is true stress and ε_p is true plastic strain. The surface generated by plotting the Hollomon strain-hardening exponent against temperature and strain rate is shown in Fig. 5.82. The trend at low temperatures suggests that m is insensitive to strain rate and rises linearly with temperature to a maximum somewhere above 400°C (750°F). At high temperatures m decreases with temperature at a rate that depends on strain rate. The value of m is thought to be related to the true strain at the ultimate strength for most materials. This does not seem to be the case for

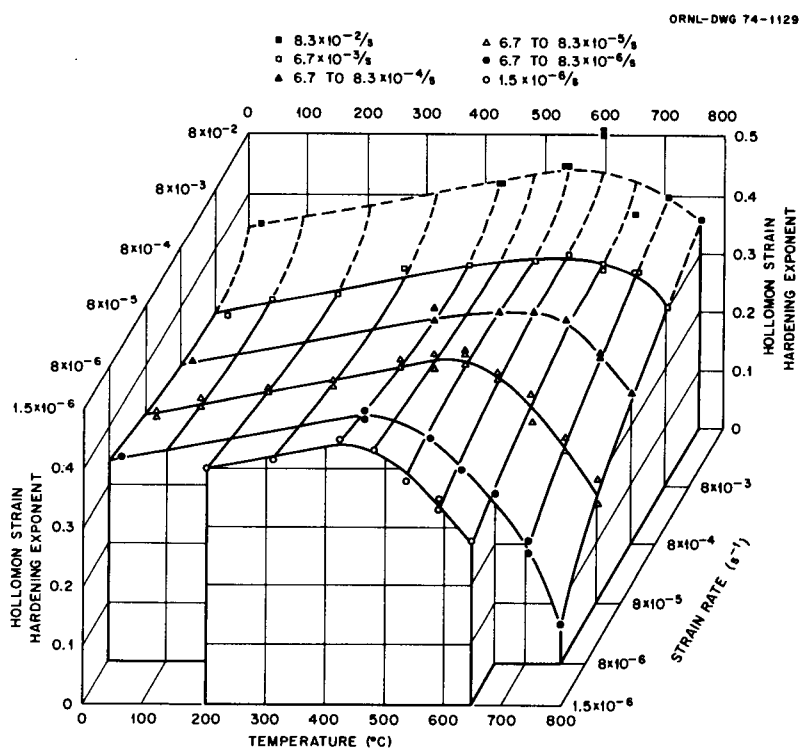

Fig. 5.82. Variation of the Hollomon Strain-Hardening Exponent with Temperature and Strain Rate for Reannealed Type 304 Stainless Steel (Heat 9T2796).

reannealed type 304 stainless steel, however, as is evident by comparing Fig. 5.79 with Fig. 5.82. Moreover, examination of the variance data provided in Table 5.35 suggests that the Hollomon expression is not a good fit to the data.

The Ludwik[27] expression was also examined. Data are given in Table 5.35 in terms of the strain-hardening exponent, m', and the strength coefficient, k', defined by the equation:

$$\sigma = k'\varepsilon^{m'} + \sigma_0' \ , \tag{5}$$

where σ_0' is a material constant, similar to S_0 in Eq. (2) in regard to temperature and strain rate sensitivity. The surface representing dependence of the Ludwik strain hardening exponent on temperature and strain rate is shown in Fig. 5.83. Again we observed a peak in the strain-hardening exponent above room temperature, but this occurred at a lower temperature than for the Hollomon strain-hardening exponent. Above 500°C (932°F) the Ludwik strain hardening exponent decreased precipitously and approached values typical of the Hollomon exponent. The variance of fit for the Ludwik equation to the data suggested a good fit at low temperatures but a poor fit at high temperatures and low strain rates.

The data were also fitted to the Voce[33] equation by T. A. Hebble of the ORNL statistics group, and the best fit values for each test are provided in Table 5.36. The constants are defined by the equation:

$$\sigma = (\sigma_0 - \sigma_\infty)e^{-\varepsilon_p/\varepsilon_c} + \sigma_\infty \ , \tag{6}$$

where again σ is the true stress and ε_p is the true plastic strain. The σ_0 term was observed to be greater than the σ_0' and S_0' terms of the Ludwik equations but exhibited a similar temperature and strain rate sensitivity. In Fig. 5.84 values for σ_0 from Eq. (6) are plotted against S_0 from Eq. (2). The trend is approximately linear and it appears that σ_0 can be represented as about $1.1S_0$. Thus Eq. (3) can be modified and used to calculate σ_0. We also observed that ε_c and σ_∞ constants in the Voce equation exhibited similar temperature and strain rate dependencies. This is illustrated

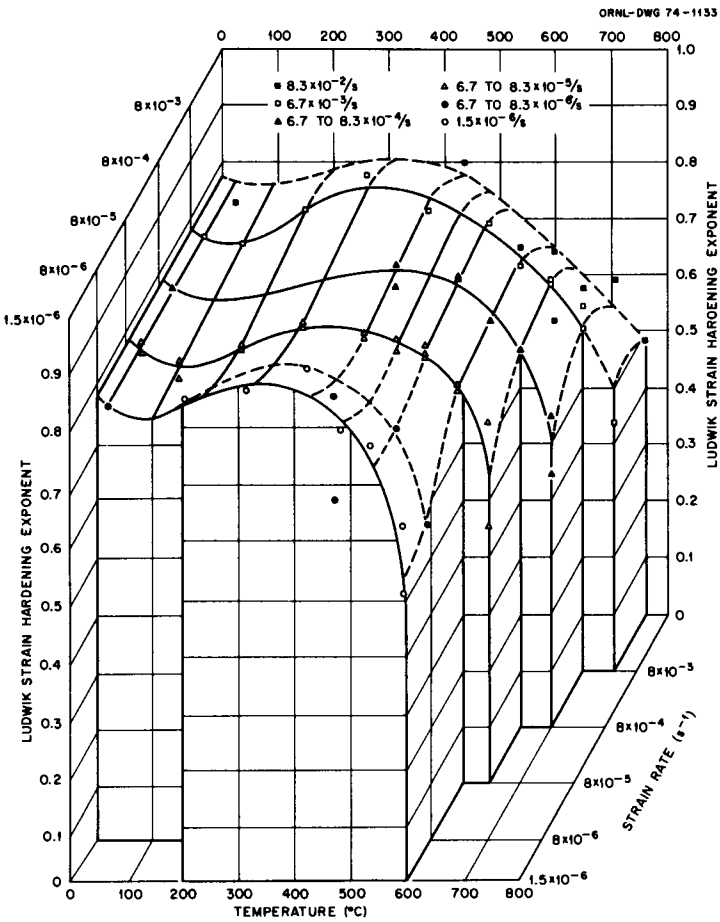

Fig. 5.83. Variation of the Ludwik Strain-Hardening Exponent with Temperature and Strain Rate for Reannealed Type 304 Stainless Steel (Heat 9T2796).

in Fig. 5.85 which plots values for σ_∞ and the associated ε_c. We are currently investigating the significance of this interrelation in regard to its impact on a flow model. As a first approximation we assume that a unique relation between σ_∞ and ε_c exists, and hence a relation describing the influence of temperature and strain rate on one material constant eliminates the need for a similar representation in regard to the other.

We have made several attempts to develop representations for σ_∞ in terms of temperature and strain rate. Currently, we are working with two relations, one independent of strain rate for low-temperature application, and one involving strain rate for high-temperature application. The low-temperature representation is simply a polynominal involving temperature as the independent variable. Thus

Table 5.36. Values for Voce Constants Obtained by Regression Analysis of Tensile Data

Specimen	Temperature (°C)	Temperature (°F)	Strain Rate (min^{-1})	σ_0 (ksi)	σ_∞ (ksi)	ε_c
7RP36[a]	25	77	0.025	30.80	229.1	0.722
7RP42[a]			0.025	28.88	244.3	0.745
7RP46[a]			0.025	27.74	243.3	0.748
7RP44[a]			0.025	28.31	243.2	0.755
7RP49			0.025	27.95	257.7	0.828
7RP175	25	77	0.0004	26.63	312.0	1.082
7RP176			0.004	28.37	317.2	1.082
7RP10			0.005	28.31	276.6	0.874
7RP177			0.04	29.69	287.5	0.948
7RP231			0.40	31.36	239.4	0.791
7RP186			5.0	31.12	172.2	0.500
7RP181	93	200	0.004	21.96	140.2	0.368
7RP204			0.004	20.14	140.2	0.373
7RP222			0.4	22.76	133.1	0.340
7RP246	204	400	0.00009	13.47	136.9	0.386
7RP183			0.004	16.38	123.6	0.316
7RP207			0.004	15.52	127.5	0.346
7RP235			0.4	17.99	121.9	0.323
7RP244	316	600	0.00009	13.15	181.8	0.535
7RP185			0.004	15.54	135.1	0.364
7RP11			0.005	13.97	146.5	0.402
7RP236			0.40	13.89	130.9	0.383
7RP253	427	800	0.00009	9.98	153.4	0.454
7RP174			0.0004	14.29	122.8	0.301
7RP224			0.0004	11.59	132.8	0.358
7RP187			0.004	12.76	131.1	0.340
7RP12			0.005	12.69	122.7	0.293
7RP178			0.04	14.57	123.7	0.320
7RP225			0.04	13.91	136.2	0.386
7RP226			0.4	13.53	121.5	0.338
7RP188			5.0	14.53	107.7	0.272
7RP252	482	900	0.00009	11.04	123.5	0.352
7RP189			0.004	12.70	127.7	0.347
7RP13			0.005	11.86	111.1	0.264
7RP254	533		0.00009	10.49	81.06	0.206
7RP227			0.0004	11.71	91.12	0.256
7RP190			0.004	10.26	105.2	0.282
7RP203			0.004	10.17	105.9	0.292
7RP14			0.005	11.16	105.6	0.266

Table 5.36. (Continued)

Specimen	Temperature (°C)	Temperature (°F)	Strain Rate (min^{-1})	σ_0 (ksi)	σ_∞ (ksi)	ε_c
7RP228			0.04	11.87	114.5	0.336
7RP229			0.4	12.10	103.4	0.286
7RP201			5.0	17.89	92.80	0.230
7RP165	593	1000	0.00009	9.676	42.97	0.0656
7RP256			0.00009	10.21	45.19	0.0790
7RP195			0.0004	11.72	52.05	0.0880
7RP192			0.004	10.04	72.12	0.170
7RP15			0.005	10.75	71.24	0.153
7RP193			0.04	10.79	82.18	0.1995
7RP182			0.4	10.83	84.99	0.202
7RP194			4.0	10.16	78.77	0.179
7RP202			5.0	11.01	88.94	0.228
7RP257	649	1200	0.00009	9.09	30.84	0.0788
7RP209			0.0004	10.10	35.09	0.053
7RP179			0.004	11.00	46.85	0.0808
7RP16			0.005	8.45	49.67	0.0895
7RP217			0.04	9.44	60.50	0.138
7RP199			0.40	10.07	69.75	0.169
7RP230			0.40	10.63	68.75	0.164
7RP206			5.0	16.60	70.49	0.156
7RP197	704	1300	0.0004			
7RP232			0.0004	9.27	22.15	0.0214
7RP180			0.004			
7RP17			0.005	9.68	32.29	0.0394
7RP184			0.04	9.33	42.87	0.080
7RP233			0.04	9.80	43.61	0.085
7RP200			0.4	9.49	52.92	0.1025
7RP223			0.4	9.30	55.15	0.1240
7RP208			5.0	12.07	69.70	0.1790
7RP221	760	1400	0.0004	10.72	14.58	0.0146
7RP161			0.004	10.05	22.19	0.0368
7RP218			0.004			
7RP242			0.04			
7RP240			0.4			
7RP196			5.0			

[a]Specimens not in standard reannealed condition: 7RP36, A 240; 7RP42, annealed at 982°C (1800°F); 7RP44, annealed at 1038°C (1900°F); 7RP46, annealed at 1065°C (1950°F).

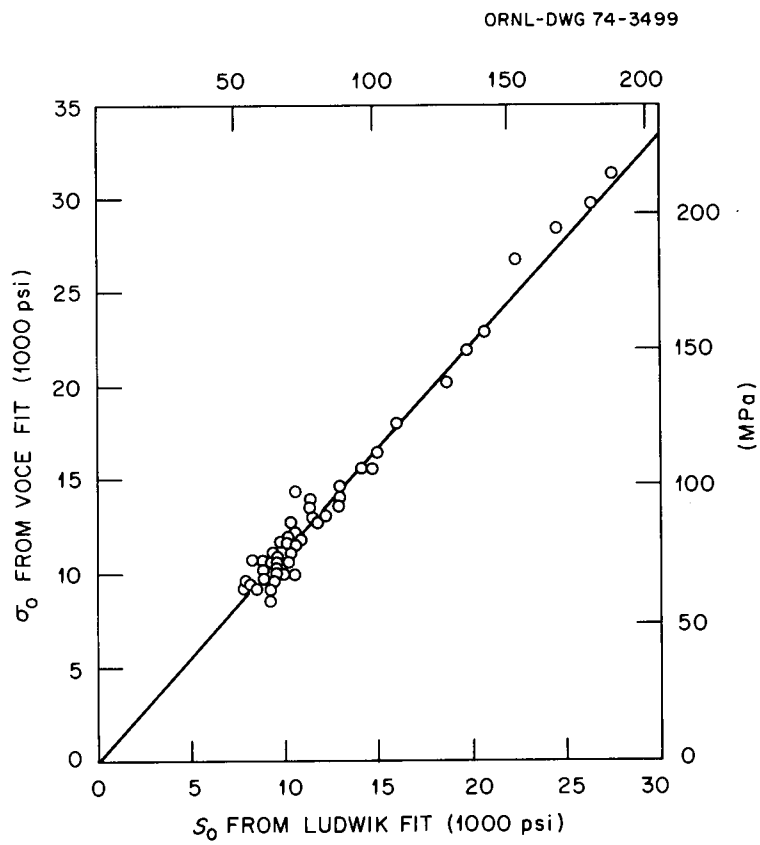

Fig. 5.84. Comparison of Voce and Ludwik Yield Constants for Type 304 Stainless Steel.

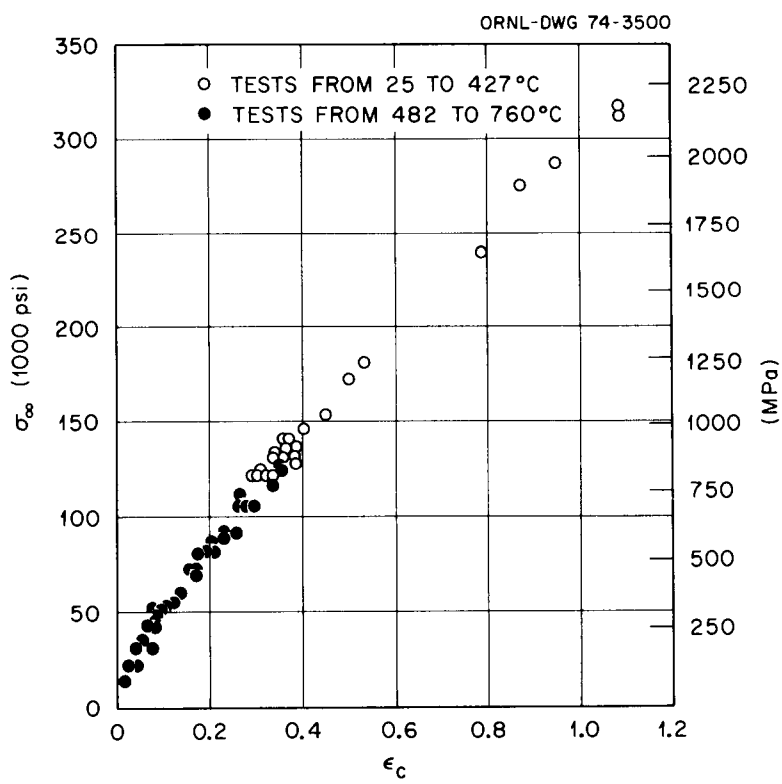

Fig. 5.85. Interrelation of Voce Constants σ_∞ and ε_c.

$$\sigma_\infty = C_0 + C_1 T + C_2 T^2 + \ldots , \tag{7}$$

where T is temperature in °C ($T_K - 298$) and C_i are determined by a least squares method.

The high-temperature representation is of the form:

$$\sigma_\infty = A_\infty \exp[\alpha(\dot{\varepsilon})(T - T_\infty)] , \tag{8}$$

where A_∞ is near 210,000 psi (1447.9 MPa), T_∞ is 700°K, and $\alpha(\dot{\varepsilon})$ is a function of engineering strain rate and is still under development. A plot of σ_∞ against temperature, which shows the range of application for Eqs. (7) and (8), is provided in Fig. 5.86. Currently, promising representations for $\alpha(\dot{\varepsilon})$, are being checked by comparing the predictions of the flow model against experimentally observed data. Of considerable interest to us is the ability of the Voce equation to predict engineering ultimate strength data, uniform tensile strains, and minimum creep rate information. By equating the increases in true stress associated in Poisson's contraction to the increase in true flow stress associated with

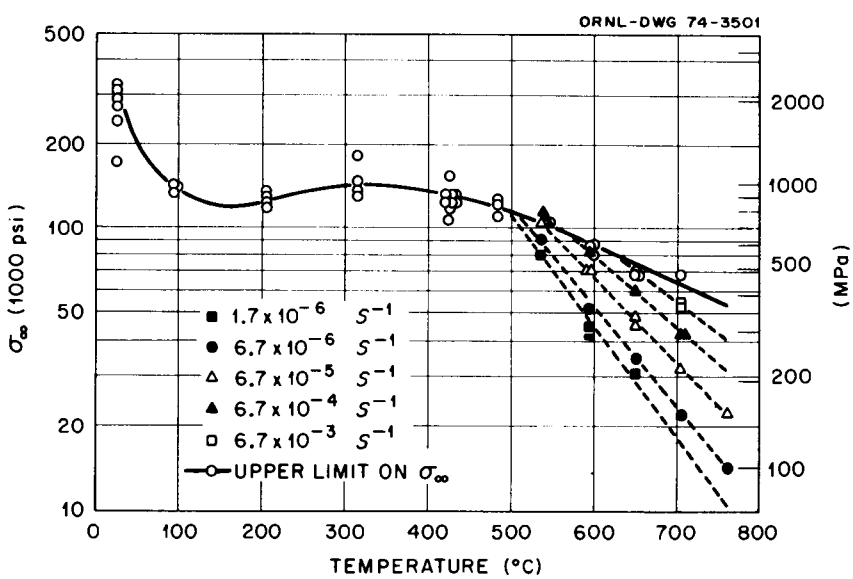

Fig. 5.86. Influence of Temperature and Strain Rate on the σ_∞ Values of the Voce Equation.

strain hardening one can show:

$$S_{uts} = \left(\frac{\sigma_\infty}{1 + \varepsilon_c}\right)^{1+\varepsilon_t} \left(\frac{\varepsilon_c}{\sigma_\infty - \sigma_0}\right)^{\varepsilon_c} , \tag{9}$$

and

$$\varepsilon_u = \left(\frac{\sigma_\infty}{1 + \varepsilon_c}\right) \left(\frac{1}{S_{uts}}\right) - 1 , \tag{10}$$

where S_{uts} is the engineering ultimate tensile strength and ε_u is the engineering uniform strain. Assuming a power relation between engineering strain rate and $\alpha(\varepsilon)$, we calculate S_{uts} and ε_u for different strain rates at temperatures above 427°C (800°F). Curves showing the predicted variation in S_{uts} with strain rate are presented in Fig. 5.87, while a curve representing the interrelation of ε_u and S_{uts} is shown in Fig. 5.88. We observed that Eq. (9) agreed very well with experimental data, while Eq. (10) overestimated the uniform strain at temperatures below 649°C (1200°F).

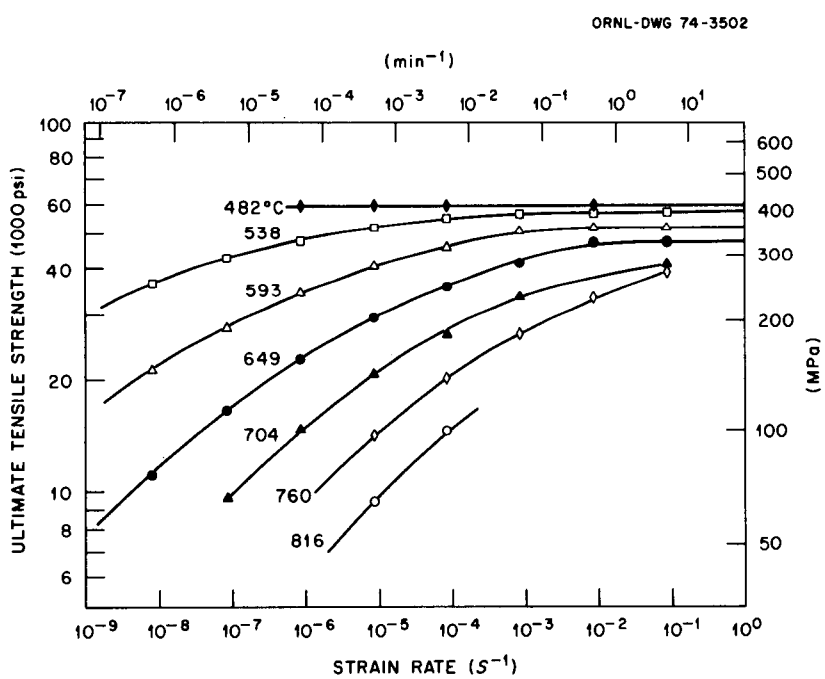

Fig. 5.87. Ultimate Tensile Strength Predicted by Voce Equation.

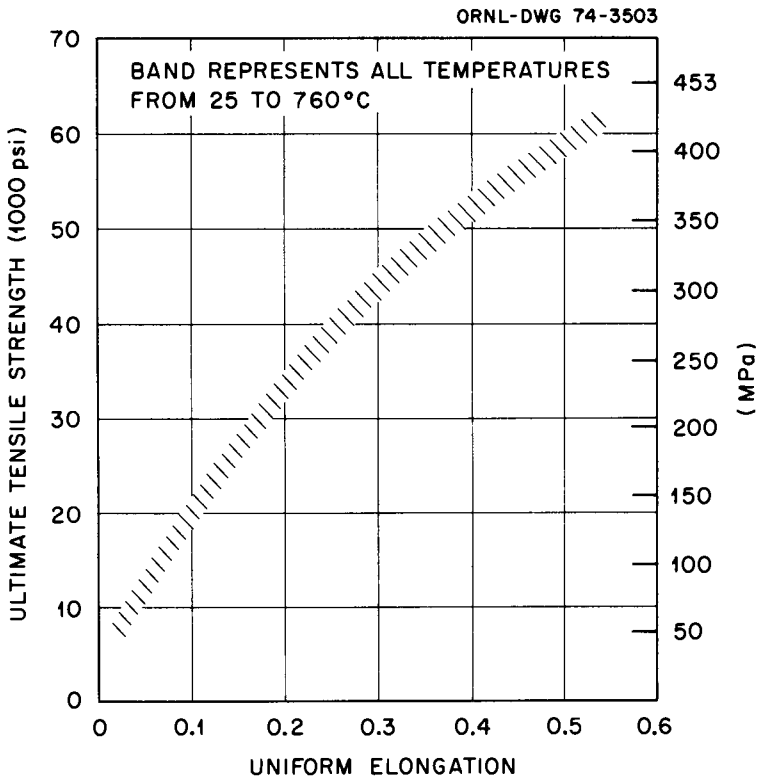

Fig. 5.88. Relation Between the Ultimate Tensile Strength and the Uniform Strain Predicted by the Voce Equation.

5.5.1.3 Creep Testing

A paper has been submitted to a session on the "Elevated Temperature Properties of Austenitic Stainless Steels" to be part of the ASME Pressure Vessels and Piping Division Meeting at Miami, Florida, June 24–28, 1974. The paper deals with the isochronous stress-strain behavior of the reference heat of type 304 stainless steel (heat 9T2796) to 5000 hr.

Other efforts on creep testing are involved with completing a report on the short time creep-rupture characterization of the reference heat (heat 9T2796) in the reannealed condition. As part of this effort, representations are being developed for the stress and temperature dependence of the minimum creep rate, initiation of tertiary creep, and rupture life. Four approaches are being considered. The first deals initially with the stress dependence of isothermal data and, having developed a representation, addresses the temperature dependence of the constants in the representation. The second approach deals initially with the temperature dependence of isostatic data and, having developed this representation, addresses the

stress dependence of the constants in the representation. The third approach examines the use of time-temperature-stress parameters to process all the data simultaneously, while in the fourth approach features common to tensile and creep tests are being examined, and we are attempting to develop relationships compatible with these and other data from both tests. This approach is very ambitious in view of the fact that the relationships are entirely empirical. Approximately 40 data sets are available from creep tests ranging in time from 1 to 10,000 hr and for temperatures from 482 to 816°C (900–1500°F).

Examination of isothermal creep-rupture data suggested to us that the Norton[34] relation

$$\text{rate} = (S/A)^n \tag{11}$$

is a good approximation over the range of temperature and stress for which data are available. Values for the constants A and n were determined by regression analysis for each temperature, and these are given in Table 5.37 for tertiary creep, rupture, and minimum creep rate. The temperature dependence of A is plotted in Fig. 5.89 and, as implied, the temperature dependence appears to follow the relation:

$$A = A_0 e^{B(T-T_0)} , \tag{12}$$

where A_0, B, and T_0 are material constants and T is the Kelvin temperature. The A values for minimum creep, rupture, and tertiary creep appear to converge at a temperature near 700 K and, assuming this for T_0, an A_0 value near 135,000 psi (931 MPa).

We are currently examining methods for describing the temperature dependence of n. At high temperatures, above 649°C, all the n values appear to converge on a value near 6.5; hence, no problem exists in this area. At temperatures of interest to the LMFBR, however, n is quite sensitive to temperature. At low temperatures there is a possibility that n for tertiary creep and rupture converges on a value near 10, while n for minimum creep rate approaches a value near 12.

Table 5.37. Values for the Strength Coefficients and Exponents in the Norton Equation[a]

Temperature		Tertiary Creep			Rupture Life			Minimum Creep Rate		
(°C)	(°F)	A_3[b]	n_3	R	A_R[b]	n_R	R	A_m[b]	n_m	R
538	1000	64.5(447)	9.83	0.997	68.5(472)	9.24	0.983	55.1(380)	11.8	0.996
593	1100	48.7(336)	8.75	0.987	49.2(339)	9.14	0.994	38.4(265)	10.9	0.997
649	1200	35.8(247)	6.62	0.968	36.3(250)	7.87	0.992	26.8(185)	7.70	0.981
704	1300	24.6(170)	7.23	0.986	27.0(186)	7.06	0.996	17.4(120)	6.67	0.998
760	1400	17.8(123)	6.72	0.993	19.3(133)	6.58	0.994	11.6(80)	6.73	0.998
816	1500	13.0(89.6)	6.70	0.998	14.1(97.2)	6.47	0.998	8.39(57.9)	6.65	0.998

[a]RATE = 1/TIME = $(\text{STRESS}/A)^n$ where Stress and A are in ksi or MPa and time is in hours. R is the correlation coefficient.

[b]Values in parentheses are in MPa.

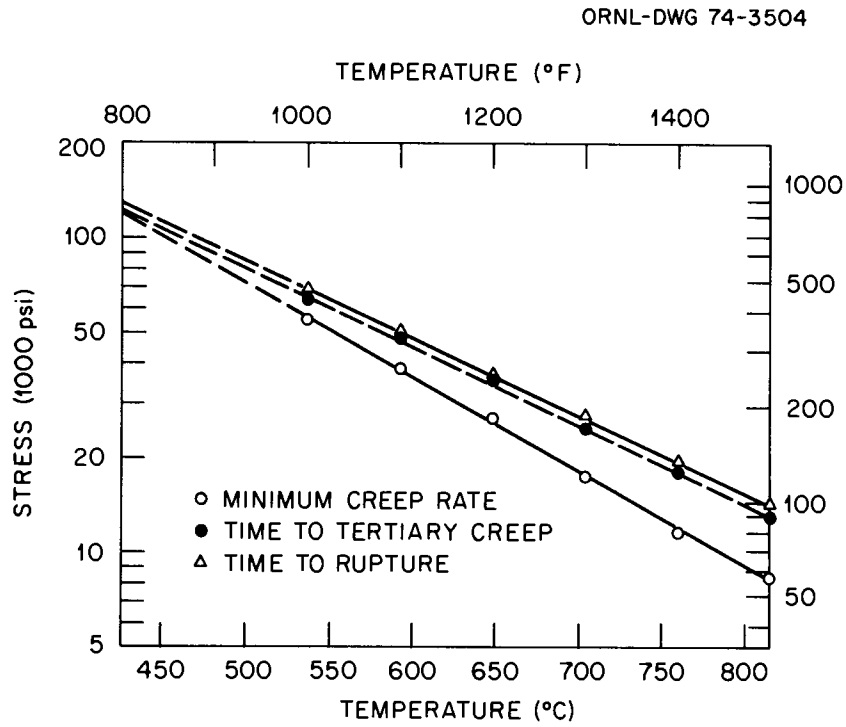

Fig. 5.89. Dependence of the Creep Strength Coefficient of the Norton Equation on Temperature.

Experimentally, most of our eight creep machines have been committed to relatively long-time creep experiments intended to produce data verifying the existing creep law developed for the reference heat of type 304 stainless steel.[35]

Cyclic creep tests are continuing, and tests performed to date are listed in Table 5.38. All but one test have been performed at 593°C (1100°F), and more recent tests, which incorporate an improved specimen design, support qualitatively our previous findings.[36] One test was performed at 649°C (1200°F), and the results are summarized in Fig. 5.90. The tensile stress was held at 12,500 psi (86.2 MPa) and the compressive stress at 10,000 psi (68.95 MPa). As is evident by examining the compressive component, the reversal strains stabilized very quickly and after the first cycle changed by less than 10%. The fourth tensile hold period was doubled (two weeks) but this did not greatly influence the reversal strains. The nonreversal strains agreed reasonably well with the monotonic creep test at 12,500 psi (86.2 MPa).

Table 5.38. Summary of Test Performed Under Cyclic Conditions

Specimen	Temperature (°C)(°F)	Stress,[a] ksi Tensile	Stress,[a] ksi Compressive	Creep Strain Per 168-hr Half Cycle,[b] % 1T	1C	2T	2C	3T	3C	5T	5C	Time in Test (hr)
CRP 9	593(1100)	24.5(169)	22.5(155)	1.47	0.49	1.18	0.57	1.55	0.52	1.62	0.68	3722
CRP 12	593(1100)	22.0(152)	20.0(138)	0.86	0.41	0.45	0.32	0.53	0.36	0.50	0.38	3179
CRP 11	593(1100)	19.5(134)	17.5(121)	0.58	0.22	0.33	0.23	0.28	0.25			1504
CRP 22[c]	593(1100)	17.5(121)	15.0(103)	0.36	0.12	0.19	0.12	0.14	0.11	0.16	0.15	2000
CRP 8	593(1100)	17.0(117)	15.0(103)	0.24	0.19	0.18	0.12	0.13	0.14			1074
CRP 20[c]	593(1100)	15.0(103)	12.5(86)	0.31	0.065	0.12[d]	0.05[d]	0.08	0.065			1000
CRP 10[e]	593(1100)	17.5(121)	17.5(121)	0.33	0.33	0.33	0.25	0.25	0.16			1292
CRP 19[c]	649(1200)	12.5(86)	10.0(69)	1.22	0.94	1.20	1.15	1.23	1.00	1.20	1.14	2490

[a]Values in parentheses are in MPa.

[b]T signifies tension; C signifies compression.

[c]Improved specimen design and extensometer system.

[d]192 hr in tension and 144 hr in compression.

[e]Started in compression.

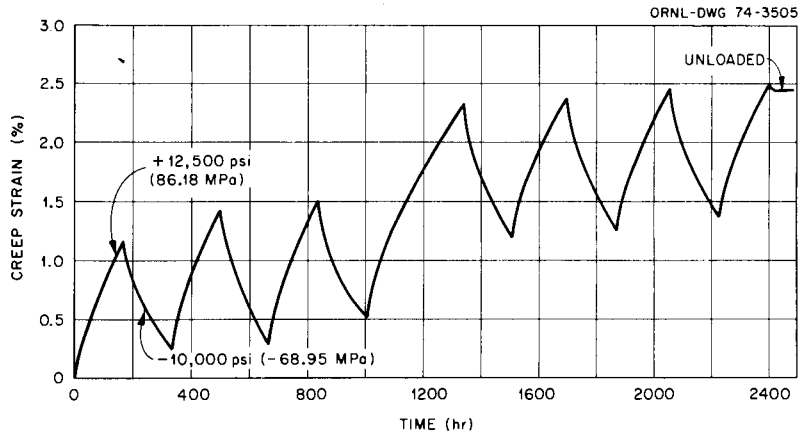

Fig. 5.90. Cyclic Creep Behavior of Type 304 Stainless Steel (Heat 9T2796) at 649°C (1200°F).

5.5.2 Characterization of Product Form — H. E. McCoy

Nothing to report.

5.5.3 Investigation of Creep Failure Under Uniaxial and Multiaxial Conditions — C. C. Schultz, Babcock & Wilcox

No report received.

5.6 MECHANICAL PROPERTIES OF HTGR STEAM GENERATOR AND PRIMARY CIRCUIT MATERIALS — P. L. Rittenhouse

The metallic components in the primary circuit and steam generator of the high-temperature gas-cooled reactor (HTGR) are exposed to helium containing parts per million levels of various contaminant gases (e.g., H_2, CO, CH_4) at temperatures up to about 800°C (1470°F). In addition, steam generator component surfaces are also exposed to steam at temperatures above 500°C (930°F). The helium environment may be oxidizing, reducing, carburizing, or decarburizing to a given alloy depending on its composition, the temperature, and the levels and ratios of the contaminant gaseous species. Because of this, evaluation of the mechanical behavior and thermal stability of these materials must include consideration of the effects of gas-metal reactions.

The purpose of this recently initiated program is to measure the elevated-temperature mechanical properties needed for validation of the design technology of HTGR primary circuit and steam generator materials, with particular emphasis given to the effects of environment. Creep, low-cycle fatigue, creep-fatigue interactions, stress relaxation, and crack growth dynamics will be investigated, and the effect of thermal aging on these will be determined where appropriate. Materials currently scheduled to be studied — in approximate order of priority — are Incoloy 800, 2 1/4 Cr-1 Mo steel, Hastelloy X, 1010/1020 steel, Inconel 617, Hastelloy S, and high-alloy ferritic steels.

Of the tests listed above, only those on subcritical crack growth in 2 1/4 Cr-1 Mo steel have been initiated. These experiments, performed as a cooperative effort with ORNL LMFBR programs, are described in Sect. 5.4.5. Similar testing of 2 1/4 Cr-1 Mo and Incoloy 800 in steam and contaminated helium environments (both materials are used in the current HTGR steam generator design) is planned, and the system and fixtures for this testing have been designed and are currently being prepared.

Most of the quarter's effort in this program has been devoted to the design and construction of the environmental creep facility scheduled to be operative in July 1974. Creep frames and associated hardware, furnaces, power supplies, etc. were procured. Particular attention was devoted to the design of the environmental chamber and to a new creep specimen (a modified double buttonhead) required to permit accurate strain measurement in the restrictive space within the chamber.

An extremely important aspect of all the mechanical property tests is the supply and control of the contaminated helium environment. Several methods for accomplishing this task have been examined and evaluated. All are either of the recirculating loop or once-through type, with various methods of gas supply and control. The method we have chosen is to supply each test chamber with a once-through flow of gas from a carefully prepared and analyzed cylinder. This allows flexibility in the choice of contaminant species and levels, reduced contaminant addition and control problems, and is adaptable to a diversity of test types and

to physically separated equipment. Test environment will be monitored by an on-line chromatograph (H_2, CO, CO_2, O_2, N_2, and CH_4 analysis) and trace moisture analyzer. The gas supply and analysis systems described above will be available for creep and subcritical crack growth experiments in July 1974.

5.7 REFERENCES

1. H. E. McCoy, *Fuels and Materials Development Program Quart. Progr. Rep. Mar. 31, 1973*, ORNL-TM-4250, pp. 89–92.
2. H. E. McCoy, *Fuels and Materials Development Program Quart. Progr. Rep. Sept. 30, 1973*, ORNL-TM-4405, pp. 55–64.
3. H. E. McCoy, *Fuels and Materials Development Program Quart. Progr. Rep. June 30, 1973*, ORNL-TM-4355, pp. 105–11.
4. H. E. McCoy, *Mechanical Properties Test Data for Structural Materials Quart. Progr. Rep. Jan. 31, 1974*, ORNL-4948, pp. 177–83.
5. G. V. Smith, *An Evaluation of the Yield, Tensile, Creep, and Rupture Strengths of Wrought 304, 316, 321, and 347 Stainless Steels at Elevated Temeprature, ASTM Data Ser. Publ.* DS 5-S2, American Society for Testing and Materials, Philadelphia, 1969.
6. W. R. Martin, *Mechanical Properties Test Data for Structural Materials Quart. Progr. Rep. Jan. 31, 1974*, ORNL-4948, Table 5.7, p. 197.
7. H. E. McCoy, *Mechanical Properties Test Data for Structural Materials Quart. Progr. Rep. Jan. 31, 1974*, ORNL-4948, pp. 204–11.
8. H. E. McCoy, *Fuels and Materials Development Program Quart. Progr. Rep. Sept. 30, 1973*, ORNL-TM-4405, pp. 113–16.
9. R. K. Penny and D. L. Marriott, *Design for Creep*, McGraw-Hill, New York, 1971, p. 175.
10. C. R. Brinkman, *Mechanical Properties Test Data for Structural Materials Quart. Progr. Rep. Jan. 31, 1974*, ORNL-4948, pp. 221–26.
11. H. E. McCoy, M. W. Moyer, and T. W. Dews, *Mechanical Properties Test Data for Structural Materials Quart. Progr. Rep. Jan. 31, 1974*, ORNL-4948, pp. 187–94.

12. A. K. Schmieder and A. T. Henry, "Axiality Measurements on Fifty Creep Machines," pp. 43–60 in *Elevated Temperature Testing Problem Areas*, ASTM-STP 488, American Society for Testing and Materials, Philadelphia, 1971.

13. J. A. Clinard and J. S. Crowell, *ORNL User's Manual for CREEP-PLAST Computer Program*, ORNL-TM-4062 (November 1973).

14. G. M. Slaughter, *Welding and Brazing Techniques for Nuclear Reactor Components*, American Society for Metals and U.S. Atomic Energy Commission, Rowman and Littlefield, New York, 1964, p. 95.

15. P. Soo, *Analysis of Structural Materials for LMFBR Coolant-Boundary Conditions*, WARD-304 5T3-5 (November 1972), p. 28.

16. R. T. King, R. E. Adams, and G. M. Goodwin, *Fuels and Materials Development Program Quart. Progr. Rep. Mar. 31, 1972*, ORNL-TM-3797, pp. 210–20.

17. R. T. King, J. K. Alley, and E. Bolling, *Fuels and Materials Development Program Quart. Progr. Rep. Mar 31, 1973*, ORNL-TM-4250, pp. 139–51.

18. R. T. King and E. Bolling, *Fuels and Materials Development Program Quart. Progr. Rep. Dec. 31, 1972*, ORNL-TM-4105, pp. 5.10–5.21.

19. R. T. King and G. M. Goodwin, *Fuels and Materials Development Program Quart. Progr. Rep. Dec. 31, 1971*, ORNL-TM-3703, p. 209.

20. J. O. Stiegler and R. T. King, *Fuels and Materials Development Program Quart. Progr. Rep. Sept. 30, 1972*, ORNL-TM-4055, pp. 5.36–5.49.

21. R. T. King and E. Bolling, Sect. 5.3.1 of this report.

22. *Liquid Metal Fast Breeder Reactor Handbook*, HEDL-TME 71-32, p. 304SS-12 (May 13, 1971).

23. B. R. Dewey, *Fuels and Materials Development Program Quart. Progr. Rep. Sept. 30, 1972*, ORNL-TM-4055, pp. 5.53–5.55.

24. R. L. Klueh, *Mechanical Properties Test Data for Structural Materials Quart. Progr. Rep. Jan. 31, 1974*, ORNL-4948, pp. 255–64.

25. G. V. Smith, *Supplement Report on the Elevated-Temperature Properties of Chromium-Molybdenum Steels (An Evaluation of 2 1/4 Cr-1 Mo Steel), ASTM Data Ser. Publ.*, DS 6-S2, American Society for Testing and Materials, Philadelphia, March 1971.

26. J. H. Hollomon, "Tensile Deformation," *Trans. AIME* 162: 268 (1945).

27. P. Ludwik, *Elemente der Technologischen Mechanik*, Springer, Berlin, 1900.

28. H. E. McCoy, *MSR Program Semiann. Progr. Rep. Aug. 31, 1972*, ORNL-4832, pp. 76–79.

29. R. L. Klueh and D. A. Canonico, *Fuels and Materials Development Program Quart. Progr. Rep. Sept. 30, 1973*, ORNL-TM-4405, pp. 32–37.

30. R. L. Klueh, *Mechanical Properties Test Data for Structural Materials Quart. Progr. Rep. Jan. 31, 1974*, ORNL-4948, pp. 275–78.

31. R. L. Klueh and D. A. Canonico, *Fuels and Materials Development Program Quart. Progr. Rep. June 30, 1973*, ORNL-TM-4355, pp. 25–32.

32. R. W. Swindeman, *Mechanical Properties Test Data for Structural Materials Quart. Progr. Rep. Jan. 31, 1974*, ORNL-4948, pp. 278–85.

33. E. Voce, "The Relationship Between Stress and Strain for Homogeneous Deformation," *J. Inst. Metals* 74: 537 (1948).

34. F. H. Norton, *The Creep of Steel at High Temperatures*, McGraw-Hill, New York, 1929.

35. C. E. Pugh, *High-Temperature Structural Design Methods for LMFBR Components Quart. Progr. Rep. Sept. 30, 1972*, ORNL-TM-4058, pp. 31–43.

36. R. W. Swindeman, *High-Temperature Structural Design Methods for LMFBR Components Quart. Progr. Rep. June 30, 1973*, ORNL-TM-4356 (December 1973), pp. 11–15.

6. WESTINGHOUSE ADVANCED REACTORS DIVISION

E. C. Bishop

6.1 INTRODUCTION

The program being performed at Westinghouse Advanced Reactors Division (ARD) is entitled "Validation of High Temperature Design Methods and Criteria," (189a No. 04165). Two of the tasks in this program are "Basic Specimen Testing" and "Tubular Specimen Testing." The objective of these tasks is to design and test specimens of increasing complexity to determine the inelastic behavior and strain tolerances of Types 304 and 316 stainless steel under complex stress distributions. This report covers the work performed during the period from December 1, 1973 to February 28, 1974.

6.2 BASIC SPECIMEN TESTING - N. J. Ettenson, M. Manjoine (Westinghouse Research Laboratories).

A variety of specimen designs have been selected for this task, as shown in Table 6.1 and Figure 6.1. Data obtained to date are presented in Table 6.2.

6.2.1 Uniaxially Loaded Specimen Models with Uniform Gage Section (304 SS, Heat 9T2796)

6.2.1.1 Test Piece Description

Types A, B, and G test piece designs, as shown in Table 6.1, are used for this part of the test program.

6.2.1.2 Current Results

Two A type test pieces were completed using the loading history shown in Figures 6.2 and 6.3.

6.2.2 Uniaxially Loaded Specimen Models with Non-Uniform Gage Section

6.2.2.1 Test Piece Description

Types C, D, and E test piece designs, as shown in Table 6.1, are used for this part of the test program.

Table 6.1. Model Types

Specimens From Base Material

Code Designation	Description
A.	Plane Stress Specimen 1/3 x 2/3 x 3 in. (8.5 x 17 x 76.2 mm) gage section.
B.	Plate Specimen 1/3 x 10/3 x 3 in. (8.5 x 85 x 76.2 mm) gage section.
C.	Plate Specimen with Central Hole of 1/3 in. (8.5 mm) Diameter, 1/3 x 10/3 x 3 inc. (8.5 x 85 x 76.2 mm) plate section.
D.	Round Circumferentially Notched Specimen, Major Diameter = 0.96 in. (24.4 mm), Minor Diameter = 0.64 in. (16.2 mm), K_t = 4, Root Radius = 0.018 in. (0.46 mm), Two nearly identical notches in specimen.
E.	Plate Specimen in bending and tension, 1/3 x 10/3 x 2 in. (8.5 x 85 x 50.8 mm) plates section, eccentric load
F.	Designation generally refers to failure or fracture; therefore, it is not used to identify a type of model.
G.	Plane Strain Specimen 1/3 x 10/3 x 1 in. (8.5 x 85 x 26 mm) gage section, Ends constrained in transverse direction
H.	Biaxially Loaded Notched Plates, Wedge-opening-loaded Plates with 1/3 in. (8.5 mm) Diameter Notch.

Specimen With Welds

BTW - B-type plate specimen with transverse weld at mid-length of gage section.

BAW - B-type plate specimen with axial weld at center of gage section.

CTW - C-type specimen with hole through transverse weld

CAW - C-type specimen with hole through axial weld

DTW - D-type specimen with notch root in transverse weld

DZTW - D-type specimen with notch root at weld fusion line of heat affected zone.

GTW - G-type specimen with transverse weld at mid-gage length.

GAW - G-type specimen with axial weld at center of gage section.

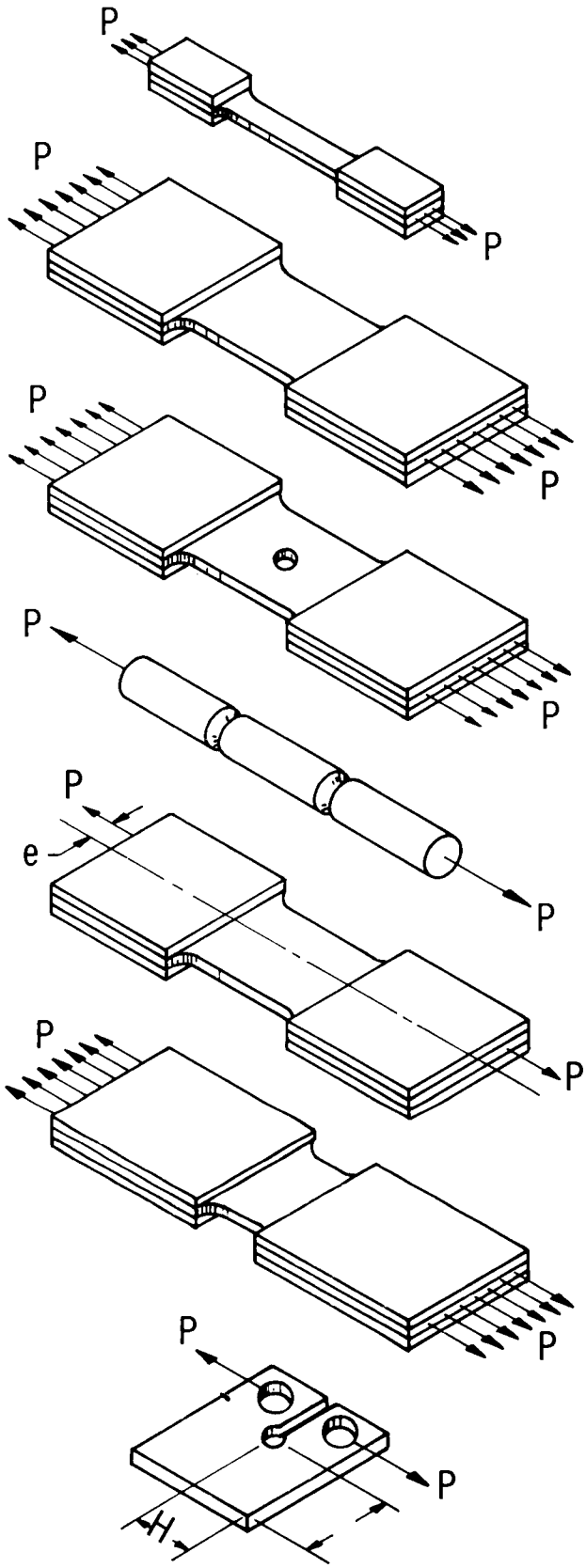

A. Uniaxially Loaded Plane Stress

B. Uniaxially Loaded Flat Plates with End Restraints

C. Uniaxially Loaded Flat Plates with Holes $K_t \sim 2.7$

D. Notched Bars $K_t \sim 4$

E. Tension + Limited Bending of Flat Plate

G. Flat Plates Under Plane Strain

H. Biaxially Loaded Notched Plate $K_t \sim 2.7$

Figure 6-1. Basic Specimen Types

6391-1

Table 6.2. Summary of Creep Data, Type 304 Stainless Steel* at 1100°F (593°C)

Test No. (Gage Section)	Loading Data: Stress (ksi)	Stress (MPa)	Plastic Strain (%)	Creep Data: Creep Rate (%/hr)	Increment: Strain (%)	Increment: Time (hr)	Accumulated: Strain (%)	Accumulated: Time (hr)	Permanent Strain (%)
A1	21.0	144.8	4.66	2.2×10^{-3}	1.10	303	1.10	303[a]	5.76
(1/2x2/3x3 in)				2.2×10^{-3}	0.89	403	1.99	706[a]	6.65
(8.5x17x76.2mm)				—	—	—	3.47	1250[b]	8.13
				—	—	—	3.65	1270[c]	8.31
				—	—	—	7.34	1286	12.00[d]
A2	10.0	68.95	0.215	8.5×10^{-5}	0.228	2180	0.228	2180[a]	0.443
(1/3x2/3x3 in)	—	—	—	6.2×10^{-5}	0.028	405	0.256	2585[e]	0.471
(8.5x17x76.2mm)	11.0	75.84	0	8.6×10^{-5}	0.124	1349	0.380	3934[e]	0.595
	12.5	85.68	0	2.0×10^{-4}	0.213	1002	0.593	4936[e]	0.808
	15.0	103.4	0.014	2.5×10^{-4}	0.811	1848	1.404[a]	6784[e]	1.619
	21.0	144.8	0.646	4.5×10^{-3}	28.75	4266	30.15	11050[h]	31.0
B1	21.0	144.8	5.34	1.4×10^{-3}	1.76	666	1.76	666[a]	7.10
(1/3x10/3x3 in)				8.8×10^{-4}	1.03	1005	2.79	1671[a]	—
(8.5x85x76.2mm)				1.7×10^{-3}	—	—	—	3000[c]	—
				—	1.72	1587	4.51	3258[a]	9.85[g]
				—	—	—	—	3525[h]	—
B2	10.0	68.95	0.273[i]	8.6×10^{-5}	0.31	1644	0.31	1644[a]	0.58
(1/3x10/3x3 in)	j	—	—	9.0×10^{-5}	0.14	1462	0.45	3106[e]	0.72
(8.5x85x76.2mm)	11.0	75.84	0	1.1×10^{-4}	0.16	1804	0.61	4910[e]	0.88
	12.5	85.68	0	2.0×10^{-4}	0.33	1364	0.94	6274[e]	1.21
	15.0	103.4	0.051	4.7×10^{-4}	1.00	1302[a]	1.93	7576[e]	1.98
	21.0	144.8	1.88	8.6×10^{-3}	16.33	1563	18.26	9139[h]	20.19

*HT 9T2796, annealed 2000F(1094C)

[a]Interrupted for photographic measurement

[b]Transition at 0.2% OFFSET

[c]Transition at double minimum rate

[d]Rupture, R

[e]Stress raised (step-loaded test)

[f]Test in progress

[g]Crack initiated

[h]Test terminated, crack tearing

[i]Strain gage average, bending noted

[j]Specimen rotated 180° to investigate bending

[k]Net Section Stress, Gross Section stress = 0.9 N.S.S.

[m]Average strain at central hole

[n]Average overall strain

[p]Test in preparation

[q]Specimen to be sectioned to determine damage at 78% of estimated rupture life

[r]Deflection of notch, inches (25.4 mm)

[t]True strain = ln(Ao/A)

[u]Test interrupted, 1/2 of specimen continued

Table 6.2. (Continued)

Test No. (Gage Section)	Loading Data			Creep Data					
	Stress		Plastic Strain	Creep Rate	Increment		Accumulated		Permanent Strain
	(ksi)	(MPa)	(%)	(%/hr)	Strain (%)	Time (hr)	Strain (%)	Time (hr)	(%)
C1	23.3[k]	160.5	8[n]	—	1.7[n]	100[c]	—	—	—
(1/3x10/3x3in)				—	—	—	22.9[n]	138[d]	—
(8.5x85x76.2mm)									
Central Hole									
1/3in(8.5mm)dia.									
C2	10.0[k]	68.95	0.14[n]	—	0.62[n]	2808[a]	0.62[n]	2808[e]	0.76[n]
Same as C1	11.0[k]	75.84	0	—	0.40[n]	1290	1.02[n]	4098	1.16[n]
	12.5[k]	25.68	0	—	0.50[n]	1300[a]	1.52[n]	5398	1.66[n]
	15.0[k]	103.4	0.28[n]	—	0.82[n]	1148	2.34[n]	6546	2.76[n]
	18.0[k]	124.1	0.06[n]	—	3.31[n]	1630[a]	5.65[n]	8176[g]	6.13[n]
				—	0.89[n]	791[a]	6.54[n]	8967	7.02[n]
				—	1.05[n]	944[a]	7.59[n]	9911	8.07[n]
				—	1.50[n]	1339[a]	9.09[n]	11250	9.57[n]
				—	—	—	—	12300[f]	
C3	21.0[k]	144.8	4.4[n]	—	1.5[n]	325[c]	—	—	—
Same as C1				—	—	—	4.1[n]	397[h]	8.5[n]
D1	30.0	206.8	—	—	—	—	—	—	—
D=.96 in(24.4mm)									
d=.64 in(16.2mm),									
R=.19 in(0.46mm)									
D1-1	30.0	206.8	2.60[t]	—	0.30[t]	137	0.30[t]	137	2.90[t]
				—	0.20[t]	102	0.50[t]	239[g]	3.10[t]

[*] HT 9T2796, annealed 2000F(1094C)

[a] Interrupted for photographic measurement

[b] Transition at 0.2% OFFSET

[c] Transition at double minimum rate

[d] Rupture, R

[e] Stress raised (step-loaded test)

[f] Test in progress

[g] Crack initiated

[h] Test terminated, crack tearing

[i] Strain gage average, bending noted

[j] Specimen rotated 180° to investigate bending

[k] Net Section Stress, Gross Section stress = 0.9 N.S.S.

[m] Average strain at central hole

[n] Average overall strain

[p] Test in preparation

[q] Specimen to be sectioned to determine damage at 78% of estimated rupture life

[r] Deflection of notch, inches (25.4 mm)

[t] True strain = ln(Ao/A)

[u] Test interrupted, 1/2 of specimen continued

Table 6.2. (Continued)

Test No. (Gage Section)	Loading Data			Creep Data					
	Stress		Plastic Strain	Creep Rate	Increment		Accumulated		Permanent Strain
	(ksi)	(MPa)	(%)	(%/hr)	Strain (%)	Time (hr)	Strain (%)	Time (hr)	(%)
D1-2	30.0	206.8	2.20[t]	—	0.26[t]	137	0.26[t]	137	2.46[t]
				—	0.22[t]	113	0.48[t]	250[c]	2.68[t]
				—	—	—	10.92[t]	305[d]	13.12[t]
D2-1	25.0	172.4	0.009[r]	—	—	—	0.006[r]	1371	0.015[r]
				—	—	—	—	1371[g]	2.17[t]
D2-2	25.0	172.4	0.009[r]	—	—	—	0.006[r]	1240[c]	—
				—	—	—	—	1371[d]	5.3[t]
D3	21.0	144.8	0.002[r]	—	—	—	—	5499[h]	—
D4	10.0	68.95	0	—	—	406	—	406[e]	—
	11.0	75.84	0	—	—	477	—	883[e]	—
	12.5	85.68	0	—	—	434	—	1317[e]	—
	15.0	103.40	0	—	—	404	—	1721[e]	—
	21.0	144.80	0.001[r]	—	0.004[r]	433	—	2154[e]	—
	25.0	172.40	0.003[r]	—	0.033[r]	1581[g]	—	3735[u]	—
D4-1	One Notch of Specimen D4 to Be Sectioned.								
D4-2	25.0	172.40	—	—	—	2904[h]	—	5058[h]	—
D5	23.0	158.4	—	—	—	1681[g]	—	1681	—
D5-1	One Notch of Specimen D5 to Be Sectioned.								
D5-2	23.0	158.4	—	—	—	150	—	1831[d]	—
D6	20.0	137.9	—	—	0.009[r]	1671[f]	—	—	—

[*] HT 9T2796, annealed 2000F(1094C)

[a] Interrupted for photographic measurement

[b] Transition at 0.2% OFFSET

[c] Transition at double minimum rate

[d] Rupture, R

[e] Stress raised (step-loaded test)

[f] Test in progress

[g] Crack initiated

[h] Test terminated, crack tearing

[i] Strain gage average, bending noted

[j] Specimen rotated 180° to investigate bending

[k] Net Section Stress, Gross Section stress = 0.9 N.S.S.

[m] Average strain at central hole

[n] Average overall strain

[p] Test in preparation

[q] Specimen to be sectioned to determine damage at 78% of estimated rupture life

[r] Deflection of notch, inches (25.4 mm)

[t] True strain = ln(Ao/A)

[u] Test interrupted, 1/2 of specimen continued

Table 6.2. (Continued)

Test No. (Gage Section)	Loading Data			Creep Data					
	Stress		Plastic Strain	Creep Rate	Increment		Accumulated		Permanent Strain
	(ksi)	(MPa)	(%)	(%/hr)	Strain (%)	Time (hr)	Strain (%)	Time (hr)	(%)
G1	25.0	172.4	2.00[i]	—	0.88[i]	47[a]	0.88	47	2.47
				3.5×10^{-3}	1.12[i]	268[a]	2.00	315	4.00
				—	0.90[i]	170[a]	2.90[c]	485[g]	4.90
				—	0.65[i]	83	3.55	568[h]	5.60
G2	21.0	144.8	0.43	3.9×10^{-4}	1.34	1195[a]	1.34	1195	1.77
(1/3x10/3x1 in)			0	1.0×10^{-4}	0.83	5520[a]	2.17	6715[e]	2.60
(8.5x85x25mm)	25.0	172.4	0.01	2.3×10^{-3}	1.80	700	—	—	—
				—	2.50	450	4.67	7865	—
				—	4.43	283[a]	6.60	8148	—
				—	—	404[d]	—	8552	—
BAW-1	25.0	172.4	0.25	8.3×10^{-3}	4.35[n]	477[a]	4.35	477	4.60[g]
B Type Specimen				1.1×10^{-2}	8.32[n]	765[a]	12.67	1242	12.92
With Central Axial				1.5×10^{-2}	3.42[n]	216[a]	16.09	1458	16.34
Weld				—	2.35[n]	71	18.44	1529	18.69
				—	—	—	—	1532[d]	—
GAW-1	23.0	158.4	0.10[n]	5.1×10^{-3}	1.55[n]	188[a]	—	188[f]	—
G Type Specimen									
With Axial Weld									
BTW-1	21.0	144.8	0.17[n]	3.2×10^{-3}	1.30[n]	339[a]	1.30	339	1.47[n]
B Type Specimen			0.01	—	—	287	2.26	626[f]	—
With Transverse Weld									
GTW-1	25.0	172.4	0.09	4.7×10^{-3}	1.62[n]	240[a]	1.62	240	1.71
G Type Specimen				—	—	208	—	448[d]	—
With Transverse Weld									

[*] HT 9T2796, annealed 2000F(1094C)

[a] Interrupted for photographic measurement

[b] Transition at 0.2% OFFSET

[c] Transition at double minimum rate

[d] Rupture, R

[e] Stress raised (step-loaded test)

[f] Test in progress

[g] Crack initiated

[h] Test terminated, crack tearing

[i] Strain gage average, bending noted

[j] Specimen rotated 180° to investigate bending

[k] Net Section Stress, Gross Section stress = 0.9 N.S.S.

[m] Average strain at central hole

[n] Average overall strain

[p] Test in preparation

[q] Specimen to be sectioned to determine damage at 78% of estimated rupture life

[r] Deflection of notch, inches (25.4 mm)

[t] True strain = ln(Ao/A)

[u] Test interrupted, 1/2 of specimen continued

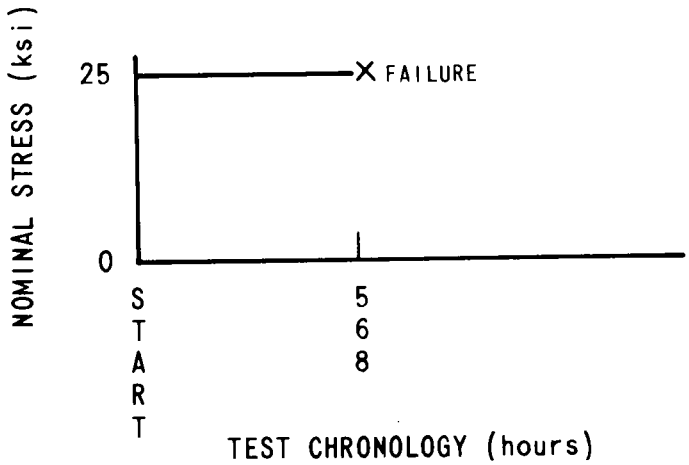

Figure 6-2 Loading History of Specimen G1

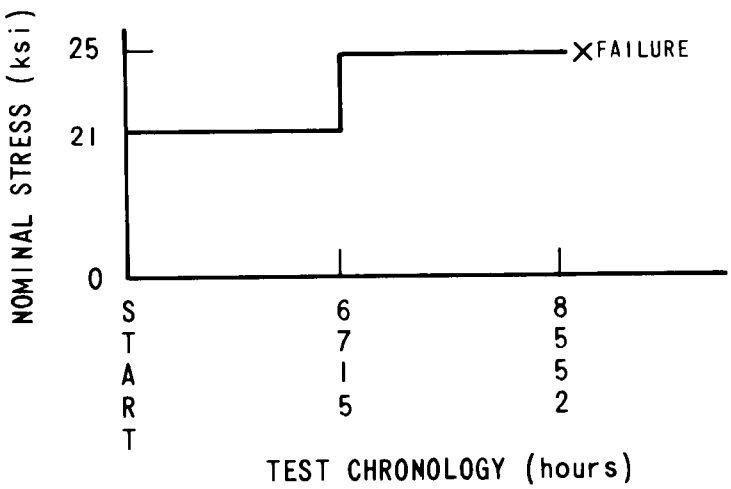

Figure 6-3. Loading History of Specimen G2

6.2.2.2 Current Results

The plate specimen with a central hole (Specimen C2) has been step loaded at the time intervals shown in Figure 6.4. The test was interrupted at 8176, 8967, and 9911 hours to record the crack growth rate at the hole.

A D-type specimen, machined from one-inch diameter bar stock and annealed after finished machining, has been tested for 1671 hours (Figure 6.5).

6.2.3 Specimens with Welds (304 SS, Heat 9T2796)

Two additional tests of welds were initiated. Specimen BTW-1, a transverse weld, in a Type B specimen (Figure 6.1) has been under test at 21 ksi and 1100°F for 626 hours. This test was interrupted at 339 hours to photograph the specimen. Additional interruptions are planned to study the initiation of cracking of these welds.

Specimen GAW-1, an axial weld in a Type G specimen, has completed 188 hours at 23 ksi. Crack initiation is estimated to occur at 1300 hours.

6.2.4 Discussion of Permanent Strain Limits

A study of the deformation characteristics of Type 304 stainless steel and other ductile alloys at elevated temperatures has led to the observations discussed below.

6.2.4.1 Flow and Fracture

The mutually dependent factors which influence flow and fracture of materials are stress, strain, strain rate, time at stress, temperature, metallurgical state, environment, and state of stress. Although these factors relative to flow and fracture are complex, a limited discussion is presented in the following paragraphs.

The modes of flow are primarily crystal lattice slip, grain boundary slip, and grain boundary rotation. Deformation of the grains can be

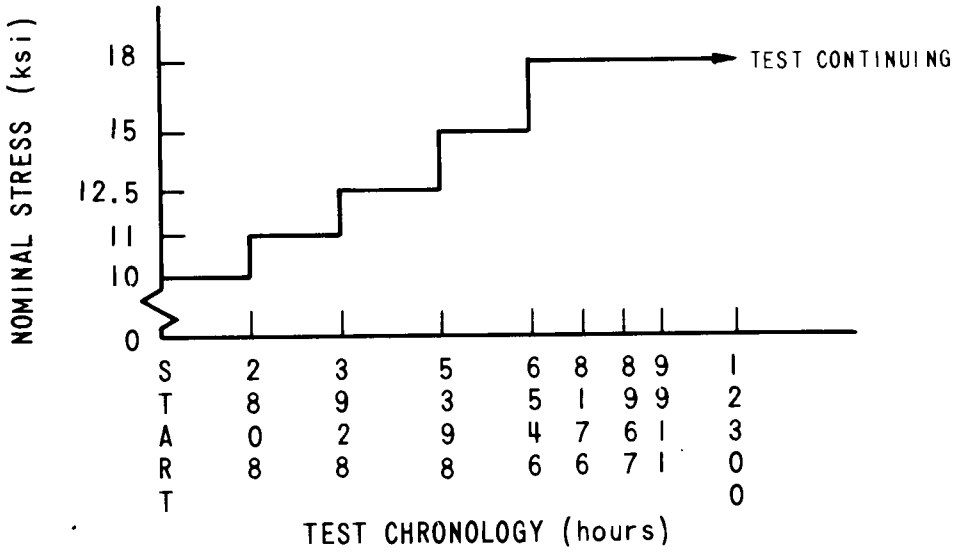

Figure 6-4 Loading History of Specimen C2

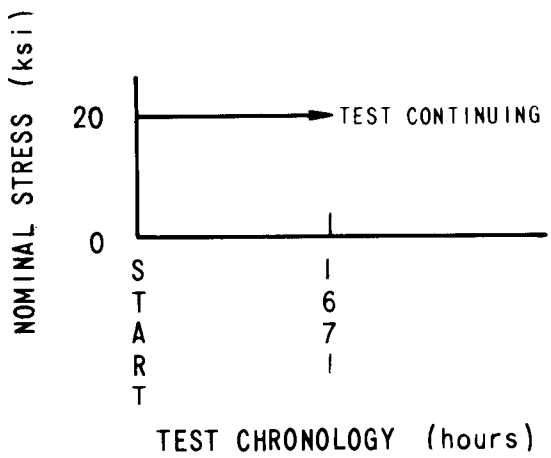

Figure 6-5. Loading History of Specimen D6

produced by slip along five independent slip systems. If there are insufficient slip systems operative, boundary slip and rotation can supplement the flow mechanisms and prevent the formation of the voids. The relative strengths of the grains and the boundaries are functions of the same factors. In general, the relative strength of the boundaries decrease with increasing temperature and decreasing strain rate. Since the volume of the boundaries is small compared with that of the grains, the overall deformation across the boundaries results in a low apparent strain at the initiation of fracture when the primary deformation mechanism is grain boundary flow.

For polycrystalline materials at elevated temperatures, creep and relaxation deformations occur continuously at rates which are a function of the effective stresses. Although the stress and deformation may appear to be homogenous on a gross scale, they are not on a microscale. Some grains easily slip in the direction of maximum shearing stress and thereby buildup a discontinuity at the grain boundaries. The deformations and stresses redistribute to adjacent grains and boundaries without forming voids. With continued deformation and creep, voids begin to form at grain boundaries that are primarily oriented perpendicular to the direction of the principal stress. These boundary cavities provide a means of redistributing the deformation but also cause a loss of load carrying ability. The linking of these grain boundary voids results in the initiation of fracture and the loss of ductility in austenitic stainless steels. Fortunately, when an individual grain boundary begins to form a void, the local stress is relieved, and additional voids are not formed for some time within distance of about four or five grain diameters away. With continued creep, voids begin to form between the prior voids, and a fracture is initiated and propagates across the stressed section. This failure process and the loss of ductility require a definition of the term "ductility."

Ductility of a material in a given metallurgical state is the ability to deform and distribute the strains, which are concentrated in local grains, to adjacent grains without exceeding the strain limit of the grains forming a "cell" volume.

The study of ductility, therefore, must concentrate on the determination of the characteristics of these "cells" and the quantitative evaluation of the "strain limit" as a function of strain rate, stress state, and temperature. A preliminary evaluation is presented in 6.2.4.2.

6.2.4.2 Deformation Characteristics

The data from tensile and creep tests for the reference heat at 1100°F are summarized in Figure 6.6. The tensile stress-strain is the curve (A) on the extreme left and also represents the loading strain, $\varepsilon\rho$, for creep tests at a constant strain rate of about 3 in/in per hour (300%/h). The creep strain, εc, is divided into three parts; i.e., $\varepsilon_o + \dot{\varepsilon}_m t_R + \varepsilon_n$.

The transient creep strain, ε_o, is taken as the strain intercept of a creep curve at zero time. The intermediate creep strain is calculated as the product of the minimum creep rate, $\dot{\varepsilon}_m$, and the rupture time, t_R, at a given constant load, strain between curve (B) and curve (C) ($\dot{\varepsilon}_m t_R$). The final segment is the necking strain, ε_n, which adds to the others to form the plane stress permanent strain curve (D). The curves of Figure 6.6 illustrate that as the stress is decreased into the design range around 8 ksi, the major portion of the permanent strain is the creep strain $\varepsilon_m t_R$ (minimum creep rate times time to rupture).

The creep strain described above is a function of the strain rate. In a constant load test, the strain rate is a function of permanent strain as shown in Figure 6.7. The rate decreases immediately after loading as the material strain hardens, reaches a minimum, and then accelerates to fracture. The strain limit at a given stress level or a given strain rate can be defined as the "useful" strain before a necking or a cracking instability develops. One method of generating the strain limit curve is illustrated in Figure 6.8 where several ductility indices are plotted as a function of strain rate. These indices are 1) the logarithmic strain (natural log of the ratio of the original cross sectional area to the final area); 2) the elongation at fracture; and 3) the intermediate creep strain ($\varepsilon_m t_R$). All of the indices decrease with decreasing strain rate.

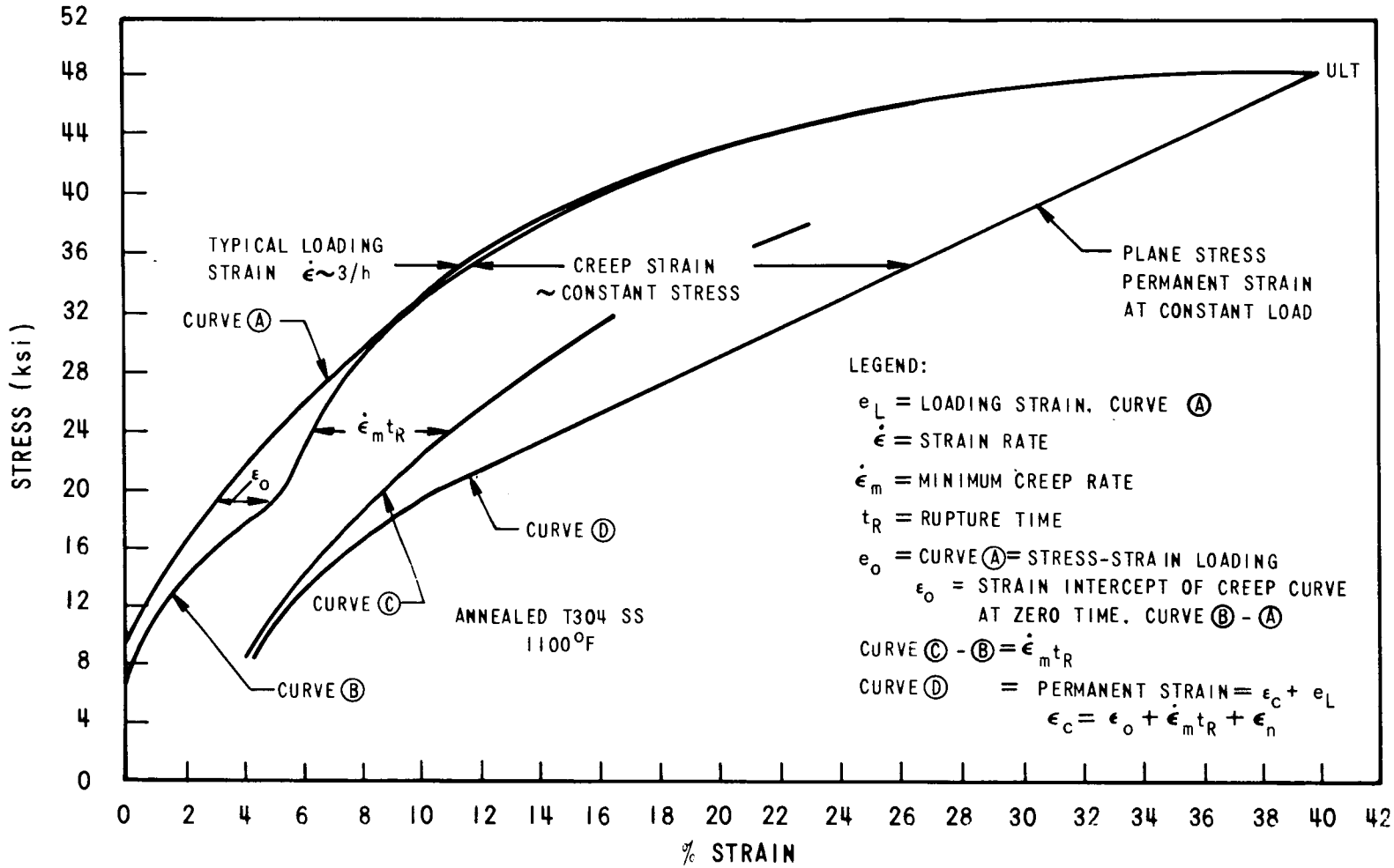

Figure 6-6. Permanent Strain Limit Under Creep Loading

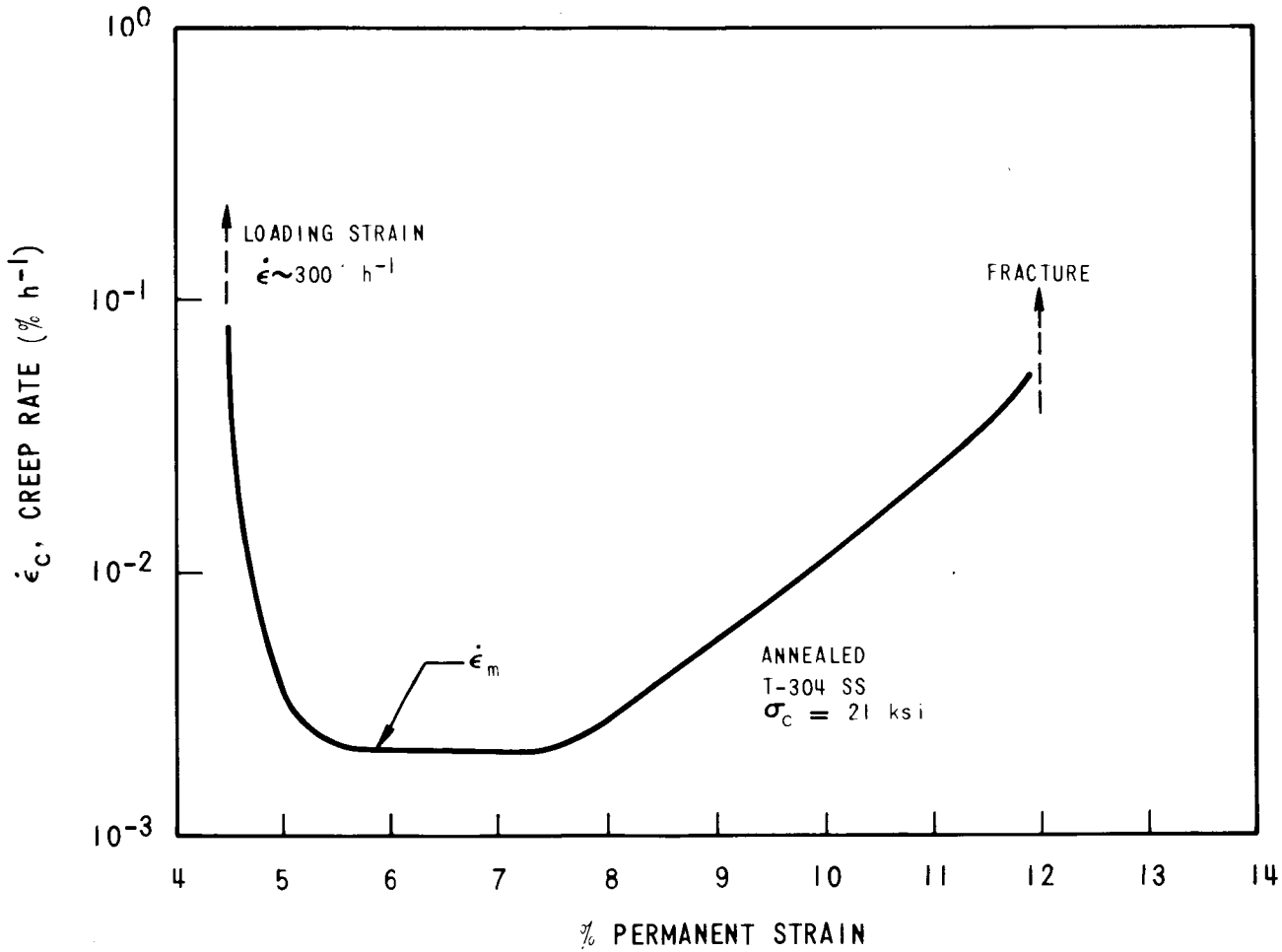

Figure 6-7. Strain Rate During Creep Test at Constant Load

The hypothesis of ductility loss implies a damage increment for a given strain increment. Therefore, a linear damage law based on a strain limit defines "damage," ΔD, for a given strain increment at a particular strain rate as the ratio of the strain increment to the strain limit for that strain rate, $\Delta D - \left(\frac{\Delta\varepsilon}{\varepsilon_L}\right)_{\dot{\varepsilon}}$, with the total damage summing up to unity $\sum \left(\frac{\Delta\varepsilon}{\varepsilon_L}\right)_{\dot{\varepsilon}} = 1$.

This implies that the strain limit can be obtained from constant strain rate tests up to the strain instability or by integrating the variable strain rate data from a creep test, Figure 6.7, and correcting for the effect of the strain rate. The strain limit obtained in this manner is given in Figure 6.9.

A more general linear damage law is proposed as follows:

$$\text{Damage, } D_1 = A \sum \left(\frac{\Delta t_i}{t_R}\right)_{\sigma_1} + B \sum \left(\frac{\Delta\varepsilon}{\varepsilon_L}\right)_{\dot{\varepsilon},\ \sigma_{ij}}$$

$$+ C \sum \left(\frac{n_{\Delta\sigma}}{n_f}\right)_{\varepsilon,\ \sigma_{ij}} + E \sum \left(\frac{N_{\Delta\varepsilon}}{N_f}\right)_{\varepsilon,\ \sigma_{ij}}$$

Terms A and B are non-cyclic loadings and are damages due to times at maximum principal stresses (σ_1) and strain-increments, respectively. The latter being a function of strain rate ($\dot{\varepsilon}$) and state of stress (σ_{ij}). Terms C and E refer to cyclic loadings and will not be discussed at this time.

6.2.4.2.1 Influence of State of Stress – The damage mechanism described for a strain limit assumes that there are constraints to the deformation process which result in limited local deformation. Theory of plasticity also imposes an extreme limit on the plastic strain under constant volume conditions since the plastic strain for isostatic tension or compression is zero.

However, the degree of multiaxial stress is much less severe in components subjected to external and thermal loads. Thus, fracture for Type 304 stainless steel is usually initiated by states of tensile stress or by positive strains (extensions) which cause void to forms. The work of Davis and Connelly[1] suggests that the ductility of strain hardening

material, such as Type 304 stainless steel, is a function of the normal stress on the octahedral plane and the octahedral shearing stress. They proposed a triaxiality factor, T.F., based on these stresses which are normalized to a value of unity for simple tension.

$$\text{T. F.} = \frac{1}{\sqrt{2}} \frac{\sigma_1 + \sigma_2 + \sigma_3}{[(\sigma_1 - \sigma_2)^2 + (\sigma_2 - \sigma_3)^2 + (\sigma_3 - \sigma_1)^2]^{1/2}}$$

Where $\sigma_1 > \sigma_2 > \sigma_3$ are the principal stresses.

It is proposed that the ductility is a function of this T. F. and that the following simple relationship is applicable for a range of Triaxiality Factors from 0.3 to 3:

$$\text{Strain Limit for Multiaxial Stress} = \frac{\text{Strain Limit for Simple Tension}}{\text{T. F.}}$$

This strain limit is plotted in Figure 6.9 for three strain rates.

6.2.4.2.2 Strain Limits- The range of multiaxial stress and strain rates for many components is limited by the geometry and rates of application of loading. Therefore, it is possible to simplify the strain limits (Figure 6.8) for engineering applications when the designer and analyst are cognizant of the influence of strain rate and state of stress. For the usual types of external loads, such as bending, tension, internal pressure, and temperature gradient, the triaxiality factor is seldom greater than about two for a component whose wall thickness is about 10 percent of the outside diameter.

For conservatism, a factor of safety (FS) of 2 on the extreme T. F. of 2, results in the reduction of the strain limit by a factor of 4. The following strain limit for a Type 304 stainless steel base metal was selected and is shown in Figure 6.8.

1. 1 percent creep strain limit for long time loadings where $\varepsilon < 10^3$% per hour.
2. 2 percent plastic strain limit for slow transients, ratcheting loading, and intermediate loading rates where $10^{-3} < \dot{\varepsilon} < 1$% per hour.
3. 5 percent permanent strain limit for start-up, shutdown, and dynamic loadings where $\dot{\varepsilon} > 1$% per hour.

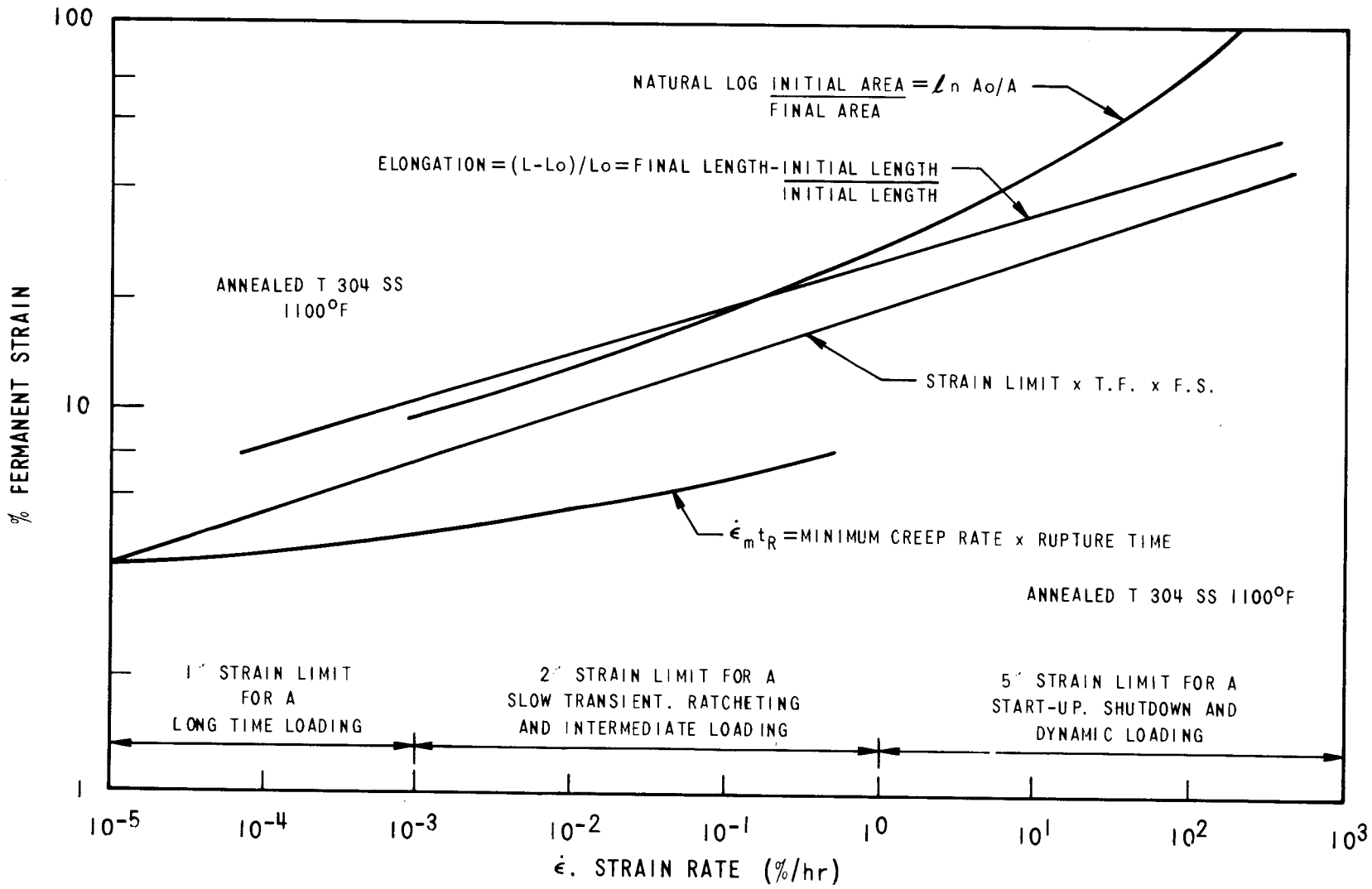

Figure 6-8. Ductility Indices Vs Strain Rate

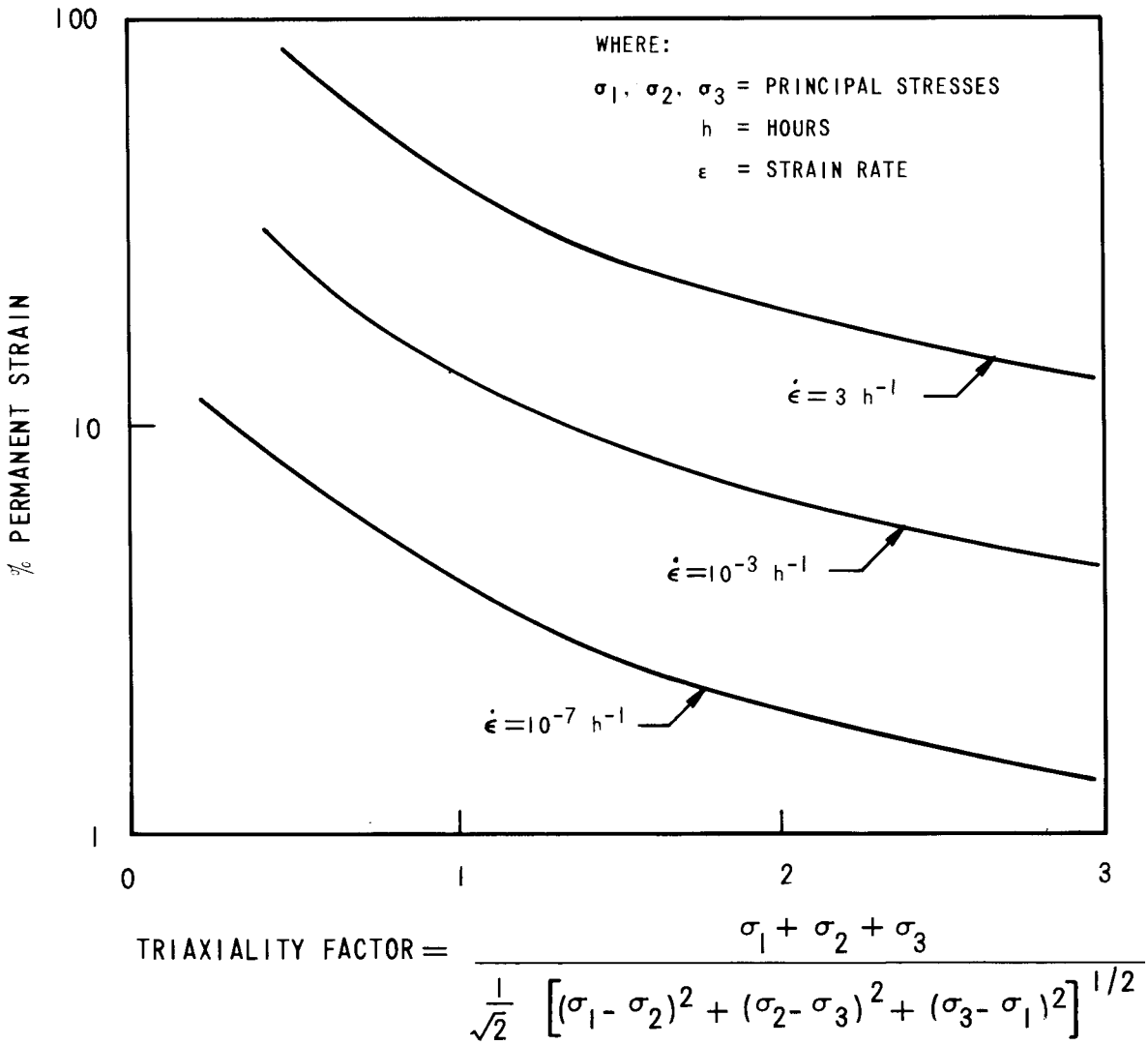

Figure 6-9. Strain Limits Annealed T 304 SS

4. Combination of these three must satisfy the damage equation:

$$D \geqq \sum \left(\frac{\Delta\varepsilon}{\varepsilon_L}\right)_{\dot{\varepsilon}} = 1$$

6.3 TUBULAR SPECIMEN TESTING - K. C. Thomas, P. C. S. Wu

6.3.1 Test Piece Description

The tubular test pieces used in this program are 304SS, Heat 9T2796, 1.8 inch OD and 1.6 inch ID and 8.7 inch length. However, thinner wall (1.8 inch OD and 1.7 inch ID) test pieces are being considered for use in future tests to reduce the stress variation through the wall thickness during multiaxial testing.

6.3.2 Uniaxial Creep Testing (304SS, Heat 9T2796 ORNL Reference Heat)

The test plan for the uniaxial tubular specimen testing program and current status are shown in Table 6.3. At the present time, all of the original uniaxial creep tests have been completed. The tests were carried out at 1100°F (866°K) and the stress level ranging from 7,700 to 25,000 psi (5.308×10^7 to 1.723×10^8 Pascal). Preliminary analyses of the uniaxial creep data for the tubular specimens have shown that the constants ε_t and $\dot{\varepsilon}_m$ in Equation 1

$$\varepsilon - \varepsilon_L = \varepsilon_t \ (1-e^{-rt}) + \dot{\varepsilon}_m t \qquad (1)$$

are both continuous functions of stress ranging from 7,700 to 25,000 psi (5.308×10^7 to 1.723×10^8 Pascal) at 1100°F (866°K). However, the constant r is a continuous function of stress only above 10,000 psi (6.894×10^7 Pascal). At 7,700 psi (5.308×10^7 Pascal) the value of r does not follow the extrapolation of high stress values. A uniaxial creep test, No. 3D, at 5,000 psi (3.447×10^7 Pascal) was added and initiated during the present report period to provide information to better clarify the stress dependence of the constant, r. The results obtained for the uniaxial creep tests are summarized in Table 6.4. Additional uniaxial creep tests are being considered to provide strain-time relationship at a stress level of 15,000 psi (1.034×10^8 Pascal). These data points are necessary to complete detailed analyses of the uniaxial creep data.

Table 6.3. Test Plan-Uniaxial Tubular Specimen Testing[a]

Test No.	Axial Stress (σ_z)	Test Duration (hr)	Status	Remarks
1A	25,000	100	b	Terminated due to over temp.
1B	25,000	100	b	0.050-inch wall thickness
2A	10,000	2000	b	Cold drawn sample
2B	10,000	2000	b	
3A	20,000	2000	b	Terminated due to pull rod failure
3B	20,000	2000	b	
3C	7,700	2000	b	Additional test
3D	5,000	2000	c	Additional test
3F	15,000	2000	d	Tentative

(a) All test specimens, except 1A and 1B, have 0.100-inch wall thickness. They are annealed at 2000°F for 30 minutes except specimen 2A which is cold drawn. All tests are at nominal 1100°F.

(b) Test complete.

(c) Test in progress.

(d) Test to be initiated.

Table 6.4. Test Results - Uniaxial Creep Test

Test No.	Nominal Test Temp. (°F)	Axial Stress (psi)	Test Hrs. Accumulated (hr)	Axial Loading Strain (%)	Axial Creep Strain[a] (%)	Total Axial Strain (%)
1B	1100	25,000	241.5	0.7988	3.5572	4.3660
2A	1100	10,000	2016	0.0490	0.0697	0.1187
2B	1100	10,000	2000	0.0780	0.0880	0.1660
3A	1100	20,000	336	- - -	0.9591	- - -
3B	1100	20,000	1990	0.1783	2.7468	2.9251
3C	1100	7,700	2002	0.0461	0.0534	0.0995
3D	1100	5,000	767	0.0253	0.0097	0.0350

(a) Average of two readings. See Section 4.2.5 on effective stress and strain in Reference 1.

The test plan for multiaxial creep tests are shown in Table 6.5. Currently, four multiaxial creep tests are completed. Test No. 4A and 5 were completed during the last quarter while No. 10 and No. 11 are completed during the present report period. The results, summarized in Table 6.6 are being compiled in the data acquisition system described in a previous report.[2] In addition, test No. 7A, a repeat of test No. 7, was initiated upon the completion of test No. 11.

References

1. E. A. Davis and F. M. Connelly, "Stress Distribution and Plastic Deformation in Rotating Cylinders of Strain-Hardening Material," Trans. Am. Soc. Mech. Engrs. 81, Series E, pp. 25-30 (1959).

2. Validation of High Temperature Design Methods and Criteria. Quarterly Progress Report for Period ending August 31, 1973, WARD-HT-3045-3.

Table 6.5. Test Plan-Multiaxial Tubular Specimen Testing[a]

Test No.	Effective Stress (psi)	Nominal Stress Ratio (σ_θ/σ_z)	Test Duration (hr)	Status	Remark
4	10,000	2.0	2000		Terminated due to malfunction of strain measuring system
4A	10,000	2.0	2000	b	Repeat test No. 4
5	15,000	2.0	2000	b	Tested at 1115°F
6	20,000	2.0	2000	c	
7	10,000	1.5	2000		Terminated due to malfunction of strain measuring system
7A	10,000	1.5	2000	d	Repeat test No. 7
8	15,000	1.5	2000	c	
9	20,000	1.5	2000	c	
10	10,000	1.0	2000	b	
11	15,000	1.0	2000	b	
12	20,000	1.0	2000	c	
13	10,000	1.5	500	c	Step loading test
	15,000	1.5	500	c	
	20,000	1.5	500	c	
	20,000	1.0	500	c	
14	15,000	2.0	500	c	Step loading test
	15,000	1.5	500	c	
	15,000	1.0	500	c	
	15,000	2.0	500	c	
15	10,000	2.0	500	c	Step loading test
	15,000	1.5	500	c	
	20,000	1.0	500	c	
	15,000	2.0	500	c	

(a) All test specimens are annealed at 2000°F for 30 minutes and tested at nominal temperature of 1100°F.

(b) Test completed.

(c) Test to be initiated.

(d) Test in progress.

Table 6.6. Test Results - Multiaxial Creep Test

Test No.	Nominal Test Temp. (°F)	Axial Load (lb)	Nominal Internal Pressure (psi)	Nominal Effective Stress (psi)	Nominal Principal Stress-Ratio σ_θ/σ_z	Test Time (hr)	Average Loading Strain (%)		Nominal Average Creep Strain (%)			
							Axial	Hoop	Radial	Hoop	Axial	Effective
4A	1100	323	1209.5	10,000	2.0	1965.7	0.01048	0.02174	-0.1274	0.12466	0.00245	0.14536
5	1115	484	1814.3	15,000	2.0	1998	0.09208	0.08499	-0.57795	0.054670	0.03125	0.64996
7[a]	1100	1211	1180	10,000	1.5							
7A	1100	1211	1180	10,000	1.5	480	0.04240	0.03521	-0.01452	0.00843	0.00609	0.01458
10	1100	2670	1049.4	10,000	1.0	338	0.04363	0.01994	-0.04112	0.01994	0.02118	0.04111
11	1100	4005	1574	15,000	1.0	197	0.03288	0.07339	-0.24753	0.10402	0.14351	0.24854

(a) Test terminated due to instability of the strain measuring systems

7. UNIVERSITY OF CINCINNATI

J. Moteff

7.1 INTRODUCTION

The objective of this program is to evaluate (a) the time, temperature and stress dependent properties of austenitic stainless steels, 316 and 304, (b) the relation of these properties to the substructure as observed principally with a 200 kV transmission electron microscope and (c) contribution of grain boundary sliding to plastic deformation at high temperature. Special consideration has been given to operating conditions typical of LMFBR applications, including the knowledge that the radiation environment can influence the substructure of these metals leading to significant changes in the mechanical property behavior. Related substructure studies on other metals (nickel) and alloys (Incoloy 800) are also being investigated. Work has also started on substructure correlation of the high temperature push-pull and bend fatigue deformation of 304 stainless steel and Incoloy 800.

7.2 EXPERIMENTAL PROGRAM

Transmission electron microscopy has been used to study the deformation substructure resulting from fatigue, tensile and creep deformation at elevated temperatures. Special studies have been initiated on the comparison of the substructure developed in Incoloy 800 following both a push-pull and a bend fatigue testing mode. Creep data from ORNL (Heat

Number 9T2796) was evaluated through regression analysis in preparation for the correlation with the substructure results. Hot hardness measurements were employed to correlate the elevated temperature mechanical properties.

The work in progress will be presented according to the separate mini-research programs for convenience. A general description and a brief discussion will be given on several of the programs that are presently active.

7.2.1 Some Aspects of Dislocation Mechanisms During Creep of AISI 316 and 304 Stainless Steel - (H. Nahm and V. K. Sikka*)

It is well known that some metals and alloys exhibit subgrain formation during creep process. However, the interaction between those dislocations going into the subgrain boundary and those presently in the subgrain boundary is not well known because of its complexity.

As a start, the creep rate can be presented by;

$$\dot{\varepsilon} = \alpha \rho b \bar{v} \qquad (1)$$

where α is a geometrical factor, ρ the mobile dislocation density, b Burger's vector, and $\bar{v}$ is the average dislocation velocity. The total dislocation density can be written as;

$$\rho_t = \rho_{sb} + \rho_m \qquad (2)$$

where ρ_t is the total dislocation density, ρ_{sb} is the dislocation density forming the subgrain boundary and ρ_m is the

* Now at ORNL

dislocation in the subgrain. The average dislocation velocity, as well as, the dislocation density tends to change during deformation, especially in the transient stage of deformation. At this time, the internal stress increases due to the formation of subgrains, increase in the number of forest dislocations, etc.

In order to develop a better understanding of the dislocation interactions during creep, a preliminary analysis based on the theoretical approach taken by Orlova and Cadek[1] was made. This study deals with the dislocations which form the subgrain boundaries in AISI 316 stainless steel[2] and also compares with other parameters, including the dislocation substructure of AISI 304 stainless steel as a function of creep strain.

The dislocation density forming the subgrain boundary, ρ_{sb}, is assumed to be following the relationship;

$$\rho_{sb} = \frac{3\Theta}{b\lambda'} \tag{3}$$

where Θ is the misorientation angle between the subgrains, b is the Burger's vector and λ' is the mean subgrain diameter.

It was found that the dislocation density within the subgrain, ρ_m, and that in the boundaries, ρ_{sb} can be expressed as a power function of the parameter consisting of the true shear stress, divided by the Burger's vector, τ/Gb with an exponent value of 2.

The dislocation density ratio ρ_{sb}/ρ_m for steady-state

creep of 316 stainless steel has been observed to be independent of both the parameter τ/Gb and the creep strain. This tendency is shown in Figure 1 and 2. The dislocation density ratio ρ_{sb}/ρ_m has a value of 4.2 for stainless steel, similar to that observed for pure metals.[3] Based on the present analysis, the recovery in steady-state for 316 stainless steel is suggested to take place by mutual annihilation of free dislocations and not by entry of these dislocations into sub-boundaries.

Figure 3 shows the relationship between the mobile dislocation density and creep strain for AISI 304 stainless steel at 593°C with an applied stress of 30 ksi. A factor of 10^3 decrease in the creep strain rate (i.e. the product of the mobile dislocation density and the dislocation velocity) observed for the case of 304 stainless steel during the period of time immediately following the application of the laod to the onset of steady-state is accounted for by a factor of $\sim$ 5 due to a decrease in the dislocation density needed to form the sub-boundaries and a factor of $\sim$ 200 due to the decrease in the average dislocation velocity caused by the increase in the internal stress as a result of the presence of the sub-boundaries and forest dislocations. Work is still progressing in this area.

7.2.2 <u>Deformation Substructure of AISI 304 Stainless Steel and Incoloy 800 from Push-Pull Fatigue at Elevated Temperatures</u> - (H. Nahm and J. Moteff)

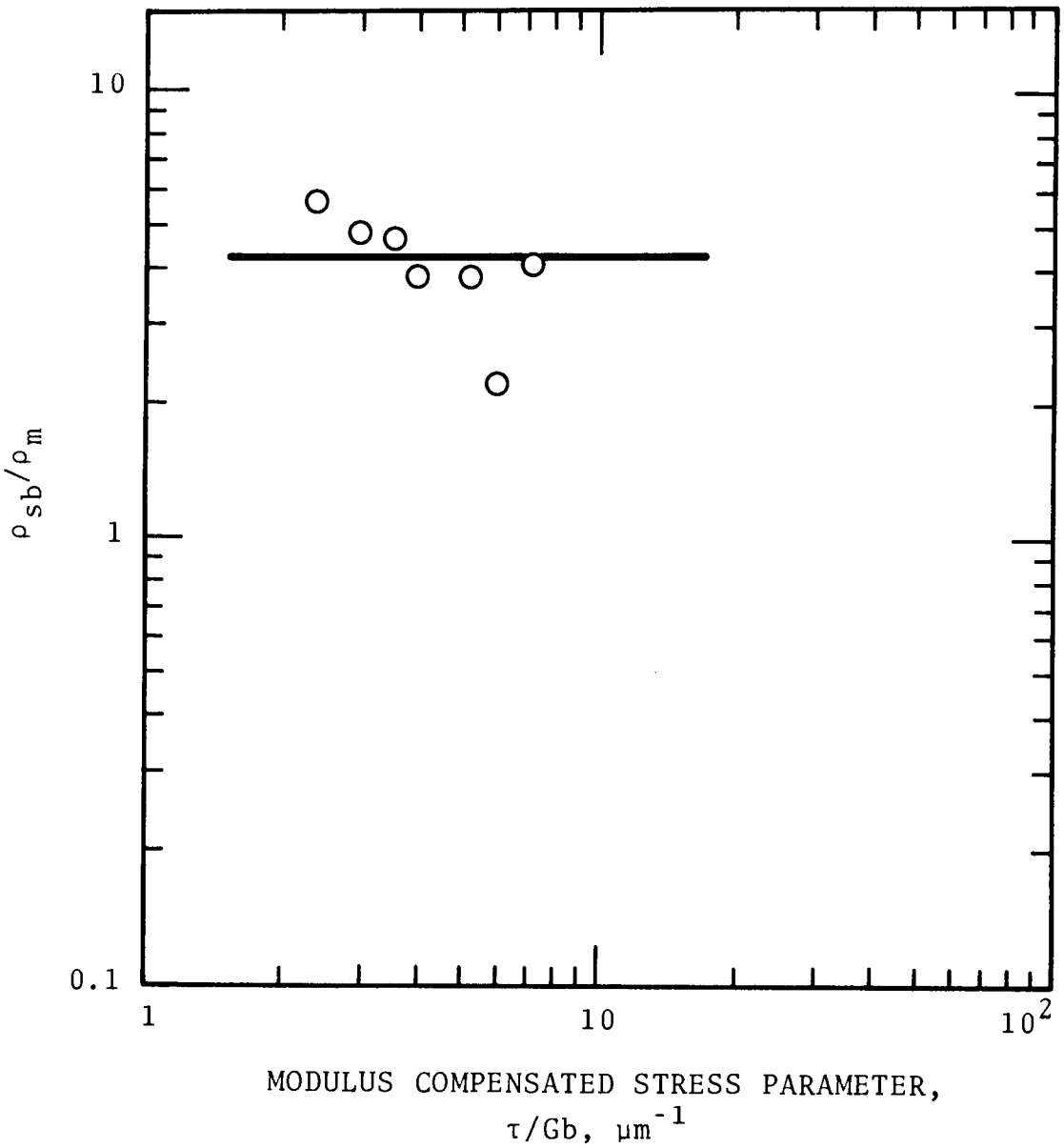

Fig. 1 The Ratio ρ_{sb}/ρ_m in Steady-State and Tertiary State Creep Plotted Against τ/Gb for 316 Stainless Steel.

Fig. 2(a)

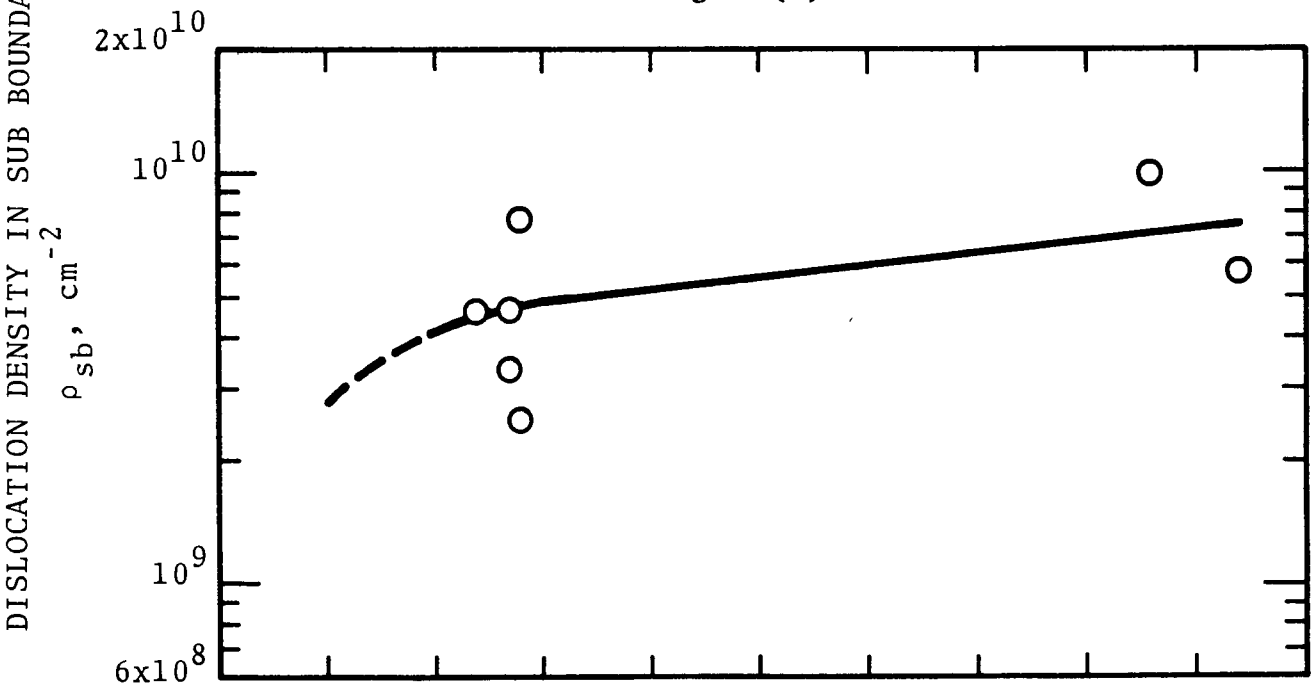

Fig. 2(b)

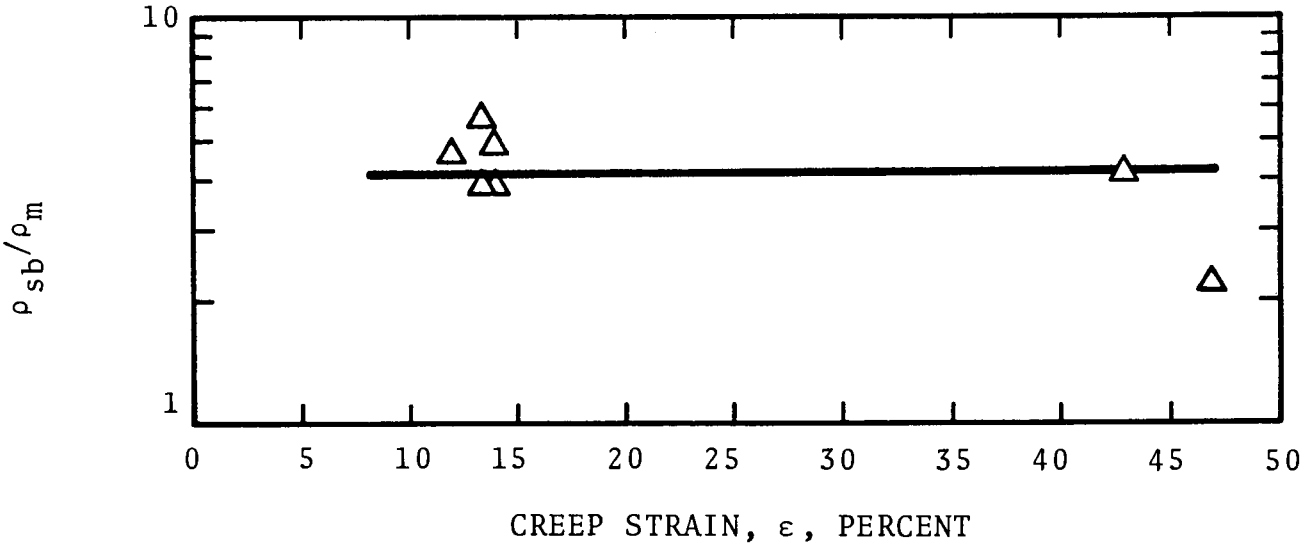

Fig. 2(a) Density of Dislocations Bound in Sub-Boundaries, ρ_{sb} as a Function of Creep Strain for 316 Stainless Steel

and

Fig. 2(b) The Ratio ρ_{sb}/ρ_m in Steady-State and Tertiary State as a Function of Creep Strain for 316 Stainless Steel.

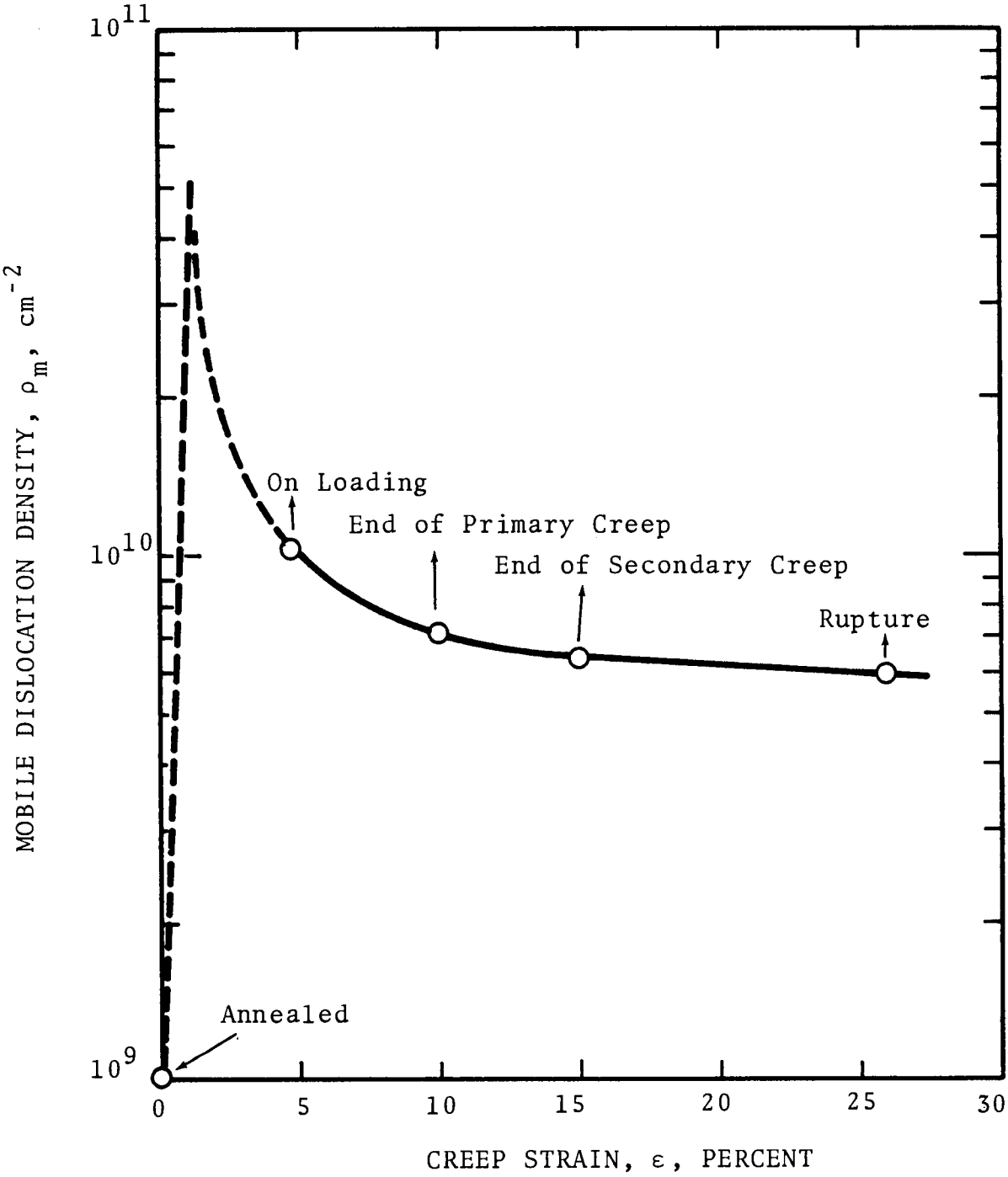

Fig. 3 Mobile Dislocation Density Versus Creep Strain for 304 Stainless Steel Tested at 593°C and at an Applied Stress of 30 Ksi.

More substructure data have been generated to further establish the substructural characteristics of specimens tested in the low cycle fatigue mode. Figure 4 shows the relationship between the cell or subgrain intercept (λ) versus the shear modulus compensated cyclic stress ($\Delta\tau/2G$) for 304, 316 stainless steel and Incoloy 800. All the data generated previously at the University of Cincinnat[4,5] are also included in this figure. As shown in this figure, the substructure properties can be represented as;

$$\lambda = A(\Delta\tau/2G)^{-2} \tag{4}$$

in the case of AISI 316 stainless steel, 304 stainless steel and Incoloy 800. No transition was observed in the slope from the characteristic -1 to -2 behavior as a function of a decrease in stress in the case of the fatigue substructure. Whereas for the case of specimens tested in the creep and tensile mode, the transition of the slope was indicated.

The apparent scatter of the data is due to the significant effect of the strain range employed in the testing. This was suggested in the previous work[4] and is shown schematically in Figure 5. It appears that the cyclic mode with the smaller strain range when tested at the elevated temperatures yields a finer substructure. In this figure, the elevated tensile substructure of Incoloy 800 is also included for the purpose of comparison and has a very large plastic strain when compared to the fatigue. As can be seen

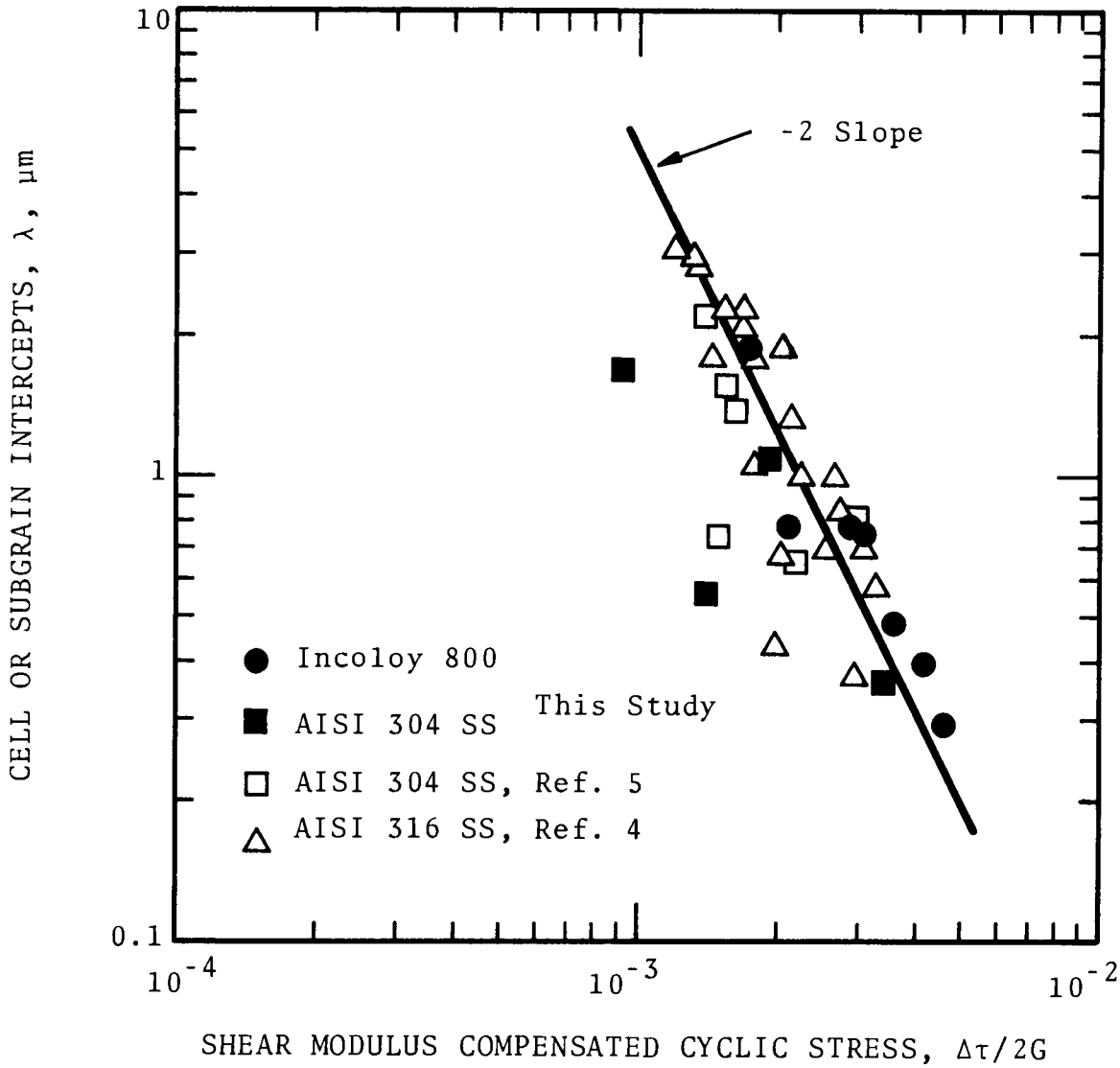

Fig. 4 Relationship between Cell or Subgrain Intercepts and Shear Modulus Compensated Cyclic Stress.

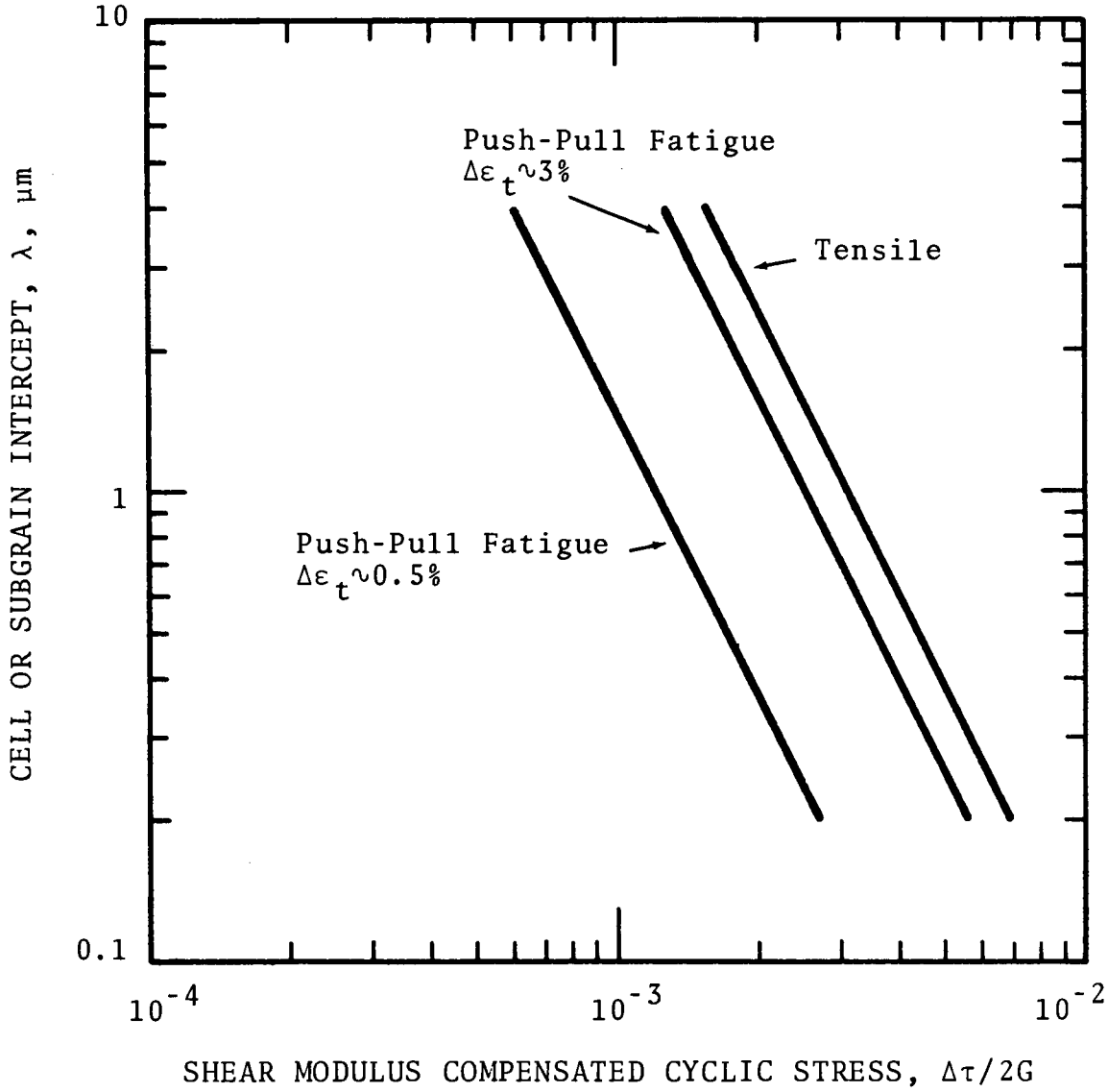

Fig. 5 Schematics showing Effect of Total Strain Range on Relationship Between Subgrain Size and Stress.

in Figure 5, the effect of strain range is only significant at the very low strain ranges. After exceeding 2 to 4 percent of strain, subgrain size approaches the case of monotonic testing with large strain. Further comparison between tensile, creep and fatigue substructure is in progress. The stacking fault energy seems to play a minor role in substructure formation at the elevated temperatures since the three different austenitic stainless steels seem to show the same behavior.

7.2.3 Substructure Strengthening of Room Temperature Mechanical Properties in Incoloy 800 and AISI 304 Stainless Steel (H. Nahm, R. Bhargava and J. Moteff)

In a recent study[6], the ambient temperature mechanical properties have been shown to be enhanced via high temperature substructure strengthening. To further study this behavior, room temperature hardness measurements were made on the specimens having different cell or subgrain sizes developed from the previous high temperature deformation. The hardness variation is shown in Figure 6. The previous data[7] by Moteff and Bhargava was also included in Figure 6. From this figure, it is clearly shown that the relationship holds as;

$$H = H_o + k\,\lambda^{-1} \qquad (5)$$

where H_o corresponds to the frictional hardness parameter. This is quite consistent with the relationship[6,8];

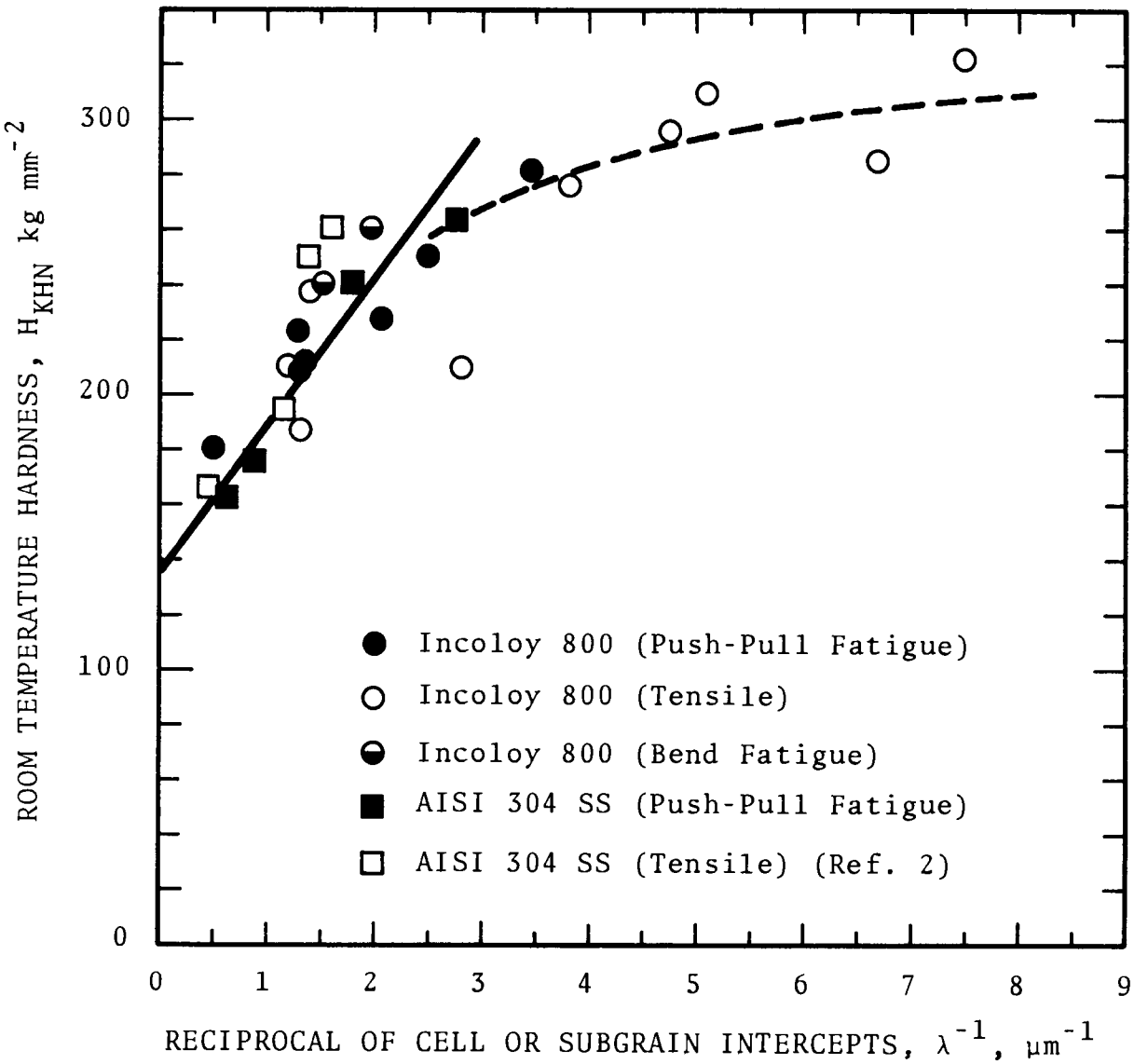

Fig. 6 Room Temperature Hardness as a Function of Reciprocal of Cell or Subgrain Intercepts.

$$\sigma = \sigma_o + k\,\lambda^{-1} \tag{6}$$

where σ_o is the frictional stress. One point to note here is that the hardness appears to deviate from its linearity approaching a saturation when the λ^{-1} parameter increases as shown in Figure 6. This trend, with decreasing cell size, will be confirmed in future studies.

7.2.4 Comparison of the Fatigue Properties when Tested in the Bend and Push-Pull Modes (H. Nahm and J. Moteff)

In order to better understand the cyclic deformation behavior of metals at elevated temperatures, several fatigue specimens tested in the bend and the push-pull modes were obtained and the substructures were characterized with the corresponding mechanical properties. Initially, two specimens from each testing mode were selected for this purpose. Fatigue properties are given as follows;

Testing Mode	Strain Rate $\Delta\dot{\varepsilon}_t$, sec^{-1}	Total Strain Range $\Delta\varepsilon$, Percent	Total Stress Range $\Delta\sigma$, ksi	Fatigue Life N_f
Push-Pull[a, c] (Hour-Glass)	4×10^{-3}	1.97	97.32	407
Bend-Fatigue[b] (Plate)	4×10^{-3}	2.00	not shown	260

a - J. B. Conway, GEMP-732, December 1969).
b - Huntington Alloy Products Division, The International Nickel Company, Inc., Huntington 17, West Virginia.
c - Test temperature for both specimens was 1300°F.

Microhardness was measured on the polished surface cut parallel to the fracture surface. Figure 7 and 8 give the

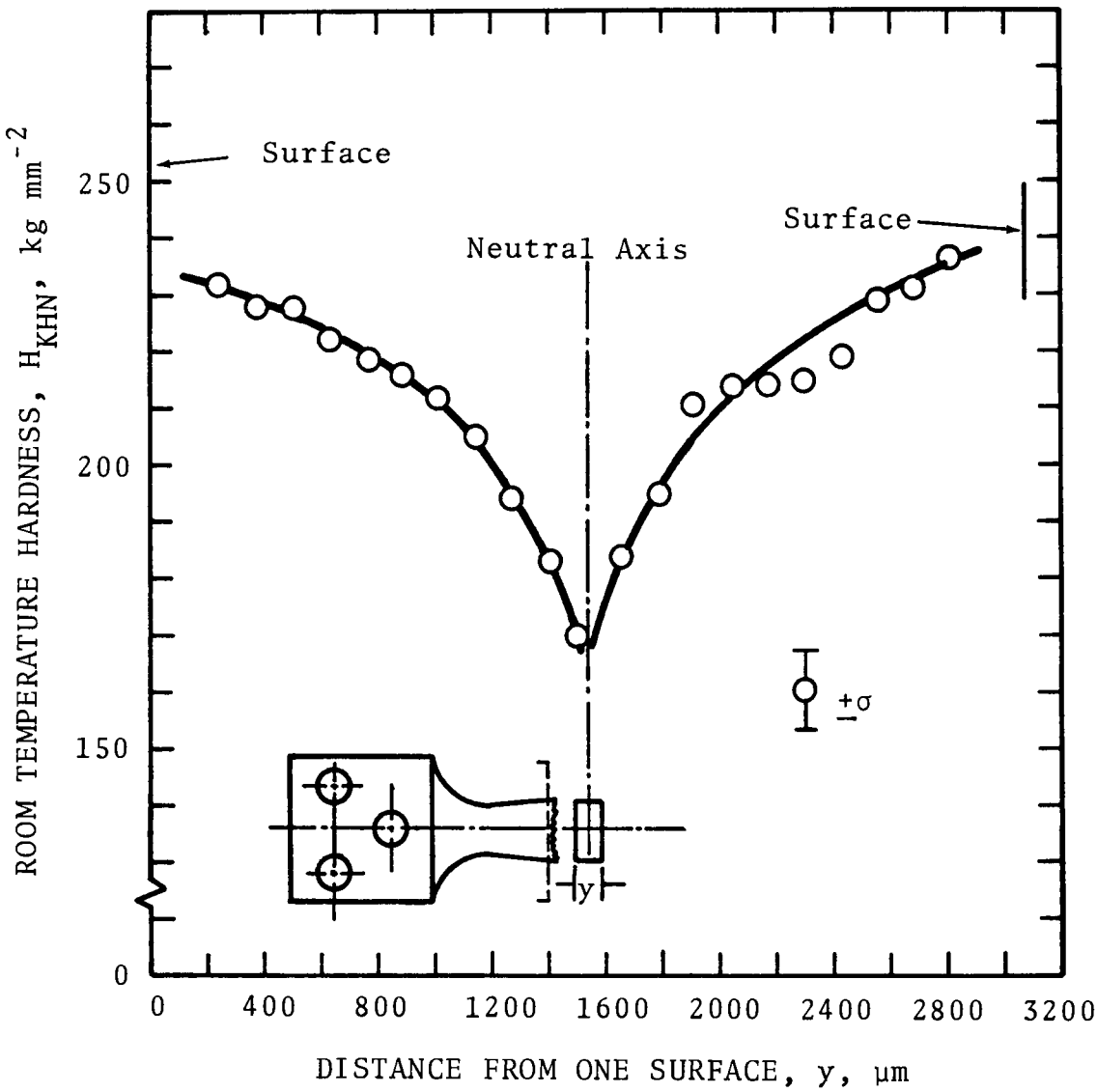

Fig. 7 Transverse Hardness Distribution of Bend Fatigue Specimen on Plane Parallel to Fracture Surface.

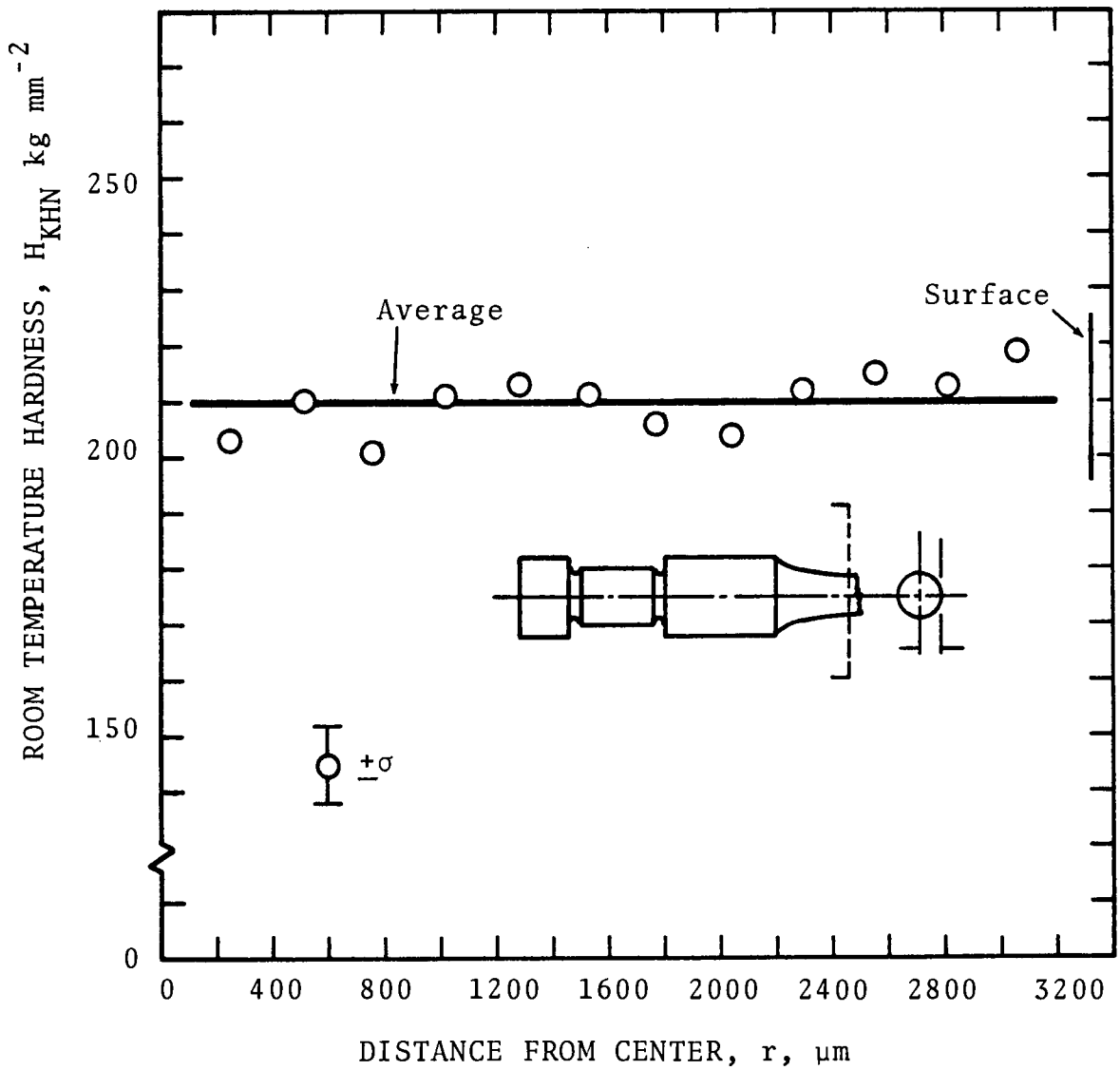

Fig. 8 Diametrical Hardness Distribution of Push-Pull Fatigue Specimen on Plane Parallel to Fracture Surface.

hardness distributions just below the fractured surface and along the thickness for the bend fatigue specimen and along the diameter from the center for the push pull fatigue specimen respectively. As expected, the hardness shows the characteristics of each testing condition. The bend-fatigued specimen shows the minimum along the neutral axis and the maximum hardness on both surfaces. It is quite interesting to note that the hardness distribution shown in Figure 7 for bend fatigue mode may reflect the tensile properties of this material under this testing condition. Quite contrary to the case of bend fatigue, no change in hardness can be observed in the specimen tested in the push-pull mode (Figure 8). Transmission electron microscope revealed the consistent substructural behavior with the hardness distribution. In the bend fatigue specimens, the dislocation cells and high dislocation densities were observed near the surface. Along the neutral axis, the substructure was similar to the control specimen from the unstressed button head. Optical microscopy indicated the same type of fracturing mode in the bend fatigued and push-pull fatigued specimen since the transgranular cracks were observed on the polished surfaces used for the hardness measurement in both cases. Detailed results and analysis with accompanying microstructures will be given in the forthcoming progress reports. It appears to be possible that the bend fatigue testing can be used more effectively for comparisons with push-pull fatigue

once the correlation is obtained between the bend and push-pull cyclic deformation mode in terms of various substructural parameters. Special consideration should also be given to the specimen design based on high temperature fracture mechanics.

7.2.5 Effect of Hold Time During Low Cycle Fatigue on the Substructure Formation Developed at Elevated Temperatures in 304 Stainless Steel (T. Kenfield and J. Moteff

The study of hold time effects in 304 stainless steel is important in the investigation of the time dependent plasticity developed during hold times that cause accelerated failures. Many nuclear power plants have a peak load cycle of 16 hours with an 8 hour log power demand each day. The rapid warming up period may cause compressive yielding in the skin of the vessel, so that when the temperature reaches equilibrium conditions there are residual tensile stresses remaining in the component. This superposition of pressure stresses accompanying both normal operating conditions plus those incorporated during the hold time period cause creep processes to be activated in the hold period even though design stresses may be actually safe under normal operating conditions.

With this capsule account of the nature of the problem, a study* was initiated to characterize the effect of hold

* Part of MS Thesis research.

time behavior in 304 stainless steel. Specifically, the substructure was investigated with electron microscopy techniques in order to correlate subgrain diameters and dislocation densities with applied stresses. Table 1 shows the conditions the specimens were tested at and the observed results determined for subgrain size. Tensile hold time specimens were primarily investigated since it has a more detrimental effect on fatigue life than an equivalent compression (symmetrical) hold time.

Figure 9 shows the relationship between subgrain diameter and the initial cyclic stress, the slope of the plot being -2 which gives a dependency of;

$$\lambda \alpha \sigma^{-2} \tag{7}$$

This correlation is in agreement with that found for cell formation in creep deformation, as well as, the fatigue data for 316 austenitic stainless at 650°C discussed previously. Low strain levels shifts the data to the left.

Work on dislocation density correlations and possible mechanisms for this interaction behavior are also being investigated.

7.2.6 <u>Analysis of Relationships of Creep Rate, Stress and Temperature for 304 Stainless Steel</u> (R. Bhargava, C. Schmidt and J. Moteff)

At the Oak Ridge National Laboratory a very extensive research program is underway to characterize the elevated

TABLE I HOLD TIME EFFECT DATA (650°C)

Spec. No.[a]	Hold Period Min. Tens.	Hold Period Min. Comp.	Strain Rate $\dot{\varepsilon}_T$, sec^{-1}	Plastic Strain Range $\Delta\varepsilon_p$, %	Initial Cyclic Stress $\Delta\sigma_i$[b]	Cyclic Life Cycles	Actual Life Hours	Subgrain Size λ, μm
54-5	0	0	$4x10^{-3}$	1.58	28.7	546	1.52	.67
53-11	0	0	$4x10^{-3}$		28.0	592	1.64	.67
56-12	.1	0	$4x10^{-3}$	1.64	28.3	545	2.42	.80
57-1	1	0	$4x10^{-3}$	1.66	27.8	331	6.43	.75
56-5	10	0	$4x10^{-3}$	1.71	25.8	193	32.7	.95
53-10	30	0	$4x10^{-3}$	1.79	23.6	146	73.4	.98
54-2	60	0	$4x10^{-3}$	1.77	25.0	144	144.3	1.0
57-6	180	0	$4x10^{-3}$	1.78	22.4	150	450.0	1.3
66-1	600	0	$4x10^{-3}$	1.80	20.4	149	1493.0	1.55
54-11	0	0	$4x10^{-3}$	.28	17.4	14,620	10.1	.78
54-12	0	0	$4x10^{-3}$	.27	17.6	13,400	9.3	.74
57-11	1	0	$4x10^{-3}$	.27	15.7	3,869	64.7	1.1
57-12	10	0	$4x10^{-3}$	.32	14.8	1.703	285	2.0
56-2	30	0	$4x10^{-3}$	.34	14.7	862	431	2.25
54-3	0	30	$4x10^{-3}$	1.7	27.0	480	241.3	1.13
53-9	30	30	$4x10^{-3}$	1.8	21.8	380	381.0	1.3

(a) Specimens obtained from Task 1516, "Evaluations of the Plastic Fatigue Properties of Heat Resistant Alloys," of the past AEC Contract AT(40-1)-2847. GE-NMPO, Cincinnati, Ohio.

(b) $\Delta\sigma_i = \Delta\sigma/2$, $\Delta\sigma$ = Total Cyclic Stress Range (kg mm^{-2}).

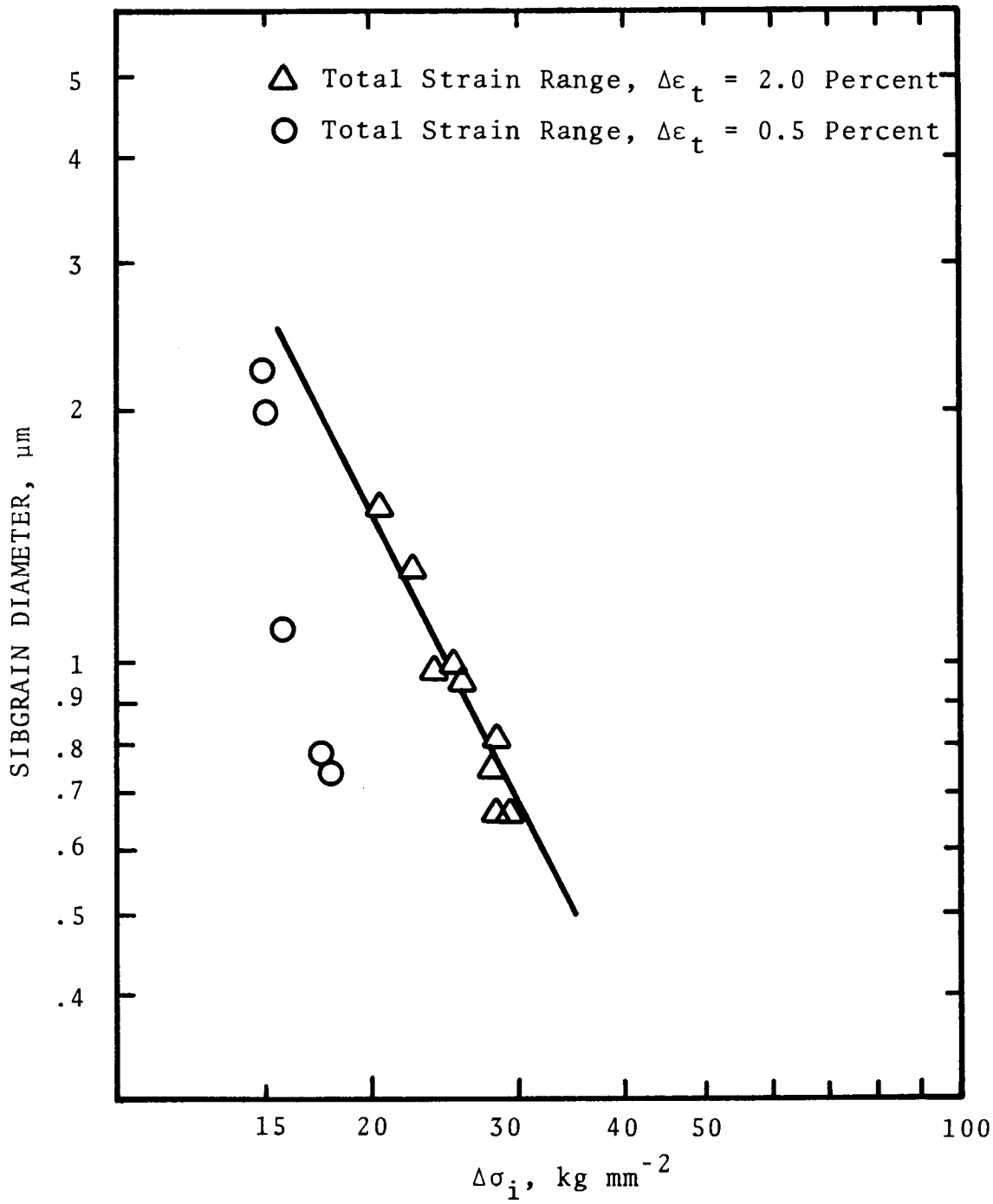

Fig. 9 Influence of Initial Cyclic Stress Range on the Subgrain Diameter for 304 Stainless Steel Tested at 650°C in the Fatigue Mode with Various Tensile Hold Times.

temperature mechanical properties of AISI 304 stainless steel. One of the reference heats is 9T2796.[9] A series of creep rupture tests are being performed on the specimens from this heat after giving an anneal at 1093°C for one-half hour. A set of data for the creep tests was made available to the University of Cincinnati through the courtesy of Mr. R. Swindeman. These data are also presented in past ORNL progress reports.

The stress range for the specimens used in the present study is from 7500 psi to 45,000 psi and the temperature range is from 1000°F to 1500°F. An extensive analysis of this data has been started using the computer and some empirical relationships are fitted for relations between creep rate, stress and temperature.

The creep rate in the secondary stage of creep, $\dot{\varepsilon}_s$ is a function of structure (S), stress (σ) and temperature (T) and can be expressed by a relation;

$$\dot{\varepsilon}_s = f(S, \sigma, T) \exp(-Q_c/RT) \qquad (8)$$

Various empirical relationships exist for the stress and temperature dependence. One of the most widely used is;

$$\dot{\varepsilon}_s = A\, \sigma^n \exp(-Q_c/RT) \qquad (9)$$

Q_c, the activation energy for creep, n is the stress exponent usually 5 ± 2 and A is the materials constant which depends to a first approximation on the substructure.

A better correlation is also suggested which involves the modulus compensated stress, namely;

$$\dot{\varepsilon}_s = A(\sigma/E)^n \exp(-Q_c/RT) \tag{10}$$

For separating effect of temperature dependency from stress a temperature compensated creep rate parameter called the Zener-Holloman parameter has also been used in creep analysis. This equation is;

$$\dot{\varepsilon} \exp \frac{Q_c}{RT} = A\ f(\sigma) \tag{11}$$

Again for stress dependency, $f(\sigma) = \sigma^n$ or $f(\sigma) = (\sigma/E)^n$.

By using regression analysis on the data from 28 specimens, it is found that activation energy for creep does depend on the temperature as previously shown by Sherby and Co-workers.[9] The activation energy values determined from various temperature selections and stresses are shown in Figure 10. In this figure, four sets of activation energy values are plotted by using the applied stress, true stress, modulus compensated applied stress and modulus compensated true stress as one of the independent variables. But for the present preliminary studies and in the temperature range from 1100°F to 1500°F (above 0.5 T_m), one value of activation energy was used, and this is indicated by the straight line.

In Figure 11(a) the $\dot{\varepsilon}_s$ is plotted versus σ at various temperatures and the data can be represented by various straight lines. The value of n, the slope of the lines,

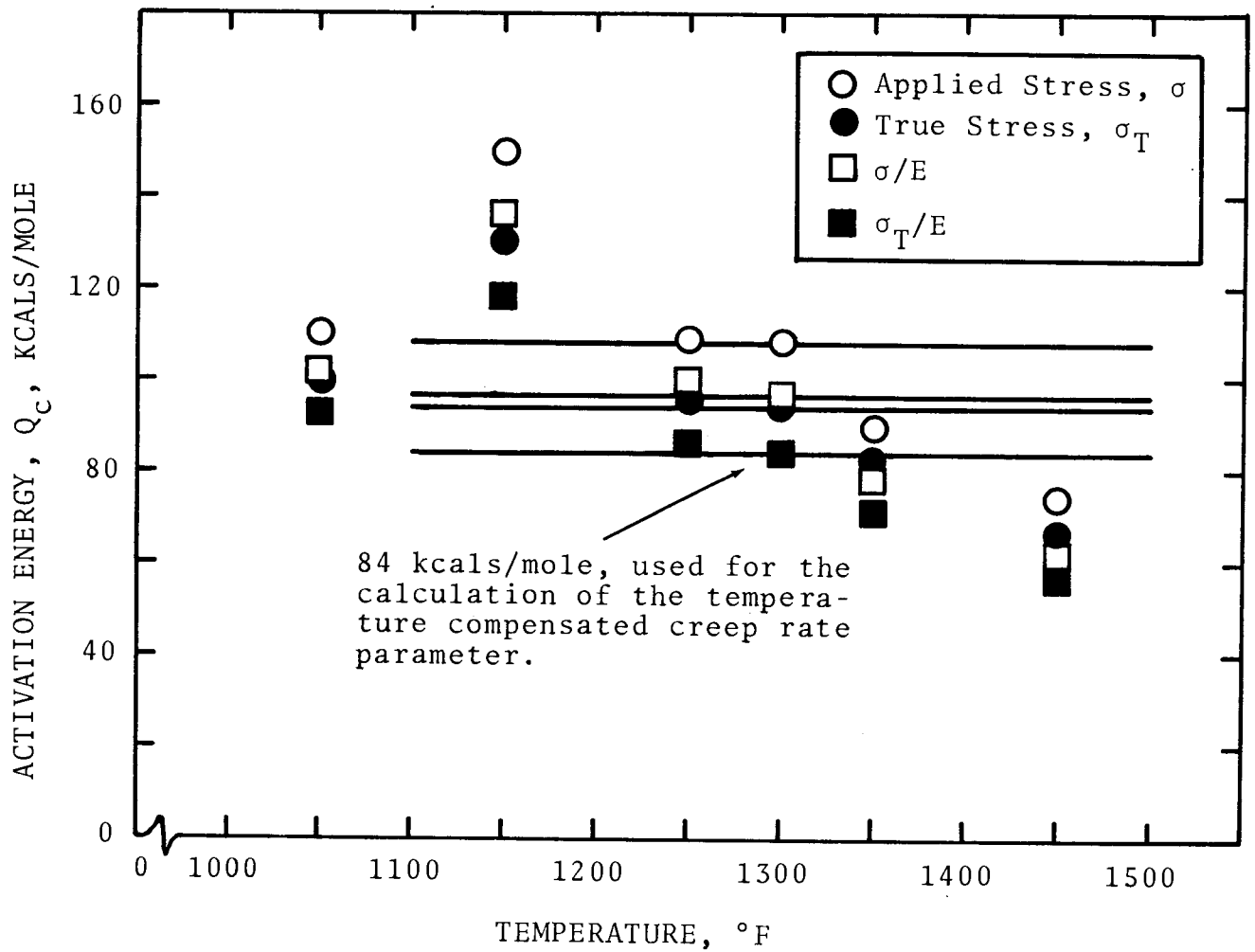

Fig. 10 Plot of Activation Energy for Creep as a Function of Temperature for 304 Stainless Steel, Heat 9T2796.

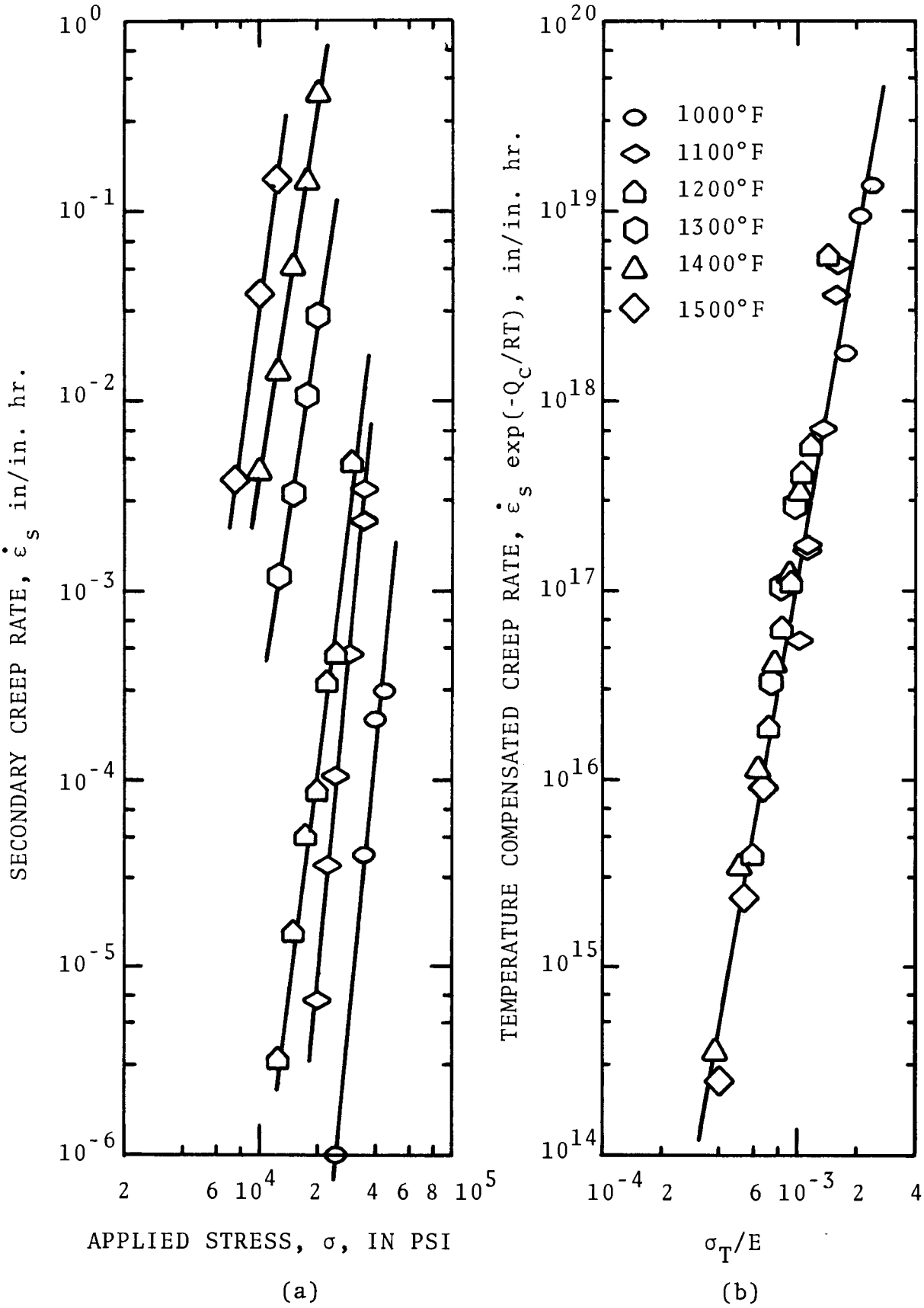

Fig. 11(a) Plot of Secondary Creep Rate $\dot{\varepsilon}_s$ vs Applied Stress and
(b) Plot of Temperature Compensated Creep Rate $\dot{\varepsilon}_s \exp(-Q_c/RT)$ vs Modulus Compensated Stress, σ_T/E.

varies between 5 and 7. In Figure 11(b), the Zener-Hollomon parameter, $\dot{\varepsilon}(\exp Q_c/RT)$ is plotted versus (σ_T/E), the modulus compensated true stress. One line with slope, $n = 6.8 \pm 0.2$ can be drawn through the points at various temperatures using an activation energy Q_c of 84 kcals/mole.

Further work on analysis of these and other possible relationships is underway and will be reported in future progress reports. Particular emphasis will be placed on the determination of the activation volume, v, for creep ($\dot{\varepsilon} = A \exp [(Q_o - v\sigma)/RT]$ and on the development of a mathematical relationship which includes the influence of the internal stress fields caused by substructural changes (i.e. cells, subgrains, dislocations, precipitates).

7.2.7 Estimation of Activation Energy for Creep from Hot Hardness Measurements of 304 Stainless Steel (R. Bhargava and J. Moteff)

The room temperature and elevated temperature mechanical properties of AISI 304 stainless steel are being studied very extensively, especially on the reference heat 9T2796.

A small sample of this reference heat was given an anneal at 1093°C for one-half hour and then electropolished in preparation for the measurement of hot hardness. The hardness in terms of DPH units were measured from RT to 1300°C. The details of the hot hardness apparatus are given elsewhere.[11] The specimen was held at the test temperature for 15 minutes before the indents were made.

The temperature variation of hardness may be given by a relation of the type;

$$H = A \exp(Q'/T) \tag{12}$$

In order to obtain Q', the apparent activation energy in units of calories per mole, Larsen-Badse[12] used the equivalent relationship;

$$H = A \exp(2Q'/RT) \tag{13}$$

where R is the gas constant. The apparent activation energy Q' has been correlated to the activation energy for creep or self diffusion.

Sherby and Armstrong[13] suggested the relation;

$$H/E = B \exp(Q_L/nRT) \tag{14}$$

where Q_L is the lattice self diffusion activation energy, E is the Young's modulus, n is the stress exponent for creep (usually n = 5) and B is a material constant. H in Equation 14 is the hot hardness above 0.75 T_m.

The H/E values are plotted versus $10^3/T$ in Figure 12. As can be seen clearly the data below and above $\sim$ 0.75 T_m can be fit by two straight lines. The break in the curve around 0.75 T_m signifies a change in mechanism of deformation and is probably associated with the power law breakdown as suggested by Sherby and Armstrong.

The activation energy, Q is calculated utilizing Equation (14) and n = 5. The value of Q = 87 kcals/mole is in

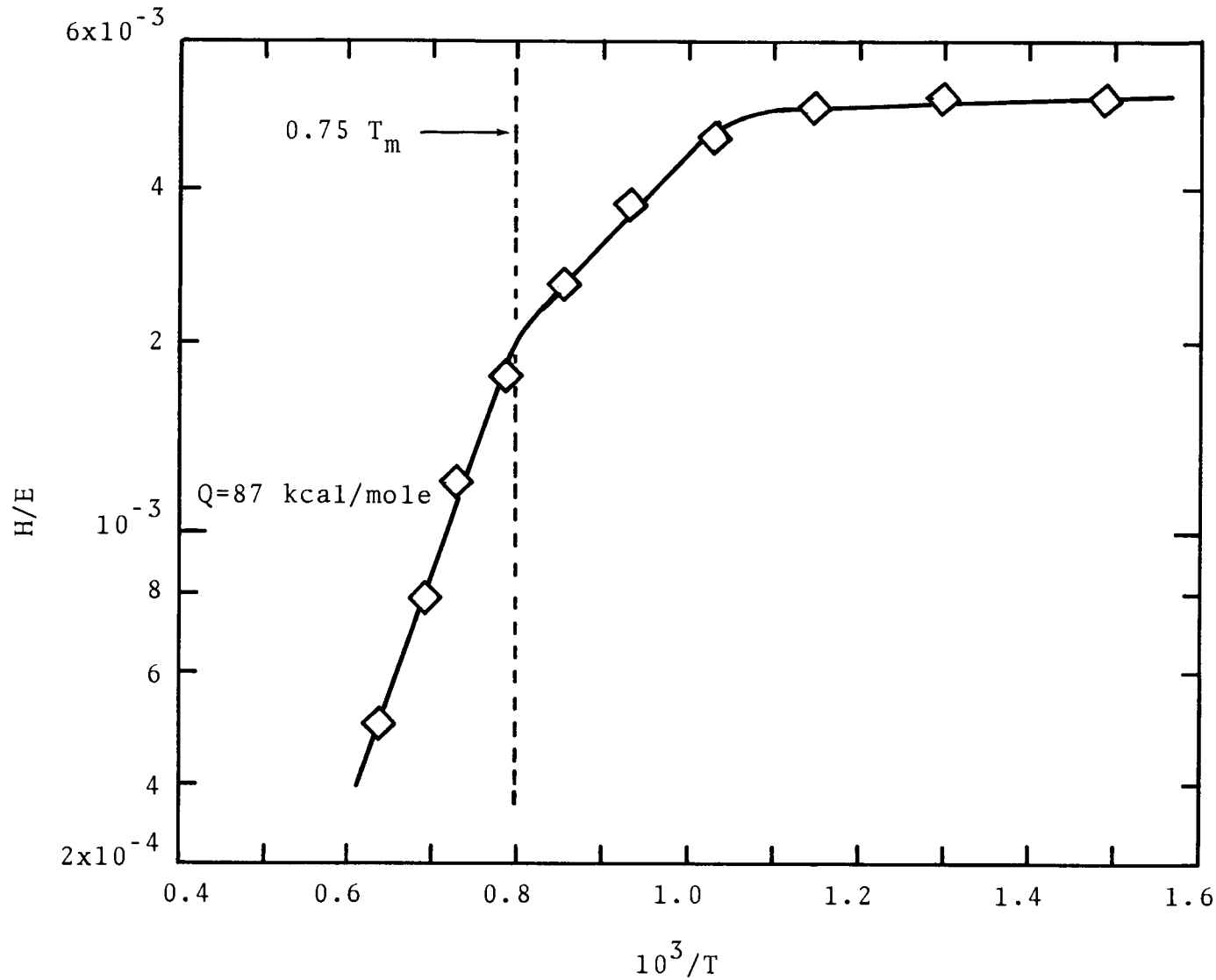

Fig. 12 Plot of Hardness/Young's Modulus Ratio as a Function of Reciprocal Temperature for 304 Stainless Steel, Heat Number 9T2796.

reasonable agreement with the 84 kcal/mole used in the creep analysis. This value of Q is in reasonable agreement with the published values in the literature. Garofalo et al.[14] determined an activation energy for creep and reported 75 kcals/mole whereas Cuddy[15] reported a value of 91±9 kcals/mole for the creep activation energy. Work is continuing in the correlation of hot hardness data with macroscopic mechanical properties at elevated temperatures.

7.2.8 Correlation of Hot Hardness with the Elevated Temperature Tensile Properties of Cold Worked 316 Stainless Steel (T. Kenfield and J. Moteff)

A preliminary study of the degree of correlation of hot tensile properties with hot hardness measurements for cold worked 316 stainless steel has been made. The present investigation reveals excellent agreement between hot hardness data and experimental hot tensile data of 20 percent cold worked 316 stainless steel at temperatures above 500°C. This trend is shown in Figure 13 along with experimental data[16-19] generated by the indicated contributors. In the previous quarterly report[20] it was shown for annealed 304 stainless steel, that agreement was achieved with experimental data above 600° to 800°C by the following relationship;

$$\sigma_u = H/C \qquad (15)$$

where C = 3.1±0.2, a constant proposed by Sieber and Moteff for austenitic alloys based on original work by Cahoon.

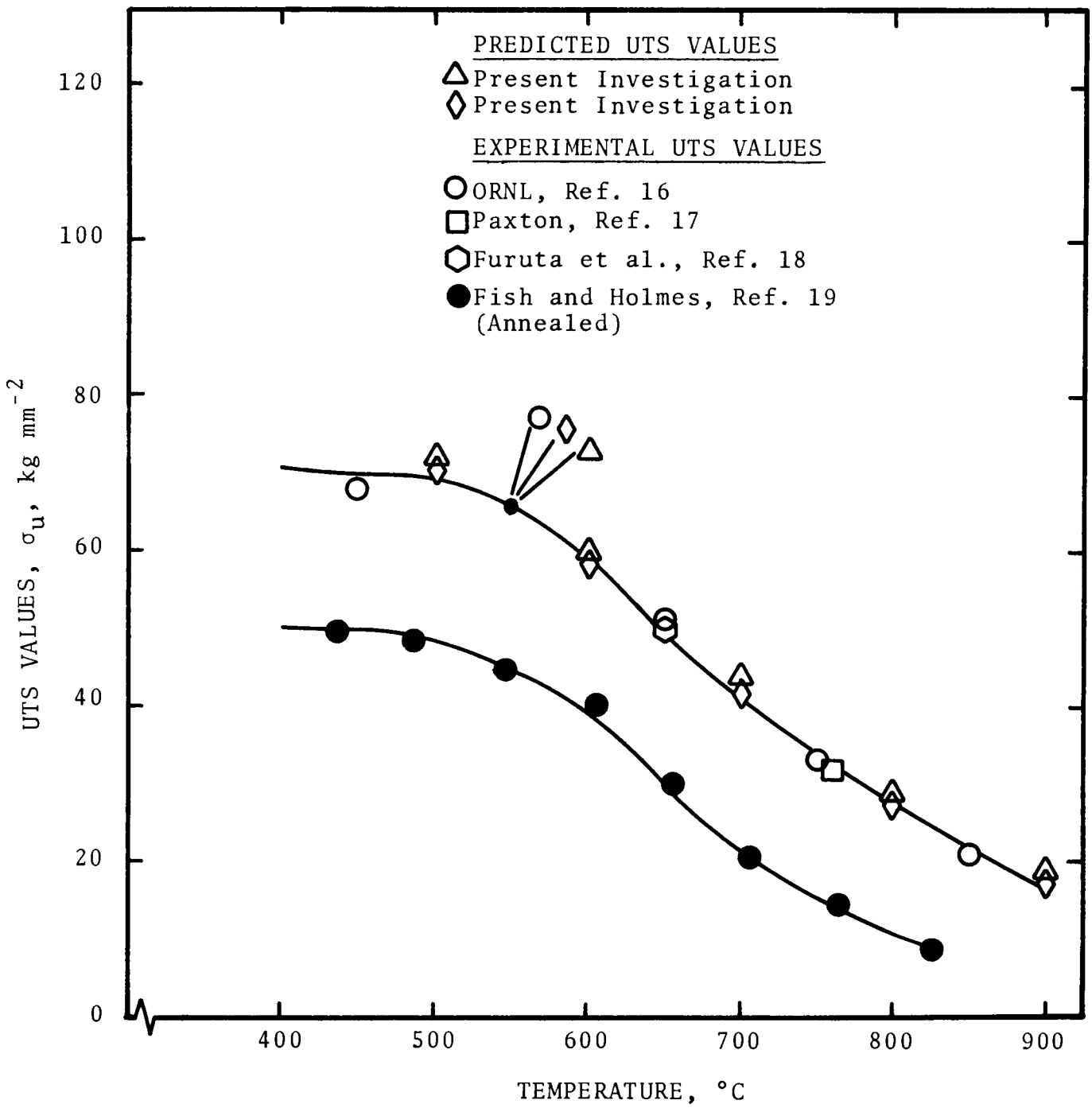

Fig. 13 Comparison of the Experimental Ultimate Tensile Strength of 20 Percent Cold Worked 316 Stainless Steel with Calculated Values Based on Hot Hardness Data.

This type of agreement is also shown for the cold worked 316 stainless steel at temperatures above about 500°C. This can be partly explained by the fact that the effect of strain hardening is resisted to a far greater extent in cold worked material thereby allowing recovery processes to proceed at lower temperatures, a region where hot hardness testing can be strongly strongly strain hardening dependent.

7.2.9 Recovery and Recrystallization Behavior of Cold Worked 316 Stainless Steel (T. Kenfield)

The recovery behavior of cold worked 316 stainless steel has been studied in detail by using room temperature hardness measurements after both isochronal and isothermal anneals.

Specimens prepared from reference heat 65808 were cold worked at 20, 35 and 50 percent reductions. Room temperature hardness measurements were made after one hour isochronal anneals at the following temperatures: 25, 200, 250, 300, 350, 400, 500, 550, 600, 700, 800, 900 and 1050°C. The isothermal anneals were performed at 710°C for times of 1, 10, 100 and 1000 hours. Knoop hardness measurements were made at room temperature using the standard 500 gram load following each anneal.

The isochronal anneals, Figure 14, suggest that recovery of cold worked 316 stainless steel starts in the temperature range of 500° - 600°C. The recovery rate is highest in the 50 percent cold work and drops with the decrease in percent

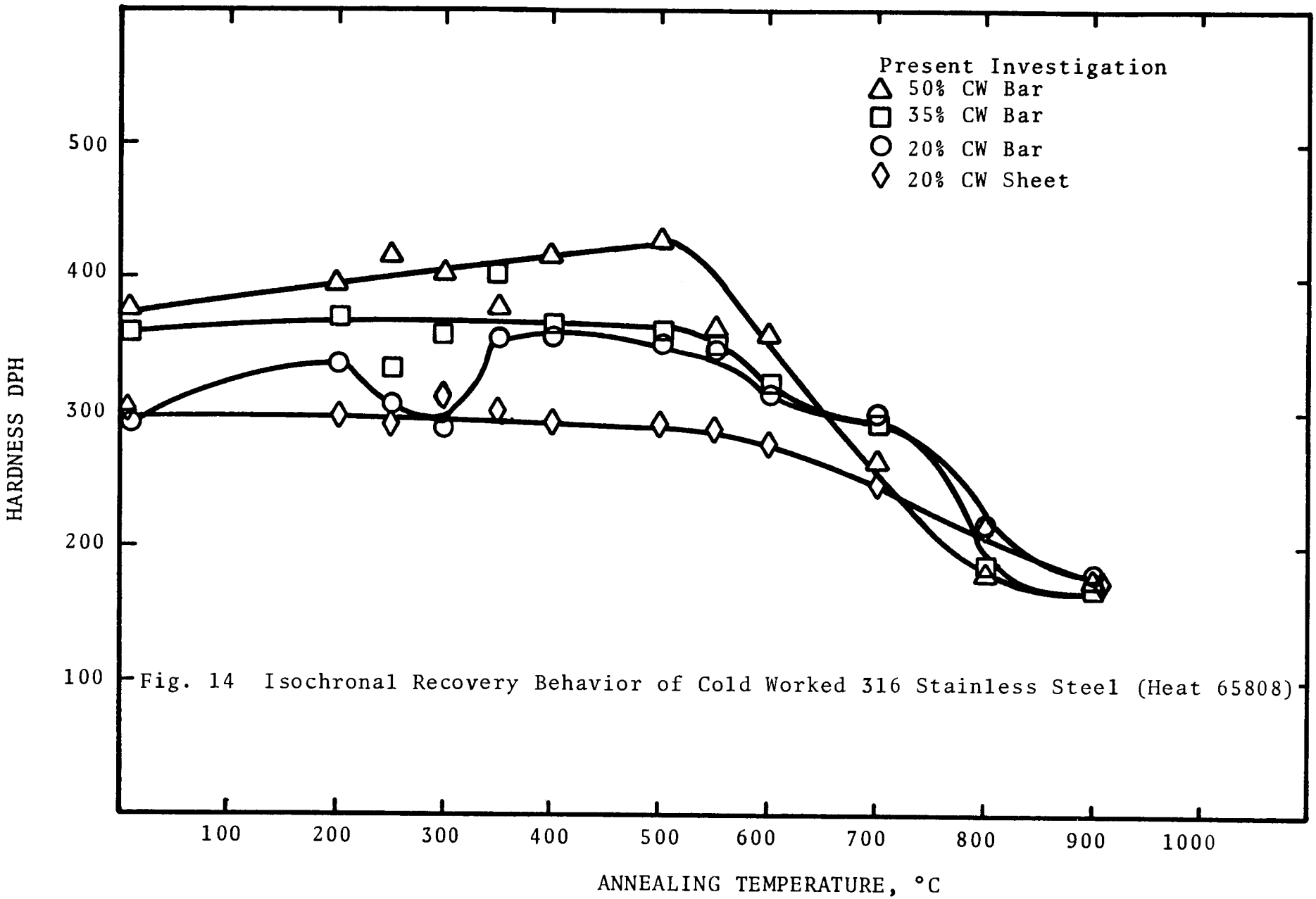

Fig. 14 Isochronal Recovery Behavior of Cold Worked 316 Stainless Steel (Heat 65808)

cold work.

The isothermal anneals at 710°C, Figure 15, show that most of the recovery occurs in the first hour of annealing and longer annealing times do not show any significant effect.

Based on other published data, the recovery temperature is a sensitive function of chemical composition. Since carbon content is one of the more sensitive elements effecting the recovery temperature, a plot (Figure 16) for 20 percent cold worked 316 stainless steel as a function of carbon content is presented. The influence of the carbon on the formation of various precipitates and the subsequent influence on the recovery behavior and also on the strength parameters is still under investigation.

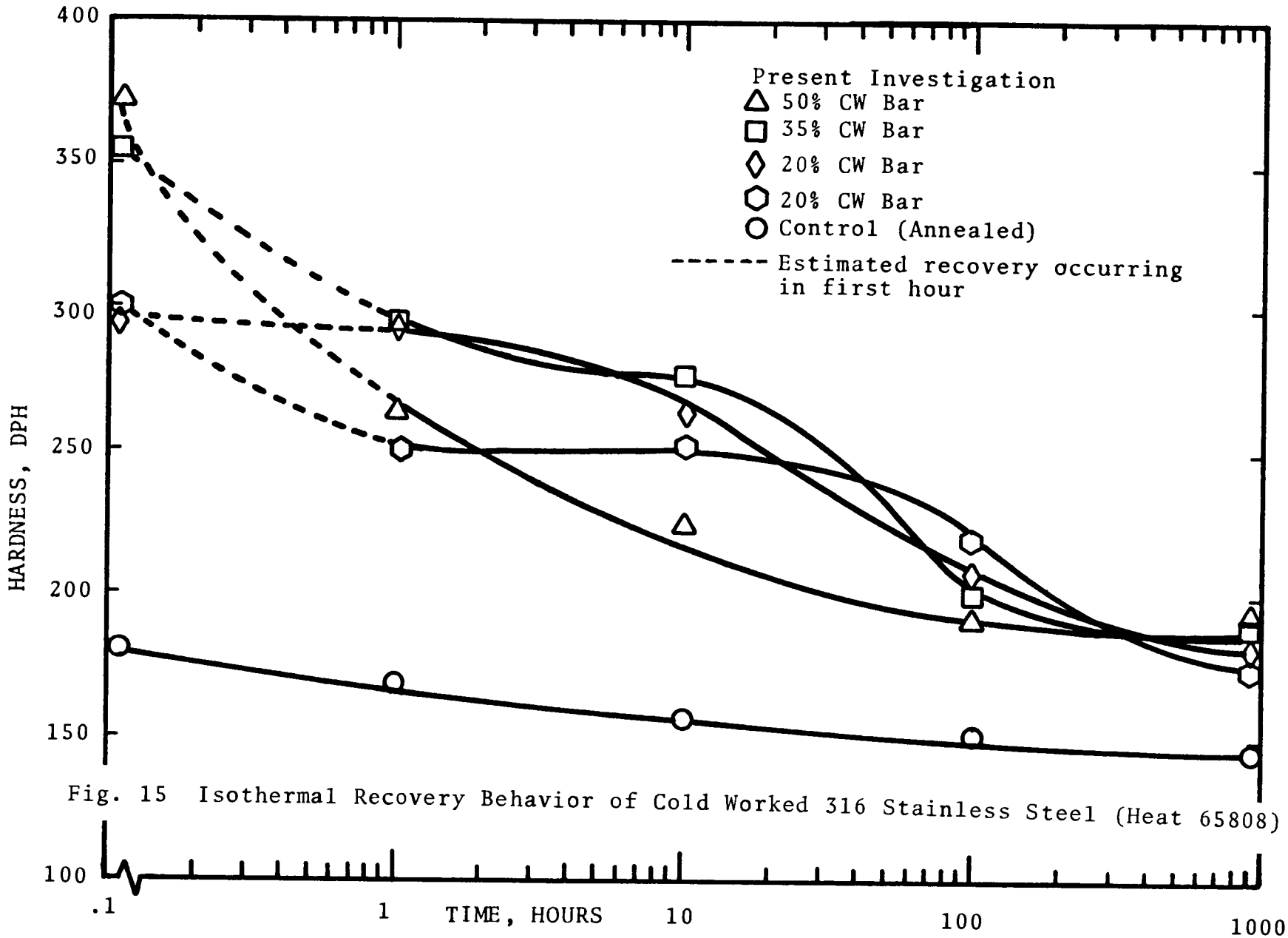

Fig. 15 Isothermal Recovery Behavior of Cold Worked 316 Stainless Steel (Heat 65808)

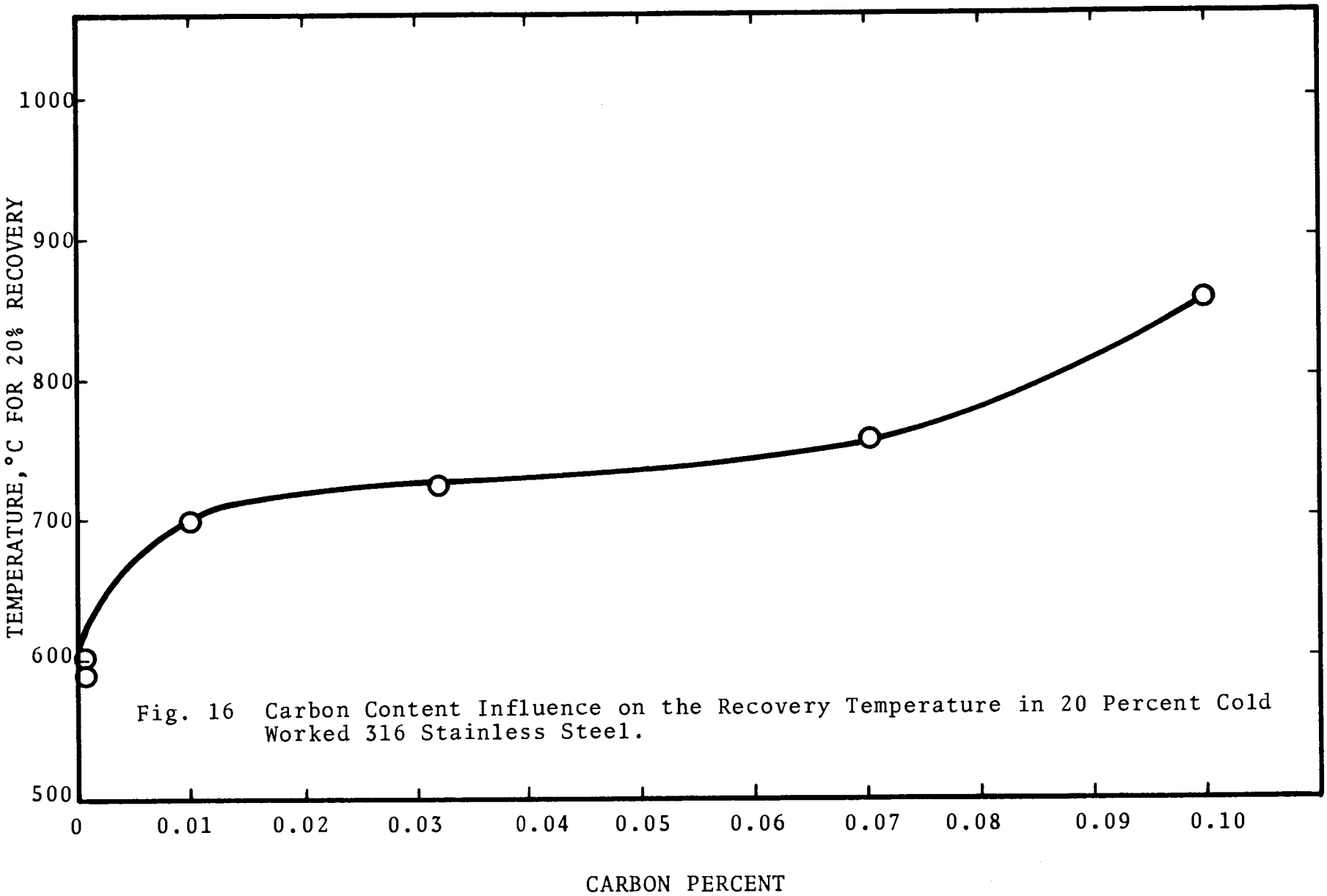

Fig. 16 Carbon Content Influence on the Recovery Temperature in 20 Percent Cold Worked 316 Stainless Steel.

7.3 REFERENCES

1. A. Orlova and J. Cadek, Phil. Mag. 28, 891 (1973).
2. K.D. Challenger and J. Moteff, Met. Trans. 4, 749 (1973).
3. J.E. Bailey and P.B. Hirsch, Phil. Mag. 5, 485 (1960).
4. K.D. Challenger and J. Moteff, Met. Trans. 3, 1675 (1972).
5. K.D. Challenger and J. Moteff, Scripta Met. 6, 155 (1972).
6. C.M. Young and O.D. Sherby, JISI 211, 640 (1973).
7. Progress Report, January-March, 1973, COO-2107-10, June 15, 1973, University of Cincinnati, Cincinnati, Ohio.
8. D.J. Abson and J.J. Jonas, J. Nucl. Mats. 42, 73 (1972).
9. ORNL-4948, "Mechanical Properties Test Data for Structural Materials," Quarterly Progress Report for Period Ending January 31, 1974; March 1974, p. 177.
10. O.D. Sherby and P.M. Burke, Prog. in Matl. Sci. 13, 325 (1966).
11. J.L. Kamphouse, J.C. Blake and J. Moteff, Rev. Sci. Instr. 40, 321 (1969).
12. Jorgen Larsen-Badse, Trans. Japan Inst. Metals 9, 312 (1968).
13. O.D. Sherby and P.E. Armstrong, Met. Trans. 2, 3479 (1971).
14. F. Garofalo, O. Richmond, W.F. Domis and F. Von Gemminger, Jt. Inter. Conf. on Creep, 1, (1963), London.
15. L.J. Cuddy, Met. Trans. 1, 395 (1970).
16. ORNL-4948, "Mechanical Properties Test Data for Structural Materials," Quarterly Progress Report for Period Ending January 31, 1974; March 1974.
17. M.M. Paxton, Hanford Engineering Development Laboratory HEDL-TME 73-34, March 1973.
18. T. Furuta, S. Kawasaki and R. Nagasaki, J. Nucl. Mater. 47, 65 (1973).

19. R.L. Fish and J.J. Holmes, J. Nucl. Mater. 46, 113 (1973)

20. COO-2107-10, "Correlation of Substructure with the Mechanical Properties of Plastically Deformed AISI 304 and 316 Stainless Steel," Progress Report for the Period Ending December 31, 1973; March 15, 1974, University of Cincinnati.

8. UNIVERSITY OF CALIFORNIA AT LOS ANGELES

P. A. Chalco and K. Ono

8.1 INTRODUCTION

During the past three years, we have examined microstructural variations as a function of time and temperature, and the concomitant effects on mechanical behavior, in 2-1/4Cr-1Mo steels of different initial carbon content. This study has been performed in conjunction with the research program being undertaken at Oak Ridge National Laboratory. Our major goals were: 1) to identify the metallurgical changes during the long-term exposure to reactor operating temperatures; 2) to characterize the mechanical properties of the exposed alloys; 3) to correlate the strength degradation to observed microstructural changes. Presently, the first two are near completion, while the latter still requires additional effects on quantification.

8.2 MICROSTRUCTURAL RESULTS

8.2.1 Normalized and Normalized and Tempered Conditions

These results have already been reported[1-3] and significant results are summarized here. Normalized alloys showed a bainitic

structure (C = 0.12%), 20% bainite plus 80% polygonal ferrite structure (C = 0.03%) and 50% irregular ferrites plus 50% polygonal ferrites (C = 0.009%) for the three carbon levels, respectively. Tempering at 1300°F, 1 hr. produced heavy carbide precipitation and recovery of the dislocation substructures in the bainite, and subgrain formation in the irregular ferrite. The polygonal ferrite structure was essentially unchanged.

8.2.2 Long-Term Tempered Conditions of Low Carbon (0.009%C) 2 1/4 Cr-1 Mo Alloy

8.2.2.1 Tempering at 850°F

Additional tempering at 850°F was performed for the durations of 4,8,12 and 19 months starting from the normalized and tempered (N & T) condition. Tempering for 12 months and especially for 19 months (Fig. 1a) caused complete recrystallization in some regions of these materials where groups of very gine grains (5 ~ 20μ) were very common, thereby decreasing the average grain size. While the grain size of the material tempered for 4 months was about 29 μm, that of those materials tempered for 8 and 12 months was 24 and 23 μm, respectively. A subsequent grain growth in the recrystallized zones was observed in the material tempered for 19 months, which had an average grain size of 28 μm. All these values are smaller than the grain size of 30 μm observed for materials in the normalized (N) and normalized and tempered (N & T) conditions. Examination by thin foil TEM of all materials tempered at 850°F revealed that the subgrain structure observed in some regions of the N & T materials had disappeared. Also, very fine, irregularly shaped, grains were often

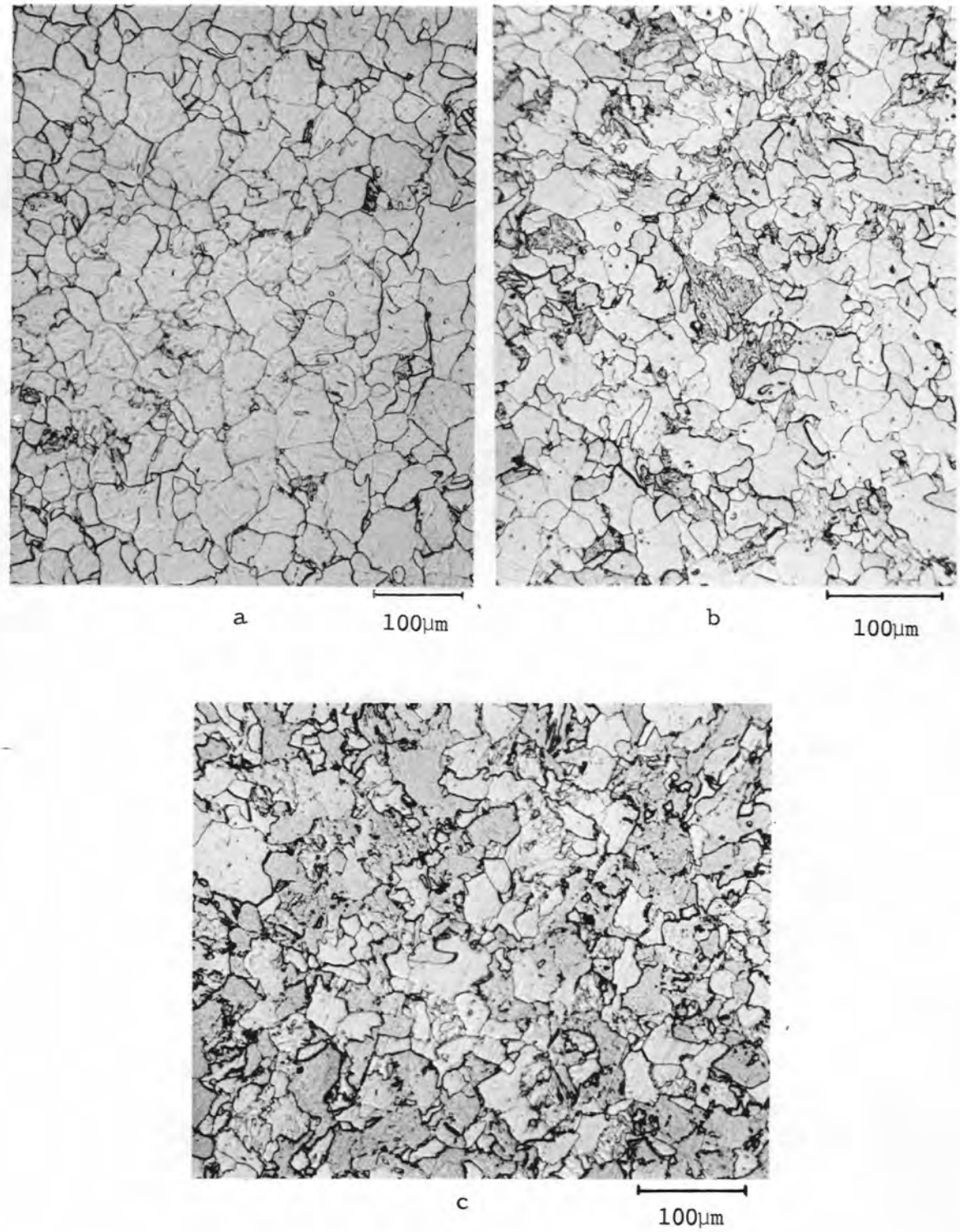

Figure 1. Optical micrographs of low carbon (.009%C) Cr-Mo steel tempered (a) 850°F, 19 months, (b) 950°F, 1 month, (c) 1050°F, 1 month.

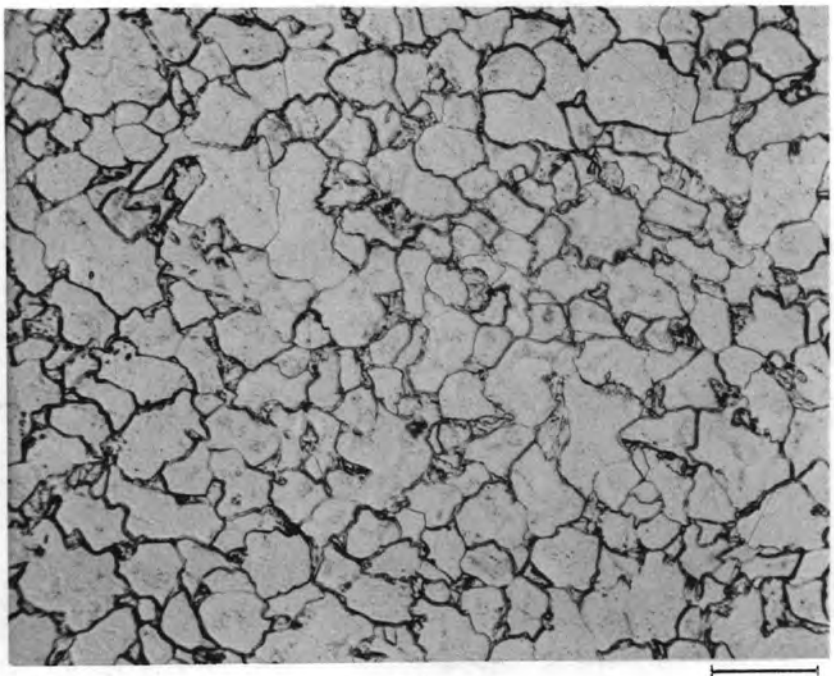

d

100μm

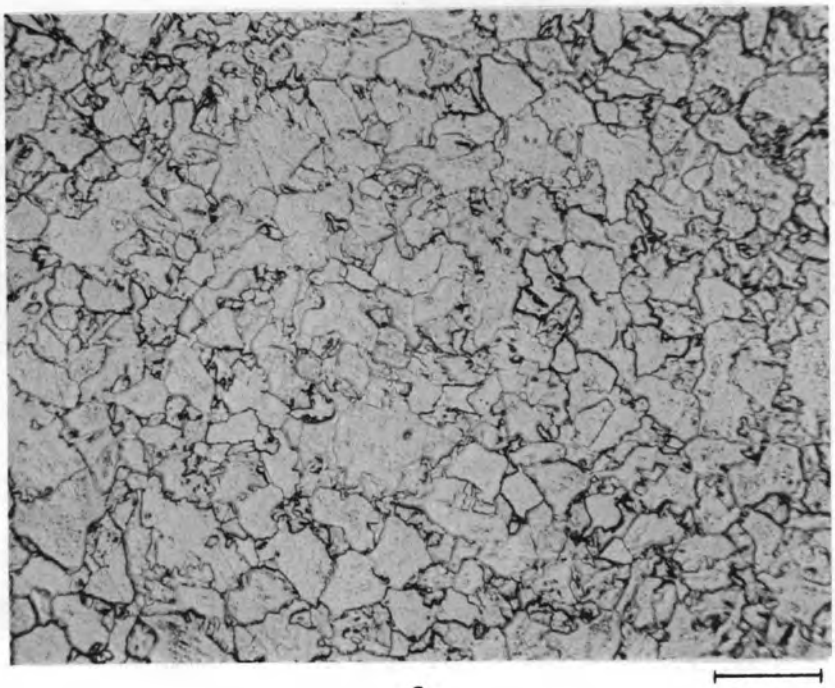

e

100μm

Figure 1. (d) 1050°F, 8 months, (e) 1050°F, 12 months.

observed throughout the alloy microstructure (Fig. 2a). Presumably, these grains were formed after the complete recrystallization of the subgrain structure. No other significant microstructural changes were observed, except for some coarsened precipitates similar to those already present in the N & T condition (Fig. 2b). These particles have been analyzed by X-ray and electron diffraction and have been identified as CrN having an fcc structure with a lattice parameter of 4.13 ± .02Å.

8.2.2.2 Tempering at 950°F

The N & T specimens were tempered for 1, 2, 4, 8, 12 and 19 months at 950°F. Optical micrographs of these materials (e.g., Fig. 1b) clearly showed regular (or polygonal) and irregular (or accicular) types of ferrite. Within the irregular ferrite regions, some recrystallization seemed to have occurred. The average grain size for materials tempered at 950°F increased slightly to 31 to 33 μm, which compares to 30 μm observed in the N & T condition. Thin film TEM studies indicated that, in general, all the materials tempered at 950°F had a microstructure very similar to that observed in the N & T condition as shown in Fig. 3a. Approximately equal amounts of irregular ferrite and regular ferrite are present in this material. Fig. 3b and c show the details of each type. The subgrain boundaries in the irregular ferrite are decorated by fine precipitates, which probably have stabilized this subgrain structure (Fig. 3b). Figs. 3d and e suggest the general shape of the subgrains to be a lath, 1 to 3 μm long. In the regular ferrite regions, dislocations were decorated

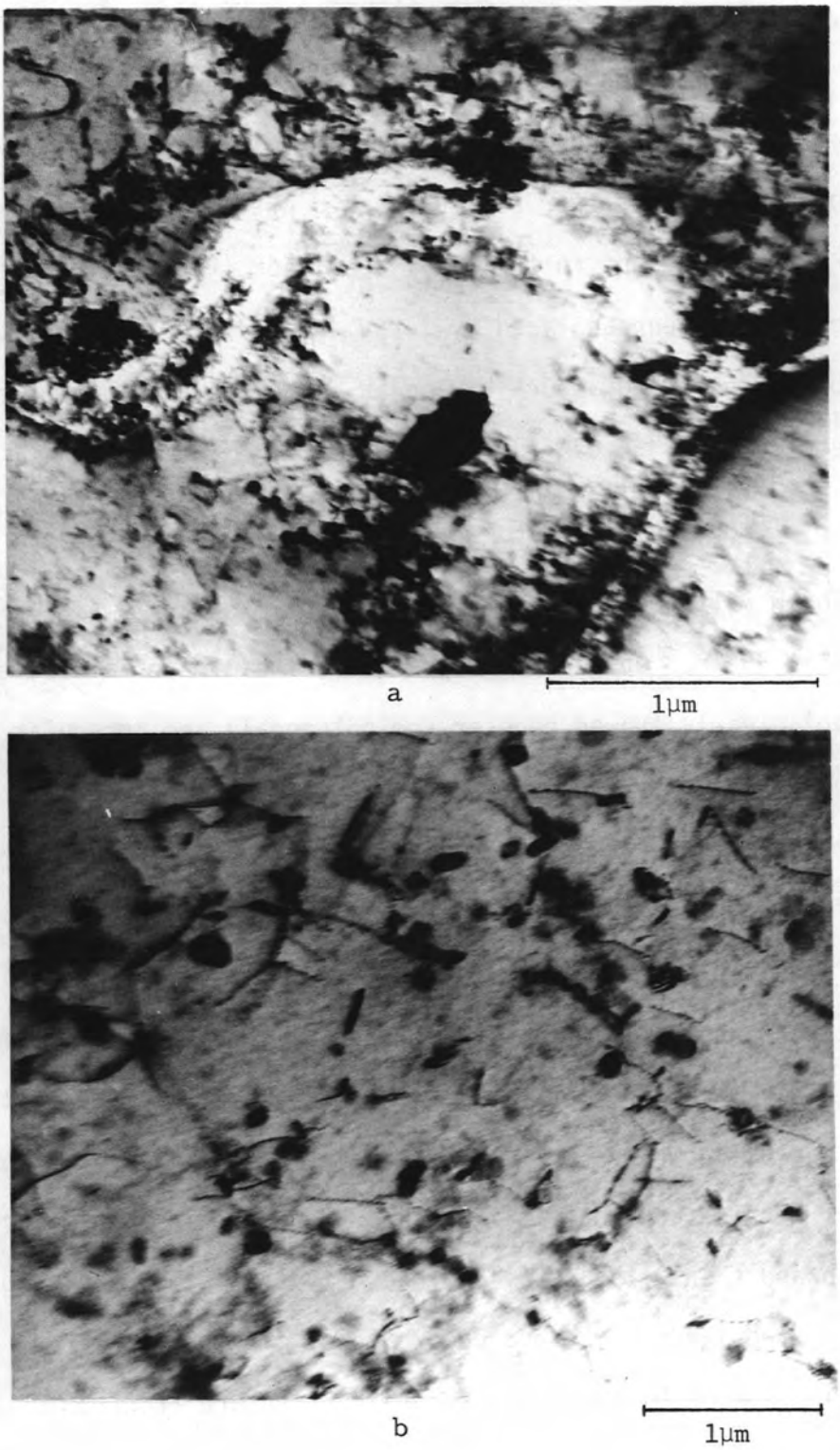

Figure 2. Electron micrographs of low carbon Cr-Mo steel tempered at 850°F for 8 months.

a 1μm

Figure 3. Electron micrographs of low carbon Cr-Mo steel tempered at 950°F for (a) 8 months.

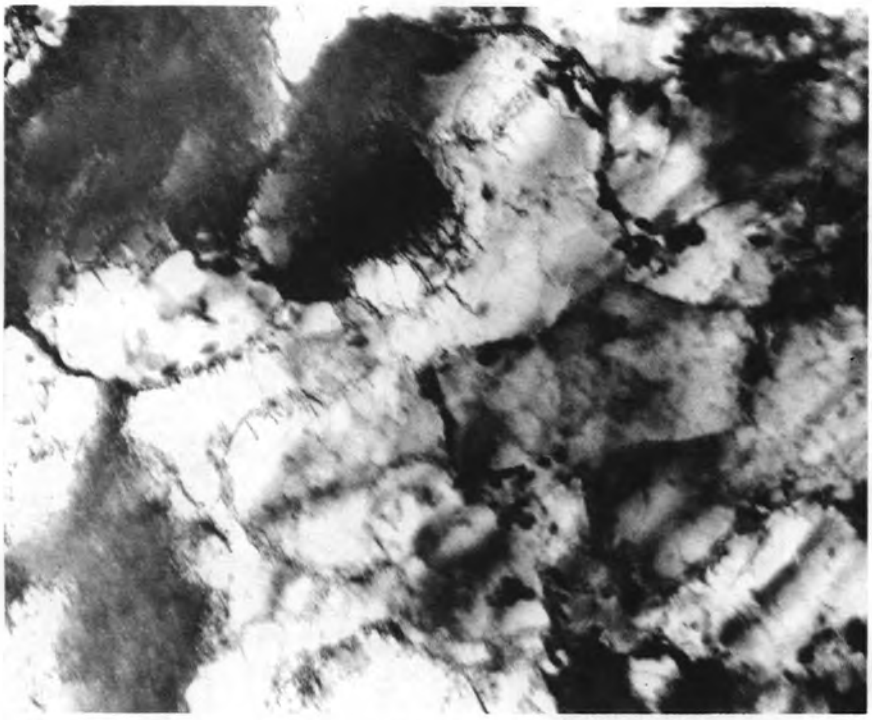

b 1μm

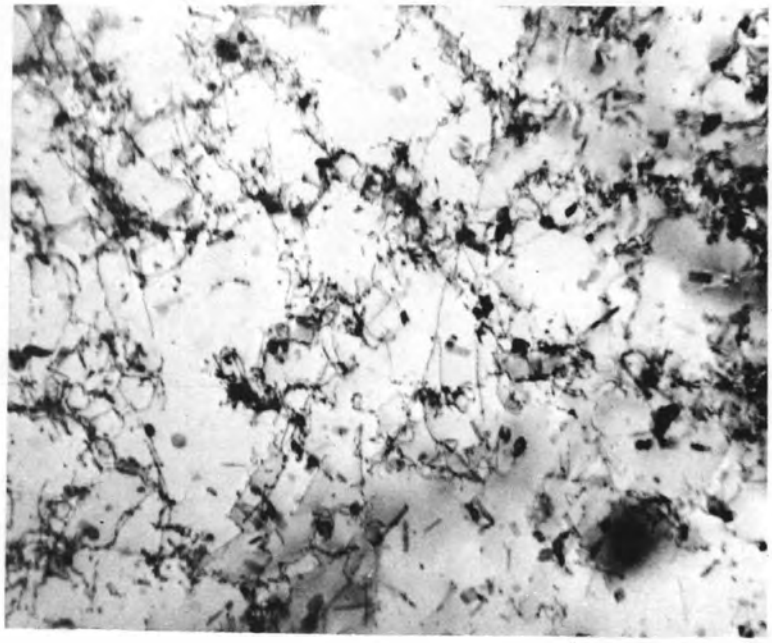

c 1μm

Figure 3. (b) 1 month, (c) 4 months.

d

1μm

Figure 3. (d) 12 months.

e

1μm

Figure 3. (e) 12 months.

by numerous fine precipitates, in addition to particles in the matrix (Fig. 3b).

8.2.2.3 Tempering at 1050°F

Tempering of this alloy at 1050°F from 1 to 12 months resulted in various types of microstructures. After one month of tempering, very little change occurred in the microstructure as shown in Fig. 1c, which is very similar to that of the N & T condition. No grain growth occurred, the average grain size being about 28 μm. Tempering for two months produced recrystallization in some areas and colonies of fine recrystallized grains reduced the grain size to 24 μm. Tempering for 4, 8 and 12 months produced significant grain growth, especially in areas that underwent complete recrystallization. For these longer tempering times, the average grain size increased to 35 to 38 μm.

Examination of these materials by TEM indicated that the subgrain structure, initially present in the N & T condition, is still present after tempering at 1050°F. Figs. 4a and b show micrographs taken from a material tempered for 1 month at 1050°F. They illustrate the coexistence of the regular ferrite and the one containing a subgrain structure. In this condition, both types of ferrite were found in about equal amounts, but in the material tempered for longer periods of time, a steady decrease of the areas containing subgrains was observed. After 12 months of tempering, only about 10% of the examined area contained a subgrain structure, where small, recrystallized grains were also found as shown in Fig. 4c. Second

a

1μm

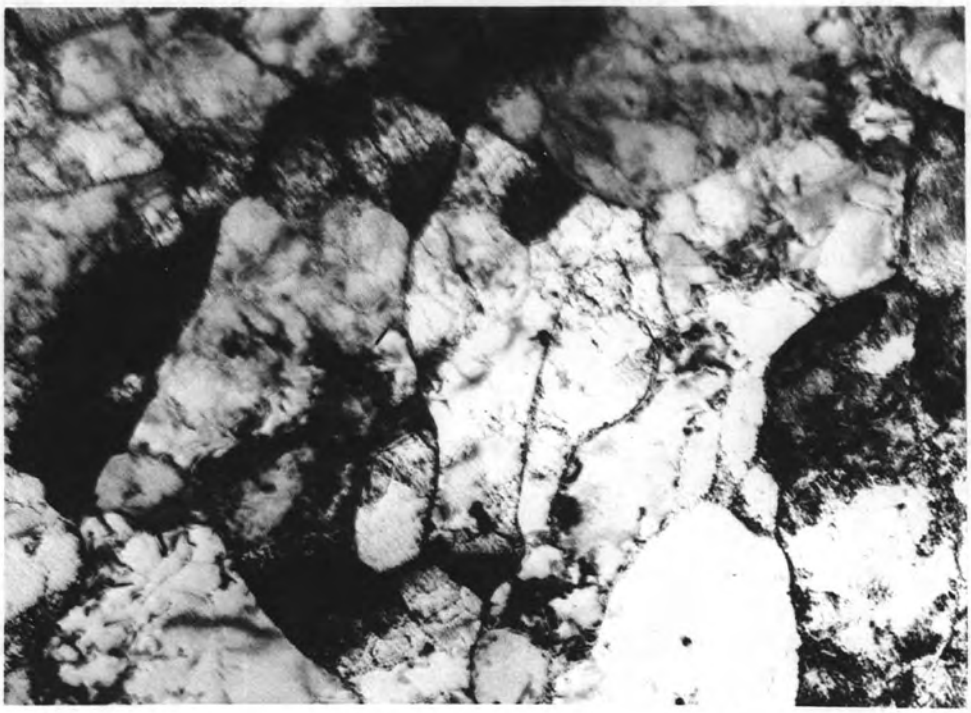

b

1μm

Figure 4. Electron micrographs of low carbon Cr-Mo steel tempered at 1050°F for (a) 1 month, (b) 1 month.

c

1μm

Figure 4. (c) 12 months.

d

1μm

Figure 4. (d) 12 months.

e 1μm

Figure 4. (e) 12 months.

phase particles were located mainly in the regular ferrite and, to a lesser extent, in the subgrain structure. In the samples tempered for 1 or 2 months, only fine precipitates in the regular ferrite regions were present (Fig. 4a). These were identified as fcc, CrN particles having a_0 = 4.11Å. In materials tempered for 4 months or more, colonies of needle-shaped precipitates were commonly found (Fig. 4d). Each of the needles averaged about 1 μm in length and 250Å in thickness, and were identified as the M_2C type. The long axis of the needles was parallel to the $\langle 211 \rangle_\alpha$ directions of the ferrite matrix, although other unidentified orientations also existed. Another important feature of these needles was the presence of very small particles on the needles themselves (Fig. 4d), which suggests that an "in-situ" carbide transformation is taking place. The new carbide being formed is expected to be of the M_6C type.[4] Fig. 4c shows a regular ferrite region indicating extensive precipitation at dislocations in these materials.

8.3 MECHANICAL PROPERTIES

8.3.1 Room Temperature Tensile Properties

Room temperature tensile testing was performed in 2-1/4Cr-1Mo steels of various carbon content (.009, .03 and .12%C) in the normalized (N), normalized and tempered (N & T), and long-term tempered conditions. The results obtained for the N and N & T conditions have already been presented.[5] This report describes the results obtained for materials tempered at 850, 950 and 1050°F for periods ranging from 1 to 19 months, subsequent to the N & T treatment.

As shown in Fig. 5, long-term tempering often produced significant changes in the yield strength of the materials. Tempering of the higher carbon material at 850 and 950°F caused a slight drop in the yield strength (3 Ksi) during the first month of tempering. No further change was detected for longer-tempering times, except for a small hardening effect after 12 or 19 months of tempering at 850°F. At the tempering temperature of 1050°F, the yield strength decreased continuously up to 12 months. This trend appears to continue for a longer tempering time.

Intermediate carbon materials (.03%C) showed a 38 to 45% drop in the yield strength when the N & T samples were tempered at 950 or 1050°F for 1 month. However, the yield strength was nearly unchanged, when they were tempered for longer periods of time at these temperatures. Tempering at 850°F, on the other hand, produced a steady drop in the yield strength as the tempering time increased. The rate of decrease beyond 4 months of tempering was higher at 850°F than those at 950 or 1050°F. Consequently, after 19 months of tempering at 850°F, the yield strength of this material was only 3 Ksi above that of materials tempered 19 months at 950 or 1050°F.

In the case of the low carbon (.009%C) materials, a similar but less drastic reduction in the yield strength occurred when these materials were tempered for long periods of time. As seen in Fig. 5, tempering at 850 and 1050°F steadily decreased the yield strength. In comparison to the initial yield strength of these materials (N & T condition), after 19 months of tempering at 850 and 1050°F, the yield strength decreased by 15 and 35%, respectively. In materials tempered

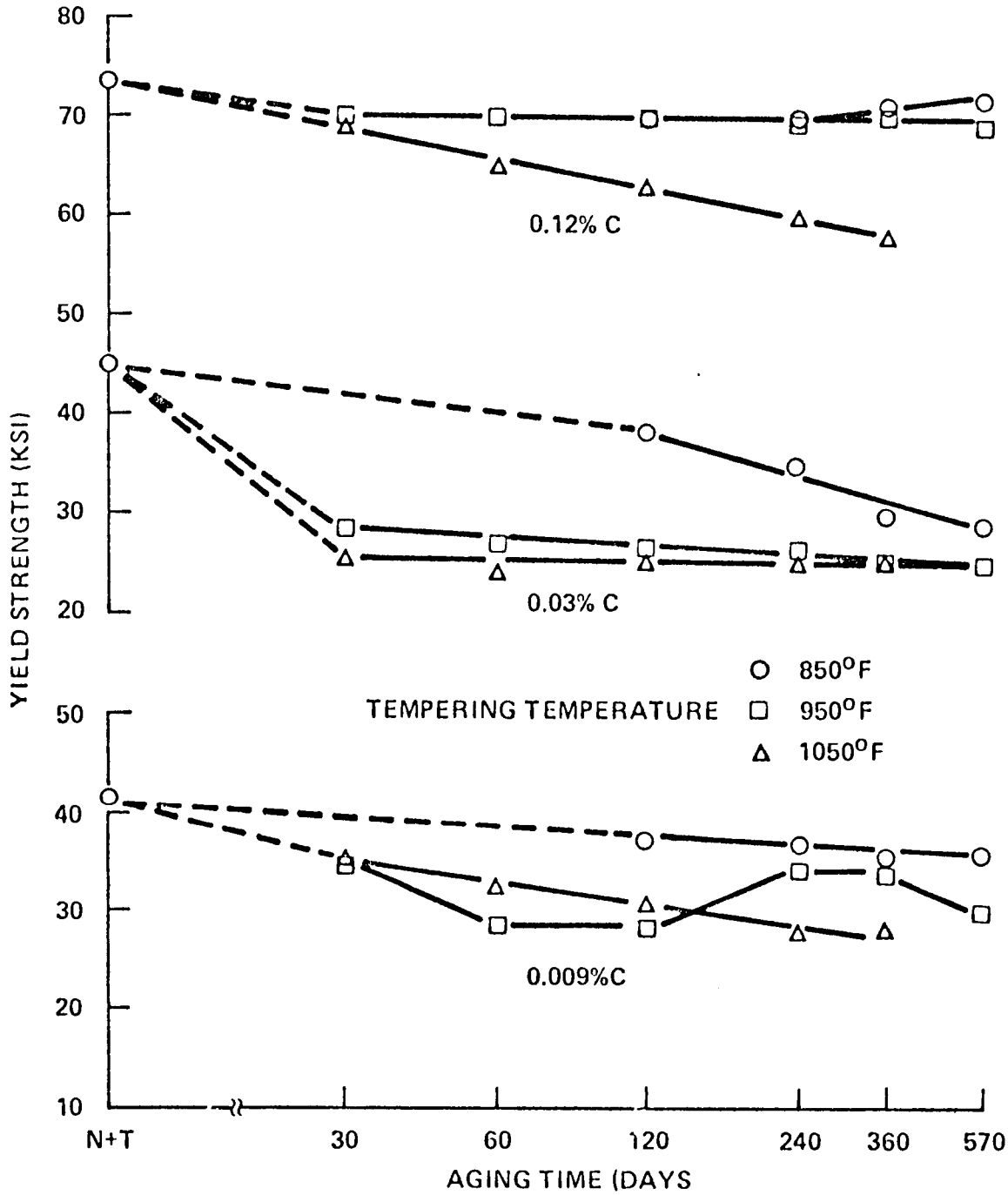

Fig. 5. Room temperature yield strength of 2-1/4Cr-1Mo steels after long tempering.

at 950°F, an initial decrease in the yield strength was followed by a hardening effect, which occurred after 4 months of tempering. This secondary hardening effect at 950°F may result from extensive carbide precipitation at dislocations. The initial softening that preceeds the hardening effect is possibly related to the recrystallization of irregular ferrite, as the microstructure of regular ferrite was not affected significantly via tempering.

8.3.2 Creep Properties

The steady state creep rate has been measured as a function of stress for three 2-1/4Cr-1Mo steels (.009, .03 and .12%C) in the normalized and tempered condition (1 hr. at 1300°F). The results are shown in Fig. 6. The creep stresses at 1050°F for the three materials decrease more steeply below the steady state creep rate of 10^{-5} to 10^{-4}. The stress exponent n, $\left(\frac{d \log \dot{\epsilon}}{d \log \sigma}\right)$, ranges from 8 to 10 in., the high stress region, decreasing to 2 at the lower stress region. While it is difficult to assign a specific creep mechanism at present, it is likely that a significant contribution to the creep rate arises from grain boundary sliding at lower stresses. A consequence of this is that creep stresses at lower creep rates decrease much more rapidly than the values extrapolated from the higher creep rate data. The creep data in Fig. 6 indicate creep strengths (0.01 % in 1000 hr) of 1.1-2.7 Ksi at 1050°F, which is significantly lower than the allowable stress prescribed by the ASME Boiler and Pressure Vessels Code for this steel (6.5 Ksi at 1050°F). At temperatures below 1050°F such as 930 or 850°F, a similar lowering of creep stress appears to occur.

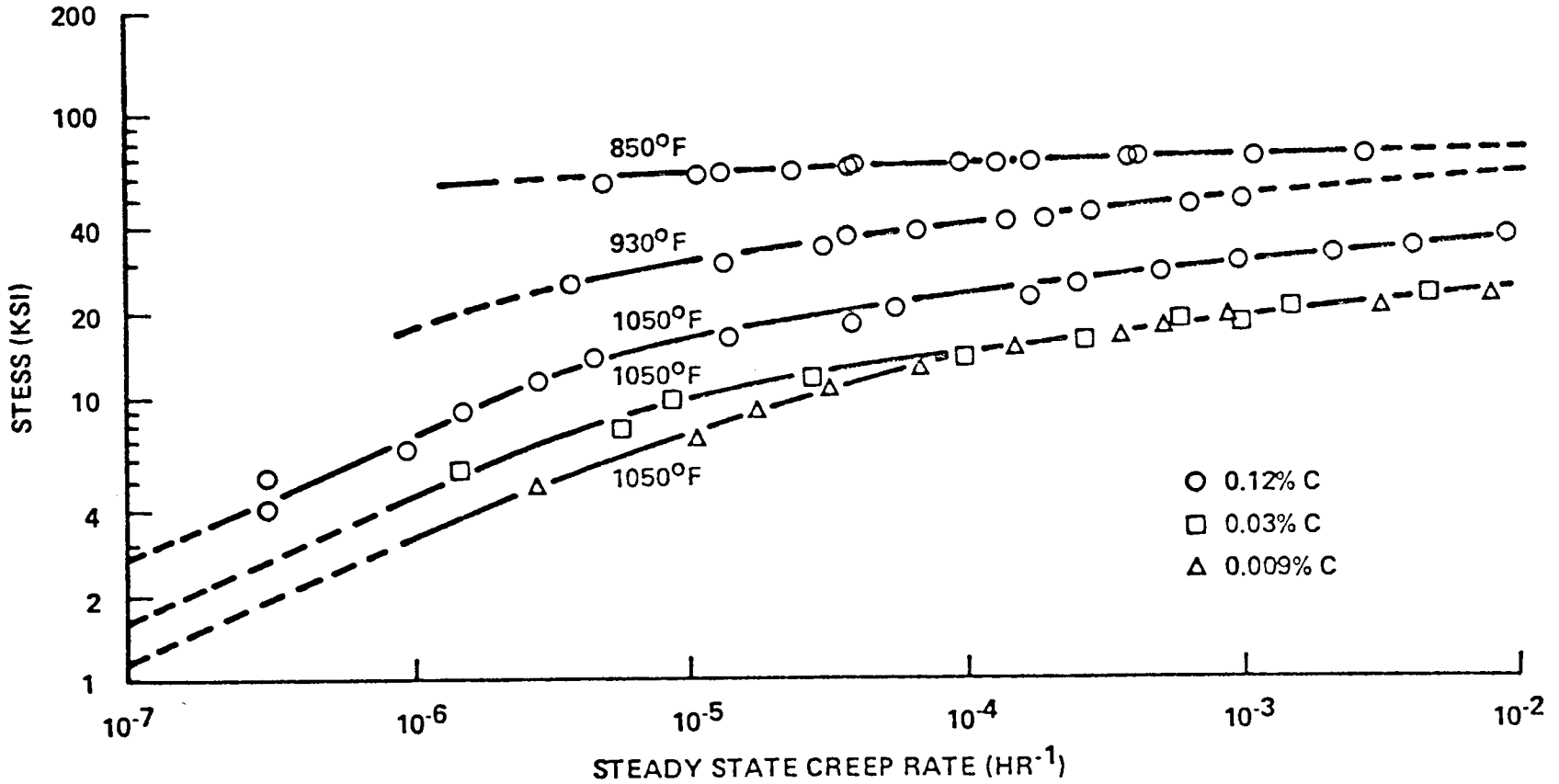

Fig. 6. Creep stress vs. steady state creep rate of 2-1/4Cr-1Mo steels, normalized and tempered (1300°F).

Creep tests of intermediate and low carbon alloys at 850 and 950°F also revealed unusually large instantaneous strains upon stress increases. As shown in the creep curves (Fig. 7), strain-bursts as large as 1% (within several seconds) were produced when the creep stress was increased slightly. This observation suggests that an overload may reduce the creep life and lead to premature failures.

8.4 REFERENCES

1. K. Ono, A.J. Ardell and A.S. Tetelman, Reactor Steels Studies, Quarterly Progress Report, UCLA-34P177-15, March 1973.
2. K. Ono, A.J. Ardell and A.S. Tetelman, Reactor Steels Studies, Quarterly Progress Report, UCLA-34P177-16, April 1973.
3. K. Ono, A.J. Ardell and A.S. Tetelman, Reactor Steels Studies, Quarterly Progress Report, UCLA-34P177-17, August 1973.
4. J.H. Woodhead and A.G. Quarrell, J.I.S.I., 1965, 203, 605-620.
5. K. Ono, A.J. Ardell and A.S. Tetelman, Reactor Steels Studies, Quarterly Progress Report, UCLA-34P177-13, September 1972.

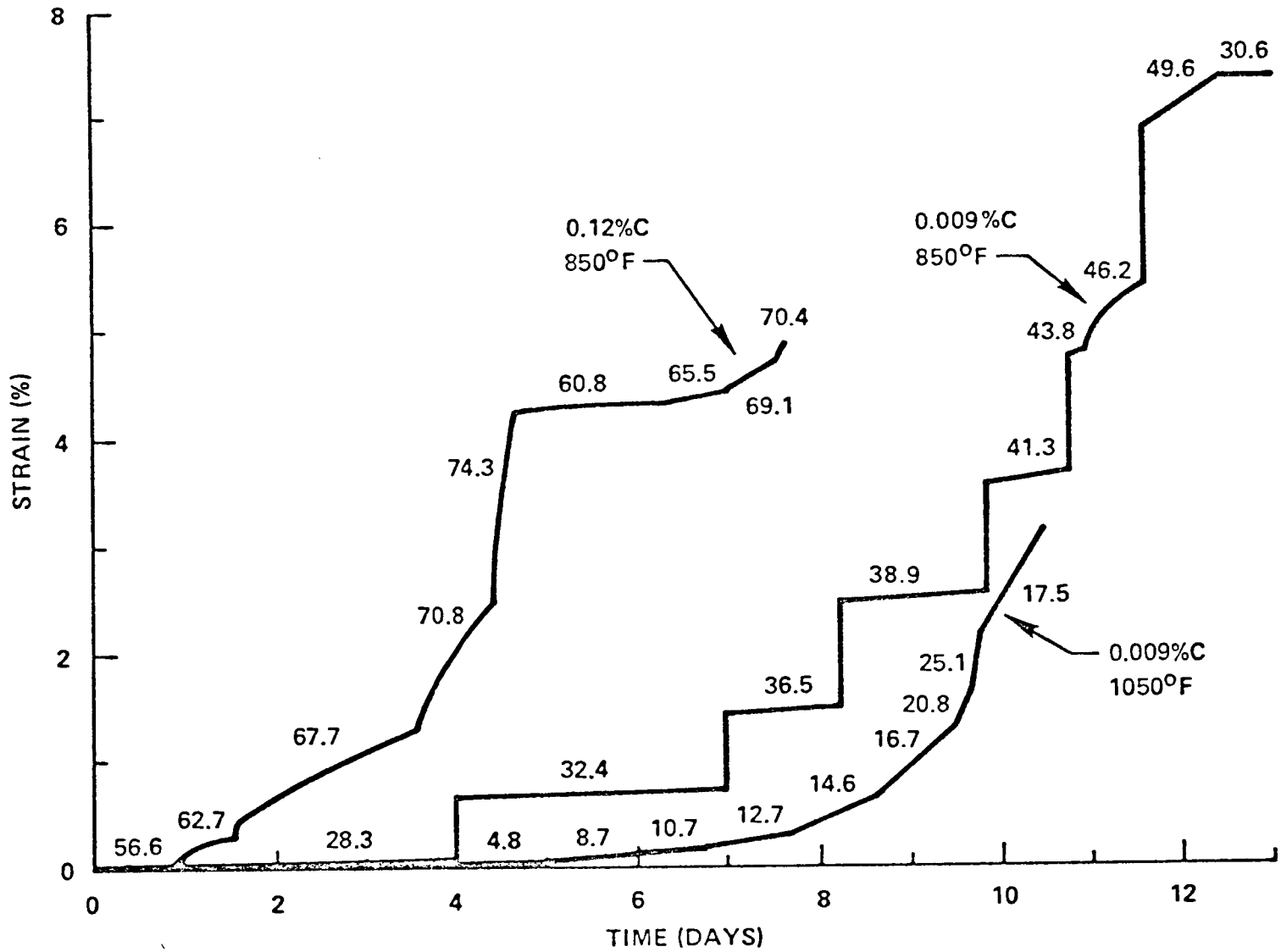

Fig. 7. Creep curves of 2-1/4Cr-1Mo steels

INDEX

Test	Material	Page
Bend		
	Inconel 718	8, 9
Chemical Analysis		
	type 316 SS	110, 111
Creep Test Data		
Base-Line Data		
	type 304 SS plate	61–81, 201–209
	type 304 SS welded plate	209
	overlaid type 304 SS forging	168–171
	type 308 CRE SS weld metal	140–143
	2 1/4 Cr-1 Mo	279–281
Correlations		
	2 1/4 Cr-1 Mo steel	169–172
	type 304 SS	190–193, 242–249
Cyclic Creep		
	decarburized 2 1/4 Cr-1 Mo	158–161
	type 304 SS	193–195
Dislocation Mechanisms		
	type 304 and 316 SS	226–31
Effects of Aging		
	type 304 SS	108–109
	type 316 SS	119–123
Heat-to-Heat Variation		
	type 304 SS	81–84
	type 316 SS	116–123
Strain Limits		
	type 316 SS	119–126
Elastic Constants		
	2 1/4 Cr-1 Mo	126–133

Test	Material	Page
Fatigue Test Data		
Correlations		
	Incoloy 800, type 304 SS	235–244
Effect of Environment and Frequency	type 304 SS	26–30
Effect of Hold Time		
	type 304 SS	1–9
Effect of Strain Rate		
	type 304 SS	1–9, 26–30
Effect of Surface Finish		
	type 304 SS	12–26
Stress and Strain Distribution Substructure	2 1/4 Cr-1 Mo	134–135
	types 304 and 316 SS, Incoloy 800	232–235
Crack Growth Rate Data		
Correlations		
	types 304 and 316 SS weldments	47–54
	type 308 SS weldment (J-Integral)	55–58
Effect of Heat Treatment		
	type 304 SS weld metal	8–13
Effect of Stress Intensity Factor	type 308 SS weld metal	8–13
	types 308 and 316 weldments	47–54
	2 1/4 Cr-1 Mo steel	172–174
Effect of Test Temperature		
	type 304 and 316 SS weldments	47–54
Hardness		
	type 304 SS	249–252
	type 316 SS	252–258

Test	Material	Page
Impact Test Data		
Effect of Heat Treatment		
	Inconel 718	1–9
Microstructure		
	type 304 SS	104–107
	2 1/4 Cr-1 Mo	261–276
Tensile Test Data		
	overlaid type 304 SS forgings	161–168
Base-Line Data		
	2 1/4 Cr-1 Mo steel	152–158, 276–279
Correlations		
	type 304 SS	175–190
Deformation Characteristics		
	type 308 CRE SS weldments	143–151
Effect of Aging		
	type 304 SS	84–103
	type 316 SS	119–123
Effect of Postweld Heat Treatment	type 308 CRE SS	135–140
Heat-to-Heat Variations		
	type 316 SS	110–116

ORNL-4948
UC-79b, -h, -k
(Liquid Metal Fast
Breeder Reactors)

INTERNAL DISTRIBUTION

(3) Central Research Library
ORNL — Y-12 Technical Library
Document Reference Section
(10) Laboratory Records Department
Laboratory Records, ORNL RC
ORNL Patent Office
G. M. Adamson, Jr.
R. J. Beaver
M. Bender
R. G. Berggren
C. R. Brinkman
D. A. Canonico
J. Corum
F. L. Culler
J. E. Cunningham
J. H. DeVan
G. Fee
M. H. Fontana
W. R. Gall
B. L. Greenstreet
J. P. Hammond
W. O. Harms
(5) M. R. Hill
D. O. Hobson
F. J. Homan
P. R. Kasten
R. T. King
R. L. Klueh
K. C. Liu
(20) A. L. Lotts
R. E. MacPherson
W. R. Martin
W. J. McAfee
H. E. McCoy
H. C. McCurdy
W. T. McDuffee
C. J. McHargue
P. Patriarca
S. Peterson
H. Postma
C. E. Pugh
P. L. Rittenhouse
A. C. Schaffhauser
J. L. Scott
Myrtleen Sheldon
G. M. Slaughter
W. J. Stelzman
J. O. Stiegler
R. W. Swindeman
D. B. Trauger
W. E. Unger
T. N. Washburn
J. R. Weir, Jr.
G. D. Whitman
J. W. Woods
R. G. Wymer
T. Yahr

Subcontractors and Consultants

Atomic International, P.O. Box 309, Canoga Park, CA 91304

R. I. Jetter
A. Little
J. Shively

Babcock & Wilcox Company, P.O. Box 835, Alliance, OH 44601

W. E. Leyda
C. C. Schultz
D. B. Van Fossen

Battelle Memorial Institute, 505 King Avenue, Columbus, OH 43201

C. E. Jaske
E. C. Rodabaugh
G. H. Workman

Brown University, Providence, RI 02912

W. N. Findley

The Catholic University of America, Washington, DC 20017

A. J. Durelli

Combustion Engineering, Inc., 911 West Main Streeet, Chattanooga, TN 37401

T. Cullen
T. Ward

E. P. Esztergar, 7993 Prospect Place, La Jolla, CA 92037

Foster Wheeler Corporation, Nuclear Department, 110 South Orange Avenue, Livingston, NJ 07039

W. R. Apblett, Jr.
R. Barratt

Franklin Institute Research Laboratories, The Benjamin Franklin Parkway, Philadelphia, PA 19103

Zenons Zudans

General Electric Company, 175 Curtner Ave., San Jose, CA 95125

Y. R. Rashid

Gulf General Atomic, P.O. Box 1608, San Diego, CA 92138

M. Jakub
D. I. Roberts

O'Donnell & Associates, Inc., 5100 Centre Avenue, Pittsburgh, PA 15232

W. J. O'Donnell

Pennsylvania State University, University Park, PA 16802

S. Y. Zamrik

G. V. Smith, Consulting Engineer, 104 Berkshire Road, Ithaca, NY 14850

Teledyne Materials Research Company, 303 Bear Hill Road, Waltham, MA 02154

W. E. Cooper
J. L. McLean

University of Alabama, College of Engineering, P.O. Box 1968, University, AL 35486

E. Carden
J. H. Frye

University of California, Lawrence Radiation Laboratory, Inorganic Materials Research Division, Berkeley, CA 94720

Leo Brewer

University of California, Revelle College, Department of Physics, P.O. Box 109, La Jolla, CA 92037

Walter Kohn

University of Cincinnati, Materials Science and Metallurgical Engineering Department, Cincinnati, OH 45221

J. Moteff

University of Illinois, Department of Physics, Urbana, IL 61801

W. S. Williams

EXTERNAL DISTRIBUTION

USAEC DIVISION OF REACTOR RESEARCH AND DEVELOPMENT, Washington, DC 20545

(2) Director

USAEC-RRD SENIOR SITE REPRESENTATIVE, Oak Ridge National Laboratory, Oak Ridge, TN 37830

USAEC OAK RIDGE OPERATIONS OFFICE, P.O. Box E, Oak Ridge, TN 37830

Research and Technical Support Division

USAEC TECHNICAL INFORMATION CENTER, Office of Information Services, P.O. Box 62, Oak Ridge, TN 37830

For distribution as shown in TID-4500 Distribution Category, UC-79b (Fuels and Materials Engineering Development); UC-79h (Structural Materials and Design Engineering); UC-79k (Components)